Surface Modification of Metal Oxides to Induce Multifunctionality at the Nanoscale

Thesis submitted for the award of the degree of

Doctor of Philosophy

in

Chemistry (Physical)

by

Monalisa Pal

Department of Chemistry

University of Calcutta

Kolkata, India

October, 2015

Dedicated to my beloved parents…

Acknowledgement

First of all I would like to convey my gratitude to my supervisor Professor Kalyan Mandal for his immense help, inspiration, valuable discussions, and humble guidance. He always encouraged and motivated me to think and execute my research work independently in challenging areas. Without his wisdom, patience, and support any of my research work would not get success. Thank you sir for providing me opportunity to work in your laboratory and making my Ph.D. life very much enjoyable.

I am grateful to S. N. Bose National Centre for Basic Sciences (SNBNCBS), Kolkata, and Department of Science and Technology (DST), India, for providing a beautiful campus, advanced instrumental facilities, wonderful research environment, and financial supports.

I would like to thank Dr. Deepak Kumar Sinha and Mr. Mahesh Agarwal from IACS, Kolkata for providing fluorescence microscopy facility. I am thankful to Dr. Krishnakumar S. R. Menon and Mr. Sukanta Barman from SINP, Kolkata for providing XPS facility. I am grateful to Mr. Subhas Chandra Bera for performing TCSPC measurements several times required for my research work.

I am also obliged to the director of S. N. Bose National Centre for Basic Sciences, Professor Arup Kumar Raychaudhuri for his great effort in increasing the experimental facility at the centre, which has proved to be a boon for our research work. I am also thankful to Professor Sandip Kumar Chakroborty whose guidance at my critical time led me towards correct way to fulfill my dream to have my Ph.D. I thank all those faculty members of our centre whose encouragement and enthusiasm have helped to improve my research work. I thank all the staff members of this institute for their sincere cooperation and help. I would like to thank all the technical staff members specially Urmi Di, Samik Da, Dipankar Da, and Amit Da for their help in sample characterization.

I would like to acknowledge my seniors and labmates: Gobinda Da, Arka Da, Shyam Da, Debasish Da, Rajasree Di, Madhuri Di, Arup Da, Ashutosh Da, Rupali, Mahebub, Keshab, Anirban, Souvanik, Indranil, and Deblina for providing me a homely and cheerful environment. We have learned a great deal from each other and I thank them for their patience and helping attitude. I must thank Arup Da and Ashutosh Da for being great source

List of Publications

*1. **M. Pal**, R. Rakshit, and K. Mandal

"Surface modification of $MnFe_2O_4$ nanoparticles to impart intrinsic multiple fluorescence and novel photocatalytic properties"

ACS Applied Materials & Interface, 2014, 6, 4903.

*2. **M. Pal**, R. Rakshit, and K. Mandal

"Facile functionalization of Fe_2O_3 nanoparticles to induce inherent photoluminescence and excellent photocatalytic activity"

Applied Physics Letter, 2014, 104, 233110.

*3. **M. Pal**, A. K. Singh, R. Rakshit, and K. Mandal

"Surface chemistry modulated introduction of multifunctionality within Co_3O_4 nanocubes"

RSC Advances, 2015, 5 (21), 16311-16318.

*4. **M. Pal**, A. Kundu, R. Rakshit, and K. Mandal

"Ligand induced evolution of intrinsic fluorescence and catalytic activity from cobalt ferrite nanoparticles"

ChemPhysChem, 2015, 8(16), 1627-1634. **(Cover Article)**

*5. **M. Pal**, R. Rakshit; M. Mandal, and K. Mandal

"Surface modification of α-Fe_2O_3 nanoparticles to develop as intrinsic photoluminescent probe and unprecedented photocatalyst"

Magnetics, IEEE Transactions on, 2014, 50 (11), 1-4.

6. R. Rakshit, **M. Pal**, M. Mandal, and K. Mandal

"Charge transfer mediated magnetic response of cobalt ferrite nanoparticles"

Materials Letters, 2015, 151, 64-67.

7. R. Rakshit, M. Mandal, **M. Pal**, and K. Mandal

"Tuning of magnetic properties of $CoFe_2O_4$ nanoparticles through charge transfer effect"

Applied Physics Letter, 2014, 104, 092412.

8. R. Rakshit, D. Sarkar, **M. Pal**, K. Serite, M. Tonouchi, and K. Mandal

"Acoustic vibration induced high electromagnetic responses of Fe_3O_4 nano-hollow spheres in THz regime"

Journal of Physics D: Applied Physics, 2015, 48, 245301.

9. A. Giri, N. Goswami, **M. Pal**, M. T. Zar Myint, S. Al-Harthi, A. Singha, B. Ghosh, J. Dutta, and S. K.Pal

"Rational surface modification of Mn_3O_4 nanoparticles to induce multiple photoluminescence and room temperature ferromagnetism"

Journal of Materials Chemistry C, 2013, 1 (9), 1885-1895.

10. R. Rakshit, **M. Pal**, and K. Mandal

"Terahertz conductivity study of magnetite nanostructures"

AIP Conference Proceedings, 2015, 1665, 050007.

11. R. Rakshit, **M. Pal**, A. Chaudhuri, M. Mandal, and K. Mandal

"Synthesis of highly porous $CoFe_2O_4$ nano-hollow spheres with

excellent bilirubin adsorption activity"

Manuscript under reveiw.

 ***12. M. Pal**, R. Rakshit , A. K. Singh, and K. Mandal

"Ultra high supercapacitance for ultrasmall Co_3O_4 nanocubes"

Manuscript under reveiw.

* These publications are included in this thesis.

Contents   Page

Chapter 2: Experimental details

Chapter 3: Chemical Functionalization of Fe_2O_3 Nanoparticles

Chapter 4: Surface Functionalization of MnFe$_2$O$_4$ Nanoparticles

Chapter 7: Improved Electrochemical Properties of Co$_3$O$_4$ Nanocubes

Chapter 8: Conclusion and Scope for Future Work   166-168

Chapter 1 | Introduction

This introductory chapter consists of literature review of various works that motivated me to work in this specific field, a brief outline of the entire work done by me, and theoretical aspects required to explain the findings.

1. Introduction

1.1. Nanomaterials

Nanomaterials (NMs) are of great excitement to the researchers due to evolution of new phenomena and significant improvement of various properties as compared to their bulk counterpart. NMs are usually defined to have at least one dimension within the range of 1-100 nm (1 nm = 10^{-9} m). Due to the large surface area to volume ratio and quantum confinement of NMs, they interact with each other, surrounding substances, light, electric, and magnetic field in different way. The property of a particular material greatly differs when the size and/or morphology changes ranging from sphere, cube, disc, rod, wire, tube, film, etc.[1-4] NMs have been synthesized with large chemical diversity, consisting metals,[5] metal oxides,[6] semiconductors,[7, 8] polymers,[9] and carbonaceous materials.[10, 11] Having novel optical, magnetic, thermal, electrochemical, electrical properties, NMs have become promising candidate to solve challenges in the field of medicine,[12, 13] energy storage,[14, 15] catalysis,[16-18] sensing,[19] and information technology.[20]

1.2. Metal Oxide Nanomaterials

Metal oxide nanostructures or nanoarrays play a very crucial role in many areas due to their unique physical and chemical properties resulting from the small size and a high density of corner or edge surface sites. Transition metal oxide nanostructures (such as oxides of iron (Fe), manganese (Mn), cobalt (Co), nickel (Ni)) have attracted key attention due to their low cost, high chemical stability, easy synthesis procedures, and superior optical, electronic, magnetic, catalytic, and electrochemical properties.[21-28]

1.2.1. Crystal Structure of Different Transition Metal Oxides

Transition metal oxides are found in a wide range of oxidation states as transition metals have five d orbitals. For example, Fe exhibits valency from -2 to +6, although

+2 and +3 are most common. Commonly found Fe oxides are Wüstite (Fe (II) Oxide, FeO), Hematite (Fe (III) Oxide, α-Fe_2O_3), Magnetite (Fe (II, III) Oxide, Fe_3O_4) and their derivatives. FeO has rock salt structure with cubic closed packed (*ccp*) structure with Fe^{2+} ions in octahedral sites. α-Fe_2O_3 demostrates corundum structure (as exhibited in Figure 1.1).[29] This structure is described as a hexagonal closed packed (*hcp*) array of oxygen atoms with two-thirds of the octahedral holes occupied by Fe atoms.[30] Fe_3O_4, also called ferrite, is a mixed oxide having cubic inverse spinel structure, where the oxide ions are in a face-centred *ccp* array, the divalent metal ions (Fe^{2+}) occupy octahedral sites and the trivalent ions (Fe^{3+}) are equally divided among tetrahedral and octahedral sites. Other members of ferrite develop replacing Fe^{2+} by other divalent ions such as Mn^{2+}, Co^{2+}, Ni^{2+} etc. Co forms compounds having its oxidation states ranging from -3 to +4, though +2 and +3 are commonly found. Cobaltous oxide (Co (II) oxide, CoO) has rock salt structure. Cobaltosic oxide (Co (II, III) oxide, Co_3O_4) adopts normal spinel structure where Co^{2+} ions acquire tetrahedral sites and Co^{3+} ions occupy octahedral sites. Figure 1.2 demonstrates crystal structure of normal spinel (AB_2O_4) where trivalent B ion and divalent A ion stay in octahedral and tetrahedral sites, respectively. During synthesis of nanostructures depending on reaction conditions such as temperature, pressure, time, nature, and amount of capping agent, atoms arrange themselves in various ways resulting growth of crystal along preferred orientation leading to formation of different crystal phases and/or different shapes of same crystal structure, with same elemental composition.
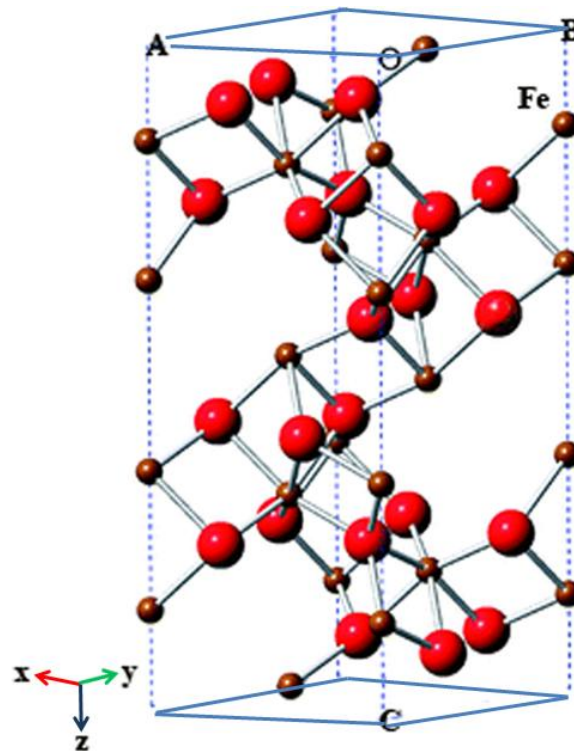
Figure 1.1. Crystal structure of the hematite. (the brown ball is Fe^{3+} and the red ball is O^{2-}). (© Xiong et al. *CrystEngComm* **2011,** *13* (23), 7114-7120.)

AB$_2$O$_4$ spinel

○ Oxygen

● B-atoms in octahedral sites

● A-atoms in tetrahedral sites
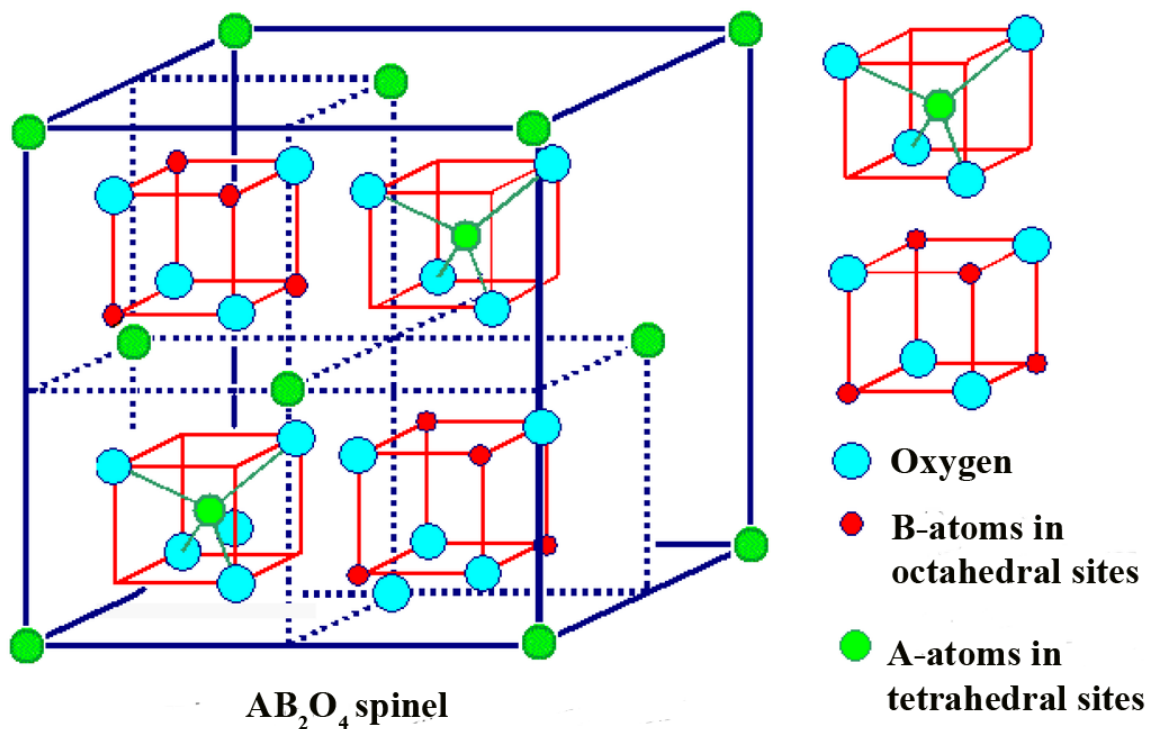
Figure 1.2. Crystal structure of AB_2O_4. (red ball is B^{3+}, green ball is A^{2+} and the blue ball is O^{2-}).(© chemwiki.ucdavis.edu)

1.2.2. Magnetic Properties

Some of the transition metal oxides (ex- MnO, NiO, FeO, CoO, Co_3O_4 etc.) show antiferromagnetism due to super exchange, where the spins on different nuclei interact cooperatively but in such a way as to cancel out the magnetic moments. For instance in the *ccp* crystal of CoO, several linear Co-O-Co arrangements exist. In each of this, the dz^2 orbital on the Co can overlap with the $2p_z$ on oxygen, leading to partial covalency. The oxide ion of Co-O bond has a closed shell and so there is another $2p_z$ electron, which must have opposite spin. This electron forms a partial bond with the next Co, as a consequence, the dz^2 on this Co pairs with the $2p_z$ electron of opposite spin. The net result is that adjacent Co ions have opposed spins. Ions on octahedral sites interact directly with each other and their spins align parallel. In cubic spinel structure, ions on octahedral sites interact directly with each other and their spins align parallel, and they also interact with those on tetrahedral sites but in this case, they interact through the oxide ions and the spins align antiparallel through super exchange. In ferrites, having molecular formula AFe_2O_4 (where A^{2+} = divalent ions of Fe, Mn, Ni, Co etc.), the Fe^{3+} ions on tetrahedral sites are aligned antiparallel to those on octahedral sites, so that there is no net magnetization from these ions. A^{2+} ions, having unpaired electrons, tend to align their spins parallel with those of Fe^{3+} on adjacent octahedral sites, and hence with those of other A^{2+} ions. This produces a resultant ferromagnetic interaction for ferrites where A^{2+} has unpaired electrons. Two key issues dominate the magnetic properties of NMs: finite-size effects and surface effects which give rise to various special features. Magnetic domains have dimensions within the range of 10-1000 nm which are comparable to the size of nanocrystals. So if the crystal size approaches to single domain dimension upon scaling down the particle size of ferromagnetic material, all the spins get aligned to each other, so the demagnetization becomes difficult. When the particle size becomes smaller than the single domain dimension, then the force aligning the spins becomes so weak that it cannot overcome thermal randomization in absence of any external magnetic field. This phenomenon is called superparamagnetism. Generally, surface anisotropy in NMs is found to be one order

of magnitude higher than the bulk value which is due to larger fraction of superficial ions in smaller particles.[31] This surface spins are disordered because they reside within an uncompensated coordination sphere due to broken bonds, vacancies and also due to bond formation with capping organic molecule.[32] Thus the surface anisotropy makes the surface layer magnetically harder than the core region of NMs.

1.2.3. Electrochemical Properties

Transition metal oxide nanostructures have attracted immense attention of researchers due to their superior electrochemical performance resulting from the multiple oxidation states. Different transition metal oxides show excellent performance in lithium (Li)-ion batteries,[33] super capacitance,[34] and water splitting.[35] Some transition-metal oxides (MO, where M is Co, Ni, Cu, Fe etc.) have excellent efficiency as Li-ion batteries.[33] RuO_2,[36] MnO_2,[34] NiO,[37, 38] Co_3O_4,[39] $Ni(OH)_2$,[40] $Co(OH)_2$,[41] $NiCo_2O_4$[42, 43] etc. show remarkable supercapacitance property. Some metal oxide semiconductors have appropriate band gap to be used as photoanode for solar-to-hydrogen conversion, such as $\alpha\text{-}Fe_2O_3$, $ZnFe_2O_4$, $CuW_{1-x}Mo_xO_4$, $Cu_3V_2O_8$ etc.[35] Supercapacitance is the storage of electrical energy by electron transfer between electrode and electrolyte through electrosorption, oxidation-reduction reactions, and intercalation processes.

There are two kinds of supercapacitors (SCs), which are differentiated by their charge-storage mechanisms. In electrical double layer capacitors (EDLC), charge is stored by rapid adsorption/desorption of electrolyte ions on high-surface-area carbon materials. In pseudocapacitors, charge is stored and released in Faradaic electron-transfer processes of a metal oxide or conducting polymer. It is also possible to combine carbon materials with metal oxides or conducting polymers.[44] SCs deliver energy at high charge-discharge rates, so they have higher power density than other energy-storage devices such as Li-ion batteries and fuel cells. However, they also have lower energy densities than batteries and fuel cells. Therefore, an important application of SCs is to assist higher energy density storage devices under intermittent high-power conditions such as in electric vehicles (trains, planes, and

automobiles), internal back-up power for computers, smart phones, smart meters, and energy harvesting.

1.3. Surface Modification of Nanomaterials

Surface modification of NMs is necessary to tune their optical, magnetic, catalytic, and electrochemical properties to suit different applications in the field of nanotechnology. There are different types of surface modification such as (a) chemical functionalization, (b) plasma assisted coating, (c) scaling down the size of NMs to improve surface to volume ratio.

Chemical functionalization is carried out for various purposes, firstly synthesis of the nanostructures, generally, involves surfactant molecules that bind to their surface, which stabilize the nuclei and larger nanoparticles (NPs) against aggregation by a repulsive force, as well as control the growth of the NPs in terms of rate, final size or geometric shape. Secondly, NPs can be functionalized with suitable ligands so that, they can be dispersed in either aqueous or organic solvent due to hydrophilic or hydrophobic behavior, respectively.[45] Polar or charged ligand molecules (citric, tartaric, mercaptopropionic, amino acids, vitamin C, glucose, etc.) provide solubility in polar or aqueous solvents.[46] With proper surface modification, NPs can be functionalized by special groups (e.g. –OH, –COOH, –NH$_2$, –SH), which are suitable for further modifications by the attachment of different bioactive molecules for various applications. NPs with nonpolar ligand molecules having long hydrocarbon chains are only soluble in nonpolar organic solvents, e.g. hexane, toluene, chloroform etc. Fabrication of oil-soluble type NPs is very important for obtaining monodisperse NPs. The most common organic compounds are oleic acid and oleyamine, which have a C$_{18}$ tail with a cis-double-bond in the middle, forming a kink. Such kinks have been postulated as being necessary for effective stabilization. Certain amphiphilic ligand molecules, like poly (ethylene glycol) (PEG), block copolymers (such as HAMAFA-b-DBAM)[47] make the NPs soluble in a number of solvents, with intermediate polarity. Another way is to use a ligand exchange

procedure to change the polarity of the hydrophobic layer for being hydrophilic. It involves adding an excess of ligand to the NP solution, resulting in the displacement of the original ligand on the surface of NPs.[48] Thirdly, ligands should be chosen according to affinity of NP core and the functional groups of the ligands, such as thiol to gold, carboxylic acids to metal oxides, trioctylphosphine (TOP), or its oxide (TOPO), binding preferentially to the Cd or Zn atoms of the quantum dots (QDs).[49, 50] The ligand molecules get bound to the particle surface by attractive interactions, such as chemisorption, electrostatic attraction or hydrophobic interaction, most commonly provided by a head group of the ligand molecule. Compared with small molecules and surfactants, polymer functionalization not only provides multifunctional groups and more colloid stability, but also plays a significant role regarding its biological fate (i.e., pharmacokinetics and biodistribution). Thus, a large number of natural and synthetic biodegradable polymers, such as poly (aspartate), poly (saccharides), gelatin, starch, alginate, poly (acrylic acid), PEG, poly (D,L-lactide) (PLA), chitosan, and poly (methylmethacrylate) (PMMA) are currently being used to functionalize magnetic nanoparticles (MNPs). Inorganic materials can possess a number of different properties such as high electron density and strong optical absorption (e.g. noble metal particles, in particular Au and Ag), fluorescence (semiconductor quantum dots, e.g. CdSe or CdTe) or phosphorescence (doped oxide materials, e.g. Y_2O_3), or magnetic moment (e.g. Fe, Mn, Ni, Co or their oxide NPs). Coating with those inorganic materials not only provide stability but also is widely used for the improvement of semiconductor efficiency, information storage, optoelectronics, catalysis, optical bioimaging, biological labeling, and so on. Especially, some inorganic materials help in binding various biological ligands to the NP surface, such as silica, Au, metal oxides, etc. Silica NPs upon surface modification with a silica oligomer, organic siloxane and surfactant produce an effective coating product having super hydrophobic behavior.[51] By chemical surface modification of NPs their properties can be tuned such as by changing the type of surfactants the coercivity of $CoFe_2O_4$ NPs can be varied.[52] Covering the MNPs with QDs shell, conjugate polymer or dye magneto fluorescent NPs can be developed,

which is used for imaging diagnosis, and therapy.[53] MNPs coated with specific antibody or aptamer help to target selectively tumer or cancer cells.[54, 55]

Another important technique for surface modification is plasma assisted coating. Plasma-deposited polymeric coatings have significant application potential as nm-thick films that can be tailored to impart any desirable surface property to any given substrate. By careful selection of the starting molecule and process parameters, a wide variety of surface types have been generated using this technology. Coatings are obtained by energizing suitable monomers (in vapor phase) in a plasma reactor so that the activated species can form a polymeric coating on the surface of a selected substrate material. This approach provides some critical advantages over conventional surface modification processes because it is a solvent-free environment-friendly process which facilitates its application in device fabrication.[56, 57]

Another type of surface modification is increment of surface-to-volume ratio by aggressive scaling down of material dimension. The properties of nanostructures differ from its bulk counterpart due to their enormous surface-to-volume ratio. With increasing surface for the same volume, the reactivity increases. Enhanced surface area plays valuable role in various technological applications (e.g. catalysis, adsorption, electrochemical performance etc.).[58]

1.4. Consequences of Chemical Functionalization on Metal Ions over Nanoparticles Surface According to Ligand Field Theory

NPs surface contains numerous uncompensated coordination spheres due to broken bonds. Metal ions residing within those uncompensated coordination spheres form complexes with ligands upon chemical functionalization resulting completely new optical, magnetic, catalytic properties.[59] Ligand field theory resulted from combination of the principles laid out in molecular orbital theory and crystal field theory, describes the loss of degeneracy of metal d orbitals in transition metal complexes. Metal d orbitals split in the following fashion as shown in the Figure 1.3.

In octahedral field, ligands approach from the direction of axes resulting in destabilization of the orbitals along the axes ($d_{x^2-y^2}$ and d_{z^2}), and stabilization of the orbitals lying in between the axes (d_{xy}, d_{yz}, d_{xz}). In case of tetrahedral field d_{xy}, d_{yz}, d_{xz} orbitals are nearer to the direction of approach of the ligands than the $d_{x^2-y^2}$ and d_{z^2} orbitals, so the inverse arrangement is observed.[60]
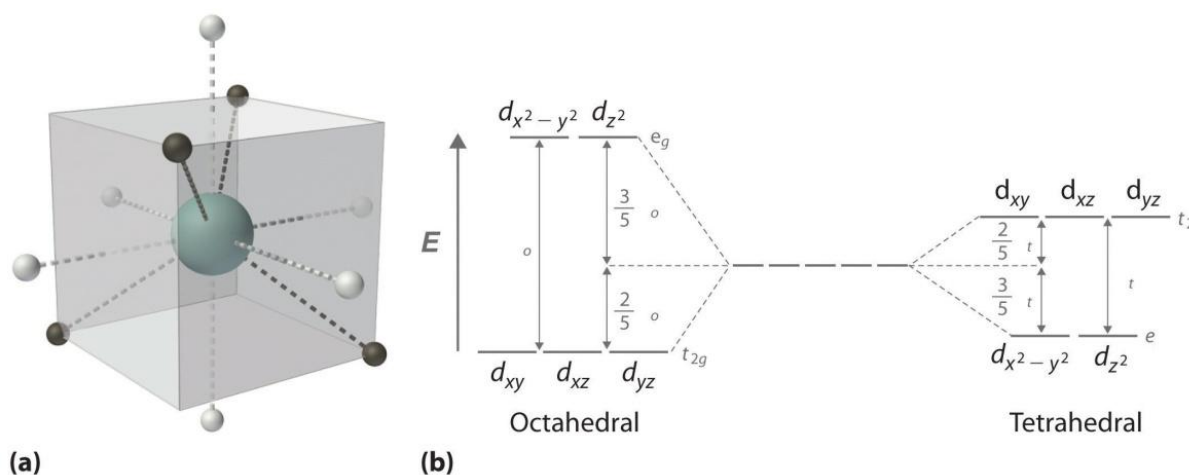
Figure 1.3. (a) White and black spheres indicate orientation of metal d orbitals in octahedral and tetrahedral coordination spheres, respectively. (b) Energy splitting of d orbitals in octahedral and tetrahedral field.

1.4.1. Spectrochemical Series

Splitting of the d orbitals (Δ) primarily depends on type of ligands, metal ions (Δ increases down the group) and charge over metal ions (Δ increases with increasing oxidation number). A spectrochemical series is a list of ligands arranged on ligand strength and a list of metal ions based on oxidation number, group and its nature as shown in Figure 1.4.[60]
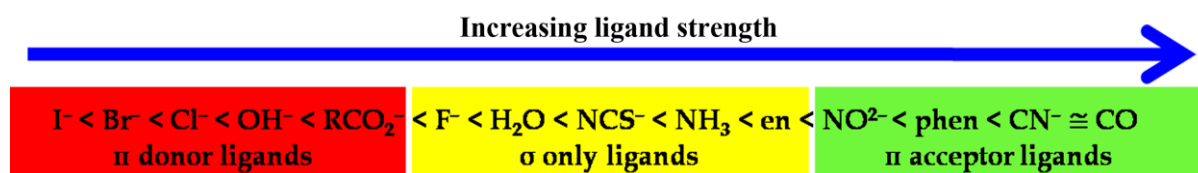
Figure 1.4. Spectrochemical series of various ligands in the increasing order of ligand strength.

π donor ligands having occupied p orbitals tend to donate π electrons to the metal ions along with the σ bonding electrons, exhibiting stronger metal-ligand interactions and an effective decrease of Δ. π acceptor ligands having vacant π* with comparable energy to metal d orbitals, can undergo π back bonding, resulting in increase of Δ. The metal ions can also be arranged in order of increasing Δ. Mn^{2+} < Ni^{2+} < Co^{2+} < Fe^{2+} < V^{2+} < Fe^{3+} < Cr^{3+} < V^{3+} < Co^{3+}.

1.4.2. Tanabe–Sugano Diagrams

Tanabe–Sugano diagrams are used in coordination chemistry to predict absorptions in the electronic spectra of coordination compounds. The x-axis of a Tanabe–Sugano diagram is expressed in terms of the ligand field splitting parameter, Dq, or Δ, divided by the Racah parameter B, denoting interelectronic repulsion. Each line corresponds to a particular electronic state. Certain Tanabe–Sugano diagrams (d^4, d^5, d^6, and d^7) also have a vertical line drawn at a specific Dq/B value, which corresponds with a discontinuity in the slopes of the excited states' energy levels. This pucker in the lines occurs when the spin pairing energy, P, is equal to the ligand field splitting energy, Dq. Complexes to the left of this line (lower Dq/B values) are high-spin, while complexes to the right (higher Dq/B values) are low-spin. There is no low-spin or high-spin designation for d^2, d^3, or d^8. For an example, Tanabe–Sugano diagram of d^7 system is demonstrated in Figure 1.5.
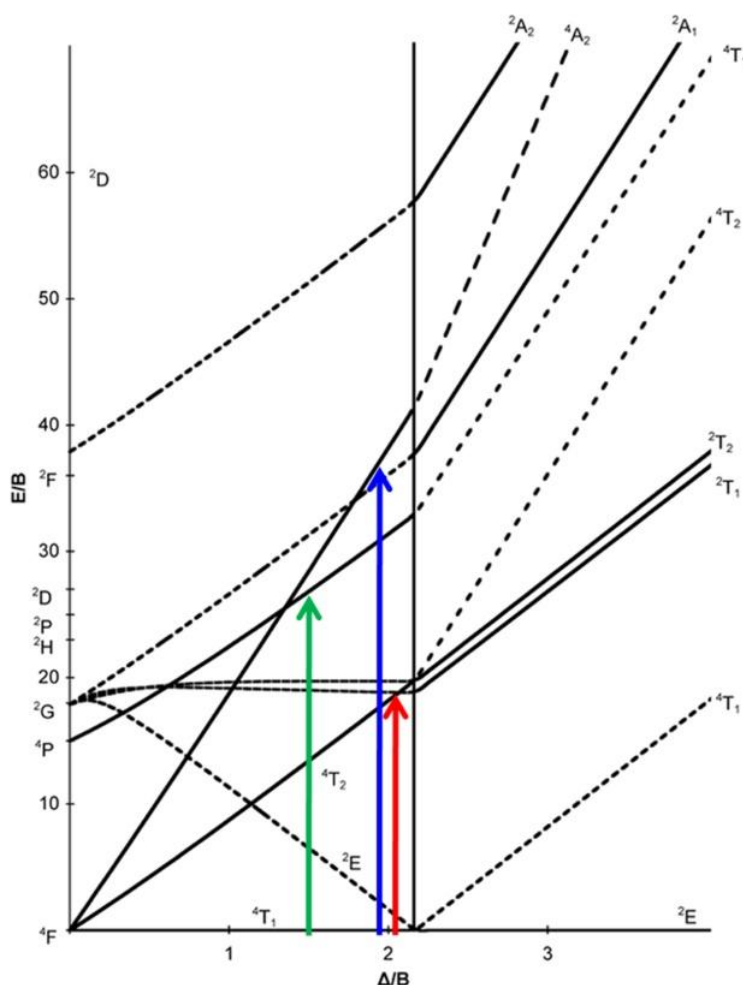
Figure 1.5. Tanabe–Sugano diagram of d^7 system showing three allowed transitions.

1.4.3. Selection Rules

There are two spectroscopic selection rules such as Laporte and spin selection rule. The Laporte rule states that electronic transitions within centrosymmetric system (e.g. octahedral co-ordination sphere) conserve parity, either symmetry or antisymmetry with respect to an inversion centre — i.e., *g* (gerade = even) → *g*, or *u* (ungerade = odd) → *u* are forbidden. Allowed transitions in such molecules must involve a change in parity, either *g* → *u* or *u* → *g*. For example, in an octahedral complex, transitions within a given set of *p* or *d* are forbidden. However, forbidden transitions get allowed upon destruction of centre of symmetry, due to distortion of complex (e.g. Jahn Teller distortion) and asymmetric vibrations.

The spin selection rule states that transitions that involve a change in multiplicity (or number of unpaired electrons) are forbidden. For example, $^3A_{2g} \rightarrow {}^1E_g$ transition involving a change of multiplicity is much weaker than $^3A_{2g} \rightarrow {}^3T_{2g}$, where multiplicity remains unchanged.

1.4.4. Jahn–Teller Effect

The complexes having electron configurations with unequal occupancy of degenerate orbitals undergo Jahn–Teller distortion to stabilize the system by minimizing the overall energy of the species. In octahedral complexes, the effect of Jahn–Teller distortion is more prominent when odd number of electrons occupy the e_g orbitals. This situation arises in complexes with the configurations d^9, low-spin d^7 or high-spin d^4 complexes, which are doubly degenerate etc. Figure 1.6 exhibits the changes in Tanabe–Sugano diagram of Mn^{3+} complex due to Jahn–Teller distortion.[61] In octahedral complexes of Mn^{3+}, the e_g orbitals point directly at the ligands, so distortion causing destruction of degeneracy can result in large energetic stabilization. This effect also occurs when there is degeneracy due to the electrons in the t_{2g} orbitals (*i.e.* configurations such as d^1 or d^2, both of which are triply degenerate). In such cases, however, the effect is much less noticeable, because there is a much smaller lowering of repulsion on taking ligands further away from the t_{2g} orbitals, which do not point directly at the ligands. The case is similar in tetrahedral complexes (e.g. manganate: distortion is very low because there is less stabilization to be gained because the ligands are not pointing directly at the orbitals).

Figure 1.6. Variation of the Tanabe-Sugano diagram for 3d[4] ions due to Jahn–Teller effect. (© Aguado et al. *Phys. Rev. B* **2007,** *76* (9), 094417.)

1.4.5. Ligand to Metal and Metal to Ligand Charge Transfer Bands

Ligands possess σ, σ*, π, π*, and nonbonding (n) molecular orbitals. If the ligand molecular orbitals are full, charge transfer may occur from the ligand molecular orbitals to the empty or partially filled metal d-orbitals. The absorptions that arise from this process are called ligand-to-metal charge-transfer bands (LMCT) (shown in Figure 1.7). LMCT transitions result in intense bands.[60]

Figure 1.7. Ligand to Metal Charge Transfer (LMCT) involving an octahedral d^6 complex.

If the metal is in a low oxidation state (electron rich) and the ligand possesses low-lying empty orbitals (e.g., CO or CN− having π* orbitals) then a metal-to-ligand charge transfer (MLCT) transition may occur. MLCT transitions are common for coordination compounds having π-acceptor ligands. Upon the absorption of light, electrons in the metal orbitals are excited to the ligand π* orbitals. Figure 1.8 illustrates the metal to ligand charge transfer in a d^5 octahedral complex. MLCT transitions result in intense bands.[60]
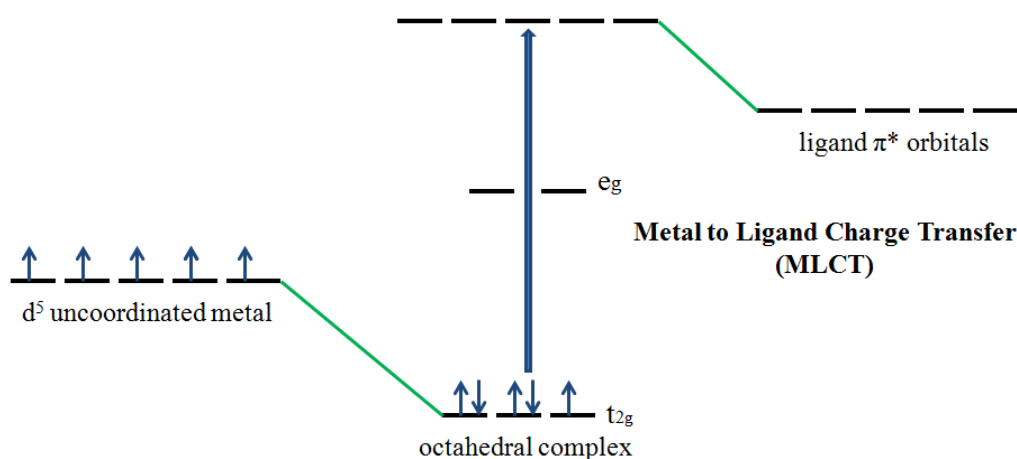
Figure 1.8. Metal to Ligand Charge Transfer (MLCT) involving an octahedral d^5 complex.

1.5. Nanocatalysis

Nanocatalysis (NPs mediated catalysis) is an important and emerging field in catalysis science, because of the small size (1–100 nm), the active metal atoms are exposed to the surface and thus minimize the specific cost per function.[62] The field of nanocatalysis has undergone an exponential growth during the past decade. Two types of studies have been carried out, homogeneous catalysis in solution and heterogeneous catalysis in which the NPs are supported on a substrate.[63] In homogeneous catalysis, NPs dispersed in an organic or aqueous solution or in a solvent mixture stabilized by polymers,[64, 65] block copolymers,[66] dendrimers,[67] surfactants,[67] other ligands,[68] are used as catalysts. In heterogeneous catalysis, NPs are supported on various substrates like carbon,[69, 70] silica,[71, 72] alumina,[73, 74] titanium dioxide,[75, 76] polymers by chemical methods, grafting,[77] lithography[78] etc. There are a number of reviews that discuss various reactions conducted using homogeneous and heterogeneous catalysts with high activity and selectivity.[67, 79, 80] Catalytic activities of NMs greatly depend on their shape and size.[81, 82] Surface functionalization of MNPs is a well-designed way to bridge the gap between heterogeneous and homogeneous catalysis due to their ease of preparation, very active surface for adsorptions or immobilization of metals and ligands, and controlled separation by magnetic decantation after the reaction. Structural miniaturization has indeed given a new freedom that allows us to tune the physical and chemical properties that are initially nonvariable for the bulk chunks by simply changing the shape and size to make use of the effect of atomic coordination reduction. The intrinsic properties of NMs and their size dependency will induce several effects on catalysis as shown in Figure 1.9. Key objectives of nanocatalysis research are to increase selectivity and activity, minimize energy consumption, and enhance lifetime of catalysts by controlling pore size and particle characteristics. Another aim is replacement of precious metal catalysts by transition metal oxide catalysts tailored at the nanoscale, thus improving chemical reactivity and reducing process costs. This can be achieved only by precisely controlling the size, shape, spatial distribution, surface composition and electronic structure, and thermal and

chemical stability of the individual nano components. In view of the numerous potential benefits that can be accrued through their use, nanostructured catalysts have been the subject of considerable academic and industrial research attention in recent times.
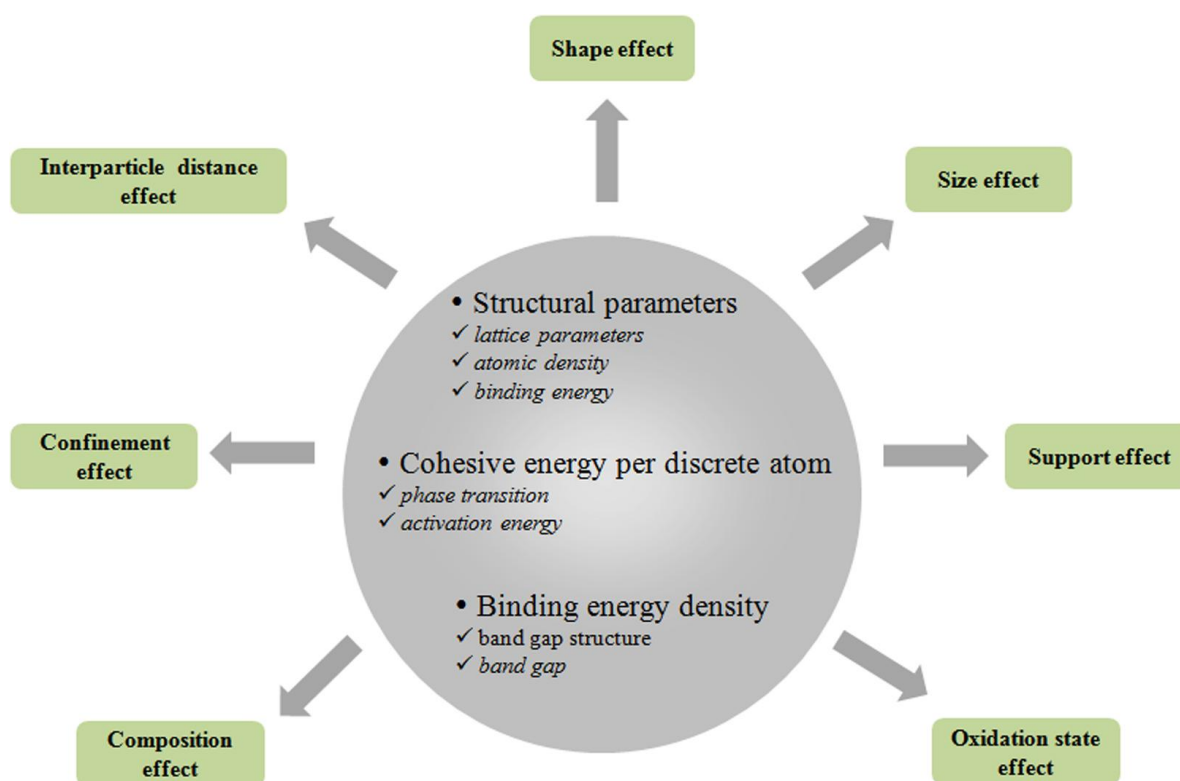
Figure 1.9. The impact of the intrinsic properties of nanomaterials on catalysis.

1.6. Multifunctional Nanoparticles

Development of multifunctional NPs combining several beneficial properties within a single system for their advanced application in diverse field of nanotechnology, especially in biomedical diagnosis and therapy has been a key topic in the past decade and resulted in a progressive development of a new emerging research area called nanobiotechnology. The properly functionalized MNPs possess several advantages which give rise to many exciting opportunities in the field of biomedical application.[83] The size tunability of MNPs from few nanometres to tens of nanometres enables them to match with that of the biomolecules and effectively enhances their interaction possibility with different biological entities from cells (10–

100 μm), viruses, genes, down to proteins (3–50 nm). Multifunctional NPs are fabricated either by chemical functionalization with small ligands, surfactants, proteins, DNA, RNA, antibodies, dyes etc. or by forming nanocomposites with other functional nanoprobes such as, metal NPs, QDs, radioactive elements etc. Rationally surface modified and highly water dispersible MNPs which can be manipulated using external magnetic field for targeting to a specific site, facilitate the enhancement of the MRI contrast and fluorescence imaging[84-87] for non-invasive diagnosis of morphology and function of healthy and ailing soft tissues *in vivo,* and AC magnetic field-assisted hyperthermia treatment of cancer.[88] Figure 1.10 demonstrates the schematic view of multifunctional NP. In the centre, there is nanocore which is surrounded by solubilizing layer consisting hydrophilic ligands. These ligands make the NPs water soluble as well as give stability. Moreover depending on the type of application any one or more beneficial systems (fluorophore, DNA, protein, radioactive nuclide, antibody, drug etc.) can be chemically attached to the functional groups of ligands. Very recently, significant attention has also been directed towards the development of MNPs as sustainable nanocatalyst for specific chemical transformations having both economic and environmental significance, considering their efficient activity, low cost, simple preparation method, high stability and controlled separation by external magnetic field.[62, 89-91]
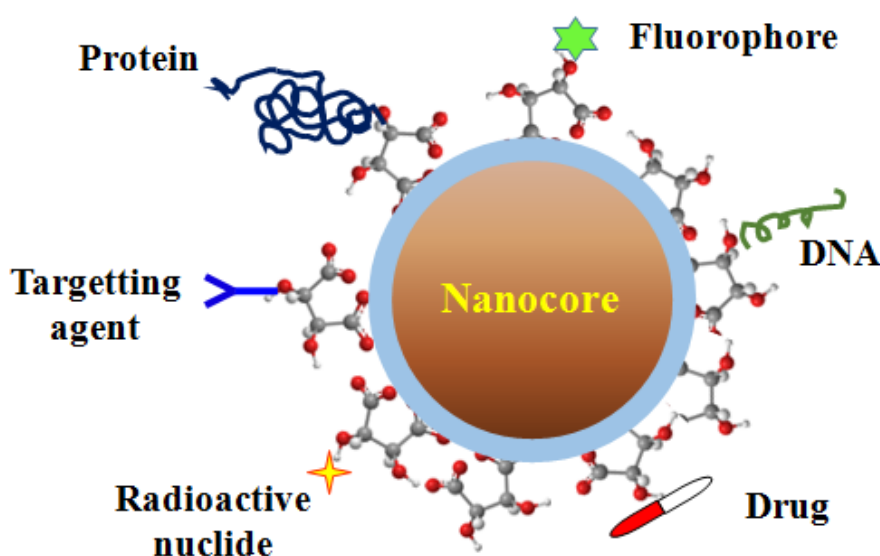
Figure 1.10. The schematic view of multifunctional nanoparticle.

1.7. Motivation and Objective of Thesis

Surface modification can have a significant influence on the materials behavior at the nanoscale and can lead to nanostructures with novel properties. Therefore, long-term endeavors have been focused on the morphology controllable synthesis and functionalization of metal oxide nanocrystals for their advanced physicochemical properties and technological applications. Among the metal oxides, MNPs of 3d transition metal oxides have witnessed enormous interest due to their potential applications in various fields ranging from catalysis,[92] energy,[93] and magnetic data storage[94] to drug delivery as well as biomedical imaging.[95] In particular, metal-oxide materials fabricated at a nanoscale exhibit improved optical, magnetic, thermal, and electrical properties as compared to their bulk counterparts.

So far, magneto-fluorescent NPs have been fabricated either by coating with fluorescent dyes or forming nanocomposite with QDs or doping with lanthanide elements.[86] In order to make the inorganic NPs biocompatible, surface modification with silica or bio-molecules like proteins, DNA, RNA, small organic ligands, and polymers is carried out, unfortunately none of them can incorporate intrinsic fluorescence within the system. Again, chemical instability, photo-bleaching of fluorescent dyes, and inherent toxicity of QDs (due to presence of heavy metals like Cd^{2+}, Pb^{2+}) restrict their direct biological applications.[96] So, incorporation of intrinsic fluorescence within pure phase transition metal ion based magnetic NMs, are highly desirable for advanced biomedical applications. Moreover, the highly water dispersible MNPs having intrinsic fluorescence may open up their several other technological applications in the field ranging from nanocatalysis, sensing to nanodevices.

In an attempt to alleviate the critical problems of escalating energy crisis and greenhouse gas pollution derived from excessive consumption of fossil fuels, some alternative energy technologies have been formulated.[15, 97] As an emerging advanced electrochemical energy storage system, SCs can offer higher power density, longer cycling life, and better safety as compared to batteries. Among various available pseudocapacitive materials, Co_3O_4 is notably attractive for application in SCs, due to

its low cost, low environmental footprint, great redox activity, and especially, extremely high theoretical specific capacitance (ca. 3560 F g^{-1}).[98] In the nano regime the benign character gets further enhanced. So, in the past decade, microspheres, nanosheets,[99] nanorods,[100] porous flower-like nanostructures etc. have been explored for superior performance in the field of supercapacitance. However, the observed specific capacitance values for Co_3O_4 are much lower than its theoretical value, and it is an ongoing challenge to further improve its energy storage capability.

The key focus of this thesis, is

- ❖ We have synthesized transition metal oxide (Fe_2O_3, $MnFe_2O_4$, Co_3O_4, and $CoFe_2O_4$) based magnetic nanostructures (NPs, and nano cubes (NCs)) by different chemical synthesis procedures.

- ❖ We have functionalized different nanostructures with small organic ligands to make the NMs water dispersible, which is an essential criterion for their biological applications.

- ❖ We have studied the optical properties of functionalized nanostructures. Very interestingly, the functionalized NMs show intrinsic multicolor fluorescence.

- ❖ We have discovered the chemistry behind the development of multicolor fluorescence from the ligand functionalized nanostructures through systematic study by various spectroscopic tools.

- ❖ We have studied catalytic efficiency of the functionalized nanostructures in degradation of biologically and environmentally harmful pigments.

- ❖ By incorporation of improved magnetic, optical, and catalytic properties simultaneously, we have developed multifunctional nanostructures that may find pioneering diverse applications ranging from diagnostics, therapeutics to environmental remediation.

- ❖ In an attempt to improve energy storage capability of Co_3O_4 based SCs, we have fabricated electrode by growing ultra small Co_3O_4 NCs directly on Ni foam through facile one step solvothermal route. Electrochemical study reveals an enhanced pseudocapacitive performance of the Co_3O_4 NCs with high rate capability.

1.8. Organization of Thesis

The entire thesis has been divided into six different chapters. A brief sketch of the chapters is given below.

Chapter 1 gives a brief introduction about transition metal based different nanostructures, their crystal structures, magnetic, and electrochemical properties. Here we have discussed the necessity of surface modification of NMs, types, procedures, and consequences of surface modification on different properties of NMs, particularly development of optical properties in the light of ligand field theory. Moreover, the motivation behind the thesis work and the outline of the work done are included in this chapter.

Chapter 2 provides the synthesis procedures of different nanostructures, and various characterization techniques including instrumental details and experimental methods.

Chapter 3 describes the facile chemical functionalization strategy of Fe_2O_3 NPs with small hydrophilic organic ligand to induce inherent photoluminescence and excellent photocatalytic activity. Meticulous investigation through UV−visible absorption and fluorescence study along with theoretical support from literature unfolds that LMCT transition from the tartrate ligand to the lowest unoccupied energy level of Fe^{3+} of the NPs and d−d transitions centered over Fe^{3+} ions in the NPs play the key role in the emergence of multiple photoluminescence from the ligand functionalized Fe_2O_3 NPs.

Chapter 4 demonstrates improvement of fluorescence and magnetic property upon surface modification of $MnFe_2O_4$ NPs due to incorporation of Mn within the system and increasing surface to volume ratio by decreasing the size of NPs. Proper investigation through UV−visible absorption, steady state, and time-resolved photoluminescence study reveals that LMCT transition from tartrate ligand to lowest unoccupied energy level of $Mn^{2+/3+}$ or Fe^{3+} of the NPs and Jahn−Teller distorted d−d transitions centered over Mn^{3+} ions in the NPs play the key role

behind the generation of multiple fluorescence from the ligand functionalized $MnFe_2O_4$ NPs. Functionalized $MnFe_2O_4$ NPs exhibit very good photocatalytic activity. We have also investigated the mechanism of catalysis.

Chapter 5 exhibits development of intrinsic fluorescence and catalytic activity upon surface modification of Co_3O_4 NCs. Systematic investigations using different spectroscopic tools reveal the mechanistic origin behind the generation of multicolor fluorescence from the ligand functionalized Co_3O_4 NCs. Moreover, from magnetic study we have found that the room temperature antiferromagnetic nature of Co_3O_4 NCs turns to ferromagnetic, after ligand functionalization due to the surface modification of the NCs. Functionalized Co_3O_4 NCs show appreciable catalytic and photocatalytic properties in degradation of biologically and environmentally harmful dyes.

Chapter 6 to improve magnetic and catalytic properties we have incorporated Fe within the Co_3O_4 system and moved to $CoFe_2O_4$ system. Through systematic investigations using different spectroscopic tools we have reconfirmed the mechanistic origin behind the generation of multicolor fluorescence from the ligand functionalized $CoFe_2O_4$ NPs. Functionalized $CoFe_2O_4$ NPs show unprecedented catalytic and photocatalytic properties in degradation of biologically and environmentally harmful dyes, respectively. We have also investigated the mechanism of catalysis.

Chapter 7 shows development of electrode with very high supercapacitance by growing ultra small Co_3O_4 NCs by one step facile solvothermal process. Enhanced supercapacitance can be attributed to very small size of NCs with nanopores, leading to greater interaction of electrolyte and active material.

Chapter 8 concludes the thesis with an idea about the scope for future work in this direction.

Bibliography

1.   Kuo, C. L.; Hwang, K. C., Does Morphology of a Metal Nanoparticle Play a Role in Ostwald Ripening Processes? *Chem. Mater.* **2013,** *25* (3), 365-371.

2.   Alexandridis, P., Gold Nanoparticle Synthesis, Morphology Control, and Stabilization Facilitated by Functional Polymers. *Chem. Eng. Technol.* **2011,** *34* (1), 15-28.

3.   Mitra, S.; Das, S.; Mandal, K.; Chaudhuri, S., Synthesis of a α-Fe$_2$O$_3$ Nanocrystal in its Different Morphological Attributes: Growth Mechanism, Optical and Magnetic Properties. *Nanotechnology* **2007,** *18* (27), 275608.

4.   Sarkar, D.; Mandal, M.; Mandal, K., Domain Controlled Magnetic and Electric Properties of Variable Sized Magnetite Nano-hollow Spheres. *J. Appl. Phys.* **2012,** *112* (6), 064318.

5.   Lopez-Sanchez, J. A.; Dimitratos, N.; Hammond, C.; Brett, G. L.; Kesavan, L.; White, S.; Miedziak, P.; Tiruvalam, R.; Jenkins, R. L.; Carley, A. F.; Knight, D.; Kiely, C. J.; Hutchings, G. J., Facile Removal of Stabilizer-Ligands from Supported Gold Nanoparticles. *Nat. Chem.* **2011,** *3* (7), 551-556.

6.   Brollo, M. E. F.; López-Ruiz, R.; Muraca, D.; Figueroa, S. J. A.; Pirota, K. R.; Knobel, M., Compact Ag@Fe$_3$O$_4$ Core-shell Nanoparticles by Means of Single-step Thermal Decomposition Reaction. *Sci. Rep.* **2014,** *4*, 6839.

7.   del Alamo, J. A., Nanometre-scale Electronics with III-V Compound Semiconductors. *Nature* **2011,** *479* (7373), 317-323.

8.   Erwin, S. C.; Zu, L.; Haftel, M. I.; Efros, A. L.; Kennedy, T. A.; Norris, D. J., Doping Semiconductor Nanocrystals. *Nature* **2005,** *436* (7047), 91-94.

9.   Cheng, C. J.; Tietjen, G. T.; Saucier-Sawyer, J. K.; Saltzman, W. M., A Holistic Approach to Targeting Disease with Polymeric Nanoparticles. *Nat. Rev. Drug Discov.* **2015,** *14* (4), 239-247.

10.   Ren, W.; Cheng, H.-M., The Global Growth of Graphene. *Nat. Nanotechnol.* **2014,** *9* (10), 726-730.

11.   Novoselov, K. S.; Falko, V. I.; Colombo, L.; Gellert, P. R.; Schwab, M. G.; Kim, K., A Roadmap for Graphene. *Nature* **2012,** *490* (7419), 192-200.

12. Juliano, R., Nanomedicine: Is the Wave Cresting? *Nat. Rev. Drug Discov.* **2013,** *12* (3), 171-172.

13. Veiseh, O.; Tang, B. C.; Whitehead, K. A.; Anderson, D. G.; Langer, R., Managing Diabetes with Nanomedicine: Challenges and Opportunities. *Nat. Rev. Drug Discov.* **2015,** *14* (1), 45-57.

14. Larcher, D.; Tarascon, J. M., Towards Greener and More Sustainable Batteries for Electrical Energy Storage. *Nat. Chem.* **2015,** *7* (1), 19-29.

15. Arico, A. S.; Bruce, P.; Scrosati, B.; Tarascon, J.-M.; van Schalkwijk, W., Nanostructured Materials for Advanced Energy Conversion and Storage Devices. *Nat. Mater.* **2005,** *4* (5), 366-377.

16. Hashmi, A. S. K.; Hutchings, G. J., Gold Catalysis. *Angew. Chem. Int. Ed.* **2006,** *45* (47), 7896-7936.

17. Grunwaldt, J.-D.; Kiener, C.; Wögerbauer, C.; Baiker, A., Preparation of Supported Gold Catalysts for Low-Temperature CO Oxidation via "Size-Controlled" Gold Colloids. *J. Catal.* **1999,** *181* (2), 223-232.

18. Garadkar, K. M.; Ghule, L. A.; Sapnar, K. B.; Dhole, S. D., A Facile Synthesis of $ZnWO_4$ Nanoparticles by Microwave Assisted Technique and its Application in Photocatalysis. *Mater. Res. Bull.* **2013,** *48* (3), 1105-1109.

19. Zhang, W.; Li, X.; Zou, R.; Wu, H.; Shi, H.; Yu, S.; Liu, Y., Multifunctional Glucose Biosensors from Fe_3O_4 Nanoparticles Modified Chitosan/Graphene Nanocomposites. *Sci. Rep.* **2015,** *5*, 11129.

20. Corr, S. A., Metal Oxide Nanoparticles. In *Nanoscience: Volume 1: Nanostructures through Chemistry*, The Royal Society of Chemistry: 2013; Vol. 1, pp 180-207.

21. Zhao, Z.; Zhou, Z.; Bao, J.; Wang, Z.; Hu, J.; Chi, X.; Ni, K.; Wang, R.; Chen, X.; Chen, Z.; Gao, J., Octapod Iron Oxide Nanoparticles as High-performance T_2 Contrast Agents for Magnetic Resonance Imaging. *Nat. Commun.* **2013,** *4*.

22. Li, C.; Han, X.; Cheng, F.; Hu, Y.; Chen, C.; Chen, J., Phase and Composition Controllable Synthesis of Cobalt Manganese Spinel Nanoparticles towards Efficient Oxygen Electrocatalysis. *Nat. Commun.* **2015,** *6*.

23.   Xiao, J.; Tian, X. M.; Yang, C.; Liu, P.; Luo, N. Q.; Liang, Y.; Li, H. B.; Chen, D. H.; Wang, C. X.; Li, L.; Yang, G. W., Ultrahigh Relaxivity and Safe Probes of Manganese Oxide Nanoparticles for in Vivo Imaging. *Sci. Rep.* **2013,** *3*, 3424.

24.   Zhang, M.; de Respinis, M.; Frei, H., Time-Resolved Observations of Water Oxidation Intermediates on a Cobalt Oxide Nanoparticle Catalyst. *Nat. Chem.* **2014,** *6* (4), 362-367.

25.   Sarkar, D.; Khan, G. G.; Singh, A. K.; Mandal, K., Enhanced Electrical, Optical, and Magnetic Properties in Multifunctional ZnO/α-Fe_2O_3 Semiconductor Nanoheterostructures by Heterojunction Engineering. *J. Phys. Chem. C* **2012,** *116* (44), 23540-23546.

26.   Sarkar, D.; Khan, G. G.; Singh, A. K.; Mandal, K., High-Performance Pseudocapacitor Electrodes Based on α-Fe_2O_3/MnO_2 Core–Shell Nanowire Heterostructure Arrays. *J. Phys. Chem. C* **2013,** *117* (30), 15523-15531.

27.   Sarkar, D.; Mandal, M.; Mandal, K., Design and Synthesis of High Performance Multifunctional Ultrathin Hematite Nanoribbons. *ACS Appl. Mater. Interfaces* **2013,** *5* (22), 11995-12004.

28.   Hankare, P. P.; Pandav, R. S.; Patil, R. P.; Vader, V. T.; Garadkar, K. M., Synthesis, Structural and Magnetic Properties of Copper Substituted Nickel Manganite. *J. Alloys Compd.* **2012,** *544*, 197-202.

29.   Xiong, S.; Xu, J.; Chen, D.; Wang, R.; Hu, X.; Shen, G.; Wang, Z. L., Controlled Synthesis of Monodispersed Hematite Microcubes and their Properties. *CrystEngComm* **2011,** *13* (23), 7114-7120.

30.   Wu, W.; Wu, Z.; Yu, T.; Jiang, C.; Kim, W.-S., Recent Progress on Magnetic Iron Oxide Nanoparticles: Synthesis, Surface Functional Strategies and Biomedical Applications. *Sci. Tech. Adv. Mater.* **2015,** *16* (2), 023501.

31.   Garanin, D. A.; Kachkachi, H., Surface Contribution to the Anisotropy of Magnetic Nanoparticles. *Phys. Rev. Lett.* **2003,** *90* (6), 065504.

32.   Salazar-Alvarez, G.; Qin, J.; Šepelák, V.; Bergmann, I.; Vasilakaki, M.; Trohidou, K. N.; Ardisson, J. D.; Macedo, W. A. A.; Mikhaylova, M.; Muhammed, M.; Baró, M. D.; Nogués, J., Cubic versus Spherical Magnetic Nanoparticles: The Role of Surface Anisotropy. *J. Am. Chem. Soc.* **2008,** *130* (40), 13234-13239.

33.   Poizot, P.; Laruelle, S.; Grugeon, S.; Dupont, L.; Tarascon, J. M., Nano-sized Transition-metal Oxides as Negative-electrode Materials for Lithium-ion Batteries. *Nature* **2000,** *407* (6803), 496-499.

34.   Xie, X.; Zhang, C.; Wu, M.-B.; Tao, Y.; Lv, W.; Yang, Q.-H., Porous MnO_2 for Use in a High Performance Supercapacitor: Replication of a 3D Graphene Network as a Reactive Template. *Chem. Commun.* **2013,** *49* (94), 11092-11094.

35.   Seabold, J. A.; Neale, N. R., All First Row Transition Metal Oxide Photoanode for Water Splitting Based on $Cu_3V_2O_8$. *Chem. Mater.* **2015,** *27* (3), 1005-1013.

36.   Wang, W.; Guo, S.; Lee, I.; Ahmed, K.; Zhong, J.; Favors, Z.; Zaera, F.; Ozkan, M.; Ozkan, C. S., Hydrous Ruthenium Oxide Nanoparticles Anchored to Graphene and Carbon Nanotube Hybrid Foam for Supercapacitors. *Sci. Rep.* **2014,** *4*.

37.   Singh, A. K.; Sarkar, D.; Khan, G. G.; Mandal, K., Unique Hydrogenated Ni/NiO Core/shell 1D Nano-heterostructures with Superior Electrochemical Performance as Supercapacitors. *J. Mater. Chem. A* **2013,** *1* (41), 12759-12767.

38.   Pang, H.; Lu, Q.; Li, Y.; Gao, F., Facile Synthesis of Nickel Oxide Nanotubes and their Antibacterial, Electrochemical and Magnetic Properties. *Chem. Commun.* **2009,** (48), 7542-7544.

39.   Xia, X.-h.; Tu, J.-p.; Zhang, Y.-q.; Mai, Y.-j.; Wang, X.-l.; Gu, C.-d.; Zhao, X.-b., Freestanding Co_3O_4 Nanowire Array for High Performance Supercapacitors. *RSC Adv.* **2012,** *2* (5), 1835-1841.

40.   Singh, A. K.; Sarkar, D.; Khan, G. G.; Mandal, K., Hydrogenated NiO Nanoblock Architecture for High Performance Pseudocapacitor. *ACS Appl. Mater. Interfaces* **2014,** *6* (7), 4684-4692.

41.   Wang, R.; Yan, X.; Lang, J.; Zheng, Z.; Zhang, P., A Hybrid Supercapacitor Based on Flower-like $Co(OH)_2$ and Urchin-like VN Electrode Materials. *J. Mater. Chem. A* **2014,** *2* (32), 12724-12732.

42.   Wu, H. B.; Pang, H.; Lou, X. W., Facile Synthesis of Mesoporous $Ni_{0.3}Co_{2.7}O_4$ Hierarchical Structures for High-Performance Supercapacitors. *Energy Environ. Sci.* **2013,** *6* (12), 3619-3626.

43.   Liu, X.; Shi, S.; Xiong, Q.; Li, L.; Zhang, Y.; Tang, H.; Gu, C.; Wang, X.; Tu, J., Hierarchical $NiCo_2O_4@NiCo_2O_4$ Core/Shell Nanoflake Arrays as High-Performance Supercapacitor Materials. *ACS Appl. Mater. Interfaces* **2013,** *5* (17), 8790-8795.

44.   Lee, J. W.; Hall, A. S.; Kim, J.-D.; Mallouk, T. E., A Facile and Template-Free Hydrothermal Synthesis of Mn_3O_4 Nanorods on Graphene Sheets for Supercapacitor Electrodes with Long Cycle Stability. *Chem. Mater.* **2012,** *24* (6), 1158-1164.

45.   Uyeda, H. T.; Medintz, I. L.; Jaiswal, J. K.; Simon, S. M.; Mattoussi, H., Synthesis of Compact Multidentate Ligands to Prepare Stable Hydrophilic Quantum Dot Fluorophores. *J. Am. Chem. Soc.* **2005,** *127* (11), 3870-3878.

46.   Giri, A.; Goswami, N.; Bootharaju, M. S.; Xavier, P. L.; John, R.; Thanh, N. T. K.; Pradeep, T.; Ghosh, B.; Raychaudhuri, A. K.; Pal, S. K., Emergence of Multicolor Photoluminescence in $La_{0.67}Sr_{0.33}MnO_3$ Nanoparticles. *J. Phys. Chem. C* **2012,** *116* (48), 25623-25629.

47.   Yang, S.; Chen, D.; Li, N.; Mei, X.; Qi, X.; Li, H.; Xu, Q.; Lu, J., A Facile Preparation of Targetable pH-sensitive Polymeric Nanocarriers with Encapsulated Magnetic Nanoparticles for Controlled Drug Release. *J. Mater. Chem. C* **2012,** *22* (48), 25354-25361.

48.   Dong, A.; Ye, X.; Chen, J.; Kang, Y.; Gordon, T.; Kikkawa, J. M.; Murray, C. B., A Generalized Ligand-Exchange Strategy Enabling Sequential Surface Functionalization of Colloidal Nanocrystals. *J. Am. Chem. Soc.* **2011,** *133* (4), 998-1006.

49.   Alivisatos, A. P., Perspectives on the Physical Chemistry of Semiconductor Nanocrystals. *J. Phys. Chem.* **1996,** *100* (31), 13226-13239.

50.   Weisbecker, C. S.; Merritt, M. V.; Whitesides, G. M., Molecular Self-Assembly of Aliphatic Thiols on Gold Colloids. *Langmuir* **1996,** *12* (16), 3763-3772.

51.   Facio, D. S.; Mosquera, M. J., Simple Strategy for Producing Superhydrophobic Nanocomposite Coatings In Situ on a Building Substrate. *ACS Appl. Mater. Interfaces* **2013,** *5* (15), 7517-7526.

52.   Rakshit, R.; Mandal, M.; Pal, M.; Mandal, K., Tuning of Magnetic Properties of $CoFe_2O_4$ Nanoparticles through Charge Transfer Effect. *Appl. Phys. Lett.* **2014,** *104* (9), 092412.

53.   Fu, A.; Wilson, R. J.; Smith, B. R.; Mullenix, J.; Earhart, C.; Akin, D.; Guccione, S.; Wang, S. X.; Gambhir, S. S., Fluorescent Magnetic Nanoparticles for Magnetically Enhanced Cancer Imaging and Targeting in Living Subjects. *ACS Nano* **2012,** *6* (8), 6862-6869.

54.   Herr, J. K.; Smith, J. E.; Medley, C. D.; Shangguan, D.; Tan, W., Aptamer-Conjugated Nanoparticles for Selective Collection and Detection of Cancer Cells. *Anal. Chem.* **2006,** *78* (9), 2918-2924.

55.   Zhang, E.; Kircher, M. F.; Koch, M.; Eliasson, L.; Goldberg, S. N.; Renström, E., Dynamic Magnetic Fields Remote-Control Apoptosis via Nanoparticle Rotation. *ACS Nano* **2014,** *8* (4), 3192-3201.

56.   Mukhopadhyay, S. M.; Joshi, P.; Datta, S.; Macdaniel, J., Plasma Assisted Surface Coating of Porous Solids. *Appl. Surf. Sci.* **2002,** *201* (1–4), 219-226.

57.   Ohl, A.; Besch, W.; Steffen, H.; Foest, R.; Arens, M.; Wandel, K., Surface Coating by Repeated Plasma-Assisted Grafting and Cross-Linking of Molecular Precursors. *Plasma Process. Polym.* **2009,** *6* (6-7), 425-433.

58.   Requejo-Isidro, J.; del Coso, R.; Solis, J.; Gonzalo, J.; Afonso, C. N., Role of Surface-to-volume Ratio of Metal Nanoparticles in Optical Properties of $Cu:Al_2O_3$ Nanocomposite Films. *Appl. Phys. Lett.* **2005,** *86* (19), 193104.

59.   Vestal, C. R.; Zhang, Z. J., Effects of Surface Coordination Chemistry on the Magnetic Properties of $MnFe_2O_4$ Spinel Ferrite Nanoparticles. *J. Am. Chem. Soc.* **2003,** *125* (32), 9828-9833.

60.   Huheey, J. E.; Keiter, E. A.; Keiter, R. L.; Medhi, O. K., *Inorganic Chemistry: Principles of Structure and Reactivity*. Pearson Education: 2006.

61.   Aguado, F.; Rodriguez, F.; Núñez, P., Pressure-induced Jahn-Teller Suppression and Simultaneous High-spin to Low-spin Transition in the Layered Perovskite $CsMnF_4$. *Phys. Rev. B* **2007,** *76* (9), 094417.

62.   Gawande, M. B.; Branco, P. S.; Varma, R. S., Nano-magnetite (Fe_3O_4) as a Support for Recyclable Catalysts in the Development of Sustainable Methodologies. *Chem. Soc. Rev.* **2013,** *42* (8), 3371-3393.

63.   Burda, C.; Chen, X.; Narayanan, R.; El-Sayed, M. A., Chemistry and Properties of Nanocrystals of Different Shapes. *Chem. Rev.* **2005,** *105* (4), 1025-1102.

64.   Sidorov, S. N.; Volkov, I. V.; Davankov, V. A.; Tsyurupa, M. P.; Valetsky, P. M.; Bronstein, L. M.; Karlinsey, R.; Zwanziger, J. W.; Matveeva, V. G.; Sulman, E. M.; Lakina, N. V.; Wilder, E. A.; Spontak, R. J., Platinum-Containing Hyper-Cross-Linked Polystyrene as a Modifier-Free Selective Catalyst for l-Sorbose Oxidation. *J. Am. Chem. Soc.* **2001,** *123* (43), 10502-10510.

65.   Borsla, A.; Wilhelm, A. M.; Delmas, H., Hydrogenation of Olefins in Aqueous Phase, Catalyzed by Polymer-protected Rhodium Colloids: Kinetic Study. *Catal. Today* **2001,** *66* (2–4), 389-395.

66.   Li, Y.; El-Sayed, M. A., The Effect of Stabilizers on the Catalytic Activity and Stability of Pd Colloidal Nanoparticles in the Suzuki Reactions in Aqueous Solution†. *J. Phys. Chem. B* **2001,** *105* (37), 8938-8943.

67.   Esumi, K.; Isono, R.; Yoshimura, T., Preparation of PAMAM− and PPI−Metal (Silver, Platinum, and Palladium) Nanocomposites and Their Catalytic Activities for Reduction of 4-Nitrophenol. *Langmuir* **2004,** *20* (1), 237-243.

68.   Giri, A.; Goswami, N.; Pal, M.; Zar Myint, M. T.; Al-Harthi, S.; Singha, A.; Ghosh, B.; Dutta, J.; Pal, S. K., Rational Surface Modification of Mn_3O_4 Nanoparticles to Induce Multiple Photoluminescence and Room Temperature Ferromagnetism. *J. Mater. Chem. C* **2013,** *1* (9), 1885-1895.

69.   Liu, Z.; Ling, X. Y.; Su, X.; Lee, J. Y., Carbon-Supported Pt and PtRu Nanoparticles as Catalysts for a Direct Methanol Fuel Cell. *J. Phys. Chem. B* **2004,** *108* (24), 8234-8240.

70.   Bulushev, D. A.; Yuranov, I.; Suvorova, E. I.; Buffat, P. A.; Kiwi-Minsker, L., Highly Dispersed Gold on Activated Carbon Fibers for Low-temperature CO Oxidation. *J. Catal.* **2004,** *224* (1), 8-17.

71.   Bianchini, C.; Dal Santo, V.; Meli, A.; Moneti, S.; Moreno, M.; Oberhauser, W.; Psaro, R.; Sordelli, L.; Vizza, F., A Comparison Between Silica-immobilized Ruthenium(II) Single Sites and Silica-supported Ruthenium Nanoparticles in the Catalytic Hydrogenation of Model Hetero- and Polyaromatics Contained in Raw Oil Materials. *J. Catal.* **2003,** *213* (1), 47-62.

72.   Lang, H.; May, R. A.; Iversen, B. L.; Chandler, B. D., Dendrimer-Encapsulated Nanoparticle Precursors to Supported Platinum Catalysts. *J. Am. Chem. Soc.* **2003,** *125* (48), 14832-14836.

73.   Balint, I.; Miyazaki, A.; Aika, K.-i., Effect of Platinum Morphology on Lean Reduction of NO with C_3H_6. *Phys. Chem. Chem. Phys.* **2004,** *6* (9), 2000-2002.

74.   Marconi, G.; Pertici, P.; Evangelisti, C.; Maria Caporusso, A.; Vitulli, G.; Capannelli, G.; Hoang, M.; Turney, T. W., Nanostructured Ruthenium on γ-Al_2O_3 Catalysts for the Efficient Hydrogenation of Aromatic Compounds. *J. Organomet. Chem.* **2004,** *689* (3), 639-646.

75.   Ishiguro, A.; Nakajima, T.; Iwata, T.; Fujita, M.; Minato, T.; Kiyotaki, F.; Izumi, Y.; Aika, K.-i.; Uchida, M.; Kimoto, K.; Matsui, Y.; Wakatsuki, Y., Nanoparticles of Amorphous Ruthenium Sulfide Easily Obtainable from a TiO_2-Supported Hexanuclear Cluster Complex $[Ru_6C(CO)_{16}]^{2-}$: A Highly Active Catalyst for the Reduction of SO_2 with H_2. *Chem. Eur. J.* **2002,** *8* (14), 3260-3268.

76.   Mallick, K.; Scurrell, M. S., CO Oxidation over Gold Nanoparticles Supported on TiO_2 and TiO_2-ZnO: Catalytic Activity Effects due to Surface Modification of TiO_2 with ZnO. *Appl. Catal., A : General* **2003,** *253* (2), 527-536.

77.   Chen, C.-W.; Chen, M.-Q., In Situ Synthesis and the Catalytic Properties of Platinum Colloids on Polystyrene Microspheres with Surface-grafted Poly(N-isopropylacrylamide)‡. *Chem. Commun.* **1998,** (7), 831-832.

78.   Yang, M. X.; Gracias, D. H.; Jacobs, P. W.; Somorjai, G. A., Lithographic Fabrication of Model Systems in Heterogeneous Catalysis and Surface Science Studies. *Langmuir* **1998,** *14* (6), 1458-1464.

79.   Haruta, M., When Gold Is Not Noble: Catalysis by Nanoparticles. *Chem Rec.* **2003,** *3* (2), 75-87.

80.   Schulz, J.; Roucoux, A.; Patin, H., Stabilized Rhodium(0) Nanoparticles: A Reusable Hydrogenation Catalyst for Arene Derivatives in a Biphasic Water-Liquid System. *Chem. Eur. J.* **2000,** *6* (4), 618-624.

81.   Ahmadi, T. S.; Wang, Z. L.; Green, T. C.; Henglein, A.; El-Sayed, M. A., Shape-Controlled Synthesis of Colloidal Platinum Nanoparticles. *Science* **1996,** *272* (5270), 1924-1925.

82.   Narayanan, R.; El-Sayed, M. A., Shape-Dependent Catalytic Activity of Platinum Nanoparticles in Colloidal Solution. *Nano Lett.* **2004,** *4* (7), 1343-1348.

83.   Reddy, L. H.; Arias, J. L.; Nicolas, J.; Couvreur, P., Magnetic Nanoparticles: Design and Characterization, Toxicity and Biocompatibility, Pharmaceutical and Biomedical Applications. *Chem. Rev.* **2012,** *112* (11), 5818-5878.

84.   Yang, J.; Lim, E.-K.; Lee, H. J.; Park, J.; Lee, S. C.; Lee, K.; Yoon, H.-G.; Suh, J.-S.; Huh, Y.-M.; Haam, S., Fluorescent Magnetic Nanohybrids as Multimodal Imaging Agents for Human Epithelial Cancer Detection. *Biomaterials* **2008,** *29* (16), 2548-2555.

85.   Gao, J.; Zhang, W.; Huang, P.; Zhang, B.; Zhang, X.; Xu, B., Intracellular Spatial Control of Fluorescent Magnetic Nanoparticles. *J. Am. Chem. Soc.* **2008,** *130* (12), 3710-3711.

86.   Kim, H.; Achermann, M.; Balet, L. P.; Hollingsworth, J. A.; Klimov, V. I., Synthesis and Characterization of Co/CdSe Core/Shell Nanocomposites: Bifunctional Magnetic-Optical Nanocrystals. *J. Am. Chem. Soc.* **2004,** *127* (2), 544-546.

87.   Gao, J.; Liang, G.; Cheung, J. S.; Pan, Y.; Kuang, Y.; Zhao, F.; Zhang, B.; Zhang, X.; Wu, E. X.; Xu, B., Multifunctional Yolk−Shell Nanoparticles: A Potential MRI Contrast and Anticancer Agent. *J. Am. Chem. Soc.* **2008,** *130* (35), 11828-11833.

88.   Johannsen, M.; Gneveckow, U.; Eckelt, L.; Feussner, A.; Waldofner, N.; Scholz, R.; Deger, S.; Wust, P.; Loening, S. A.; Jordan, A., Clinical Hyperthermia of Prostate Cancer Using Magnetic Nanoparticles: Presentation of a New Interstitial Technique. *Int. J. Hyperther.* **2005,** *21* (7), 637-647.

89.   Gawande, M. B.; Bonifacio, V. D. B.; Varma, R. S.; Nogueira, I. D.; Bundaleski, N.; Ghumman, C. A. A.; Teodoro, O. M. N. D.; Branco, P. S., Magnetically Recyclable Magnetite-Ceria (Nanocat-Fe-Ce) Nanocatalyst - Applications in Multicomponent Reactions Under Benign Conditions. *Green Chem.* **2013,** *15* (5), 1226-1231.

90.   Gawande, M. B.; Rathi, A. K.; Nogueira, I. D.; Varma, R. S.; Branco, P. S., Magnetite-Supported Sulfonic acid: a Retrievable Nanocatalyst for the Ritter Reaction and Multicomponent Reactions. *Green Chem.* **2013,** *15* (7), 1895-1899.

91.   Zhang, P.; Zhan, Y.; Cai, B.; Hao, C.; Wang, J.; Liu, C.; Meng, Z.; Yin, Z.; Chen, Q., Shape-controlled Synthesis of Mn_3O_4 Nanocrystals and their Catalysis of the Degradation of Methylene blue. *Nano Res.* **2010,** *3* (4), 235-243.

92.   Hudson, R.; Riviere, A.; Cirtiu, C. M.; Luska, K. L.; Moores, A., Iron-iron Oxide Core-shell Nanoparticles are Active and Magnetically Recyclable Olefin and Alkyne Hydrogenation Catalysts in Protic and Aqueous Media. *Chem. Commun.* **2012,** *48* (27), 3360-3362.

93.   Simon, P.; Gogotsi, Y., Materials for Electrochemical Capacitors. *Nat. Mater.* **2008,** *7* (11), 845-854.

94.   Hyeon, T., Chemical Synthesis of Magnetic Nanoparticles. *Chem. Commun.* **2003,** (8), 927-934.

95.   Lee, J. W.; Hall, A. S.; Kim, J.-D.; Mallouk, T. E., A Facile and Template-Free Hydrothermal Synthesis of Mn3O4 Nanorods on Graphene Sheets for Supercapacitor Electrodes with Long Cycle Stability. *Chemistry of Materials* **2012,** *24* (6), 1158-1164.

96.   Resch-Genger, U.; Grabolle, M.; Cavaliere-Jaricot, S.; Nitschke, R.; Nann, T., Quantum Dots versus Organic Dyes as Fluorescent Labels. *Nat. Methods* **2008,** *5* (9), 763-775.

97.   Yang, N.; Zhai, J.; Wang, D.; Chen, Y.; Jiang, L., Two-Dimensional Graphene Bridges Enhanced Photoinduced Charge Transport in Dye-Sensitized Solar Cells. *ACS Nano* **2010,** *4* (2), 887-894.

98.   Cheng, H.; Lu, Z.; Deng, J.; Chung, C. Y.; Zhang, K.; Li, Y., A Facile Method to Improve the High Rate Capability of Co_3O_4 Nanowire Array Electrodes. *Nano Res.* **2010,** *3* (12), 895-901.

99.   Xiong, S.; Yuan, C.; Zhang, X.; Xi, B.; Qian, Y., Controllable Synthesis of Mesoporous Co_3O_4 Nanostructures with Tunable Morphology for Application in Supercapacitors. *Chem. Eur. J.* **2009,** *15* (21), 5320-5326.

100.   Wang, G.; Shen, X.; Horvat, J.; Wang, B.; Liu, H.; Wexler, D.; Yao, J., Hydrothermal Synthesis and Optical, Magnetic, and Supercapacitance Properties of Nanoporous Cobalt Oxide Nanorods. *J. Phys. Chem. C* **2009,** *113* (11), 4357-4361.

Chapter 2 | Experimental Details

In this chapter we have described different synthesis methods of nanomaterials and also various techniques to characterize them.

2. Material Synthesis and Characterization Techniques

2.1. Preamble

In this chapter different experimental procedures used to synthesize various nanostructures of diverse materials such as wet chemical route and solvothermal methods along with their surface modification process are described in detail.

The phase and morphology of the synthesized nanostructures are studied using X-ray Diffraction (XRD), Field Emission Scanning Electron Microscope (FESEM), Transmission Electron Microscope (TEM), High Resolution Transmission Electron Microscope (HRTEM), Energy Dispersive X-ray Analysis (EDX), Selected Area Electron Diffraction (SAED). The chemical analysis on the oxidation state of the nanostructures is conducted by employing X-ray photoelectron spectroscopy (XPS). Optical analyses are carried out using UV-visible spectrophotometer, Fourier Transformed Infrared Spectrometer (FTIR), Fluorescence microscope, Steady state and time resolved fluorometer. The magnetic characterizations are carried out employing Vibrating Sample Magnetometer (VSM). Electrochemical characterizations are carried out by cyclic voltammetry (CV) and galvanostatic charging-discharging (GCD) by using software controlled conventional three-electrode electrochemical cell.

2.2. Synthesis of Nanomaterials

All the methods of nanomaterials synthesis can be generally classified as top-down (i.e. bulk to nanoparticles (NPs)) and bottom-up (i.e. atom to NPs) approaches.

2.2.1. Top-Down Approach

Top down approach refers to slicing or successive cutting of a bulk material to get nanosized particle. This method includes high energy ball milling, etching, electro explosion, sonication etc. NPs produced through top-down methods usually have

imperfection in surface structures, such as broad size distribution, undefined shape, impurities, and defects, which are drawbacks of the top-down process.

2.2.2. Bottom-up Approach

This method refers to synthesis of nanostructures from bottom level (i.e. from atoms or molecules) by nucleation followed by growth. This approach ensures better possibility to produce nanostructures with fewer defects, more homogeneity in chemical composition, narrow size distribution and high crystallinity. The ability to assemble nanoscale functional building blocks is a useful and modular way for scientists to design valuable materials with specific physical and chemical properties.[1]

2.3. Formation of Nanoparticles

Homogeneous nucleation occurs when nuclei form uniformly throughout the parent phase, called supersaturation. This condition can be achieved by rational control of reaction conditions such as solvent, capping agents, temperature etc. The process of homogeneous nuclei formation can be considered thermodynamically by looking at the total free energy (ΔG) of a NP defined as the sum of the surface free energy and the bulk free energy. The overall free energy changes (ΔG) associated with the homogeneous nucleation process, which is the total change in free energy between a small solid particle of a solute and the solute in solution. The excess surface free energy, ΔG_S, is the excess surface energy between the NPs and the corresponding bulk material. Excess volume free energy, ΔG_V, is the excess free energy between a very large particle and the solute in the solution. Dependence of ΔG_S and ΔG_V on particle size with radius (r) can be observed from Equation 2.1 and also depicted in the Figure 2.1.[2]

$$\Delta G = \Delta G_S + \Delta G_V = 4\pi r^2 \gamma + (4/3)\pi r^3 \Delta G_v \qquad (2.1)$$

Where, ΔG_v is the free energy change per unit volume and γ is the interfacial tension between the growing NP surface and the supersaturated solution.
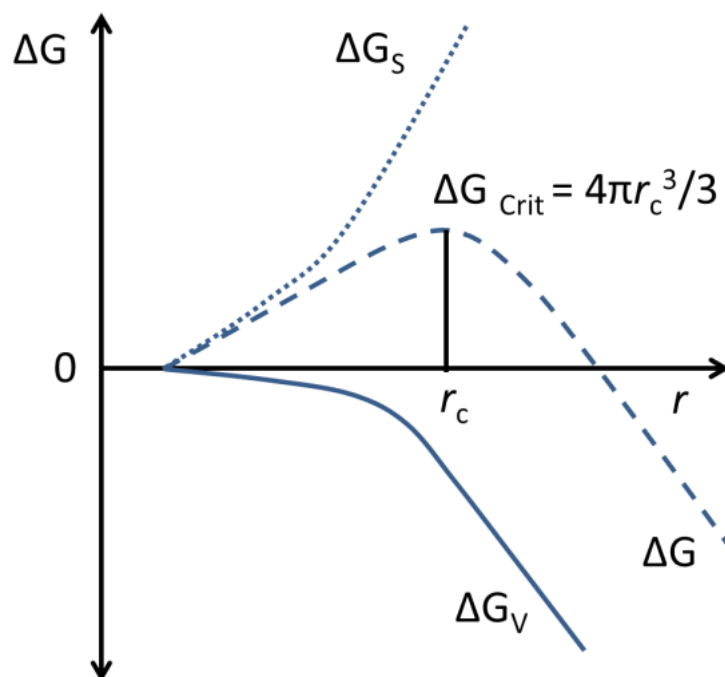
Figure 2.1. Free-energy diagram for nucleation process. (© Kumar et al. *Small* **2006,** *2* (3), 316-329.)

As ΔG_S is always positive and ΔG_V is always negative, it is possible to find a ΔG for a stable nucleus having an optimum size (critical radius, r_c) by differentiating ΔG with respect to r and setting it to zero, which gives a critical free energy, as shown in Equation 2.2. The critical radius is defined in Equation 2.3. It is evident from Figure 2.1, that the total excess free energy, ΔG, passes through a maximum, ΔG_{crit}, corresponding to the critical nucleus size, r_c,

$$\frac{d(\Delta G)}{dr}\bigg|_{r=r_c} = 8\pi r_c \gamma + 4\pi r_c^2 \Delta G_v = 0 \tag{2.2}$$

$$\Rightarrow r_c = -\frac{2\gamma}{\Delta G_v} \tag{2.3}$$

From equations (2.1) and (2.3), we can obtain the critical value of ΔG as

$$\Delta G\big|_{r=r_c} = \Delta G_{Crit} = \frac{16\pi\gamma^3}{3\left(\Delta G_v\right)^2} = \frac{4\pi\gamma r_c^2}{3} \qquad (2.4)$$

i.e. the minimum energy barrier that a nucleation process must overcome is ΔG_{crit}, which corresponds to the minimum size of a stable spherical nucleus (r_c). This critical radius corresponds to the minimum size at which a particle can survive in solution without being redissolved.

Crystal structure, size and morphology of the growing particles mainly depend on the system and reaction parameter. The growth of NPs is dependent on two mechanisms: the surface reaction and the monomer's diffusion to the surface.

Different theories have been proposed to explain the nucleation and growth mechanism of various reactions.[3] Such as, in the LaMer mechanism, the process of nucleation and growth is divided into three portions. Firstly, a rapid increase in the concentration of free monomers in solution, secondly, the monomer undergoes "burst nucleation" which significantly reduces the concentration of free monomers in solution. The rate of nucleation is described as "effectively infinite" and after this point, nucleation almost stops due to the low concentration of monomers; In third stage growth occurs under the control of the diffusion of the monomers through solution. Ostwald and digestive ripening mechanism say that, growth is caused by the change in solubility of NPs dependent on their size. According to Ostwald ripening, due to the high solubility and surface energy of smaller particles within solution, these redissolve and in turn allow the larger particles to grow even more. Digestive ripening, described by Lee et al., is effectively the inverse of Ostwald ripening, where smaller particles grow at expense of the larger ones by surface energy controlled process.[4] The Finke-Watzky two step mechanism is a process of nucleation and growth where both steps happen simultaneously.[5] The first is a slow continuous nucleation, (shown in Equation 2.5) and the second is the autocatalytic surface growth which is not diffusion controlled, (shown in Equation 2.6).

$$A \rightarrow B \qquad (2.5)$$

$$A + B \rightarrow 2B \qquad (2.6)$$

Shape of the crystallites occurs either in order to minimize the surface energy of the particles or because of the kinetics of the growth. If kinetics dominates, the shape is then determined by the rate at which different crystal faces grow. In thermal equilibrium, crystal shape is determined by minimization of surface energy.[2]

2.4. Fabrication Techniques of Different Nanostructures

2.4.1. Wet Chemical Method

Wet chemical method refers to a particular group of methods where generally nano or ultra-dispersed inorganic materials have been produced in aqueous or non-aqueous solutions. It is different from conventional solid state procedure in respect to that it can only be done in liquid phase and more importantly it can produce much smaller, monodisperse grains or crystallites usually at lower temperature and have shorter duration of phase formation. It is mainly a "bottom-up" method to synthesize NPs basically by chemical reduction of metal salts, electrochemical trails or through controlled decomposition of different metastable organometallic compounds.

2.4.2. Formation of Metal Oxides by Refluxing Organometallic Compounds

Reflux is carried out by dissolving salts or organometallic compounds containing constituent elements with proper ratio in aqueous or non-aqueous solvents in presence of suitable capping agents, followed by heating at temperature at about the boiling point of the solvent, in a flask with the condenser placed over it. After the completion of reaction, the reaction medium is cooled to room temperature, and the product is precipitated by altering the polarity of the medium (e.g. in case of organic solvent, NPs are precipitated by adding ethanol) and washed several times to eliminate impurities followed by drying. This method is employed extensively in material science and industry to synthesize complex oxides with high crystallinity,

compositional homogeneity and better stoichiometry. The refluxing setup used in our laboratory for fabrication of various oxide NPs is shown in Figure 2.2. Fe_2O_3, $MnFe_2O_4$, and $CoFe_2O_4$ NPs were prepared by template free wet chemical process following a previous report with some modification,[6] which involves the high-temperature (270 °C) reflux of metal ion salts (only Iron (III) acetylacetonate, $Fe(acac)_3$ in case of Fe_2O_3 and addition of Manganese (II) acetate $(Mn(ac)_2)$/ Cobalt (II) acetate $(Co(ac)_2)$ in case of $MnFe_2O_4$, and $CoFe_2O_4$ NPs respectively) with proper molar ratio (Mn or Co: Fe in 1:2) in a high boiling organic solvent, di-phenyl ether, for 1 h, in the presence of capping agents, cetyl alcohol ($C_{16}H_{33}OH$), oleylamine ($CH_3(CH_2)_7CH=CH(CH_2)_7NH_2$), and oleic acid ($CH_3(CH_2)_7CH=CH(CH_2)_7COOH$).
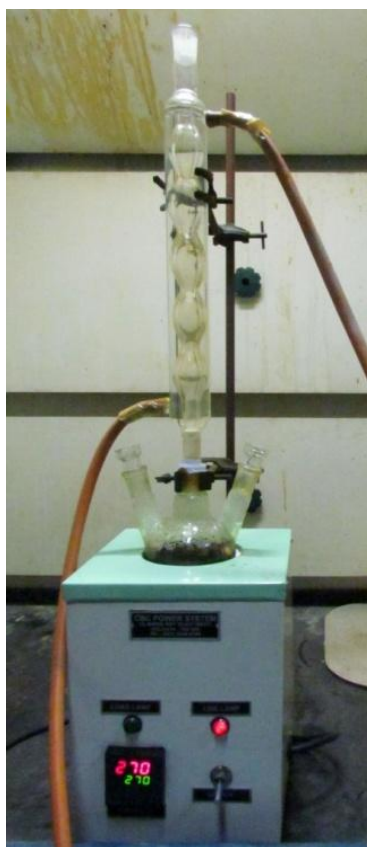
Figure 2.2. Setup for refluxing.

2.4.3. Solvothermal Method

Solvothermal technique is a method for fabrication of nanostructures of various metals, semiconductors, ceramics and also polymers from aqueous or non-aqueous

medium by controlling temperature, pressure, capping agent, chemical composition, and duration of reaction. This process involves different polar (like, water, ethanol etc.) or non-polar solvents (like benzene, ethylene glycol, ethylene di-amine etc.) under high pressure and temperature (generally above the boiling point of solvent) to facilitate the interaction of different precursor molecules during the synthesis procedure. Solvothermal chemistry being the use of a sealed reaction vessel and temperature above the boiling point of the solvent used, autogeneous pressure (*i.e.* self-developing and not externally applied) is developed.[7] The pressure within the sealed reaction container is found to increase dramatically with temperature, but also depends on other experimental factors, such as the percentage fill of the vessel, any dissolved salts, and capping agents. This method is called hydrothermal route when the solvent is water. A number of fundamental properties of solvents are greatly affected by pressure and temperature. For example, the viscosity of water decreases with increasing temperature, such as at 500 °C and 10 bar viscosity of water is only 10% of its magnitude under ambient conditions.[8] Thus it is evident that the mobility of dissolved ions and molecules is higher under solvothermal conditions than at ambient pressure and temperature. Similarly, the dielectric constants of solvents are considerably reduced above the critical pressure and temperature; this can have major implications on the solubility of solid reagents under reaction conditions.[7]

In this technique precursors are dissolved in the solvent by magnetic stirring or sonication, the homogeneous mixture is transferred into teflon lined stainless steel autoclave chamber, as shown in Figure 2.3.

The precursor solution is poured in the chamber in such a way that 70% of it should be filled. The autoclave is then sealed and heated to a certain temperature in an oven. This method can be used to prepare various types of nanostructures such as particles, wires, rods, hollow spheres, spindles etc. The advantageous aspects of the solvothermal synthesis route, in particular the formation of homogeneous sample of complex mixed-metal solids, the isolation of metastable phases not seen at high temperature, and the control of crystal form, make the method particularly attractive for future study.
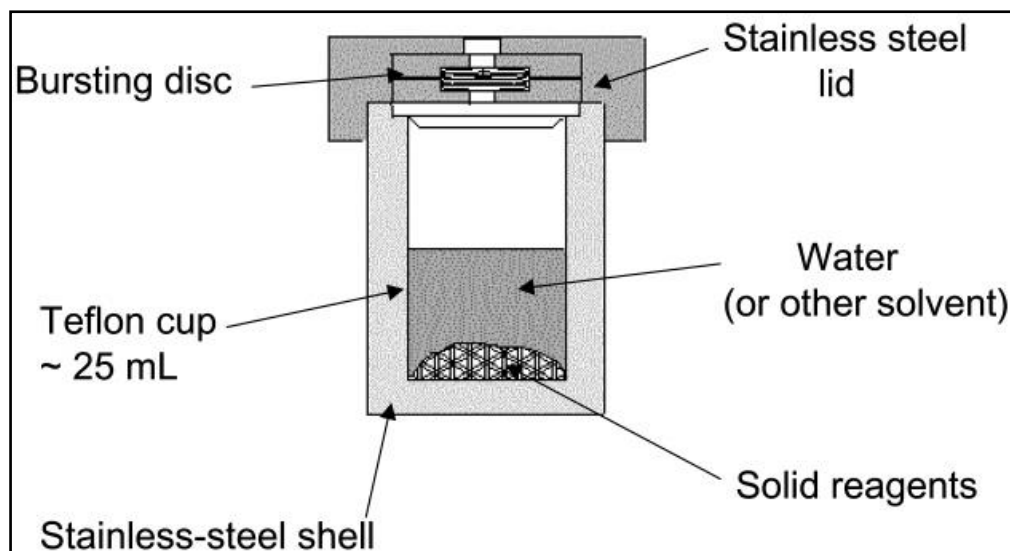
Figure 2.3. Schematic diagrams of an autoclave and a teflon chamber used in solvothermal synthesis. (© Walton et al. *Chem. Soc. Rev.* **2002,** *31* (4), 230-238.)

Dissolution and crystallization mechanism of solvothermal method are greatly influenced by different thermodynamic and crystallographic effects behind the formation of various fascinating nanostructures such as oriented attachment of phases, selective adsorption of solvent or ligand molecules, molecular template mechanism etc.[2, 9] We have synthesized Co_3O_4 nanocubes (NCs) by solvothermal route following a previous report with some modification where, 0.70 g of Co $(CH_3COO)_2 \cdot 4H_2O$ was dissolved in 35 ml of ethanol, and 12 ml of 25% ammonia was added under vigorous stirring. The mixture was stirred in air for about 10 min to form homogeneous slurry. Then the suspension was transferred into a 50 ml teflon lined autoclave and heated at 150 ºC for 3 h.[10]

2.5. Functionalization Procedure of Different Nanostructures

As-prepared nanostructures were cyclomixed with small hydrophilic organic ligand tartrate (0.5 M solution of tartaric acid was prepared in Milli-Q water and pH of the solution were made ~7 after drop wise addition of NaOH solution, Figure 2.4 shows the structure of tartaric acid) for 12 h at room temperature. The nonsolubilized larger

nanostructures were filtered out with a syringe filter of 0.22 μm diameter. The as obtained colorless filtrate was tartrate functionalized nanostructures (called T-Fe_2O_3, T-$MnFe_2O_4$, T-$CoFe_2O_4$ NPs and T-Co_3O_4 NCs). To amplify their optical response, functionalized nanostructures were heated at about 70 °C under extensive stirring condition maintaining the pH of the solution at ~12 after drop wise addition of NaOH solution. After this high pH and temperature treatments, color of the solution got darker and showed intense fluorescence under UV light irradiation. The solid powdered samples required for FTIR spectroscopic measurement and magnetic study (VSM) were prepared by dialysis and lyophilization of the functionalized nanostructures' solution (to remove excess ligands) followed by drying over a water bath.
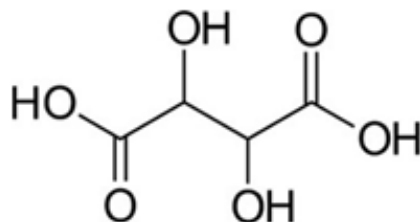
Figure 2.4. Chemical structure of a tartaric acid molecule.

2.6. Phase and Morphology Characterization Techniques

2.6.1. X-ray diffractometer (XRD)

XRD is used to probe the crystal structure of micro and nanostructures, thin films and bulk samples in a nondestructive way. In this method of determining molecular and atomic structure of a crystalline material, atomic planes of the material diffract incident X-rays in different specific directions depending on their orientations. By measuring the angle and intensity of the diffracted beams, a three dimensional idea of the density of electrons within the specified crystal can be obtained. From this density of electrons, mean position of the atoms in the crystal can be determined.

In XRD instrument as shown in Figure 2.5, monochromatic beam of X-rays fall on a crystalline sample. Those X-rays are scattered elastically by the electrons

within the crystal planes. Then, the scattered waves interfere constructively in few specific directions that can be determined by Bragg's law given as Equation 2.7:

$$2d \sin \theta = n\lambda \qquad (2.7)$$

Where, d is the crystal plane spacing, θ is the diffraction angle, n is an integer, and λ is the wavelength of incident light. The angles and intensities of the diffracted beams are processed and recorded electronically using a detector, resulting in intensity vs. 2θ plot for a specific sample.
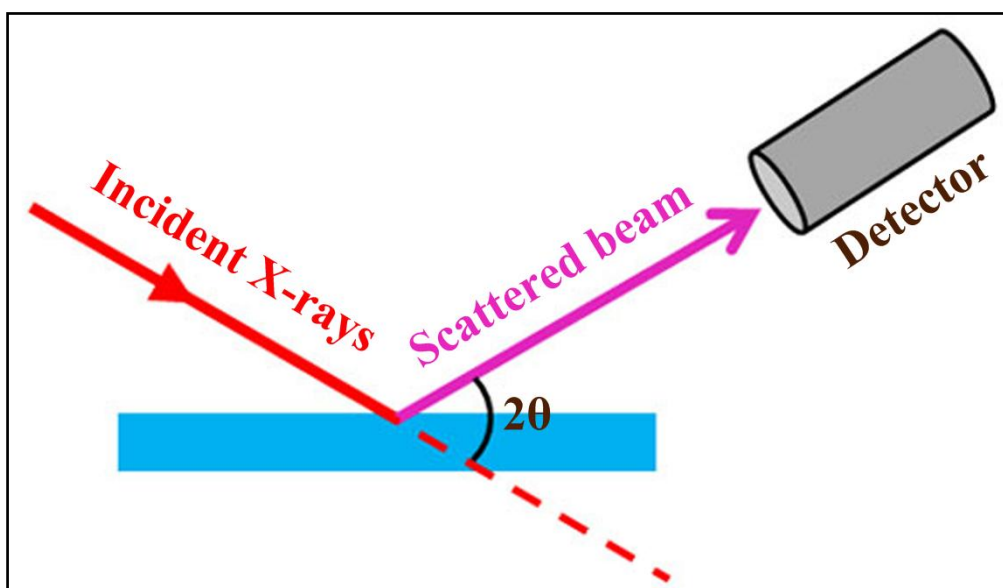
Figure 2.5. Schematic diagram of X-ray diffractometer.

The grain size (d) of the sample can be calculated by observing the width of the diffraction peaks and using the relation as given by Debye-Scherrer Equation 2.8:

$$d = 0.9\lambda / (\beta \cos \theta) \qquad (2.8)$$

Where, β is the full width at the half maximum of the diffraction peak at a diffraction angle of 2θ. XRD patterns of our samples were obtained by applying a scanning rate of 0.02° s^{-1} in the 2θ range from 20° to 80° by Rigaku miniflex II diffractometer equipped with Cu K$_\alpha$ (λ~1.54 Å) radiation (at 40 mA and 40 kV).

2.6.2. Electron Microscopes

An electron microscope is a type of microscope that uses a beam of highly energetic electrons to illuminate a specimen and produce its magnified image. We have used two types of electron microscopes to analyze our samples as described below.

2.6.2.1. Scanning Electron Microscope (SEM)

In a SEM (schematically shown in Figure 2.6), a tiny electron beam, formed either thermo-ionically or field emission,[11] is focused onto the sample. Simultaneous to scanning the beam across a selected rectangular area of sample, generated signals are recorded and thereby an image is formed pixel by pixel. Valuable information about morphology, surface topology and composition can be obtained. It works within the voltage ranging from 2 to 50 kV. The interactions which are responsible for a multitude of signal types are backscattered electrons (BSEs), secondary electrons (SEs), X-rays, Auger electrons, and cathadoluminescence. Inelastic events occur when an incident beam electrons interact with the electric field of sample atom electrons, resulting transfer of energy leading to potential expulsion of an electron from that atom as a SE. SEs by definition are less than 50 eV. If the vacancy due to the formation of a SE is filled from a higher level orbital, an X-ray characteristic of that energy transition is produced. Elastic events occur when a beam electron interacts with the electric field of the nucleus of a specimen atom, resulting in change of direction of electrons without altering energy of the electron significantly (< 1eV). Among the elastically scattered electrons which are deflected backward are called BSE. BSEs have energy in between 50 eV to the energy of incident beam. Generally, the image displayed by a SEM is a mapping of the varying intensity of the signal produced by the SEs into the image in a position corresponding to the exact position of the beam on the specimen. Whereas the characteristic X-rays are used for elemental analysis, this method is known as Energy dispersive analysis of X-rays (EDX). Morphology of our samples was tested by field emission scanning electron microscope (FESEM, FEI QUANTA FEG-250) operating at 5-10 kV.
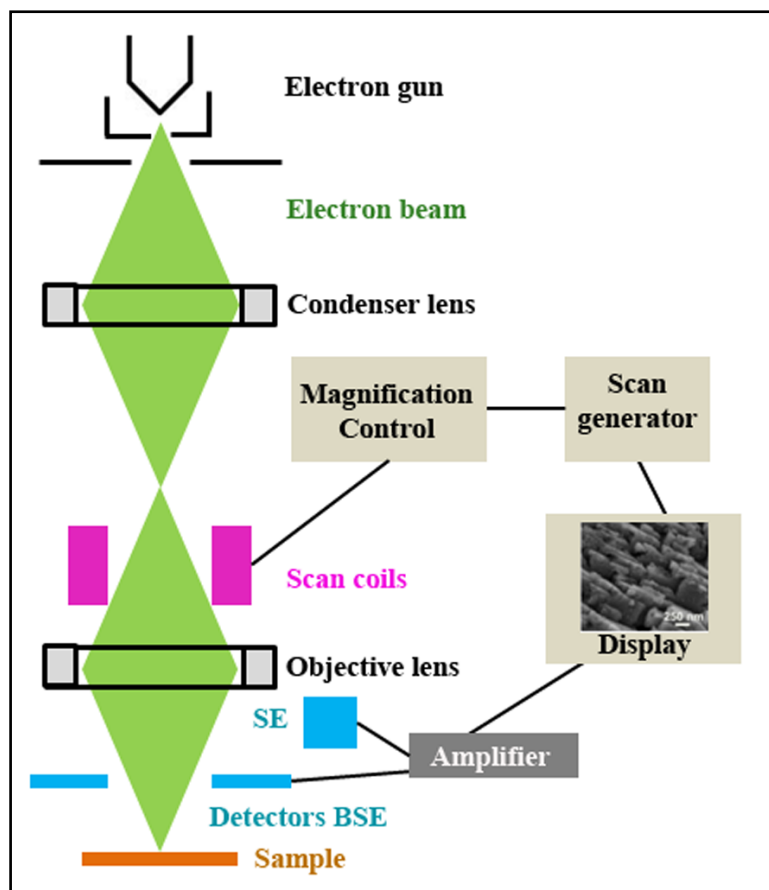
Figure 2.6. Schematic diagram of SEM; display shows SEM image of Co_3O_4 NCs over Ni foam.

2.6.2.2. Transmission Electron Microscope (TEM)

TEM uses mainly two different types of interactions between the electron beam and specimen to construct an image; such as unscattered electrons (transmitted beam) and elastically scattered electrons (diffracted beam). Schematic diagram of a TEM is shown in Figure 2.7. In this process, incident electrons are transmitted through the thin specimen without causing any interaction within the specimen. The transmission of unscattered electrons is inversely proportional to the specimen thickness. Areas of the specimen that are thicker will have fewer transmitted unscattered electrons and so will appear darker, conversely the thinner areas will have more transmitted and thus will appear lighter. This mode of operation to create contrast in image is known as bright field imaging mode.
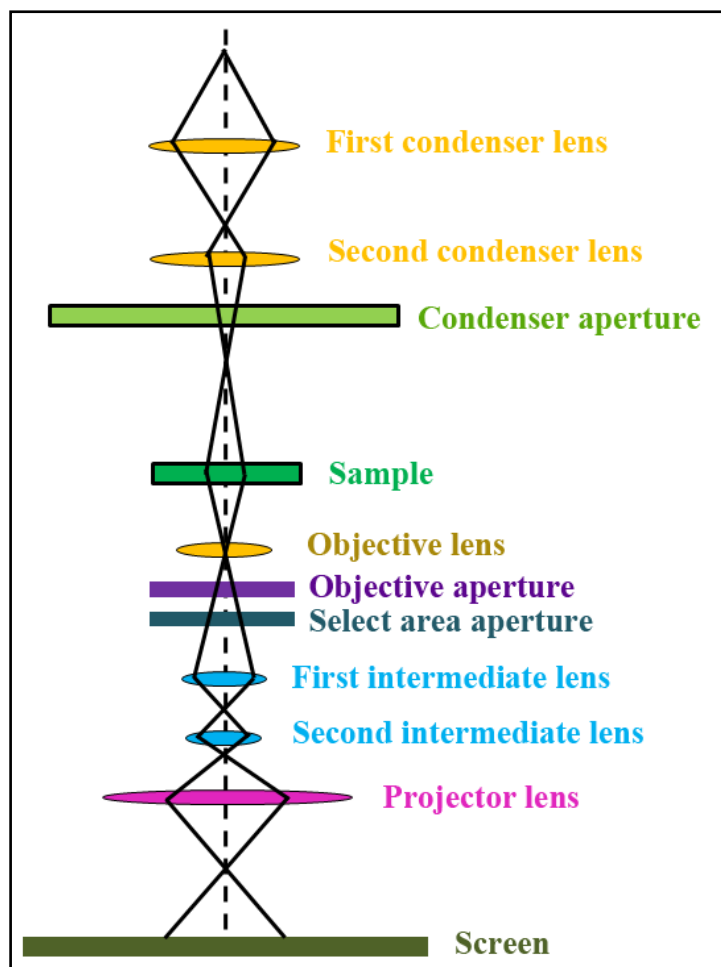
Figure 2.7. Schematic diagram of TEM.

Another important mode of TEM imaging is electron diffraction. In case of crystalline sample the electron beam undergoes Bragg scattering in accordance with the Bragg's law as given by Equation 2.7. All incident electrons have the same energy (thus wavelength) and enter the specimen perpendicularly to its surface. Now, the electrons that are scattered by the same set of parallel planes can be collated using magnetic lenses to form a pattern of spots; each spot corresponding to a specific atomic spacing (or crystalline plane). This pattern can then yield information about the orientation, atomic arrangements, and phases present in the area being examined.

In case of high resolution TEM (HRTEM) mode we can achieve a resolution around 0.2 nm which is very efficient in observing the lattice fringes of the specimen under observation. As the electron beam is transmitted through the thin section, a

variety of beam specimen interactions occur that yield transmitted electrons, elastically and inelastically scattered (energy-loss) electrons, SEs, BSEs, Auger electrons, and X-ray photons. TEM-based elemental analysis techniques use X-ray photons in EDX and inelastically scattered electrons or the "energy-loss" electrons in electron energy-loss spectroscopy (EELS) and Energy filtered transmission electron microscopy (EFTEM).

For TEM study, we prepared samples by drop casting NPs in ethanol, water, or hexane on 300-mesh carbon coated copper grid and dried overnight in air. Particle size was calculated from TEM micrographs and elemental analysis was carried out from EDX spectrum recorded by a FEI Tecnai TF-20 field-emission high resolution transmission electron microscope operating at 200 kV.

2.6.3. X-ray Photoelectron Spectroscopy (XPS)

XPS is a quantitative spectroscopic technique to measure the elemental composition, chemical formula, oxidation state and electronic state of elements that exist within the material under observation. XPS spectra is obtained by illuminating the sample by X-rays and simultaneously measuring the kinetic energies and the number of electrons that escape from the top 1-10 nm of the substance of interest. As the energy of the irradiating X-ray photon (E_{Photon}) is known, the binding energy ($E_{Binding}$) of each electron emitted from the surface of the material can be calculated using the Ernest Rutherford equation as given below:

$$E_{Binding} = E_{Photon} - (E_{Kinetic} + \Phi)$$

(2.9)

Where, $E_{Kinetic}$ is the kinetic energy of the emitted electron and Φ is the work function of the spectrometer. XPS spectrum is a plot of the number of electrons detected (Y-axis) vs. the binding energy of that electrons (X-axis). Each material produces its characteristics spin orbital splitting and peak area ratios, which assist in element identifications. XPS peaks that correspond to the electronic configuration of the electrons in different orbitals such as 1s, 2s, 2p etc. and the number of electrons detected is directly proportional to the amount of that element present in the irradiated portion of the sample. As the electron counting detector in XPS

instruments is about 1 m away from the X-ray irradiated sample, so, XPS must be performed in ultra-high vacuum condition. The schematic diagram of the XPS system is shown in Figure 2.8.
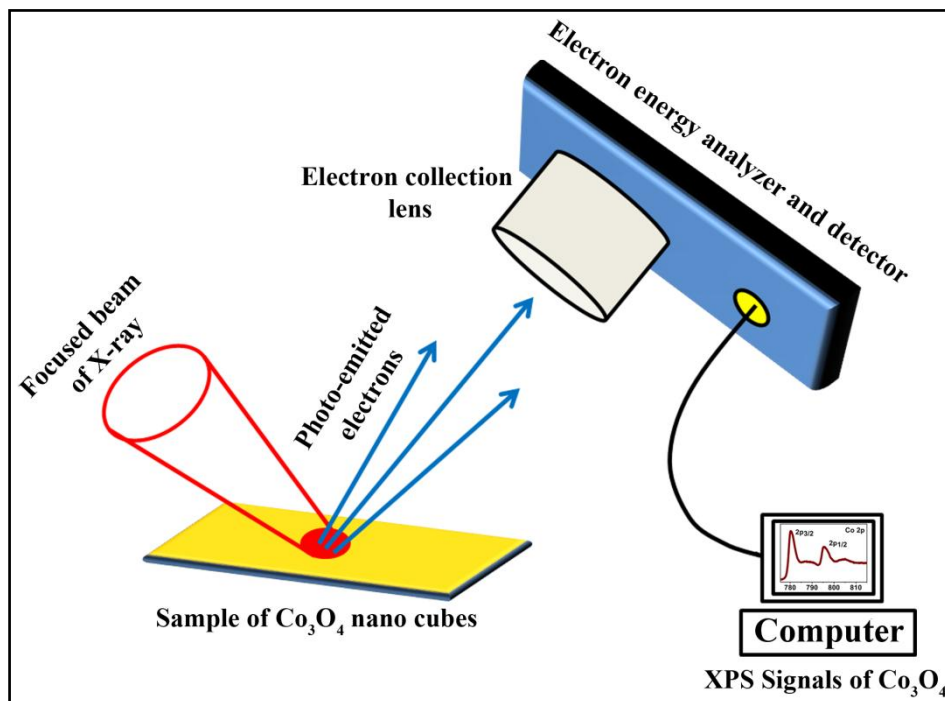
Figure 2.8. Schematic diagram of an XPS spectrometer.

2.7. Magnetic Characterization Techniques

In a vibrating sample magnetometer (VSM), the sample is placed in a direct current (DC) magnetic field (*H*) and vibrated sinusoidally so that the resulting variation of magnetic flux (*B*) can induce a voltage in pickup coils. According to Faraday's law of electromagnetic induction, the voltage induced (*V*) in a pickup coil of *N* turns with a cross-sectional area of *A* is given by Equation 2.10

$$V = -NA \frac{dB}{dt} \quad ……………..(2.10)$$

Where, $B = \mu_0 H$ (here μ_0 is a constant called the vacuum permeability)

Now, if a sample having magnetization *M* is placed in the pickup coil, the total magnetic induction *B* can be written as

$$B = \mu_0(H + M) \qquad (2.11)$$

So, change in flux due to sample insertion, $\Delta B = \mu_0 M$

Hence, the Equation 2.10, can be rewritten as $Vdt = -\mu_0 NAM$ $\qquad$ (2.12)

The intensity of the signal is proportional to the magnetic moment of the sample and the frequency is the same as that of the sinusoidal motion. The schematic diagram of the sample holder and detection mechanism of a VSM is shown in Figure 2.9. Magnetic study of our sample was performed in a Lake Shore VSM equipped with an electromagnet, capable of generating field of up to 1.6 T at 300 K.
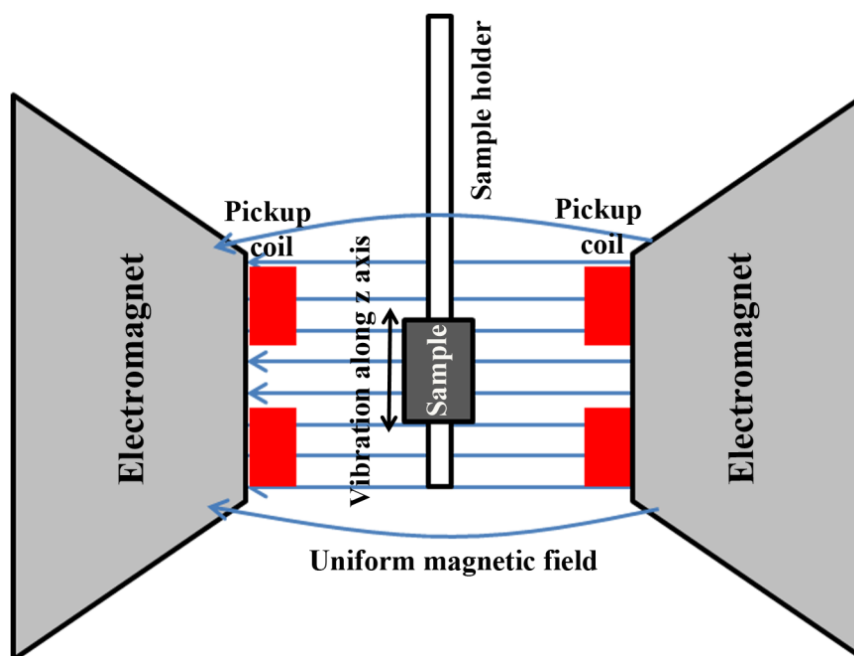
Figure 2.9. VSM sample holder and detection mechanism.

2.8. Optical Characterization Techniques

2.8.1. UV-Visible Absorption Spectrometer

Upon absorption of energy, in visible and adjacent (near-UV and near-infrared (NIR)) region of electromagnetic spectrum the molecules undergo electronic transition from ground state to another excited state. This technique is often used to

measure the concentration of an absorbing species in solution using Beer-Lambert law as given below.

$$A = \log_{10}(I_0 / I) = \varepsilon \cdot c \cdot l$$ ………………(2.13)

Where, A is the absorbance of sample, I_0 is the intensity of the incident light at a given wavelength, I is that for the transmitted light, l is the path length of light covered through the sample, c is the concentration of the absorbing species, and ε is the molar absorptivity or molar extinction coefficient that is characteristics of a particular absorber and constant at a particular wave length. The schematic diagram of the UV-visible spectrometer is demonstrated in Figure 2.10. UV-visible absorbance spectra of our samples were obtained from a Shimadzu Model UV-2600 spectrophotometer using a quartz cuvette of 1 cm path length. We have studied catalytic and photocatalytic activities of our samples by using UV-visible spectrophotometer.
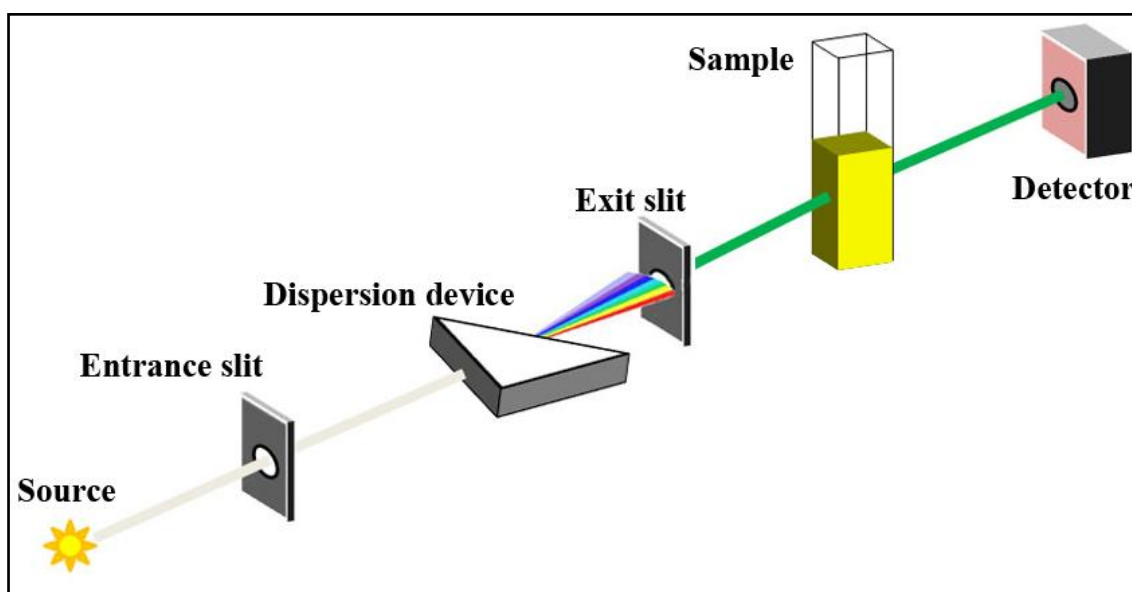
Figure 2.10. Schematic diagram of a UV-visible spectrometer.

2.8.1.1. Catalysis

For the study of catalysis, we have chosen biologically harmful pigment bilirubin (BR), which is an yellow-orange breakdown product of normal heme catabolism in mammalian systems, introduces great biological and diagnostic values.[12] Molecular

formula of BR is $C_{33}H_{36}N_4O_6$, and its chemical structure is demonstrated in Figure 2.11. Both antioxidant and toxic properties have been attributed to BR,[13] which is normally conjugated with glucuronic acid and then excreted in the bile. However, when its conjugation with glucuronic acid is inhibited, as in neonatal jaundice and in hereditary forms of congenital jaundice, excess BR bind and deposit to various tissues, giving rise to severe hyperbilirubinemia and neurotoxicity. During the study of catalysis, aqueous NPs solution were added in the aqueous solution of BR kept in a quartz cuvette in the dark maintaining the pH of the solution ~7, with stirring condition and the absorbance of BR in the reaction mixture was measured time to time by the UV-visible spectrophotometer.
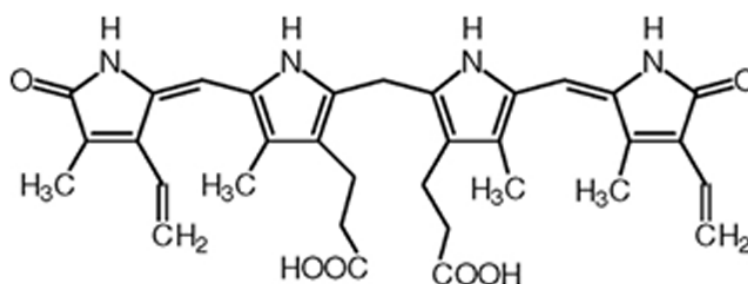
Figure 2.11. Chemical structure of BR.

2.8.1.2. Photocatalysis

For the study of photo-catalysis we have chosen methylene blue (MB). MB is a heterocyclic aromatic chemical compound with molecular formula: $C_{16}H_{18}ClN_3S$. It has many uses in a range of different fields. At room-temperature it appears as a solid and is odourless and a dark green powder, which yields a blue solution when dissolved in water. They are widely used as model water contaminant.[14] Its structure is given in Figure 2.12. When dissolved in water, the UV-visible spectrum of MB showed three absorption maxima. The first band was observed at 246 nm and then 291 nm and more intensely 663 nm. The absorption maxima wavelength of MB (λ_{max} = 663 nm) was used for the analysis during decolorization of MB dye. During the study of photocatalysis we used 8 W UV lamp as UV light and a 100 W incandescent light bulb as visible light source from Philips. Aqueous solution of MB and aqueous

NPs solution were homogeneously mixed for 1 h in a quartz cuvette in the dark maintaining the pH of the solution ~3. Then the cuvette was kept ~2 cm apart from the light source and the absorbance of MB in the reaction mixture was recorded time to time by the UV-visible spectrophotometer.
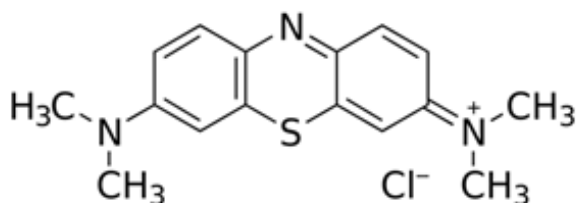
Figure 2.12. Chemical structure of MB.

2.8.2. Photoluminescence (PL) Spectroscopy

PL is a process where a specimen is excited with light, resulting absorption of photons of particular energy and then emission of photons with different energies. Quantum mechanically, this can be described as excitation of an electron to a higher energy state by absorbing photons and then return to a lower energy state with the emission of photons. The period between absorption and emission is very short, in the order of 10 nanoseconds. Schematic diagram of the PL spectrometer is shown in Figure 2.13. Steady state fluorescence emission and excitation spectra of different samples were recorded on Horiba Jobin Yvon Model Fluorolog fluorometer.

Fluorescence quantum yields (QYs) of the NPs have been calculated following the relative method of Williams et al.,[15] following the Equation 2.14.

$$Q_s = \frac{I_s A_r n_s^2}{I_r A_s n_r^2} Q_r \qquad (2.14)$$

Where, Q_r is the fluorescence quantum yield of reference. *I* stands for the integrated area under the emission curves. The subscripts *s* and *r* stand for sample and reference, respectively. *A* is the absorbance at a particular excitation wavelength. *n* is the refractive index of the medium. The absorbance of the dye at the excitation

wavelength was always kept nearly similar to that of sample. For our study we have used standard fluorescent compounds, such as 2-aminopurine (2AP), 4',6-diamidino-2-phenylindole (DAPI), Hoechst 33258, and Rhodamine B (RhB). Chemical structures of these dyes are exhibited in Figure 2.14.
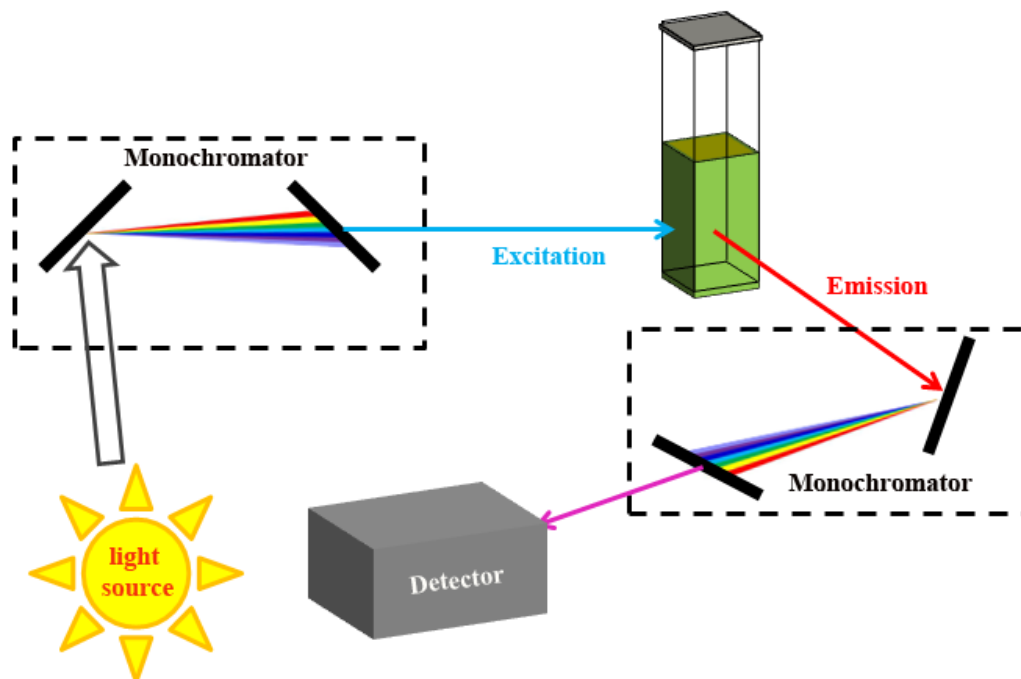
Figure 2.13. Schematic diagram of photoluminescence spectrometer.
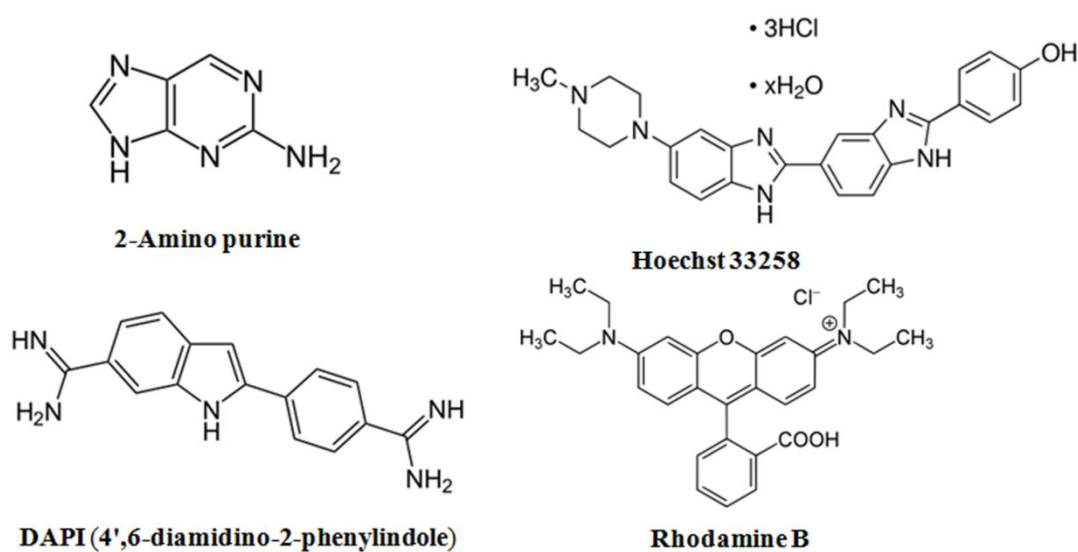
Figure 2.14. Chemical structure of dyes.

2.8.3. Fluorescence Microscope

A fluorescence microscope is similar to the conventional light microscope with added features to enhance its capabilities where fluorescence can be used as a label or tag when preparing specific biological probes. The fluorescence microscope uses visible light with very high intensity light source (Xenon or Mercury arc-discharge lamp) to illuminate fluorochromes in a sample of interest. Fluorochromes in turn emit a lower energy light of a longer wavelength that produces the magnified image instead of the original light source. In fluorescence microscope, several light filtering components are used. Specific filters are used to isolate the excitation and emission wavelengths of a fluorochrome. First, the microscope has a filter that only lets through radiation with the specific wavelength that matches the fluorescing material. A dichroic beam splitter (partial mirror) isolates the emitted light from the excitation wavelength by reflecting shorter wavelengths of light and allowing longer wavelengths to pass. To become detectable (visible to the human eye) the fluorescence emitted from the sample is separated from the much brighter excitation light in a second filter (Figure 2.15). This works because the emitted light is of lower energy and has a longer wavelength than the light that is used for illumination. Most of the fluorescence microscopes used in biology, now a days are epi-fluorescence microscopes, where both the excitation and the observation of the fluorescence occur above the sample. Fluorescence micrographs of NPs were captured using an Olympus BX61 fluorescence microscope employing 365, 436, and 546 nm excitation wavelengths.
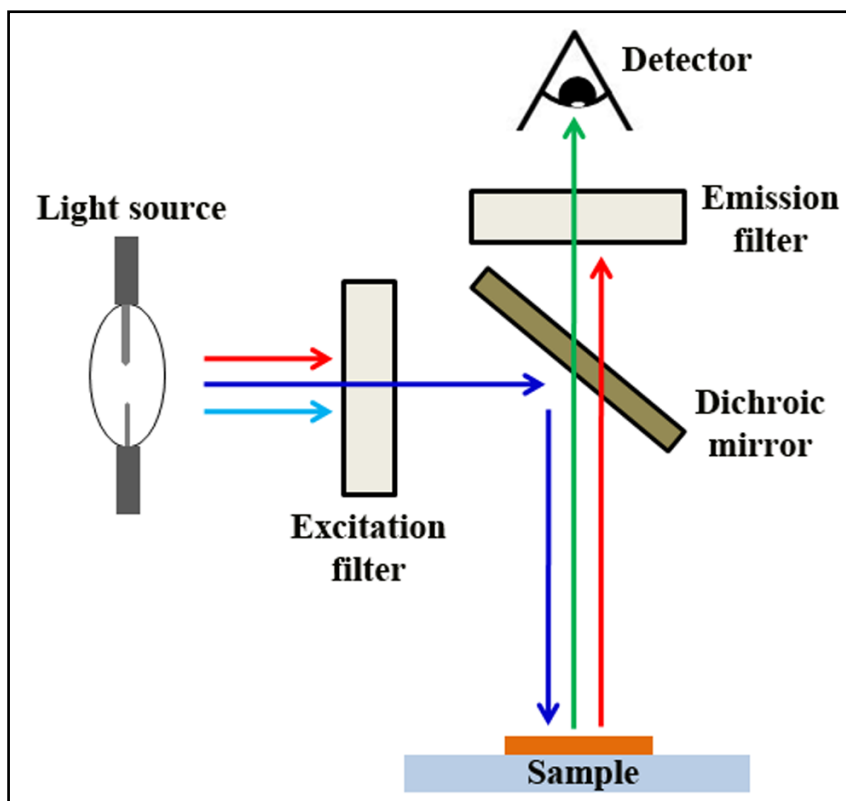
Figure 2.15. Schematic diagram of fluorescence microscope.

2.8.4. Time Correlated Single Photon Counting (TCSPC)

Time-resolved fluorescence transients of NPs solution were obtained using a picoseconds (ps) pulsed diode laser [nano LED from HORIBA JOBIN YVON] based time correlated single photon counting (TCSPC) fluorescence spectrometer, against excitation at 471, 377, and 294 nm, employing microchannel plate-photomultiplier tube (MCP-PMT) as a detector. The emitted light from NPs solution was collected at a right angle to the direction of the excitation beam maintaining magic angle polarization (54.7°) with a band pass of 2 nm. For 377 nm laser source the full width at half-maximum (FWHM) of the instrument response function was 270 ps, and the resolution was 28 ps per channel. In case of 294, 377, and 471 nm excitations, pulse duration was <1 ns, <100 ps, and <150 ps respectively. The data were fitted to multi exponential functions after deconvolution of the instrument response function by an iterative reconvolution technique using IBH DAS 6.2 data analysis software in which reduced χ^2 and weighted residuals serve as parameters for goodness of fit. All the

optical studies were performed at room temperature (298 K). The schematic block diagram of a TCSPC system is shown in Figure 2.16.
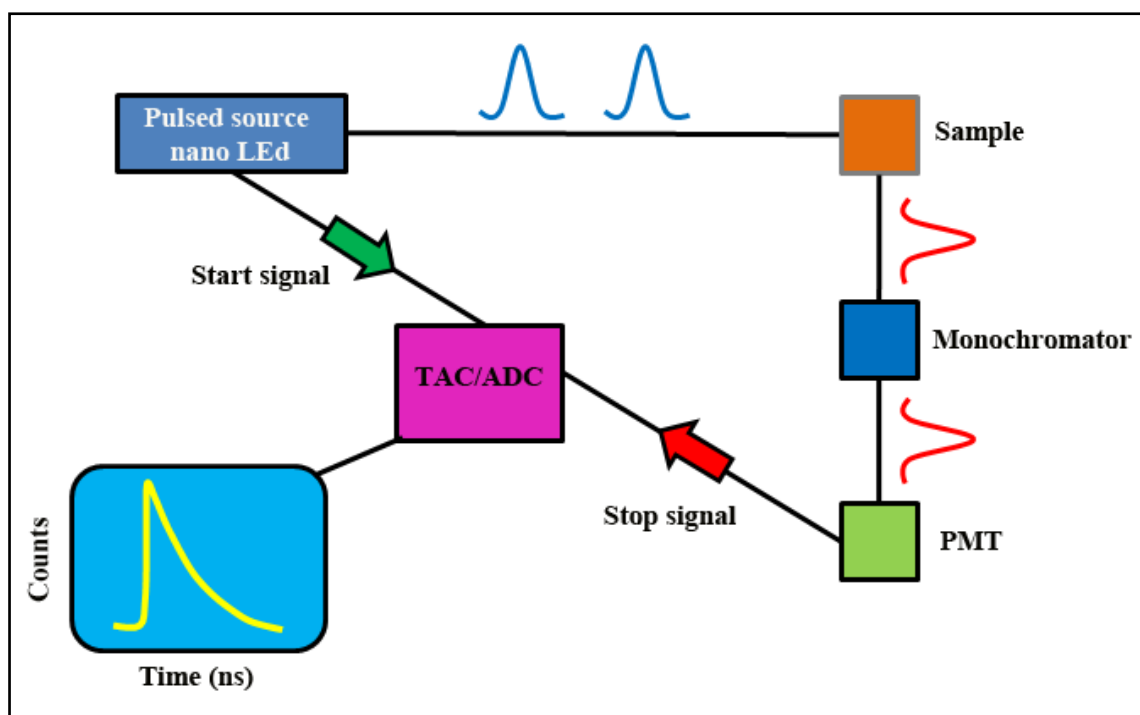
Figure 2.16. Schematic block diagram of a TCSPC system.

2.8.5. Fourier Transformed Infrared Spectroscopy (FTIR)

FTIR, a powerful tool to identify functional groups and chemical bonds within a molecule, is called molecular fingerprint. When the frequency of a polar vibrational mode of a bond matches with the incident IR frequency then due to absorbance of IR, FTIR signal is obtained. Additionally, the peaks get shifted or broadened due to interaction of functional groups with solvent molecules or NPs surface. Figure 2.17 shows schematic diagram of FTIR instrument.
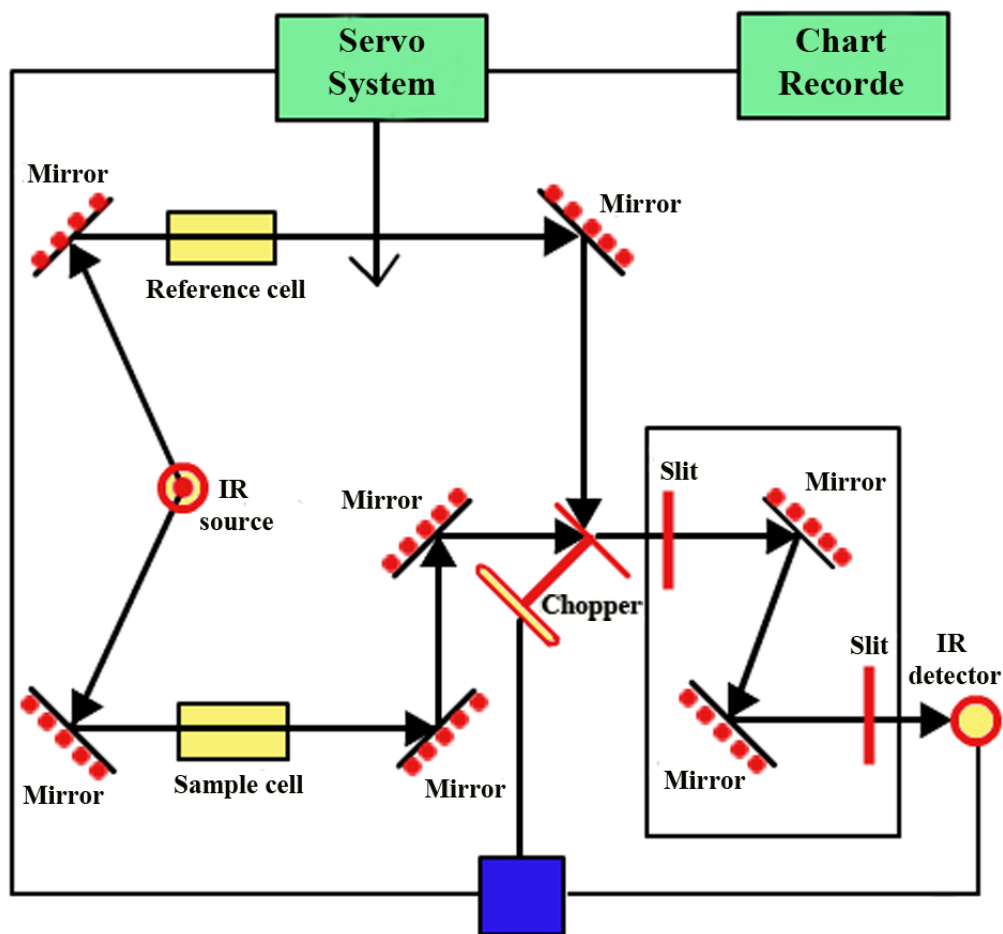
Figure 2.17. Schematic diagram of Michelson Interferometer, configured for FTIR.

As shown in the diagram, there are mainly two components in IR spectroscopy instrument, source and detector. The most common source of IR spectrometer is Nernst glower which consists of a rod of a sintered mixture of the oxides of Zirconium, Ytterbium and Erbium. The rod is electrically heated upto 1773 K to produce IR radiations. To change these IR radiations to monochromatic light, optical prism or grating can be used. Sodium chloride or other alkali metal halides are the best material to form prism and cell container as they are transparent in IR region. Light beam is split into two beams; one of the beams is passed through the sample and known as sample beam. Another beam is the reference beam. Due to absorption of radiation by sample compound, the intensity of sample beam decreases. Hence there will be some difference in intensity of reference beam and sample beam. These two beams are directed to fall on the segmented mirror with the help of two

supporting mirrors. The segmented mirror, also known as chopper, rotates at a definite speed reflecting the sample and reference beams to a monochromatic grating. As the grating rotates, it sends individual frequencies to the detector, which converts IR energy to electrical energy. This is then amplified. Because of the difference in intensity of both beams, alternating current starts flowing from the detector to amplifier. The amplifier is coupled with a small motor which drive an optical wedge and further coupled with a pen recorder, used to draw absorption bands on the calibration chart. A JASCO FTIR-6300 spectrometer was used to carry out FTIR studies. For the FTIR measurements, powdered samples were mixed with KBr powder and pelletized. The background correction was made using a reference pure KBr pellet before every measurement.

2.9. Electrochemical Characterization Techniques

The electrochemical properties of the samples were investigated by cyclic voltammetry (CV), and galvanostatic (GV) charge/discharge tests by using a software controlled conventional three-electrode electrochemical cell (potentiostat AutoLab-30) consisted of the as-prepared samples as the working electrode, saturated Ag/AgCl as the reference electrode, the Pt wire as the counter electrode and 0.5 M KOH solution as electrolyte, at room temperature. Figure 2.18 (a) shows electrochemical workstation of our laboratory. Figure 2.18 (b) exhibits zoomed image of three electrodes system.
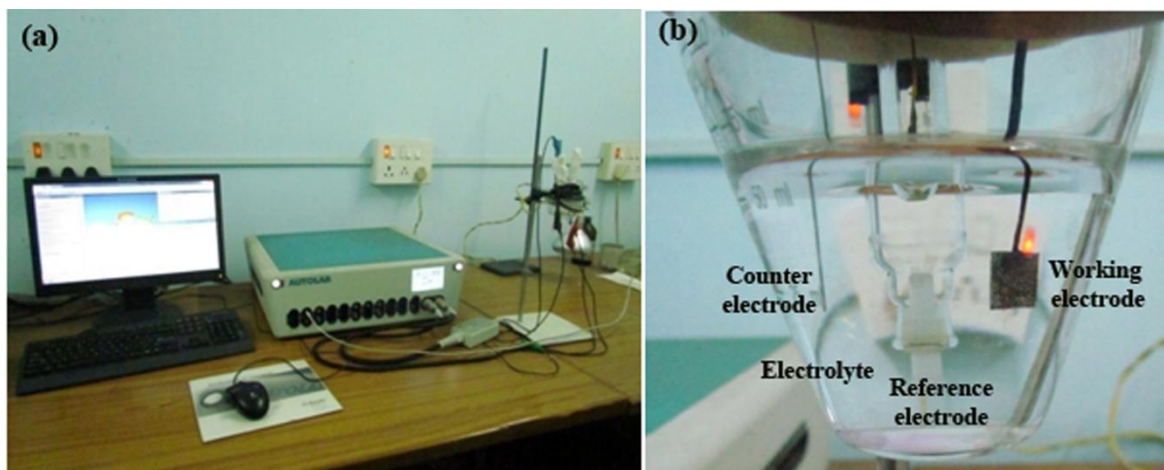
Figure 2.18. (a) Electrochemical workstation. (b) Three electrodes system.

2.9.1 Cyclic Voltammetry (CV)

In CV the voltage applied to the working electrode is scanned linearly from an initial value, E_i, to a predetermined limit, E_t, (known as the switching potential) where the direction of the scan is reversed. A cyclic voltammogram is obtained when current response is plotted as a function of the applied potential.[16] Figure 2.19 shows a cyclic voltammogram resulting from a reversible single electron oxidation and reduction:

$$M \rightleftharpoons M^+ + e^- \quad \ldots\ldots\ldots\ldots..(2.15)$$
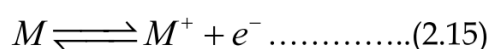
In Figure 2.19, the oxidation process occurs from the potential E_i to E_t as in this region the potential is scanned positively. The resulting current is called anodic current (I_{pa}). The corresponding peak potential is called anodic peak potential (E_{pa}), where all of the active material at the surface of the electrode get oxidized. After reaching E_t, the potential scans negatively towards E_i. Cathodic current (I_{pc}) generates due to reduction. The peak potential is called the cathodic peak potential (E_{pc}). At E_{pc}, all of the active materials at the surface of the electrode get reduced.
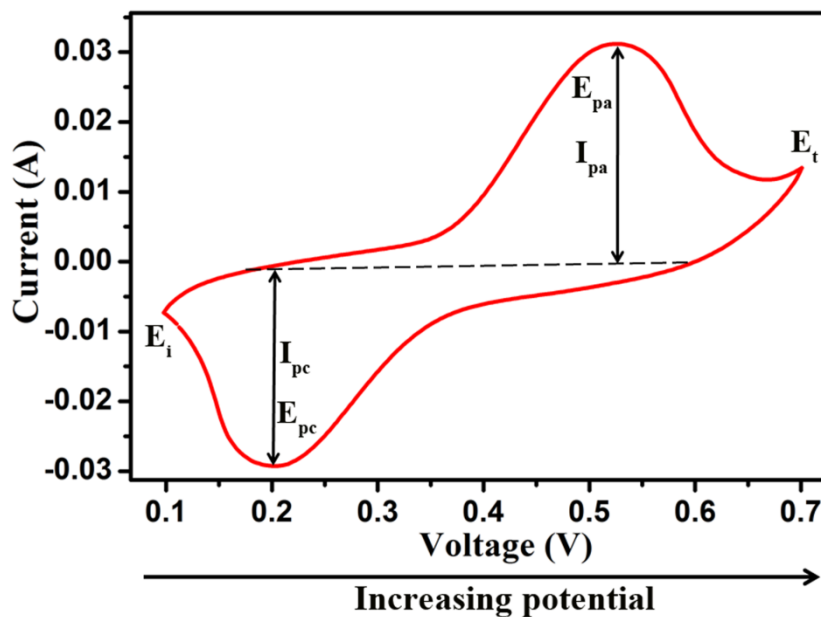
Figure 2.19. CV of a Single electron oxidation-reduction.

2.9.2. Galvanostatic Charge-discharge (GCD)

The typical GCD curves are shown in Figure 2.20. From a curve, the specific capacitance (C_{sp}) of a supercapacitor can be calculated according to Equation (2.16):

$$C_{sp} = \frac{I\Delta t}{m\Delta V} \qquad\qquad (2.16)$$

In which I (in A) is the discharge current, m (in g) is the mass of active materials, Δt (in s) is the discharge time, ΔV (in V) is the potential difference during the discharge process.
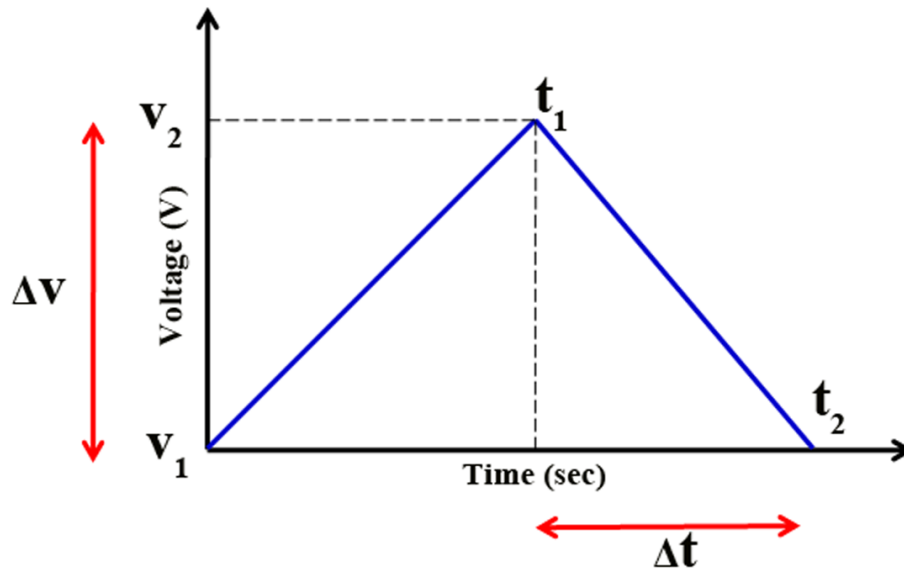
Figure 2.20. Typical GCD curves of an electrode.

Energy density and power density are two important parameters to evaluate the capacitive performance of a supercapacitor cell. The energy density is the capacity to perform work, whereas the power density exhibits how fast the energy is delivered. The maximum energy stored (E_{max}, in *Wh/kg*) and power delivered (P_{max}, in *W/kg*) for a supercapacitor cell is given by equations (2.17) and (2.18) respectively.[17]

$$E_{max} = \frac{0.5C_{sp}(\Delta V)^2}{3.6} \qquad (2.17)$$

$$P_{max} = \frac{E_{max}\,3600}{\Delta t} \qquad (2.18)$$

Bibliography

1.   Min, Y.; Kwak, J.; Soon, A.; Jeong, U., Nonstoichiometric Nucleation and Growth of Multicomponent Nanocrystals in Solution. *Acc. Chem. Res.* **2014,** *47* (10), 2887-2893.

2.   Kumar, S.; Nann, T., Shape Control of II–VI Semiconductor Nanomaterials. *Small* **2006,** *2* (3), 316-329.

3.   Thanh, N. T. K.; Maclean, N.; Mahiddine, S., Mechanisms of Nucleation and Growth of Nanoparticles in Solution. *Chem. Rev.* **2014,** *114* (15), 7610-7630.

4.   Lee, W.-r.; Kim, M. G.; Choi, J.-r.; Park, J.-I.; Ko, S. J.; Oh, S. J.; Cheon, J., Redox−Transmetalation Process as a Generalized Synthetic Strategy for Core−Shell Magnetic Nanoparticles. *J. Am. Chem. Soc.* **2005,** *127* (46), 16090-16097.

5.   Watzky, M. A.; Finke, R. G., Nanocluster Size-Control and "Magic Number" Investigations. Experimental Tests of the "Living-Metal Polymer" Concept and of Mechanism-Based Size-Control Predictions Leading to the Syntheses of Iridium(0) Nanoclusters Centering about Four Sequential Magic Numbers. *Chem. Mater.* **1997,** *9* (12), 3083-3095.

6.   Sun, S.; Zeng, H.; Robinson, D. B.; Raoux, S.; Rice, P. M.; Wang, S. X.; Li, G., Monodisperse MFe_2O_4 (M = Fe, Co, Mn) Nanoparticles. *J. Am. Chem. Soc.* **2004,** *126* (1), 273-279.

7.   Walton, R. I., Subcritical Solvothermal Synthesis of Condensed Inorganic Materials. *Chem. Soc. Rev.* **2002,** *31* (4), 230-238.

8.   Rabenau, A., The Role of Hydrothermal Synthesis in Preparative Chemistry. *Angew. Chem. Int. Ed. in English* **1985,** *24* (12), 1026-1040.

9.   Li, Y.-D.; Liao, H.-W.; Ding, Y.; Qian, Y.-T.; Yang, L.; Zhou, G.-E., Nonaqueous Synthesis of CdS Nanorod Semiconductor. *Chem. Mater.* **1998,** *10* (9), 2301-2303.

10.   Dong, Y.; He, K.; Yin, L.; Zhang, A., A Facile Route to Controlled Synthesis of Co_3O_4 Nanoparticles and their Environmental Catalytic Properties. *Nanotechnology* **2007,** *18* (43), 435602.

11.   Groves, T. R.; Pfeiffer, H. C.; Newman, T. H.; Hohn, F. J., EL3 System for Quarter-micron Electron Beam Lithography. *J. Vac. Sci. Technol., B* **1988,** *6* (6), 2028-2032.

12.   Ostrow, J. D., *Bile Pigments and Jaundice: Molecular, Metabolic and Medical Aspects*. Marcel Dekker: New York, 1986.

13.   Stocker, R.; Glazer, A. N.; Ames, B. N., Antioxidant Activity of Albumin-Bound Bilirubin. *Proc. Natl. Acad. Sci. U.S.A.* **1987,** *84*, 5918-5922.

14.   Xu, N.; Shi, Z.; Fan, Y.; Dong, J.; Shi, J.; Hu, M. Z. C., Effects of Particle Size of TiO_2 on Photocatalytic Degradation of Methylene Blue in Aqueous Suspensions. *Ind. Eng. Chem. Res.* **1999,** *38* (2), 373-379.

15.   Williams, A. T. R.; Winfield, S. A.; Miller, J. N., Relative Fluorescence Quantum Yields Using A Computer-Controlled Luminescence Spectrometer. *Analyst* **1983,** *108* (1290), 1067-1071.

16.   Mabbott, G. A., An Introduction to Cyclic Voltammetry. *J. Chem. Educ.* **1983,** *60* (9), 697.

17.   Singh, A. K.; Sarkar, D.; Khan, G. G.; Mandal, K., Hydrogenated NiO Nanoblock Architecture for High Performance Pseudocapacitor. *ACS Appl. Mater. Interfaces* **2014,** *6* (7), 4684-4692.

Chapter 3 | Chemical Functionalization of Fe₂O₃ Nanoparticles

In this chapter we have demonstrated chemical functionalization strategy of Fe$_2$O$_3$ nanoparticles with small hydrophilic organic ligand to induce inherent photoluminescence and excellent photocatalytic activity.

3. Facile Functionalization of Fe$_2$O$_3$ Nanoparticles to Induce Inherent Photoluminescence and Excellent Photocatalytic Activity

3.1. Preamble

Development of multifunctional nanoprobe combining various beneficial properties within a single entity has been a pivotal research area since the past decade. In this respect, transition metal oxide nanoparticles (NPs) have attracted utmost interest in recent years, because of their unique optical, electronic, magnetic, and catalytic properties. Moreover, nanotechnology and biology have synergized in dynamic development of a promising emerging research area called nanobiotechnology. In particular, properly functionalized magnetic NPs (MNPs) possess manifold advantages[1] which give rise to numerous exciting opportunities in the field of biomedical applications such as magnetic tweezers in magnetic separation of proteins or cells,[2] extraction of DNA molecules,[3] and therapeutic applications including AC magnetic field-assisted hyperthermia.[4] Noticeably, MNPs can be controlled by an external field,[5] which promotes targeted delivery of radioactive isotopes and drugs for radiotherapy and chemotherapy as well as gene targeting and in noninvasive diagnosis, enhancing contrast in magnetic resonance imaging (MRI),[6] and fluorescence imaging.[7-9]

Additionally, tunable size of MNPs ranging from a few nanometers to tens of nanometers facilitates their interaction probability with different biological entities. On the other hand, MNPs have been proved to be a promising candidate in catalysis for selective chemical transformations having both economic and environmental benefits, considering their high activity, low cost, facile preparation method, adequate stability, and controlled separation by an external magnetic field.[10-14]

So far, MNPs for fluorescence imaging have been prepared either by molecular attachment with fluorescent dyes or polymers or forming nanocomposites with quantum dots.[8, 15] Poor photostability of fluorescent dyes and inherent toxicity of QDs impose severe concern to their bio-imaging applications.[16] So, to solve these

problems, the development of biocompatible MNPs having intrinsic photoluminescence property and photostability, is highly desirable.

Among the magnetic nanomaterials, Fe_2O_3 nanostructures have attracted significant attention of the researchers because of their innate environmental benign character, low cost, high resistance to corrosion, and outstanding thermal stability in practical applications such as in targated drug delivery,[17] magnetic data storage, gas sensing,[18] Li-ion battery,[19, 20] fabrication of photoanodes for photo-assisted electrolysis,[21] pigments, and catalysis.[22-25] But the development of intrinsic photoluminescence, playing with the surface electronic structure of functionalized Fe_2O_3 NPs is sparse in literature. In spite of enormous efforts of different groups, aqueous phase insolubility and the absence of any inherent photoluminescence properties of the NPs inhibit their direct biomedical and several technological applications. Thus, fabrication of appropriately surface modified Fe_2O_3 NPs having intrinsic photoluminescence to explore its diverse biological and technological applicability is highly desirable.

In this chapter, we report the development of Fe_2O_3 NPs as a multifunctional nanoprobe having inherent multicolor photoluminescence, ferromagnetism, and excellent photocatalytic activity, simultaneously. Utilizing the reactivity of tartrate ligands, we have solubilized the as-prepared NPs into a water medium. Upon further surface modification of water-solubilized tartrate-functionalized Fe_2O_3 NPs, we have discovered the emergence of multicolor photoluminescence, starting from blue, cyan to green. Mystery of the generation of this multicolor photoluminescence property can be satisfactorily solved with ligand field theory. It has been found that the ligand-to-metal charge-transfer (LMCT) from tartrate ligand to the lowest unoccupied energy levels of Fe^{3+} metal ions in the NPs and d−d transitions play the key role. Finally, we have intended to exploit the broad photo excitation (covering a large portion of UV-visible region) of the functionalized Fe_2O_3 NPs in photocatalysis. Interestingly, the functionalized Fe_2O_3 NPs exhibit excellent photocatalytic property in the degradation of methylene blue (MB), a commonly used organic dye in textile industries and a model water-contaminant.[26]

3.2. Experimental Section

3.2.1. Material Used

Fe (III) acetylacetonate (Fe(acac)$_3$), oleylamine, 2-aminopurine (2AP), 4',6-diamidino-2-phenylindole (DAPI), Hoechst 33258 and methylene blue (MB) were obtained from Sigma-Aldrich. Diphenyl ether, oleic acid and cetyl alcohol were received from Loba Chemie. Tartaric acid and sodium hydroxide (NaOH) were purchased from Merck. All the reagents are of analytical grade and used without further purification.

3.2.2. Synthesis Procedure and Functionalization of Fe$_2$O$_3$ NPs

Fe$_2$O$_3$ NPs were synthesized by template free wet chemical route following a previous report with some modification, involving the high-temperature (260 ^{o}C) reflux of Fe(acac)$_3$ in di-phenyl ether in the presence of oleic acid, oleylamine and cetyl alcohol, followed by annealing at 550 ^{o}C for 1 h. For surface modification of NPs, as-prepared Fe$_2$O$_3$ NPs were cyclomixed with 0.5 M aqueous Na-tartrate solution for 12 h at room temperature after adjusting the pH of the solution at $\sim$ 7 with addition of NaOH solution. The non-functionalized larger Fe$_2$O$_3$ NPs were filtered out with a syringe filter of 0.22 μm diameter. The obtained colorless filtrate was tartrate functionalized Fe$_2$O$_3$ NPs which was heated at about 70 ^{o}C for 8 h under extensive stirring condition after maintaining the pH of the solution at $\sim$12 by dropwise addition of NaOH solution. To prepare the solid powdered samples required for magnetic study (Vibrating sample magnetometry, VSM) and Fourier transform infrared (FTIR) spectroscopic measurements, we dialyzed the tartrate functionalized Fe$_2$O$_3$ NPs solution (to eliminate excess ligands) and lyophilized followed by drying over a water bath.

3.2.3. Catalysis

For the study of photocatalysis we used 8 W UV lamp as UV light source and a 100 W incandescent bulb (its optical spectra exactly mimics sunlight having a continuum throughout the visible region) as visible light source, from Philips. Aqueous solution

of MB (4.6 µM) and functionalized Fe_2O_3 NPs were homogeneously mixed for 1 h in a quartz cuvette in the dark maintaining the pH of the solution at ~3. Then the cuvette was placed ~2 cm apart from the light source and the absorbance of MB in the reaction mixture was measured time to time by the UV-visible spectrophotometer.

3.3. Result and Discussions

We have synthesized Fe_2O_3 NPs following a wet chemical method previously reported by Sun et al.,[27] with slight modification and functionalized with tartrate ligands (described in chapter 2 in detail). TEM study was performed to characterize the size and morphology of the as-prepared NPs shown in Figure 3.1 (a). TEM image of Fe_2O_3 NPs demonstrates that average size of the particles was ~50 nm. XRD pattern of the as-prepared NPs, shown in Figure 3.1 (b) exactly matches with the α phase of Fe_2O_3 (hematite, JCPDS, file no. 33-0664).[28] The presence of a very low intensity peak corresponding to (400) plane of γ-Fe_2O_3 (maghemite, JCPDS, file no. 39-1346) in the XRD pattern of as-prepared NPs indicates that the as-prepared NPs were predominantly in α phase.[29] EDX spectrum of the NPs as shown in Figure 3.1 (c) confirms the presence of both Fe and O. Figure 3.1 (d) shows the selected area electron diffraction (SAED) pattern, indicating high crystallinity of the as-prepared Fe_2O_3 NPs.
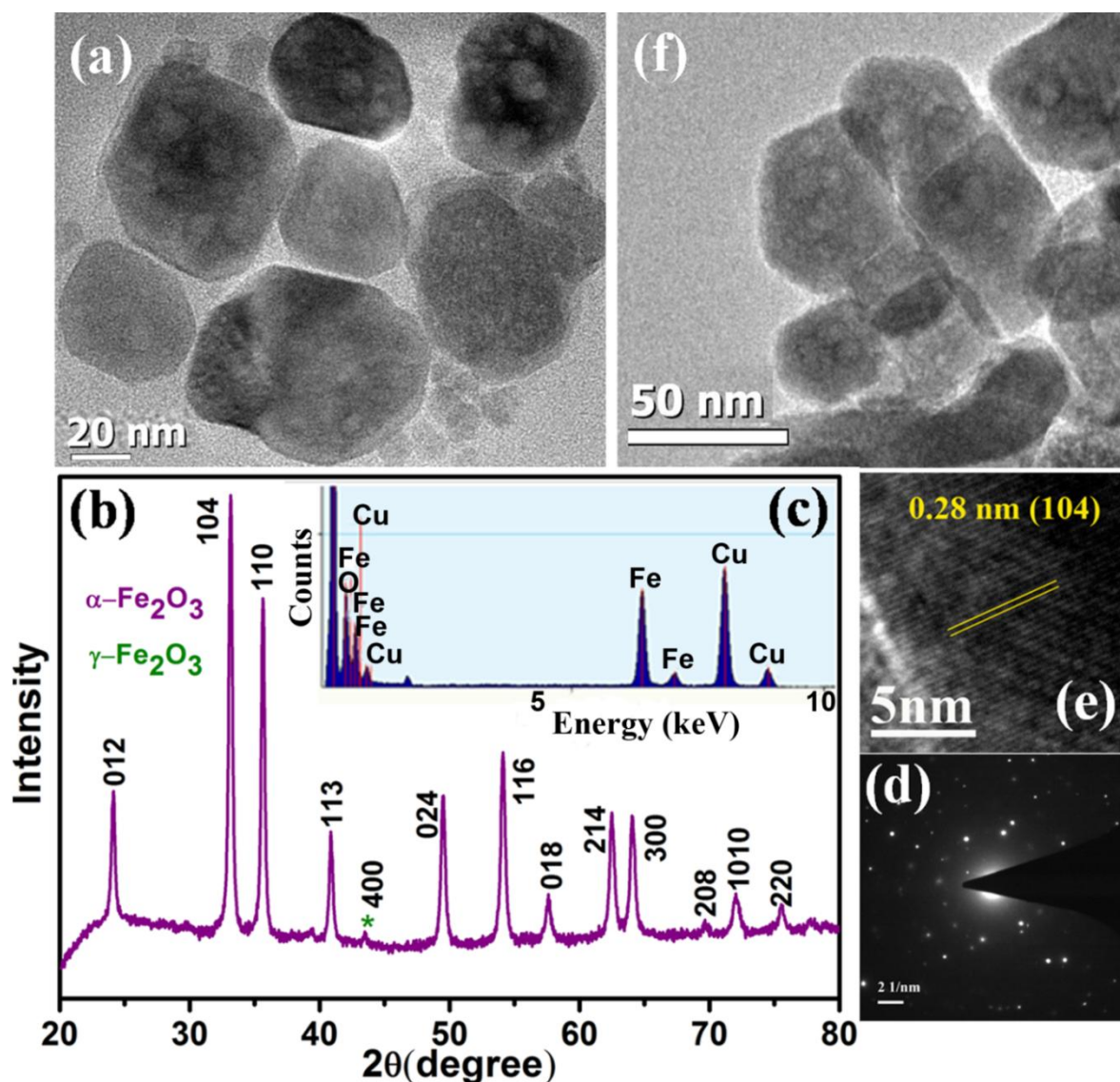
Figure 3.1. (a) TEM image of the as-prepared bare Fe_2O_3 NPs. (b) XRD pattern of as-prepared Fe_2O_3 NPs. All diffraction peaks in the figure are perfectly indexed in the literature to the rhombohedral corundum structure of α-Fe_2O_3 NPs along with only one impurity peak corresponding to (400) plane of α-Fe_2O_3. (c) EDX spectrum of the NPs indicates the presence of both Fe and O. (d) SAED pattern of as-prepared Fe_2O_3 NPs indicates high crystallinity. (e) HRTEM image of tartrate-functionalized Fe_2O_3 NPs indicates high crystallinity remains unaltered after surface modification and shows lattice fringes. (f) TEM image of the tartrate-functionalized Fe_2O_3 NPs.

To solubilize Fe_2O_3 NPs in an aqueous environment, we functionalized the as-prepared NPs with a biocompatible organic ligand, Na-tartrate. After surface functionalization, size of the highly water-solubilized NPs remained almost unchanged as evident from Figure 3.1 (f). The HRTEM image of tartrate-

functionalized Fe_2O_3 NPs (T-Fe_2O_3 NPs) (as shown in Figure 3.1 (e)) clearly exhibits high crystalline nature of the NPs. The calculated interplanar distance between the fringes has been found to be 0.28 nm corresponding to (104) plane of the α-Fe_2O_3 crystal lattice.
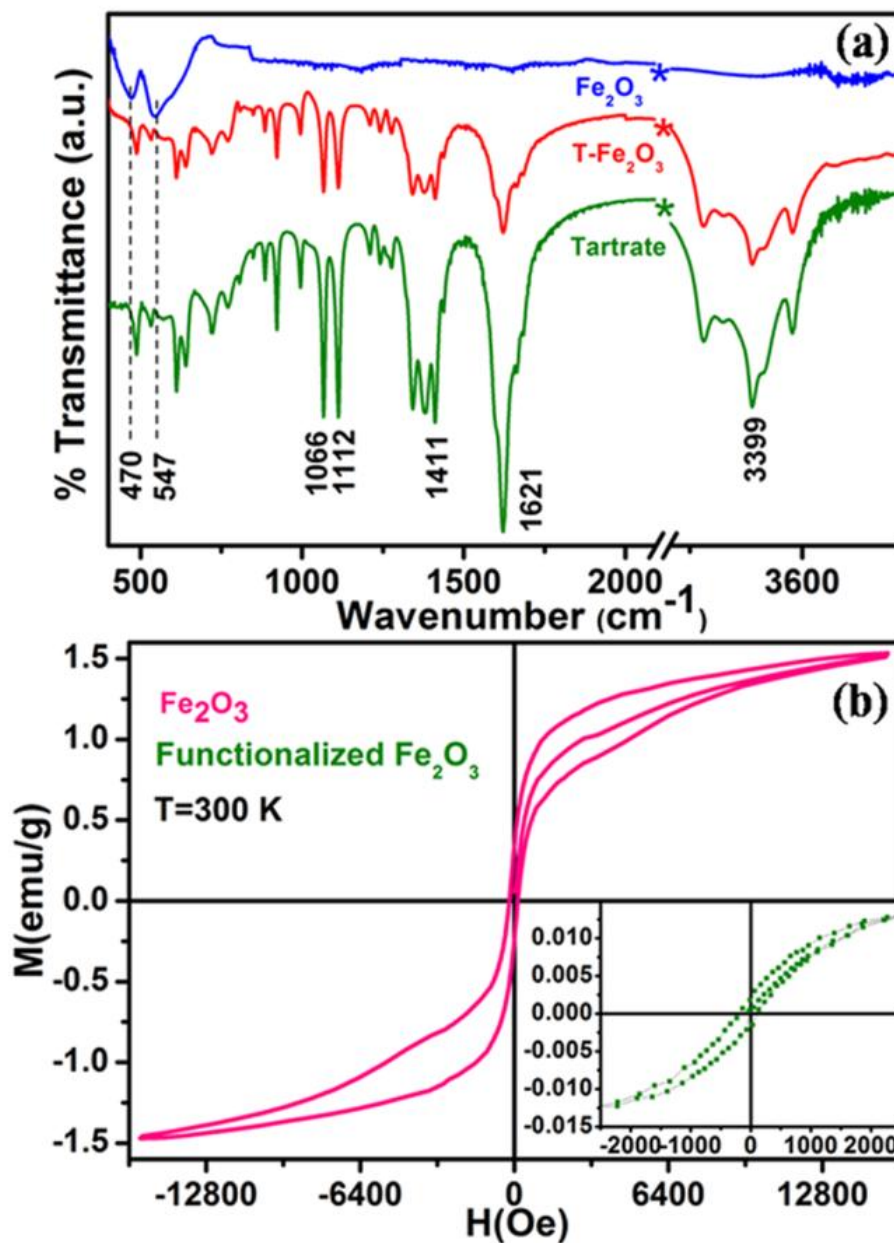
Figure 3.2. (a) FTIR spectra of as-prepared Fe_2O_3 and functionalized Fe_2O_3 NPs along with Na-tartrate alone. (b) Magnetization versus applied magnetic field plot for the as-prepared bare Fe_2O_3 NPs. In the inset hysteresis loop of functionalized Fe_2O_3 NPs indicates ferromagnetic nature at room temperature (300 K).

FTIR study were carried out for Fe_2O_3 NPs before and after functionalization along with the ligand alone, to confirm the attachment of ligand molecules with NPs' surface. As shown in Figure 3.2 (a), the characteristic peaks of Fe_2O_3 NPs at 547 and 470 cm^{-1} can be assigned to Fe-O stretching and bending vibration mode respectively.[30] Those peaks are not distinctly visible after functionalization (i.e. in the case of the functionalized Fe_2O_3 NPs), which suggests that, effective surface modification of the NPs has taken place upon interaction with tartrate ligands. Whereas, in case of tartrate, two sharp peaks arising at 1066 and 1112 cm^{-1} are due to the C–OH stretching modes,[31] and peaks at 1411 and 1621 cm^{-1} are attributed to symmetric and asymmetric stretching modes of the carboxylate groups (COO^-) of tartrate, respectively.[32] Upon interaction with the NPs' surface (i.e. in case of functionalized Fe_2O_3), all these different bands are perturbed significantly along with the band at 3399 cm^{-1}, generated due to the stretching vibrational modes of hydroxyl group (O–H),[31] clearly indicates that both –COO^- and –OH groups are involved in the functionalization process.

Figure 3.2 (b) shows the magnetic study of both as-prepared and functionalized Fe_2O_3 NPs (inset) at room temperature. It is noteworthy that the shape of the hysteresis loop is constricted. Constricted loops are typically observed in a system having mixture of soft and hard magnetic phases. Thus at room temperature the observed response could be due to combination of α and very small amount of γ phases (as evident from the XRD). The γ phase is a soft phase with higher moment, whereas, the α phase have higher coercivity but lower moment. Combination of these two magnetic properties leads to a constricted hysteresis loop. Coercivity of as-prepared sample was found to be 174.34 Oe and the magnetization curve did not saturate up to the maximum applied magnetic field of 1.6 T. After functionalization, the magnetic behaviour of Fe_2O_3 NPs converted to typical ferromagnetic pattern with slight decrease in coercivity (145.46 Oe) and saturation magnetization. The change in magnetic behaviour upon functionalization can be explained by ligand field theory.[33] Although the oxygen coordination for Fe^{3+} ions in bulk or core Fe_2O_3, having corundum structure, is quite symmetrical in the forms of octahedron or tetrahedron, the coordination symmetry is greatly reduced for metal cations at the

surface due to missing of some coordination oxygen atoms. Consequently, the magnetic structure at the surface layer could be drastically different than the core. Surface usually exhibits some degree of spin disorder and pinning. Qualitatively, adsorbed ligands can be viewed as effectively taking the positions of the missing oxygen atoms, which makes the symmetry and crystal field of the surface metal ion more closely resembling that of the core, and therefore reduces the spin disorder and pinning. Such changes certainly affect the surface anisotropy and consequently the coercivity of NPs. Tartrate ligand, containing both the σ-donor (–OH⁻) and π-donor (–COO⁻) functional group favours the quenching of magnetic moments of Fe^{+3} ions in the surface of $T-Fe_2O_3$ NPs, resulting a decrease in the saturation magnetization.[34] In the other hand, quenching of the magnetic moments reduces its spin-orbit coupling, leading to decrease in magnetocrystalline anisotropy, which results in reduction of coercivity [33] in $T-Fe_2O_3$ NPs as compared to the as-prepared NPs.
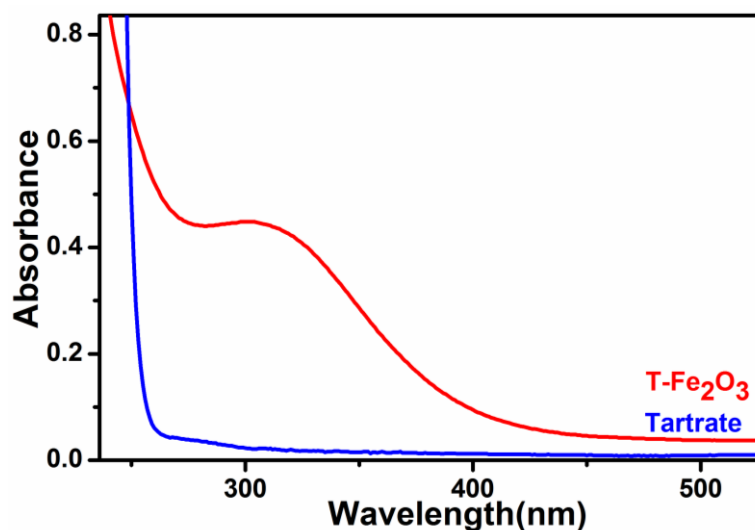
Figure 3.3. UV-visible absorption spectrum of functionalized Fe_2O_3 NPs and Na-tartrate.

UV-visible absorbance spectrum of $T-Fe_2O_3$ NPs as depicted in Figure 3.3 consists of a broad band having maximum at around 320 nm. Interestingly, upon exciting the sample at 320 nm, we observed photoluminescence at 410 nm, although with a low intensity. To increase the photoluminescence intensity, we performed further surface modification by heating after high pH treatment, which resulted in

generation of two more photoluminescence peaks with multiple fold increase in overall intensity, upon excitation at proper wavelengths.
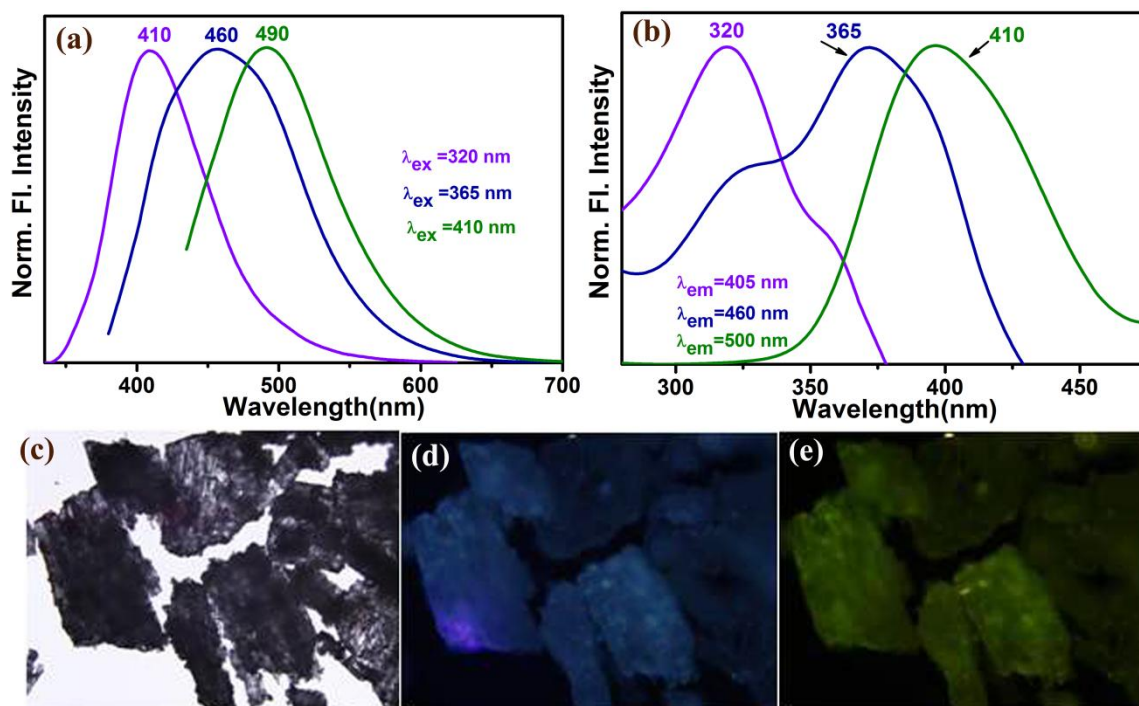
Figure 3.4. (a) Normalized steady-state photoluminescence emission spectra obtained from tartrate-functionalized Fe_2O_3 NPs with three different excitation wavelengths of 320, 365, and 410 nm, respectively. (b) Photoluminescence excitation spectra of functionalized Fe_2O_3 NPs at different emission maxima of 405, 460, and 500 nm, respectively. Photoluminescence micrographs of powder functionalized Fe_2O_3 NPs under (c) bright field, (d) UV (365 nm), and (e) blue (436 nm) light irradiation.

The reason for enhancement of the photoluminescence intensity as well as generation of two more optical bands upon surface modification could be due to increased coordination between the ligand functional groups (carboxylate and hydroxyl moieties) and Fe^{3+} centers at the NP surface. Figure 3.4 (a) shows normalized steady-state photoluminescence emission spectra obtained from surface modified Fe_2O_3 NPs. Upon excitation at wavelengths of 320, 365, and 410 nm, the NPs solution gave rise to intense photoluminescence peaks at 410, 460, and 490 nm, respectively.[26] Except 320 nm, other observed excitation bands at around 365 and 410 nm were not observed in the absorption spectrum (Figure 3.3), presumably because these bands were masked by the more intense 320 nm absorption, however, were

distinctly visible in the excitation spectrum as shown in Figure 3.4 (b). The photoluminescence micrographs of T-Fe_2O_3 NPs, demonstrate that the black powder of functionalized NPs under bright field (Figure 3.4 (c)), gives rise to photoluminescent colors like cyan (Figure 3.4 (d)) and green (Figure 3.4 (e)) upon excitation at 365 and 436 nm, respectively, by using proper filters.
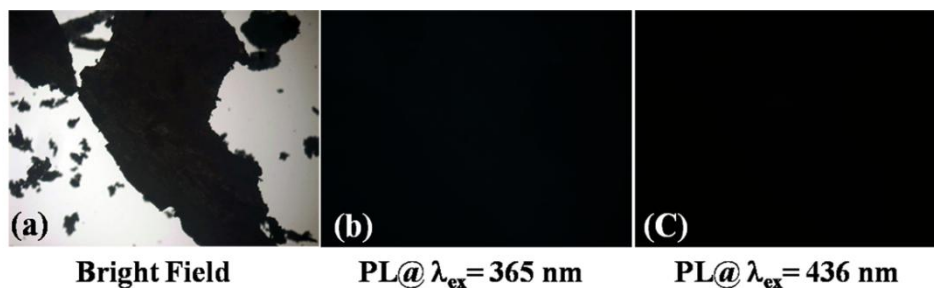
Figure 3.5. Fluorescence micrographs of bare Fe_2O_3 NPs under bright field (a) , UV (b) and blue (c) light.

Noticeably, the photoluminescence microscopic images of as-prepared bare Fe_2O_3 NPs (as shown in Figure 3.5) and Na-tartrate (as shown in Figure 3.6) under identical conditions have no such coloration. Photoluminescence quantum yields (QY) of the functionalized Fe_2O_3 NPs, have been calculated by following the relative method of Williams et al.,[35] which involves the use of well characterized standard fluorescent compounds with known QY values. Photoluminescence QYs of 8.958% (for 410 nm band), 0.2% (for 460 nm band), and 0.5% (for 490 nm band) were obtained relative to the standard fluorescent compounds such as 2-aminopurine (2AP), 4',6-diamidino-2-phenylindole (DAPI), and Hoechst 33258, respectively. Thus, the emergence of multicolor photoluminescence in Fe_2O_3 NPs was activated by tartrate functionalization and then reinforced by further pH and heat treatment.

Bright Field   **PL@λ_{ex}= 365 nm**   **PL@λ_{ex}= 436 nm**
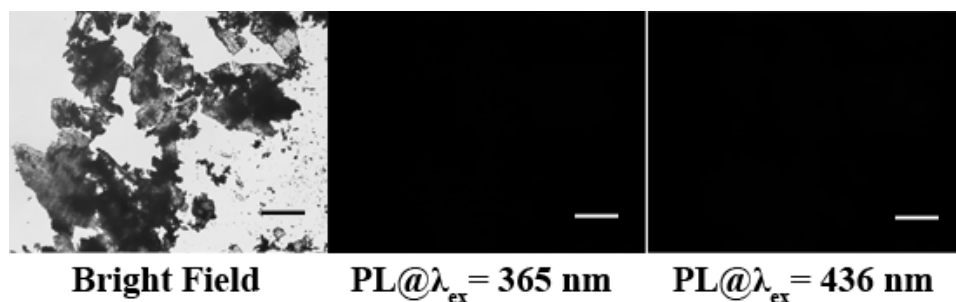
Figure 3.6. Fluorescence micrographs of Na-tartrate under bright field (a), UV (b) and blue (c) light.

The mystery of the generation of intrinsic photoluminescence can also be solved by ligand field theory.[33, 36] On the basis of ligand field theory, the ligand coordination provides the crystal field splitting energy (CFSE) Δ generated from d orbitals splitting with a magnitude determined by the ligands at a given coordination symmetry. As a ligand becomes more basic, the strength of the metal-ligand σ bond increases, and consequently CFSE, Δ associated with the ligand increases, which ultimately lead to the splitting between the degenerate d orbitals. On the other hand, due to the strong ligand-to-metal charge-transfer transition (LMCT) from HOMO (Highest occupied molecular orbital, centered in the ligand) to LUMO (lowest unoccupied molecular orbital, centered in metal ions), bonding interaction between the metal and ligand increases significantly. Photoluminescence peak arising at 410 nm can be attributed to LMCT involving HOMO of tartrate ligand and LUMO centered over metal ion Fe^{+3}.[37] The other emission peaks at 460 and 490 nm upon excitation at 365 and 410 nm can be attributed to $^6A_{1g} \rightarrow {}^4T_{1g}$ and $^6A_{1g} \rightarrow {}^4T_{2g}$ transitions involving d-d orbitals of Fe^{3+} ions, respectively, due to the crystal field splitting of a FeO_6 octahedron with O_h symmetry as the first approximation. Both the d-d transitions are formally dipole and spin forbidden transitions, however, they can have considerable strengths due to the relaxation of selection rules by octahedral distortion and spin-orbit coupling as discussed in other Fe^{3+} ($3d^5$) containing materials. [38, 39]
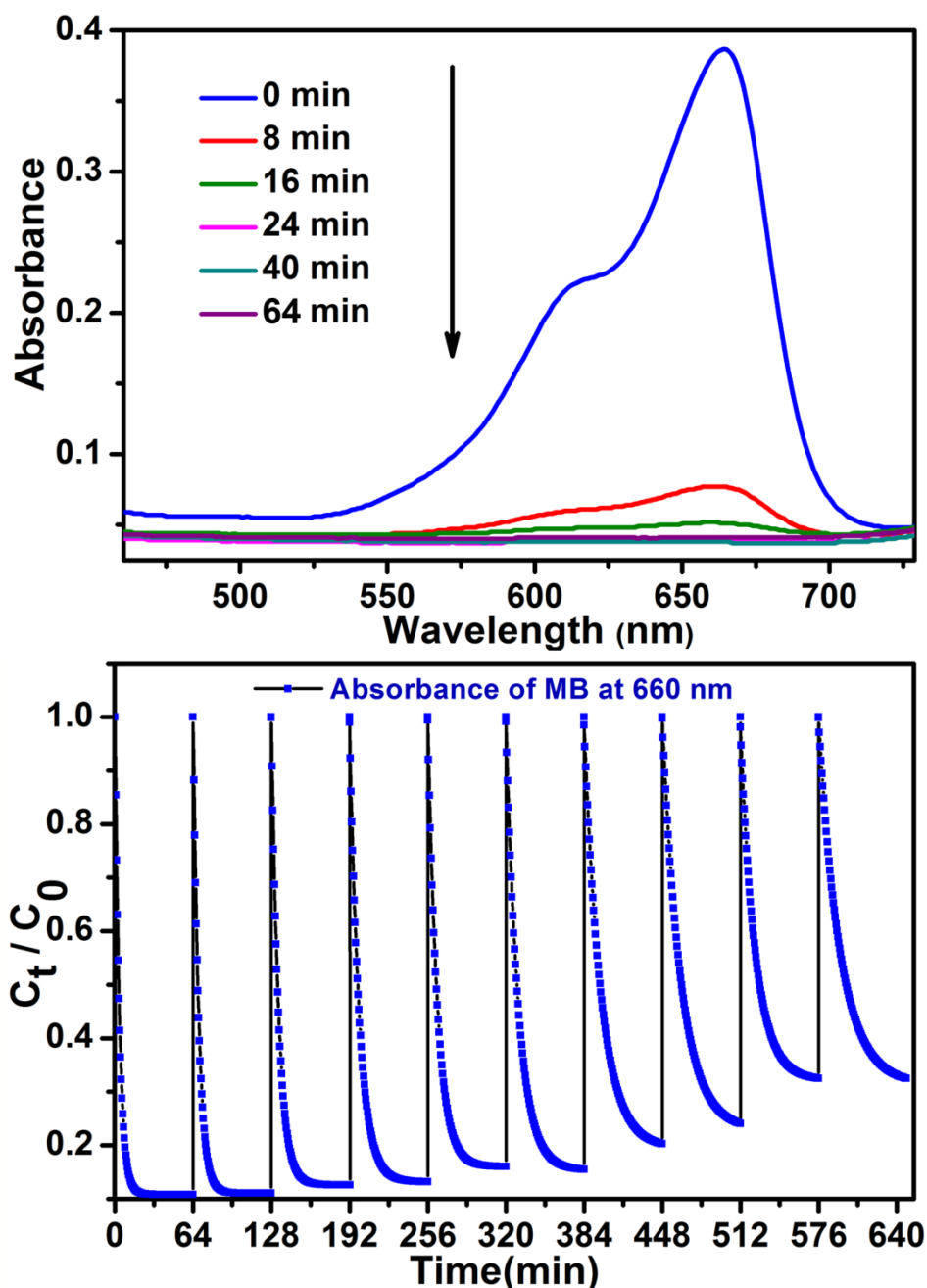
Figure 3.7. (a) UV-visible spectral changes of aqueous solution of methylene blue (MB) with time in presence of functionalized Fe_2O_3 NPs, under UV irradiation. (b) Shows the plots of relative concentration of MB monitored at 660 nm versus time for consecutive 10 cycles, showing reusability of functionalized Fe_2O_3 NPs in MB degradation under UV light.

Considering the recent remarkable growth of nanocatalysis by engineering and manipulating various materials at the nanoscale to accelerate the rate of several beneficial reactions, we intended to utilize the strong broad excitation of the functionalized Fe_2O_3 NPs throughout the UV-visible region, in photocatalysis for

waste-water treatment. Functionalized Fe_2O_3 NPs showed unprecedented photocatalytic property (as shown in Figure 3.7 (a)) towards the degradation of methylene blue (MB), a commonly used dye in textile industries and a model water-contaminent, upon UV light irradiation. We have found that the photodegradation of MB in presence of functionalized Fe_2O_3 NPs takes place exponentially with time following first-order rate equation with a kinetic rate constant (k) of 27.55×10^{-2} min^{-1}.

We also checked the reusability of the catalyst, in every 64 min of interval. We added same dose of MB into the reaction mixture up to 10 dose, keeping the catalyst concentration fixed (without addition of extra catalyst after the 1st cycle), MB decomposition rates of different cycles were measured by monitoring the decrease of MB absorbance at 660 nm using UV-visible spectroscopy. Figure 3.7 (b) shows the plots of relative concentration of MB versus time, upto 10 consecutive cycles, affirming the reusability of functionalized Fe_2O_3 NPs catalyst with almost consistent degradation rate. From the previous literature on methylene blue degradation in presence of NPs, we anticipate that, the photodegradation process may follow radical pathway involving reactive oxygen species (ROS).[40-42] Furthermore, we investigated whether visible light can also activate the photocatalytic efficiency of T-Fe_2O_3 NPs.

As shown in Figure 3.8, we found that T-Fe_2O_3 NPs can degrade MB in presence of visible light also, following 1st order reaction kinetics having rate constant (k) of 54×10^{-4} min^{-1}. Decrease in rate of photocatalysis in presence of visible light as compared to UV light can be attributed to higher energy of UV light than visible light as well as lower absorbance of functionalized Fe_2O_3 NPs in visible region in comparison with UV region.
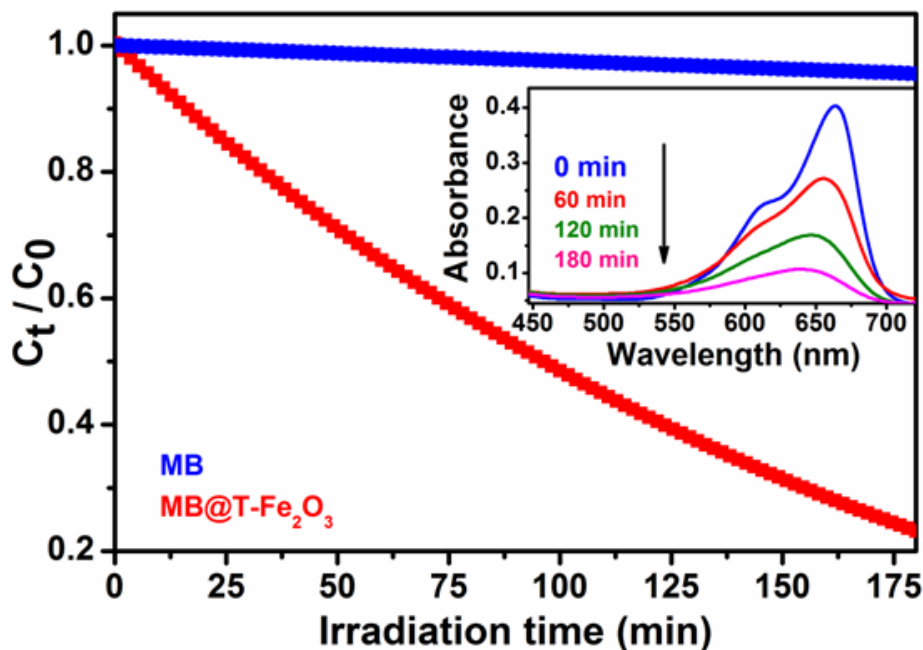
Figure 3.8. Shows the rate of photocatalytic degradation of MB (monitored at 660 nm) in absence and presence of T-Fe$_2$O$_3$ NPs under visible light irradiation. Inset shows the full absorption spectra of MB in presence of T-Fe$_2$O$_3$ NPs with time, under visible-light irradiation.

3.4. Conclusions

In conclusion, development of surface modified Fe$_2$O$_3$ NPs as multifunctional nanoprobe having simultaneously intrinsic multiple photoluminescence covering a broad range of UV-visible region from blue, cyan, to green, inherent ferromagnetism, and excellent photocatalytic properties has been achieved by a very facile ligand functionalization and subsequent surface modification strategy. Moreover, correlating with the reported theoretical aspect, we have rationally explained the emergence of the interesting optical properties. Development of intrinsic multicolor fluorescence can be attributed to LMCT involving HOMO centered over ligand and LUMO centered over Fe^{3+} metal ions and ligand induced d-d transitions within Fe^{3+} metal ions. We hope that, the magneto-photoluminescent Fe$_2$O$_3$ NPs will have great relevance to fundamental research as well as diverse field of biological and technological applications ranging from bioimaging, drug delivery to nanocatalysis.

Bibliography

1. Reddy, L. H.; Arias, J. L.; Nicolas, J.; Couvreur, P., Magnetic Nanoparticles: Design and Characterization, Toxicity and Biocompatibility, Pharmaceutical and Biomedical Applications. *Chem. Rev.* **2012,** *112* (11), 5818-5878.

2. Kuhara, M.; Takeyama, H.; Tanaka, T.; Matsunaga, T., Magnetic Cell Separation Using Antibody Binding with Protein a Expressed on Bacterial Magnetic Particles. *Anal. Chem.* **2004,** *76* (21), 6207-6213.

3. Yoza, B.; Arakaki, A.; Maruyama, K.; Takeyama, H.; Matsunaga, T., Fully Automated DNA Extraction from Blood Using Magnetic Particles Modified with a Hyperbranched Polyamidoamine Dendrimer. *J. Biosci. Bioeng.* **2003,** *95* (1), 21-26.

4. Johannsen, M.; Gneveckow, U.; Eckelt, L.; Feussner, A.; Waldofner, N.; Scholz, R.; Deger, S.; Wust, P.; Loening, S. A.; Jordan, A., Clinical Hyperthermia of Prostate Cancer Using Magnetic Nanoparticles: Presentation of a New Interstitial Technique. *Int. J. Hyperther.* **2005,** *21* (7), 637-647.

5. Sundar, S.; Mariappan, R.; Piraman, S., Synthesis and Characterization of Amine Modified Magnetite Nanoparticles as Carriers of Curcumin-anticancer Drug. *Powder Technol.* **2014,** *266,* 321-328.

6. Na, H. B.; Song, I. C.; Hyeon, T., Inorganic Nanoparticles for MRI Contrast Agents. *Adv. Mater.* **2009,** *21* (21), 2133-2148.

7. Yang, J.; Lim, E.-K.; Lee, H. J.; Park, J.; Lee, S. C.; Lee, K.; Yoon, H.-G.; Suh, J.-S.; Huh, Y.-M.; Haam, S., Fluorescent Magnetic Nanohybrids as Multimodal Imaging Agents for Human Epithelial Cancer Detection. *Biomaterials* **2008,** *29* (16), 2548-2555.

8. Gao, J.; Zhang, W.; Huang, P.; Zhang, B.; Zhang, X.; Xu, B., Intracellular Spatial Control of Fluorescent Magnetic Nanoparticles. *J. Am. Chem. Soc.* **2008,** *130* (12), 3710-3711.

9. Kim, H.; Achermann, M.; Balet, L. P.; Hollingsworth, J. A.; Klimov, V. I., Synthesis and Characterization of Co/CdSe Core/shell Nanocomposites: Bifunctional Magnetic-optical Nanocrystals. *J. Am. Chem. Soc.* **2005,** *127* (2), 544-546.

10.   Wang, H.; Zhang, L.; Tan, X.; Holt, C. M. B.; Zahiri, B.; Olsen, B. C.; Mitlin, D., Supercapacitive Properties of Hydrothermally Synthesized Co3O4 Nanostructures. *The Journal of Physical Chemistry C* **2011,** *115* (35), 17599-17605.

11.   Zhang, P.; Zhan, Y.; Cai, B.; Hao, C.; Wang, J.; Liu, C.; Meng, Z.; Yin, Z.; Chen, Q., Shape-controlled synthesis of Mn_3O_4 nanocrystals and their catalysis of the degradation of methylene blue. *Nano Res.* **2010,** *3* (4), 235-243.

12.   Gawande, M. B.; Bonifacio, V. D. B.; Varma, R. S.; Nogueira, I. D.; Bundaleski, N.; Ghumman, C. A. A.; Teodoro, O. M. N. D.; Branco, P. S., Magnetically Recyclable Magnetite-Ceria (Nanocat-Fe-Ce) Nanocatalyst - Applications in Multicomponent Reactions Under Benign Conditions. *Green Chem.* **2013,** *15* (5), 1226-1231.

13.   Gawande, M. B.; Rathi, A. K.; Nogueira, I. D.; Varma, R. S.; Branco, P. S., Magnetite-Supported Sulfonic acid: a Retrievable Nanocatalyst for the Ritter Reaction and Multicomponent Reactions. *Green Chem.* **2013,** *15* (7), 1895-1899.

14.   Gawande, M. B.; Branco, P. S.; Varma, R. S., Nano-magnetite (Fe_3O_4) as a Support for Recyclable Catalysts in the Development of Sustainable Methodologies. *Chem. Soc. Rev.* **2013,** *42* (8), 3371-3393.

15.   Kim, H.; Achermann, M.; Balet, L. P.; Hollingsworth, J. A.; Klimov, V. I., Synthesis and Characterization of Co/CdSe Core/Shell Nanocomposites: Bifunctional Magnetic-Optical Nanocrystals. *J. Am. Chem. Soc.* **2004,** *127* (2), 544-546.

16.   Resch-Genger, U.; Grabolle, M.; Cavaliere-Jaricot, S.; Nitschke, R.; Nann, T., Quantum Dots versus Organic Dyes as Fluorescent Labels. *Nat. Methods.* **2008,** *5* (9), 763-775.

17.   Milošević, I.; Guillot, S.; Tadić, M.; Duttine, M.; Duguet, E.; Pierzchala, K.; Sienkiewicz, A.; Forró, L.; Saboungi, M.-L., Loading and Release of Internally Self-assembled Emulsions Embedded in a Magnetic Hydrogel. *Appl. Phys. Lett.* **2014,** *104* (4), 043701.

18.   Han, J. S.; Bredow, T.; Davey, D. E.; Yu, A. B.; Mulcahy, D. E., The Effect of Al Addition on the Gas Sensing Properties of Fe_2O_3-based Sensors. *Sens. Actuators, B : Chemical* **2001,** *75* (1–2), 18-23.

19.   Wu, C.; Yin, P.; Zhu, X.; OuYang, C.; Xie, Y., Synthesis of Hematite (α-Fe_2O_3) Nanorods: Diameter-Size and Shape Effects on Their Applications in Magnetism, Lithium Ion Battery, and Gas Sensors. *J. Phys. Chem. B* **2006,** *110* (36), 17806-17812.

20.   Wu, Z.; Yu, K.; Zhang, S.; Xie, Y., Hematite Hollow Spheres with a Mesoporous Shell: Controlled Synthesis and Applications in Gas Sensor and Lithium Ion Batteries. *J. Phys. Chem. C* **2008,** *112* (30), 11307-11313.

21.   Ohmori, T.; Takahashi, H.; Mametsuka, H.; Suzuki, E., Photocatalytic Oxygen Evolution on a-Fe_2O_3 Films Using Fe^{3+} Ion as a Sacrificial Oxidizing Agent. *Phys. Chem. Chem. Phys.* **2000,** *2* (15), 3519-3522.

22.   Chauhan, P.; Annapoorni, S.; Trikha, S. K., Humidity-sensing Properties of Nanocrystalline Haematite Thin Films Prepared by Sol-gel Processing. *Thin Solid Films* **1999,** *346* (1–2), 266-268.

23.   Comini, E.; Guidi, V.; Frigeri, C.; Riccò, I.; Sberveglieri, G., CO sensing properties of titanium and iron oxide nanosized thin films. *Sens. Actuators, B* **2001,** *77* (1–2), 16-21.

24.   Weiss, W.; Zscherpel, D.; Schlögl, R., On the Nature of the Active Site for the Ethylbenzene Dehydrogenation over Iron Oxide Catalysts. *Catal. Lett.* **1998,** *52* (3-4), 215-220.

25.   Li, Z.; Li, P.; Wan, Q.; Zhai, F.; Liu, Z.; Zhao, K.; Wang, L.; Lü, S.; Zou, L.; Qu, X.; Volinsky, A. A., Dehydrogenation Improvement of $LiAlH_4$ Catalyzed by Fe_2O_3 and Co_2O_3 Nanoparticles. *J. Phys. Chem. C* **2013,** *117* (36), 18343-18352.

26.   Pal, M.; Rakshit, R.; Mandal, K., Facile Functionalization of Fe_2O_3 Nanoparticles to Induce Inherent Photoluminescence and Excellent Photocatalytic Activity. *Appl. Phys. Lett.* **2014,** *104* (23), -.

27.   Sun, S.; Zeng, H.; Robinson, D. B.; Raoux, S.; Rice, P. M.; Wang, S. X.; Li, G., Monodisperse MFe_2O_4 (M = Fe, Co, Mn) Nanoparticles. *J. Am. Chem. Soc.* **2004,** *126* (1), 273-279.

28.   Prabhu, Y.; Rao, K. V.; Kumar, V. S. S., Surfactant-Assisted Combustion Method for the Synthesis of α-Fe_2O_3 Nanocrystalline Powders. *Int. J. Pure Appl. Sci. Technol* **2013,** *18* (1), 1-11.

29.   Huang, G.; He, E.; Wang, Z.; Fan, H.; Shangguan, J.; Croiset, E.; Chen, Z., Synthesis and Characterization of γ-Fe_2O_3 for H_2S Removal at Low Temperature. *Ind. Eng. Chem. Res.* **2015,** *54* (34), 8469-8478.

30.   Sahoo, S. K.; Agrawal, K.; Singh, A. K.; Polke, B. G.; Raha, K. C., Characterization of γ- and α-Fe_2O_3 Nano Powders Synthesized by Emulsionprecipitation-Calcination Route and Rheological Behaviour of α-Fe_2O_3. *Int. J. Eng. Sci. Tech.* **2010,** *2*, 218.

31.   Kaneko, N.; Kaneko, M.; Takahashi, H., Infrared and Raman Spectra and Vibrational Assignment of Some Metal Tartrates. *Spectrochim. Acta, Part A* **1984,** *40* (1), 33-42.

32.   Ramakrishnan, V.; Maroor, J. M. T., IR and Raman Studies of Gel Grown Manganese Tartrate. *Infrared Phys.* **1988,** *28* (4), 201-204.

33.   Vestal, C. R.; Zhang, Z. J., Effects of Surface Coordination Chemistry on the Magnetic Properties of $MnFe_2O_4$ Spinel Ferrite Nanoparticles. *J. Am. Chem. Soc.* **2003,** *125* (32), 9828-9833.

34.   Rakshit, R.; Mandal, M.; Pal, M.; Mandal, K., Tuning of Magnetic Properties of $CoFe_2O_4$ Nanoparticles through Charge Transfer Effect. *Appl. Phys. Lett.* **2014,** *104* (9), 092412.

35.   Williams, A. T. R.; Winfield, S. A.; Miller, J. N., Relative Fluorescence Quantum Yields Using A Computer-Controlled Luminescence Spectrometer. *Analyst* **1983,** *108* (1290), 1067-1071.

36.   Giri, A.; Goswami, N.; Bootharaju, M. S.; Xavier, P. L.; John, R.; Thanh, N. T. K.; Pradeep, T.; Ghosh, B.; Raychaudhuri, A. K.; Pal, S. K., Emergence of Multicolor Photoluminescence in $La_{0.67}Sr_{0.33}MnO_3$ Nanoparticles. *J. Phys. Chem. C* **2012,** *116* (48), 25623-25629.

37.   Pozdnyakov, I. P.; Kolomeets, A. V.; Plyusnin, V. F.; Melnikov, A. A.; Kompanets, V. O.; Chekalin, S. V.; Tkachenko, N.; Lemmetyinen, H., Photophysics of Fe(III)–tartrate and Fe(III)–citrate Complexes in Aqueous Solutions. *Chem. Phys. Lett.* **2012,** *530* (0), 45-48.

38.   Xu, X. S.; Brinzari, T. V.; Lee, S.; Chu, Y. H.; Martin, L. W.; Kumar, A.; McGill, S.; Rai, R. C.; Ramesh, R.; Gopalan, V.; Cheong, S. W.; Musfeldt, J. L., Optical

Properties and Magnetochromism in Multiferroic BiFeO$_3$. *Phys. Rev. B* **2009,** *79* (13), 134425.

39.   Jung, J. H.; Matsubara, M.; Arima, T.; He, J. P.; Kaneko, Y.; Tokura, Y., Optical Magnetoelectric Effect in the Polar GaFeO$_3$ Ferrimagnet. *Phys. Rev. Lett.* **2004,** *93* (3), 037403.

40.   Pal, M.; Rakshit, R.; Mandal, K., Surface Modification of MnFe$_2$O$_4$ Nanoparticles to Impart Intrinsic Multiple Fluorescence and Novel Photocatalytic Properties. *ACS Appl. Mater. Interfaces* **2014,** *6* (7), 4903-4910.

41.   Giri, A.; Goswami, N.; Pal, M.; Zar Myint, M. T.; Al-Harthi, S.; Singha, A.; Ghosh, B.; Dutta, J.; Pal, S. K., Rational Surface Modification of Mn$_3$O$_4$ Nanoparticles to Induce Multiple Photoluminescence and Room Temperature Ferromagnetism. *J. Mater. Chem. C* **2013,** *1* (9), 1885-1895.

42.   Giri, A.; Goswami, N.; Sasmal, C.; Polley, N.; Majumdar, D.; Sarkar, S.; Bandyopadhyay, S. N.; Singha, A.; Pal, S. K., Unprecedented Catalytic Activity of Mn$_3$O$_4$ Nanoparticles: Potential Lead of a Sustainable Therapeutic Agent for Hyperbilirubinemia. *RSC Adv.* **2014,** *4* (10), 5075-5079.

Chapter 4 | Surface Functionalization of MnFe$_2$O$_4$ Nanoparticles

This chapter demonstrates improvement of fluorescence and magnetic property upon surface modification of MnFe$_2$O$_4$ nanoparticles due to incorporation of Mn within the system and increasing surface to volume ratio by decreasing the size of nanoparticles.

4. Surface Modification of MnFe₂O₄ Nanoparticles to Impart Intrinsic Multiple Fluorescence and Novel Photocatalytic Properties

4.1. Preamble

Among the magnetic nanoparticles (MNPs) extensive studies on iron oxide and ferrite nanoparticles (NPs) have been performed due to their excellent superparamagnetic behaviour and chemical stability. Particularly, among the ferrites, research on MnFe₂O₄ has been a key topic because of their highest magnetization which enables them potentially useful as MRI contrast agents and magnetic probes capable of being manipulated under external magnetic field.[1-14] Recently, significant efforts have also been given for the development of MnFe₂O₄ NPs as targeted multimodal imaging agents, upon conjugating fluorescent dye molecules and cancer cell surface receptors with the NPs surface.[15-18] However, despite recent advancement, aqueous phase insolubility and absence of any inherent optical properties of the NPs possess a huge concern for their direct biomedical applications. Thus, the designing of appropriate surface modification and functionalization strategy is highly desirable to expedite the diverse biological applicability of the NPs.

In an attempt to improve the fluorescence and magnetic property of Fe₂O₃ system (discussed in chapter 3), we employed our newly developed facile chemical functionalization strategy for surface modification of MnFe₂O₄ NPs through incorporation of Mn within the system and increasing surface to volume ratio by decreasing the size of NPs. In this chapter, we report the development of MnFe₂O₄ as a multifunctional nano probe having intrinsic multicolor fluorescence, superparamagnetism and novel photocatalytic activity. We have synthesized 4-5 nm MnFe₂O₄ NPs following a wet chemical method previously reported by Sun et al., with slight modification.[19] We have used the reactivity of tartrate ligands to solubilize the as-prepared NPs into aqueous environment. Employing a further surface modification approach we have observed the emergence of multi-color

fluorescence (starting from blue, cyan, green to red) from the water soluble tartrate functionalized $MnFe_2O_4$ NPs (T-$MnFe_2O_4$ NPs). In order to investigate the mechanistic origin of this novel multicolor fluorescence property, we have used several spectroscopic techniques. It has been found that the ligand-to-metal charge transfer (LMCT) transitions from tartrate ligand to lowest unoccupied energy level of $Mn^{2+/3+}$ or Fe^{3+} metal ions in the NPs and Jahn-Teller (J-T) distorted d−d transitions centered over Mn^{3+} ions play the key role. Finally, we intended to exploit the photoexcitation (UV-visible) behaviour of the T-$MnFe_2O_4$ NPs in catalysis. It has been found that, the T-$MnFe_2O_4$ NPs exhibit unprecedented photocatalytic property in the degradation of an organic dye used in textile industries and a model water contaminant.[20]

4.2. Experimental Section

4.2.1. Material Used

Fe (III) acetylacetonate (Fe(acac)$_3$), oleylamine, Methylene blue (MB), 2-amino-purine (2AP), 4', 6-diamidino-2-phenylindole (DAPI), Hoechst 33258, and Rhodamine B (RhB) were obtained from Sigma-Aldrich. Mn (II) acetate (Mn(ac)$_2$), diphenyl ether, oleic acid, and cetyl alcohol were received from Loba Chemie. Tartaric acid, ethanol (EtOH), sodium hydroxide (NaOH) and potassium bromide were purchased from Merck. All the reagents are analytical grade and used without further purification.

4.2.2. Synthesis Procedure and Functionalization of MnFe$_2$O$_4$ NPs

$MnFe_2O_4$ NPs were synthesized by template free wet chemical process following a previous report with some modification,[19] which involves the high-temperature (260 ^{o}C) reflux of Mn(ac)$_2$ and Fe(acac)$_3$ in di-phenyl ether in the presence of oleic acid, oleylamine, and cetyl alcohol. As-prepared $MnFe_2O_4$ NPs were cyclomixed with 0.5 M Na-tartrate solution (prepared in Milli-Q water and pH of the solution were made ~ 7) for 12 h at room temperature. The non solubilized larger $MnFe_2O_4$ NPs were filtered out with a syringe filter of 0.22 μm diameter. The as obtained pale yellow

colored filtrate was tartrate functionalized $MnFe_2O_4$ NPs, called T-$MnFe_2O_4$ NPs. To induce the multicolor fluorescence property, T-$MnFe_2O_4$ NPs were heated at about 70 °C for 8 h under extensive stirring condition after maintaining the pH of the solution at ~12 with dropwise addition of NaOH solution. After this high pH and temperature treatment, color of the solution turned to brownish and showed intense fluorescence under UV light (inset of Figure 4.3 (a)). To prepare the solid powdered samples required for magnetic study (Vibrating sample magnetometry, VSM) and fourier transform infrared (FTIR) spectroscopic measurements, we dialyzed T-$MnFe_2O_4$ NPs solution (to remove excess ligands) and lyophilized followed by drying over a water bath.

4.2.3. Catalysis

For the study of photocatalysis we used 8 W UV lamp as UV light source and a 100 W incandescent bulb (its optical spectra exactly mimics sunlight having a continuum throughout the visible region) as visible light source from Philips. 1:1 (4.6 µM each) aqueous solution of MB and T-$MnFe_2O_4$ NPs were homogeneously mixed for 1 h in a quartz cuvette in the dark maintaining the pH of the solution ~3. Then the cuvette was placed ~2 cm apart from the light source and the absorbance of MB in the reaction mixture was measured time to time by the UV-visible spectrophotometer.

4.3. Result and Discussions

TEM study has been carried out to evaluate the morphology and monodispersity of both the as-prepared $MnFe_2O_4$ NPs and highly water soluble T-$MnFe_2O_4$ NPs, in details. As shown in Figure 4.1 (a), as-prepared $MnFe_2O_4$ NPs have nearly homogeneous size distribution (3.5-7 nm) with an average diameter of 4.80 ± 0.16 nm (Figure 4.1 (c)) and most of the NPs have been found to be spherical in shape.
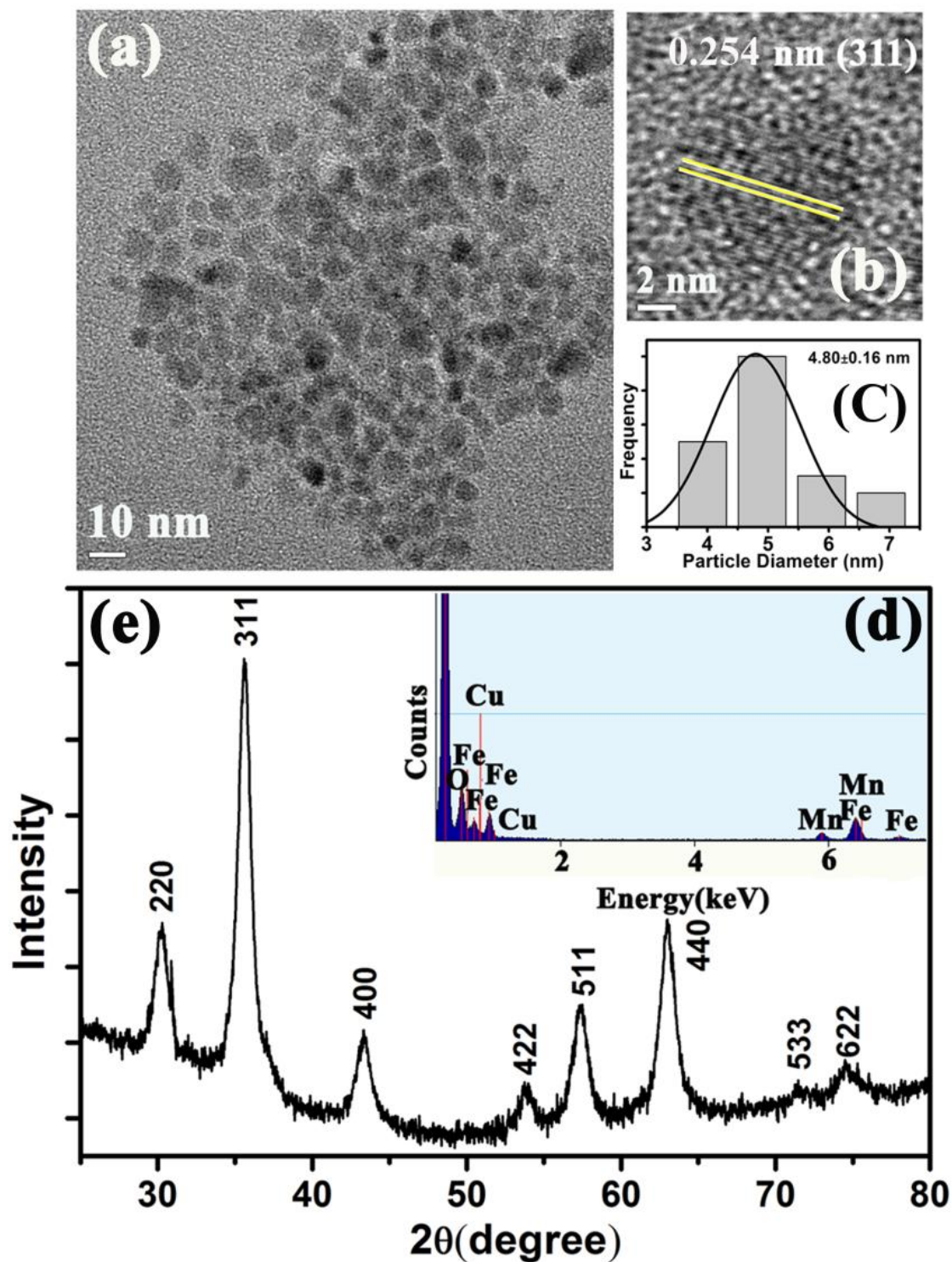
Figure 4.1. (a) TEM image of the as-prepared bare $MnFe_2O_4$ NPs. (b) Corresponding HRTEM image indicates high crystallinity and shows lattice fringes. (c) Size distribution of as-prepared $MnFe_2O_4$ NPs. (d) EDX spectrum of the NPs indicating the presence of Mn, Fe, and O. (e) XRD pattern of as-prepared $MnFe_2O_4$ NPs. All diffraction peaks in the figure are perfectly indexed in the literature to the cubic spinel structure of $MnFe_2O_4$ NPs.

The corresponding HRTEM image (Figure 4.1(b)) confirms the crystallinity of the NPs. The calculated interplanar distance between the lattice fringes is about 0.254 nm which corresponds to the distance between (311) planes of $MnFe_2O_4$ crystal lattice. Energy dispersive X-ray (EDX) spectroscopic analysis of $MnFe_2O_4$ NPs (Figure 4.1(d)) confirms the elemental composition of only manganese, iron and oxygen. Figure 4.1 (e) shows the XRD pattern of as-prepared $MnFe_2O_4$ NPs. All the diffraction peaks in the figure perfectly matches with the cubic spinel structure of $MnFe_2O_4$ NPs as obtained from the literature.[19]

In order to study the effect of surface functionalization on the properties of $MnFe_2O_4$ NPs, we have functionalized the as-prepared $MnFe_2O_4$ NPs with tartrate ligands. Figure 4.2 (a) shows the TEM image of $T-MnFe_2O_4$ NPs having spherical shape with an average diameter of ~3 nm (Figure 4.2 (c)). From the HRTEM image of $T-MnFe_2O_4$ NPs (shown in Figure 4.2 (b)) highly crystalline nature of the NPs is clearly evident. The calculated interplanar distance between the fringes has been found to be 0.254 nm corresponding to (311) plane of the crystal lattice. As shown in Figure 4.2 (d), $T-MnFe_2O_4$ NPs (at pH ~7) exhibit distinct absorption pattern in the UV-visible region, indicating a significant variation to the surface electronic structure of the NPs upon functionalization with tartrate ligand. The observed peak at 315 nm having relatively higher absorbance (shown in the inset) can be attributed to ligand to metal charge transfer (LMCT) transitions involving the interaction between highest occupied energy level of tartrate and lowest unoccupied energy levels of $Mn^{2+}/Mn^{3+}/Fe^{3+}$ metal ion centres on the NPs surface.[21] Additional three peaks with gradually decreasing intensities, observed around 375, 435, and 576 nm can be due to the possible d-d transitions involving $Mn^{2+/3+}$ or Fe^{3+} ions in the $T-MnFe_2O_4$ NPs surface (although Mn in 3+ oxidation state was not supposed to be present in the $MnFe_2O_4$ NPs, however, due to the strong pH dependence of oxidation states of Mn, upon solubilization of the NPs into aqueous environment at pH~7, formation of Mn^{3+} states is highly probable).[22, 23] The possibility of d-d transitions in case of both Fe^{3+} (d^5) and Mn^{2+} (d^5) ions is very low, as in both cases this transition is forbidden (both Laporte and spin forbidden) according to the selection rule of fundamental atomic spectroscopy.[24]
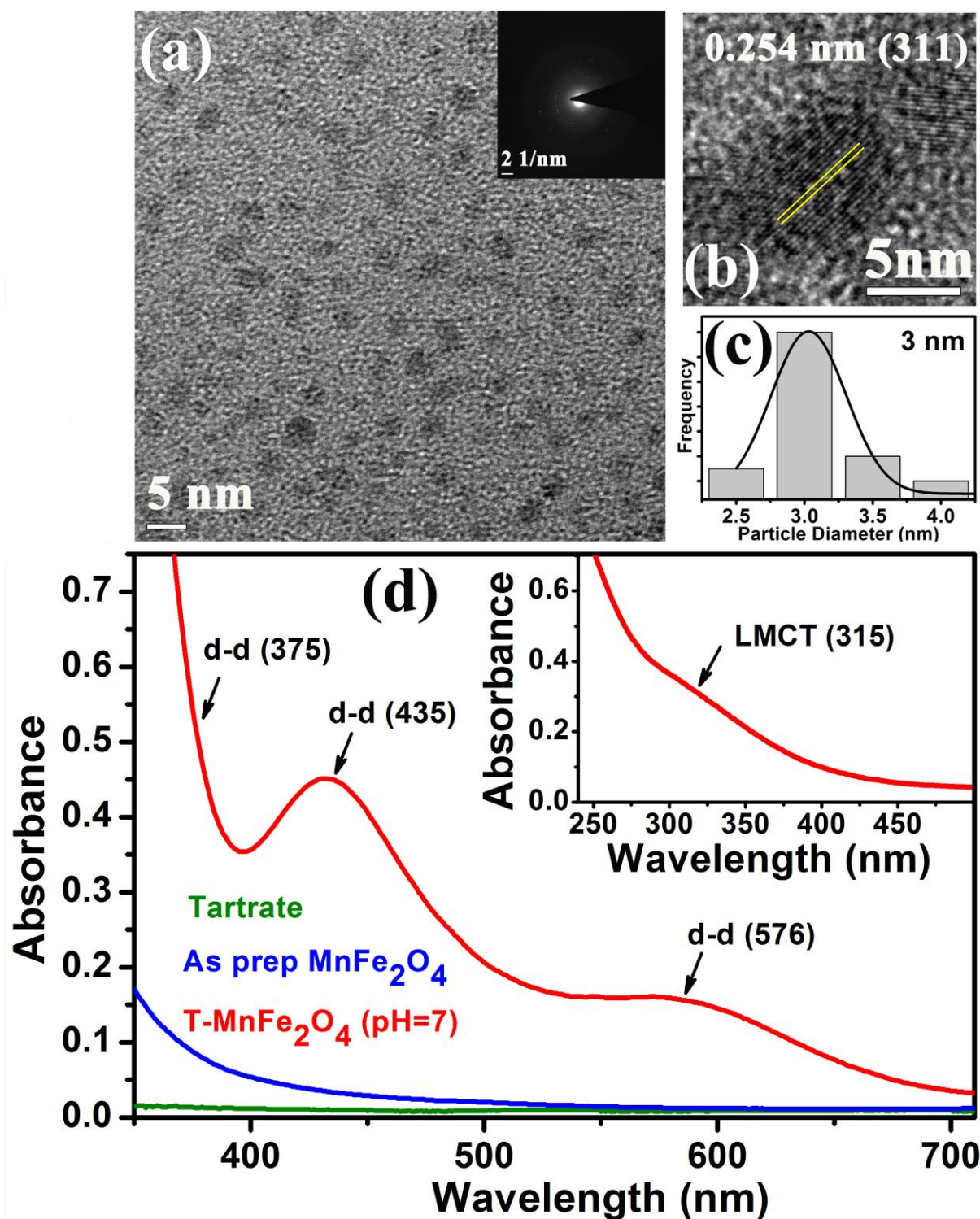
Figure 4.2. (a) TEM image of highly dispersible T-MnFe₂O₄ NPs.in aqueous medium. (b) Lattice fringes in the corresponding HRTEM image, indicating high crystalline nature of the NPs. (c) Size distribution of T-MnFe₂O₄ NPs. (d) UV-visible absorption spectrum for T-MnFe₂O₄ NPs, as prepared MnFe₂O₄ NPs, and Na-tartrate at pH ~7. Inset shows higher energy strong absorption band due to LMCT transitions for very dilute T-MnFe₂O₄ NPs solution.

However, in the case of Mn^{3+} (d^4), the degeneracy of t_{2g} and e_g levels could be lost due to Jahn-Teller (J-T) distortion in the high spin octahedral environment. In terms of spectroscopic term symbols we can explain the generation of three bands (375, 435, and 576 nm) due to the transitions of $5B_{1g} \rightarrow 5E_g$, $5B_{1g} \rightarrow 5B_{2g}$ and $5B_{1g} \rightarrow 5A_{1g}$, respectively.[25, 26] Interestingly, when we had excited T-$MnFe_2O_4$ NPs (pH ~7) at these different UV-visible absorption peak/band positions, we found multiple fluorescence. Although, the fluorescence observed upon excitation of the sample at LMCT band (315 nm) was very strong, fluorescence from d-d excited states (J-T distorted states) was found to be considerably weak. So, in order to make the d-d excited states highly fluorescent, pH of the as-prepared T-$MnFe_2O_4$ NPs was adjusted to ~12 (to convert all the Mn ions into +3 oxidation state), [23] by dropwise addition of NaOH solution, followed by heat treatment at 70 °C for 8 h. This further surface modification step significantly enhanced the fluorescence intensity from d-d (J-T distorted) as well as from LMCT excited states. Figure 4.3 (a) shows the normalized multiple fluorescence spectra of T-$MnFe_2O_4$ NPs (pH~12) having emission maximum at 413, 460, 513, and 560 nm, covering the whole visible region from blue, cyan, green to red, against excitation at 315, 360, 430, and 520 nm, respectively.[20] Nice correlation between the corresponding excitation spectrum of different emission maximum, as shown in Figure 4.3 (b), and UV-visible absorption spectra of fluorescence modified T-$MnFe_2O_4$ NPs (Figure 4.6 (a)), further substantiate the exact excitation positions of the respective fluorescence emissions. Noticeably Na-tartrate and as prepared $MnFe_2O_4$ NPs do not exhibit any absorbance peak, except very small LMCT band due to participation of capping agents with long tail (oleic acid, oleylamine, and cetyl alcohol). But, as prepared $MnFe_2O_4$ NPs cannot generate any fluorescence (Figure 4.4). Photographs of the aqueous solution of T-$MnFe_2O_4$ NPs under visible and UV light are shown in the inset of Figure 4.3 (a). The amazing fluorescence microgarphs of T-$MnFe_2O_4$ NPs powder, as shown in Figure 4.3 (c) demonstrates that the black powder of T-$MnFe_2O_4$ NPs under bright field, gives rise to fluorescent colors like cyan, green, and red upon excitation at 365, 436, and 546 nm, respectively, by using proper filters. Figure 4.4 and 4.5 shows that the fluorescence microscopic images of as-prepared $MnFe_2O_4$ NPs and Na-tartrate,

respectively under identical conditions have no such fluorescence. Fluorescence quantum yields (QYs) of the T-MnFe$_2$O$_4$ NPs, have been calculated by following the relative method of Williams et al.,[27] which involves the use of well characterized standard fluorescent compounds with known QY values. Fluorescence QYs of 11.83% (for 413 nm band), 2.4% (for 460 nm band), 2% (for 513 nm band) and 0.14% (for 560 nm band) were obtained relative to the standard fluorescent compounds such as 2-aminopurine (2AP), 4′, 6-diamidino-2-phenylindole (DAPI), Hoechst 33258, and Rhodamine B (RhB), respectively. Thus, the emergence of multicolor fluorescence in MnFe$_2$O$_4$ NPs was induced by tartrate functionalization and then reinforced by further surface modification.
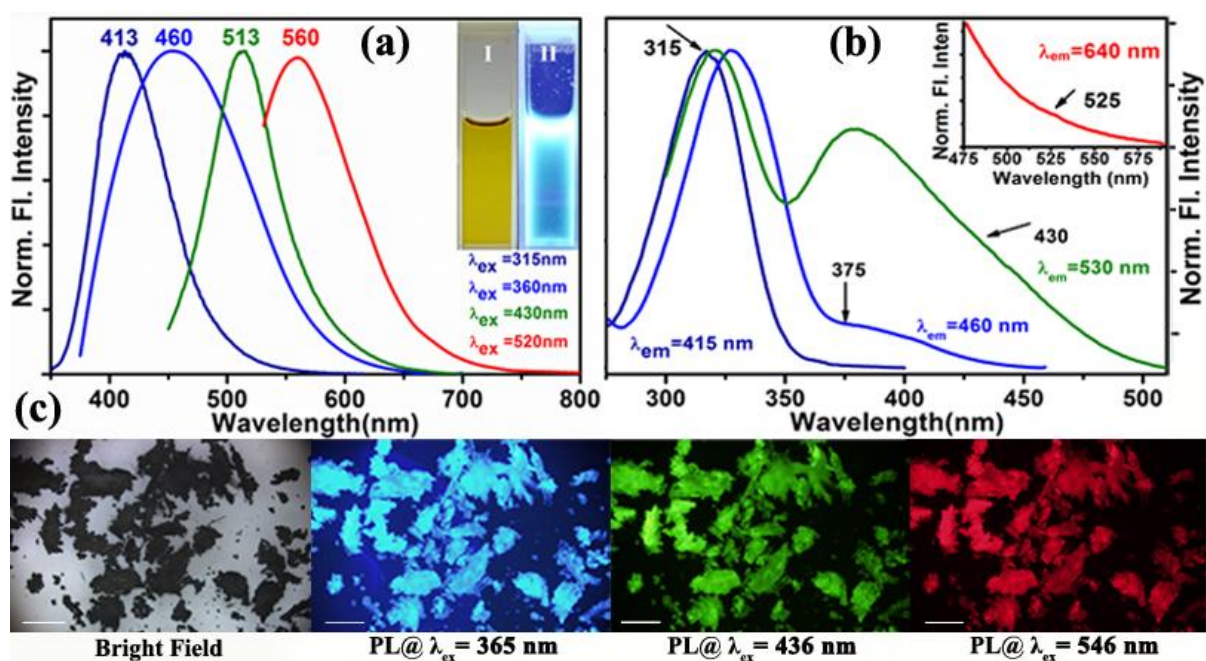
Figure 4.3. (a) Normalized steady-state fluorescence emission spectra collected from T-MnFe$_2$O$_4$ NPs with four different excitation wavelengths of 315, 360, 430, and 520 nm. I and II in the inset shows the photograph of aqueous T-MnFe$_2$O$_4$ NPs solution under visible and UV light respectively. (b) Fluorescence excitation spectra of T-MnFe$_2$O$_4$ NPs at different emission maximum of 415, 460, 530, and 640 nm. (c) Fluorescence micrographs of T-MnFe$_2$O$_4$ NPs powder under bright field, UV (365 nm), blue (436 nm), and green (546 nm) light irradiation. The scale bars in all the images are 500 µm.
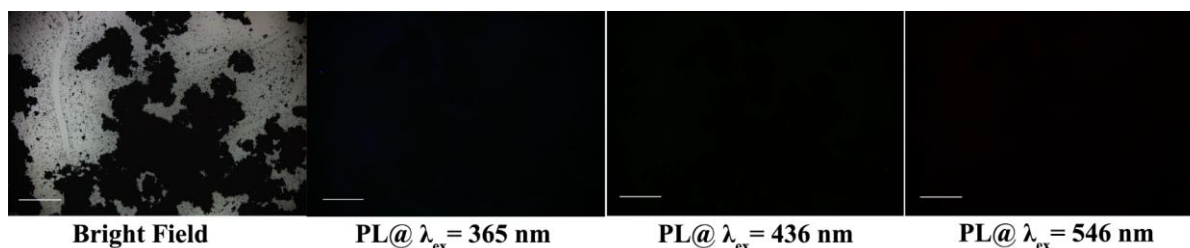
Figure 4.4. Fluorescence micrographs of as prepared MnFe$_2$O$_4$ NPs under bright field, UV, blue, and green light. The scale bars in all the images are 500 µm.
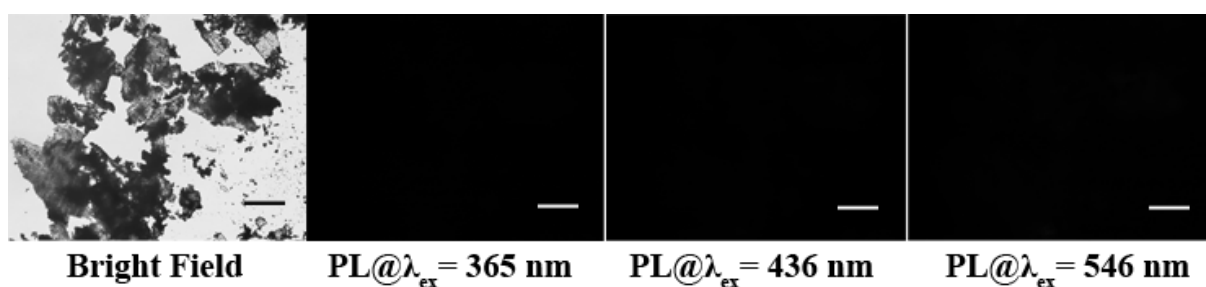
Figure 4.5. Fluorescence micrographs of Na-tartrate under bright field, UV, blue, and green light. The scale bars in all the images are 500 µm.
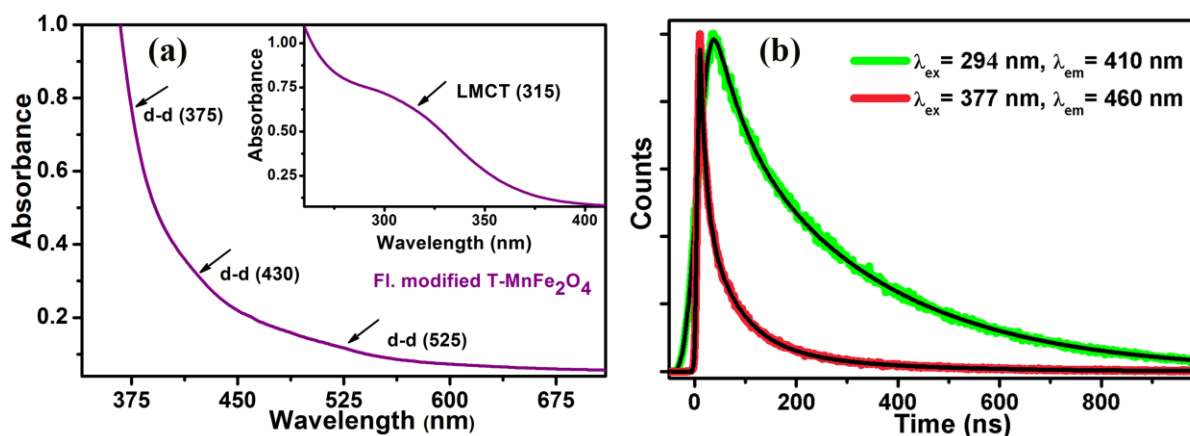
Figure 4.6. (a) UV-visible absorption spectrum for fluorescence modified T-MnFe$_2$O$_4$ NPs at pH ~12. (b) Picosecond-resolved fluorescence transients of T-MnFe$_2$O$_4$ NPs studied at emission wavelengths of 410 and 460 nm upon excitation with laser sources of 294 and 377 nm wavelengths, respectively.

To get deeper mechanistic insight into the appearance of multiple fluorescence, we have carried out picosecond-resolved fluorescence decay transient measurements of T-MnFe$_2$O$_4$ NPs employing TCSPC technique. Figure 4.6 (b) represents the time resolved fluorescence decay transients of T-MnFe$_2$O$_4$ NPs at two

different fluorescence maxima of 410 and 460 nm using two different pulsed diode laser excitation sources of 294 and 377 nm wavelengths, respectively. As evident from the figure, significantly larger average excited-state lifetime (τ) of T-MnFe$_2$O$_4$ NPs observed for 410 nm fluorescence band (6.06 ns) compared to that for 460 nm fluorescence band (1.27 ns), strongly suggests mechanistic difference in the origin of these two fluorescence bands. The lifetime components and their corresponding weight percentages are mentioned in Table 4.1.

Table 4.1. Lifetime values of picosecond time-resolved fluorescence transients of T-MnFe$_2$O$_4$ NPs, detected at fluorescence maxima 410 and 460 nm upon excitation at 294 and 377 nm wavelengths, respectively. The relative weight percentages of the time components are mentioned in parentheses.

System	Excitation wavelength, λ_{ex} (nm)	Fluorescence peak, λ_{em} (nm)	τ_1(ns)	τ_2(ns)	τ_3(ns)	τ_{av}(ns)
Fl. modified T-MnFe$_2$O$_4$ NPs	294	410	1.46 (35.32)	8.58 (64.68)	-	6.06
	377	460	1.88 (34.06)	7.14 (6.23)	0.31 (59.71)	1.27

With this fluorescence lifetime study, proposition regarding the origin of this multiple fluorescence made from steady state experiments are reconfirmed and we reasonably conclude that LMCT excited state is responsible for 410 nm fluorescence, while 460 nm fluorescence is attributed to J-T distorted d-d transition. It is quite obvious that other two lower energy fluorescence at 513 and 560 nm would also correspond to other probable d-d transitions.

To obtain definite evidence for the involvement of Mn^{3+} ions in the generation of multicolor fluorescence, we have studied the pH dependency of the fluorescence intensity. Since, at acidic/neutral pH, Mn^{3+} ions are unstable and tend to disproportionate into Mn^{2+} and Mn^{4+}, whereas, in alkaline pH, comproportionation

of Mn^{2+} and Mn^{4+} to Mn^{3+} ions takes place.[23, 28] We have monitored the fluorescence intensity of T-$MnFe_2O_4$ NPs at 413 and 460 nm (against excitation at 315 and 360 nm, respectively), upon decreasing the pH of the NPs solution from 12 to 3. Gradual reduction of fluorescence intensity with decreasing pH is clearly evident from Figure 4.7, which further corroborates our conclusion that both the LMCT and d-d transitions (J-T distorted) are associated with Mn^{3+} ions on the NPs surface.
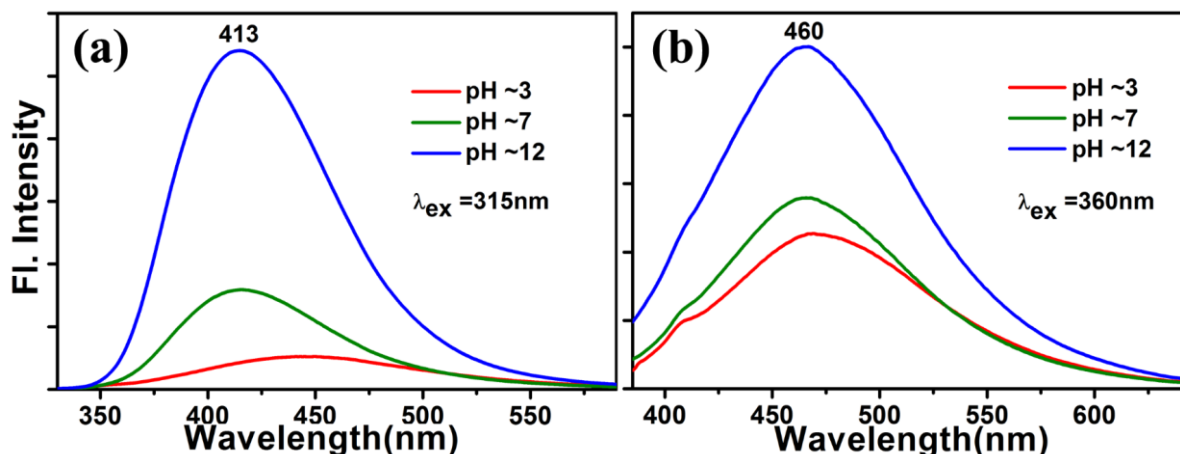
Figure 4.7. (a) and (b) show the decrease of fluorescence intensity at emission maxima of T-$MnFe_2O_4$ NPs at 413 and 460 nm upon excitation at 315 and 360 nm respectively with decrease in pH of the system upon addition of hydrochloric acid (HCl).

Considering the possibility of photo-induced electron transfer from excited composites to H^+, we have performed pH dependent picosecond-resolved fluorescence transient measurements of T-$MnFe_2O_4$ NPs, at pH=12 and 5. At lower pH (~5), if it was the case of photo-induced electron transfer from excited composites (T-$MnFe_2O_4$ NPs) to H^+ (causing the decrease of fluorescence intensity), we were supposed to get a quenching in the excited state lifetime of the composite. However, as shown in Figure 4.8, we have found almost similar excited state transients of the composite at both the pH of 12 and 5. So, we strongly believe that change in the oxidation state of the metal ions plays the key role behind the decrease of fluorescence intensity.
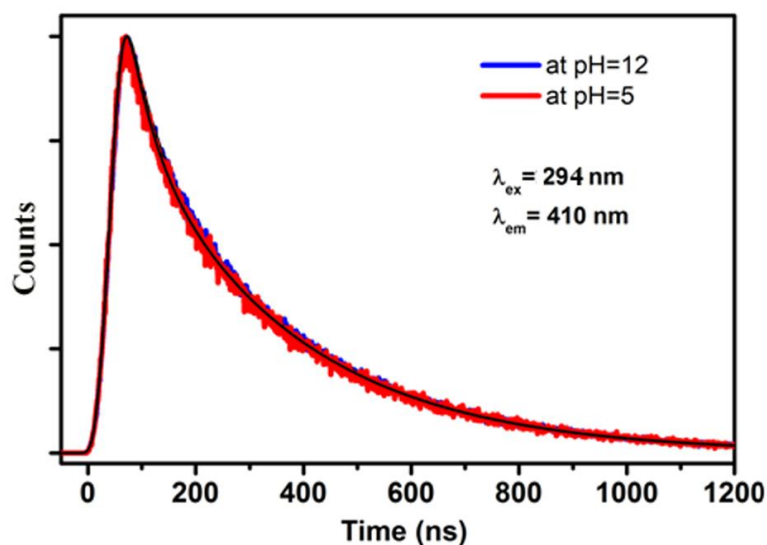
Figure 4.8. pH dependent picosecond-resolved fluorescence transients of T-MnFe$_2$O$_4$ NPs studied at emission wavelength of 410 nm upon excitation with laser source of 294 nm wavelength.

In order to confirm the attachment of tartrate ligands to the NP surface, comparative FTIR spectroscopic study was performed on bare and tartrate functionalized MnFe$_2$O$_4$ NPs along with Na-tartrate alone (Figure 4.9 (a)). As shown in the figure, in case of tartrate, two sharp peaks arising at 1066 and 1112 cm^{-1} are due to the C–OH stretching modes,[29] and peaks at 1412 and 1622 cm^{-1} are attributed to symmetric and asymmetric stretching modes of the carboxylate groups (COO$^-$) of tartrate, respectively.[30] Upon interaction with the NP surface i.e. in case of T-MnFe$_2$O$_4$, all these different bands are perturbed significantly along with the band at 3400 cm^{-1} corresponding to the stretching vibrational modes of hydroxyl group (O–H),[29] clearly indicates the involvement of both –COO$^-$ and –OH groups in the functionalization process.
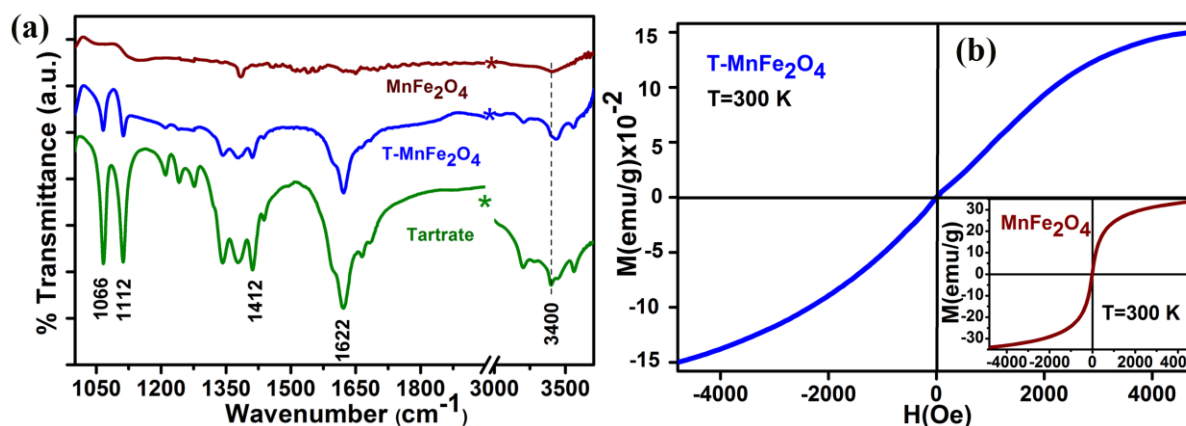
Figure 4.9. (a) FTIR spectra of as-prepared MnFe₂O₄ and T-MnFe₂O₄ NPs along with Na-tartrate alone. (b) Plot of magnetisation versus applied magnetic field (M-H) for T-MnFe₂O₄ NPs at 300 K. Inset shows M-H plot for as-prepared MnFe₂O₄ NPs at 300 K.

To study the magnetic behaviour of MnFe₂O₄ NPs before and after functionalization with tartrate ligands, we have investigated applied field dependent magnetization measurements (M-H) for both the samples using VSM. The superparamagnetic nature of as-prepared bare MnFe₂O₄ NPs is evident from inset of Figure 4.9 (b). In case of T-MnFe₂O₄ NPs also this superparamagnetic nature remains unchanged (evident from Figure 4.9 (b)), although, with a decrease in saturation magnetization, which could be due to the presence of diamagnetic ligand coating around the NPs after functionalization.
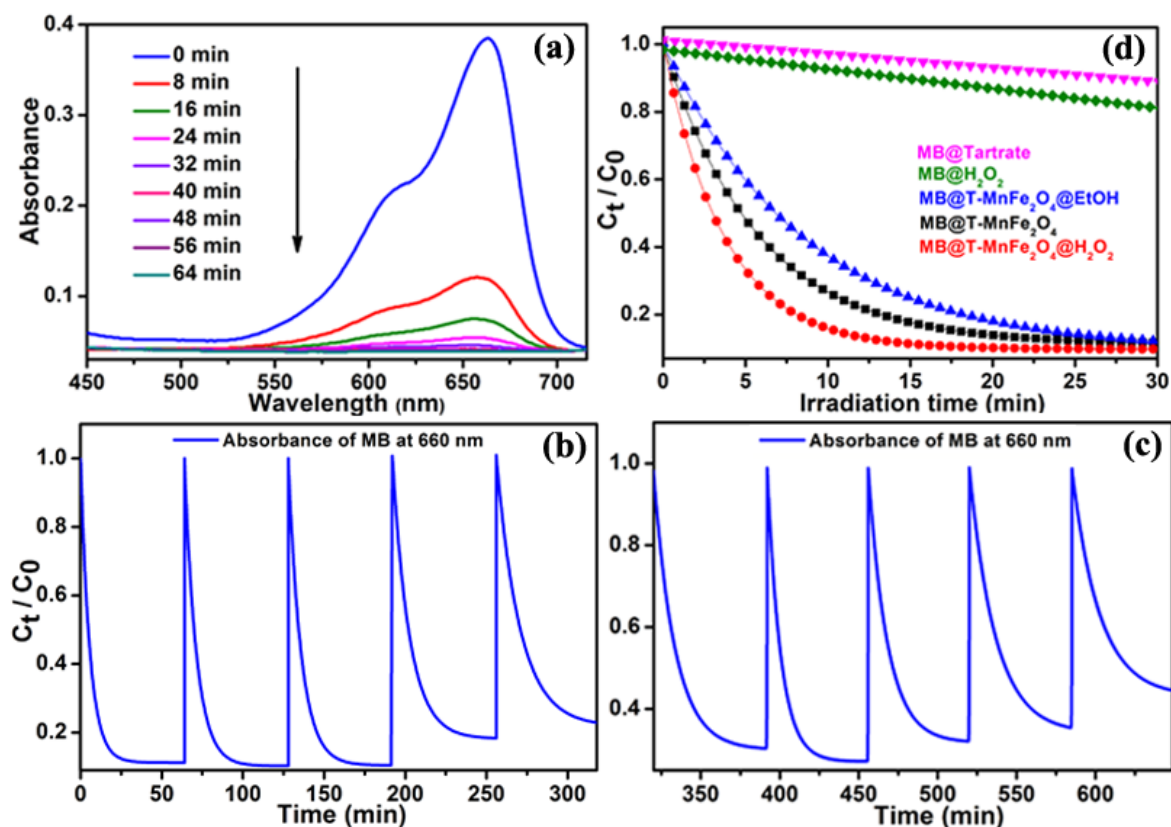
Figure 4.10. (a) UV-visible spectral changes of aqueous solution of methylene blue (MB) in presence of T-MnFe$_2$O$_4$ NPs with time, under UV irradiation. (b, c) Show the plot of relative concentration of MB monitored at 660 nm versus time for consecutive 10 cycles, showing reusability of T-MnFe$_2$O$_4$ in MB degradation under UV light. (d) Shows the rate of photocatalytic degradation of MB (monitored at 660 nm) under UV radiation in presence of Na-tartrate, H$_2$O$_2$, T-MnFe$_2$O$_4$ NPs, T-MnFe$_2$O$_4$ NPs@EtOH and T-MnFe$_2$O$_4$ NPs@H$_2$O$_2$.
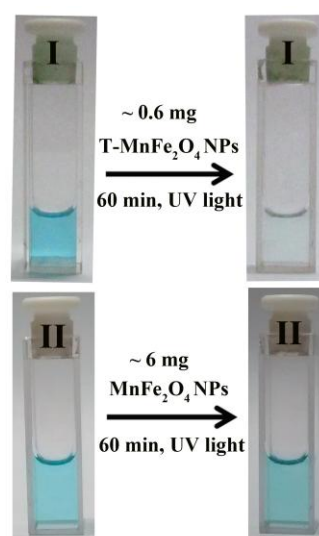
Figure 4.11. Visible changes of aqueous solution of MB in presence of T-MnFe$_2$O$_4$ NPs (I) and MnFe$_2$O$_4$ NPs (II), under UV irradiation for 60 min.

Having developed MnFe$_2$O$_4$ NPs as multicolor fluorescent material, we saught to exploit their broad optical excitation (absorption) throughout UV-visible region, for photocatalysis. In our study, as an analyte we have used methylene blue (MB), which is a model water contaminant. Figure 4.10 demonstrates the unprecedented photocatalytic efficiency of T-MnFe$_2$O$_4$ NPs in MB degradation under UV light irradiation. Figure 4.10 (a) shows the full absorption spectrum of MB in presence of T-MnFe$_2$O$_4$ NPs with time, under UV irradiation at pH~3. We have found that the photo induced discoloration of MB in presence of T-MnFe$_2$O$_4$ NPs takes place exponentially with time following first-order rate equation with a kinetic rate constant (k) of 17.46×10^{-2} min^{-1} and a total photodegradation of 70% takes place within first 8 minutes and 90% occurs within 40 minutes of UV irradiation. To ensure that the catalyst could be recycled without any significant loss of activity, we started the experiment with 1:1 (4.6: 4.6 µM) MB: catalyst for first cycle and after every 64 min we added same dose of MB (4.6 µM) into the reaction mixture up to 10 dose. Keeping the catalyst concentration fixed at 4.6 µM (without addition of extra catalyst after the 1st cycle), MB decomposition kinetics of different cycles was studied by monitoring the decrease of MB absorbance at 660 nm using UV-visible spectroscopy. Figure 4.10 (b) and (c) demonstrate the plots of relative concentration of MB versus time, upto consecutive 10 cycles, revealing the reusability of T-MnFe$_2$O$_4$ NPs catalyst. To investigate whether the catalytic process is associated with radical pathway, we have performed the MB degradation study (as shown in Figure 4.10 (d)) in presence of a radical initiator (H$_2$O$_2$, a source of •OH radicals) and a radical scavenger (EtOH), separately. Figure 4.10 (d) shows the comparative study of MB degradation rate in presence of Na-tartrate (as blank experiment), H$_2$O$_2$, T-MnFe$_2$O$_4$ NPs, T-MnFe$_2$O$_4$ NPs@EtOH, and T-MnFe$_2$O$_4$ NPs@H$_2$O$_2$. It has been observed that, upon addition of radical scavanger, the rate of MB degradation decreases effectively (k=11.82×10^{-2} min^{-1}), whereas, with addition of very small concentration (156 nM) of H$_2$O$_2$, photodegradation rate increases cosiderably (k=26.85×10^{-2} min^{-1}). The above study confirms that the photodegradation follows radical pathway involving reactive oxygen species (ROS). We propose that, due to very small size of T-MnFe$_2$O$_4$ NPs and negatively charged surafce ligands (tartrate),

MB molecules (cationic dye) get opportunity for greater interaction with the NPs, which ultimately leads to efficient catalytic degradation. As anticipated, in presence of only tartrate, bare $MnFe_2O_4$ NPs or H_2O_2, the degradation takes place negligibly. Figure 4.11 shows the visible change of MB solution in presence of ~ 0.6 mg T-$MnFe_2O_4$ NPs (I) and 6 mg bare $MnFe_2O_4$ NPs (II) under UV light irradiation for 60 min. Additionaly, we have also checked the catalytic efficiency of the NPs towards MB degradation, in presence of visible light activation (Figure 4.12). Interestingly, T-$MnFe_2O_4$ NPs show photocatalytic degradation of MB under visible light also, although, with a moderate rate ($k=1.83 \times 10^{-2}$ min^{-1}). Relatively less photocatalytic efficiency of the NPs under visible light excitation can be attributed to the higher enegy of UV light as compared to visible light as well as higher extinction coefficient of T-$MnFe_2O_4$ NPs in the UV region than its visible counterpart.
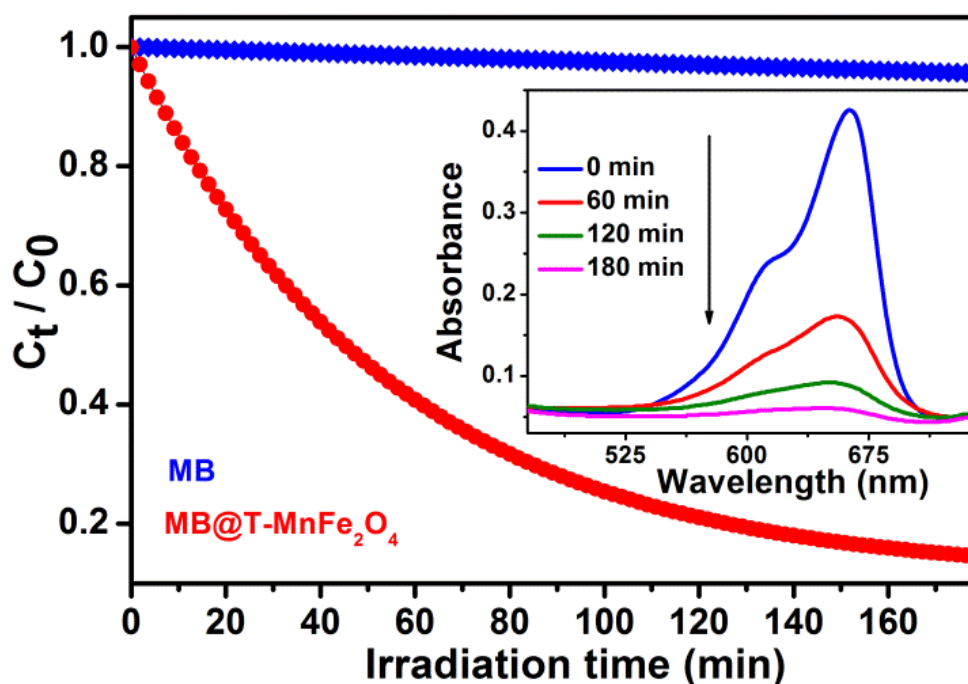
Figure 4.12. Shows the rate of photocatalytic degradation of MB (monitored at 660 nm) in absence and presence of T-$MnFe_2O_4$ NPs under visible light. Inset shows the full absorption spectra of methylene blue (MB) in presence of T-$MnFe_2O_4$ NPs with time, under visible-light irradiation.

4.4. Conclusions

In summary, we have demonstrated a facile functionalization and further surface modification strategy for the development of MnFe$_2$O$_4$ NPs as a biocompatible novel multifunctional biological probe, simultaneously having superparamagnetism and inherent multicolor fluorescence covering the whole UV-visible region from blue, cyan, and green to red. Employing various spectroscopic techniques we have investigated the exact mechanistic origin of the remarkable optical properties of MnFe$_2$O$_4$ NPs upon functionalization with tartrate. We believe that this novel functionalized material (T-MnFe$_2$O$_4$ NPs) might open up new opportunities to their prospective use in bio-imaging, drug delivery and other biomedical applications in future, due to the coexistence of its biocompatibility, ligand induced intrinsic multicolor fluorescence and superparamagnetism. Furthermore, we have also demonstrated the unprecedented photocatalytic activity of the functionalized material for the degradation of a model water contaminant. Given the possibility of ligand induced appearance of new magneto-fluorescence properties in the nanomaterials and excellent photocatalytic activity, we expect that this work will contribute significantly to the design and development of new materials for their advanced technological application.

Bibliography

1.   Li, Z.; Wang, S. X.; Sun, Q.; Zhao, H. L.; Lei, H.; Lan, M. B.; Cheng, Z. X.; Wang, X. L.; Dou, S. X.; Lu, G. Q., Ultrasmall Manganese Ferrite Nanoparticles as Positive Contrast Agent for Magnetic Resonance Imaging. *Adv. Healthcare Mater.* **2013,** *2* (7), 958-964.

2.   Kim, D. H.; Thai, Y. T.; Nikles, D. E.; Brazel, C. S., Heating of Aqueous Dispersions Containing $MnFe_2O_4$ Nanoparticles by Radio-Frequency Magnetic Field Induction. *IEEE Trans. Magn.* **2009,** *45* (1), 64-70.

3.   Huang, H.; Delikanli, S.; Zeng, H.; Ferkey, D. M.; Pralle, A., Remote Control of Ion Channels and Neurons Through Magnetic-Field Heating of Nanoparticles. *Nat. Nanotechnol.* **2010,** *5* (8), 602-606.

4.   Na, H. B.; Song, I. C.; Hyeon, T., Inorganic Nanoparticles for MRI Contrast Agents. *Adv. Mater.* **2009,** *21* (21), 2133-2148.

5.   Lee, J.; Yang, J.; Seo, S.-B.; Ko, H.-J.; Suh, J.-S.; Huh, Y.-M.; Haam, S., Smart Nanoprobes for Ultrasensitive Detection of Breast Cancer Via Magnetic Resonance Imaging. *Nanotechnology* **2008,** *19* (48), 485101.

6.   Vamvakidis, K.; Katsikini, M.; Sakellari, D.; Paloura, E. C.; Kalogirou, O.; Dendrinou-Samara, C., Reducing the Inversion Degree of $MnFe_2O_4$ Nanoparticles through Synthesis to Enhance Magnetization: Evaluation of their 1H NMR Relaxation and Heating Efficiency. *Dalton Trans.* **2014,** *43* (33), 12754-12765.

7.   Li, Z.; Gao, K.; Han, G.; Wang, R.; Li, H.; Zhao, X. S.; Guo, P., Solvothermal Synthesis of $MnFe_2O_4$ Colloidal Nanocrystal Assemblies and their Magnetic and Electrocatalytic Properties. *New J. Chem.* **2015,** *39* (1), 361-368.

8.   Hu, J.; Lo; Chen, G., Fast Removal and Recovery of Cr(VI) Using Surface-Modified Jacobsite ($MnFe_2O_4$) Nanoparticles. *Langmuir* **2005,** *21* (24), 11173-11179.

9.   Sen, S.; Konar, S.; Pathak, A.; Dasgupta, S.; DasGupta, S., Effect of Functionalized Magnetic $MnFe_2O_4$ Nanoparticles on Fibrillation of Human Serum Albumin. *J. Phys. Chem. B* **2014,** *118* (40), 11667-11676.

10.   Bateer, B.; Tian, C.; Qu, Y.; Du, S.; Yang, Y.; Ren, Z.; Pan, K.; Fu, H., Synthesis, Size and Magnetic Properties of Controllable MnFe$_2$O$_4$ Nanoparticles with Versatile Surface Functionalities. *Dalton Trans.* **2014,** *43* (26), 9885-9891.

11.   Zeng, H.; Rice, P. M.; Wang, S. X.; Sun, S., Shape-Controlled Synthesis and Shape-Induced Texture of MnFe$_2$O$_4$ Nanoparticles. *J. Am. Chem. Soc.* **2004,** *126* (37), 11458-11459.

12.   Rondinone, A. J.; Liu, C.; Zhang, Z. J., Determination of Magnetic Anisotropy Distribution and Anisotropy Constant of Manganese Spinel Ferrite Nanoparticles. *J. Phys. Chem. B* **2001,** *105* (33), 7967-7971.

13.   Zhai, F.; Li, P.; Sun, A.; Wu, S.; Wan, Q.; Zhang, W.; Li, Y.; Cui, L.; Qu, X., Significantly Improved Dehydrogenation of LiAlH$_4$ Destabilized by MnFe$_2$O$_4$ Nanoparticles. *J. Phys. Chem. C* **2012,** *116* (22), 11939-11945.

14.   Kumar, S.; Nair, R. R.; Pillai, P. B.; Gupta, S. N.; Iyengar, M. A. R.; Sood, A. K., Graphene Oxide–MnFe$_2$O$_4$ Magnetic Nanohybrids for Efficient Removal of Lead and Arsenic from Water. *ACS Appl. Mater. Interfaces* **2014,** *6* (20), 17426-17436.

15.   Yang, J.; Lim, E.-K.; Lee, H. J.; Park, J.; Lee, S. C.; Lee, K.; Yoon, H.-G.; Suh, J.-S.; Huh, Y.-M.; Haam, S., Fluorescent Magnetic Nanohybrids as Multimodal Imaging Agents for Human Epithelial Cancer Detection. *Biomaterials* **2008,** *29* (16), 2548-2555.

16.   Lim, E.-K.; Yang, J.; Park, M.-y.; Park, J.; Suh, J.-S.; Yoon, H.-G.; Huh, Y.-M.; Haam, S., Synthesis of Water Soluble PEGylated Magnetic Complexes Using mPEG-Fatty Acid for Biomedical Applications. *Colloids Surf., B* **2008,** *64* (1), 111-117.

17.   Lee, T.; Lim, E.-K.; Lee, J.; Kang, B.; Choi, J.; Park, H. S.; Suh, J.-S.; Huh, Y.-M.; Haam, S., Efficient CD44-Targeted Magnetic Resonance Imaging (MRI) of Breast Cancer Cells Using Hyaluronic Acid (HA)-Modified MnFe$_2$O$_4$ Nanocrystals. *Nanoscale Res. Lett.* **2013,** *8* (1), 149.

18.   Beji, Z.; Hanini, A.; Smiri, L. S.; Gavard, J.; Kacem, K.; Villain, F.; Grenèche, J. M.; Chau, F.; Ammar, S., Magnetic Properties of Zn-substituted MnFe$_2$O$_4$ Nanoparticles Synthesized in Polyol as Potential Heating Agents for Hyperthermia. Evaluation of their Toxicity on Endothelial Cells. *Chem. Mater.* **2010,** *22* (19), 5420-5429.

19. Sun, S.; Zeng, H.; Robinson, D. B.; Raoux, S.; Rice, P. M.; Wang, S. X.; Li, G., Monodisperse MFe_2O_4 (M = Fe, Co, Mn) Nanoparticles. *J. Am. Chem. Soc.* **2003,** *126* (1), 273-279.

20. Pal, M.; Rakshit, R.; Mandal, K., Surface Modification of $MnFe_2O_4$ Nanoparticles to Impart Intrinsic Multiple Fluorescence and Novel Photocatalytic Properties. *ACS Appl. Mater. Interfaces* **2014,** *6* (7), 4903-4910.

21. Bodini, M. E.; Willis, L. A.; Riechel, T. L.; Sawyer, D. T., Electrochemical and Spectroscopic Studies of Manganese(II), -(III), and -(IV) Gluconate Complexes. 1. Formulas and Oxidation-Reduction Stoichiometry. *Inorg. Chem.* **1976,** *15* (7), 1538-1543.

22. Giri, A.; Goswami, N.; Pal, M.; Zar Myint, M. T.; Al-Harthi, S.; Singha, A.; Ghosh, B.; Dutta, J.; Pal, S. K., Rational Surface Modification of Mn_3O_4 Nanoparticles to Induce Multiple Photoluminescence and Room Temperature Ferromagnetism. *J. Mater. Chem. C* **2013,** *1* (9), 1885-1895.

23. Takashima, T.; Hashimoto, K.; Nakamura, R., Mechanisms of pH-Dependent Activity for Water Oxidation to Molecular Oxygen by MnO_2 Electrocatalysts. *J. Am. Chem. Soc.* **2011,** *134* (3), 1519-1527.

24. Huheey, J. E.; Keiter, E. A.; Keiter, R. L., *Inorganic Chemistry-Principles of Structure and Reactivity*. Fourth ed.; Pearson Education: Singapore.

25. Matzapetakis, M.; Karligiano, N.; Bino, A.; Dakanali, M.; Raptopoulou, C. P.; Tangoulis, V.; Terzis, A.; Giapintzakis, J.; Salifoglou, A., Manganese Citrate Chemistry: Syntheses, Spectroscopic Studies, and Structural Characterizations of Novel Mononuclear, Water-Soluble Manganese Citrate Complexes. *Inorg. Chem.* **2000,** *39* (18), 4044-4051.

26. Aguado, F.; Rodriguez, F.; Núñez, P., Pressure-Induced Jahn-Teller Suppression and Simultaneous High-Spin to Low-spin Transition in the Layered Perovskite $CsMnF_4$. *Phys. Rev. B: Condens. Matter Mater. Phys.* **2007,** *76* (9), 094417.

27. Williams, A. T. R.; Winfield, S. A.; Miller, J. N., Relative Fluorescence Quantum Yields Using A Computer-Controlled Luminescence Spectrometer. *Analyst* **1983,** *108* (1290), 1067-1071.

28.   Giri, A.; Goswami, N.; Bootharaju, M. S.; Xavier, P. L.; John, R.; Thanh, N. T. K.; Pradeep, T.; Ghosh, B.; Raychaudhuri, A. K.; Pal, S. K., Emergence of Multicolor Photoluminescence in $La_{0.67}Sr_{0.33}MnO_3$ Nanoparticles. *J. Phys. Chem. C* **2012,** *116* (48), 25623-25629.

29.   Kaneko, N.; Kaneko, M.; Takahashi, H., Infrared and Raman Spectra and Vibrational Assignment of Some Metal Tartrates. *Spectrochim. Acta, Part A* **1984,** *40* (1), 33-42.

30.   Ramakrishnan, V.; Maroor, J. M. T., IR and Raman Studies of Gel Grown Manganese Tartrate. *Infrared Phys.* **1988,** *28* (4), 201-204.

Chapter 5 | Surface Modification of Co_3O_4 Nanocubes

This chapter exhibits development of intrinsic fluorescence, ferromagnetism, and catalytic activity upon surface modification of Co_3O_4 nanocubes and explains the mechanism of generation of novel properties.

5. Surface Chemistry Modulated Introduction of Multifunctionality within Co₃O₄ Nanocubes

5.1. Preamble

As an important transition metal oxide, Co_3O_4 has attracted immense attention owing to its applications in many fields ranging from catalysis,[1, 2] toxic gas sensing,[1, 3] in lithium ion batteries,[4, 5] and supercapacitors.[6-9] Development of nanostructured Co_3O_4 with desirable size and morphologies like cubes, rods, wires, tubes, dendrites, and sheets have been explored for superior performance in its traditional arena and also leading to other unique properties.[10, 11] Recently, Co_3O_4 is found to be an active agent for photocatalytic degradation of organic pollutants under light irradiation, which is a novel finding that paves the way for exploitation and application of Co_3O_4 in such oxidative venture.[12] Nowadays, Co_3O_4 based nano materials are also being promoted for biomedical applications by protein assisted synthesis or surface modification or designing suitable nanoarchitechture.[13, 14] However, to the best of our knowledge, the development of intrinsic fluorescence upon playing the surface chemistry through facile functionalization and incorporation of multifuntionality within a single Co_3O_4 nanostructure having intrinsic fluorescence, ferromagnetism, and catalytic properties, simultaneously, have not been reported so far.

Excellent efficiency of Mn^{3+} (d^4 system, in case of tartrate capped $MnFe_2O_4$ NPs) in development of intense intrinsic fluorescence property due to its allowed d-d transitions, as discussed in chapter 4, and generation of weak fluorescence in case of Fe^{3+} (d^5 system, in case of tartrate capped Fe_2O_3 NPs) due to forbidden d-d transitions, as discussed in chapter 3, inspired us to explore other spin allowed d systems, such as d^6 and d^7, which are Co^{3+} and Co^{2+} respectively, so we got interested in Co_3O_4 system. In this chapter, we have synthesized Co_3O_4 nanocubes (NCs) by solvothermal route following a previous report by Zhang et al., with some modification.[15] Detailed characterization through XRD (X-ray diffraction) and TEM (Transmission electron microscopy) confirms the formation of uniform Co_3O_4 NCs of small size (~8 nm) with narrow size distribution. We have generated intrinsic

multicolor fluorescence covering the whole visible region, ranging from blue, cyan, and green to red by functionalization of Co_3O_4 NCs with Na-tartrate. Systematic investigation through UV-visible absorption, steady state and time-resolved photoluminescence study reveals that ligand-to-metal charge transfer transition from tartrate ligand to the lowest unoccupied energy level of $Co^{2+/3+}$ of the NCs and d−d transitions centered over $Co^{2+/3+}$ ions in the NCs play the important role behind the generation of multiple fluorescence from the ligand functionalized Co_3O_4 NCs. FTIR (Fourier transform infrared spectroscopy) study infers the attachment of ligand to Co_3O_4 NCs surface. Interestingly, we have found that the magnetic behavior of the NCs can be tuned from room temperature antiferromagnetic to ferromagnetic, by surface modification of NCs with the ligands. Then the functionalized Co_3O_4 NCs have been used in catalysis. The functionalized Co_3O_4 NCs show very important catalytic efficiency (in absence of any photo activation) towards degradation of bilirubin (BR, the pigment responsible for yellow coloration of skin in jaundice), along with photocatalytic activity in degradation of methylene blue (MB, a model water pollutant), which opens up its possible applications toward therapeutic as well as waste water treatment. So, by combining manifold beneficial activities within a single entity at the nanoscale, we have developed multifunctional Co_3O_4 NCs having great potential toward diverse applications ranging from bioimaging, drug delivery, and therapeutics, to waste water treatment.[16]

5.2. Experimental Section

5.2.1. Materials Used

Methylene blue (MB), sodium hydroxide (NaOH), 2-amino-purine (2AP), 4', 6-diamidino-2-phenylindole (DAPI), Hoechst 33258, and Rhodamine B (RhB) were obtained from Sigma-Aldrich. Co (II) acetate, and bilirubin (BR) were received from Loba Chemie. Tartaric acid, ethanol, ammonia, and potassium bromide were purchased from Merck. All the reagents were of analytical grade and used without further purification.

5.2.2. Synthesis Procedure and Functionalization of Co₃O₄ NCs

Co_3O_4 NCs were synthesized by solvothermal route following a previous report[15] with some modification. In a typical procedure, 0.70 g of Co $(CH_3COO)_2 \cdot 4H_2O$ was dissolved in 35 ml of ethanol, and 12 ml of 25% ammonia was added under vigorous stirring. The mixture was stirred in air for about 10 min to form homogeneous slurry. Then the suspension was transferred into a 50 ml teflon lined autoclave, sealed and maintained at 150 °C for 3 h. Then, the autoclave was cooled to room temperature naturally. The resulting black solid products were washed with water followed by ethanol via centrifugation redispersion, dried at 60 °C over a hotplate, and collected for characterization. As-prepared Co_3O_4 NCs were cyclomixed with 0.5 M Na-tartrate solution (prepared in Milli-Q water and pH of the solution were made ~ 7) for 12 h at room temperature. The non-functionalized larger Co_3O_4 NCs were filtered out with a syringe filter of 0.22 μm diameter. The as obtained colorless filtrate was tartrate functionalized Co_3O_4 NCs, called T-Co_3O_4 NCs. To induce the multicolor fluorescence property, T-Co_3O_4 NCs were heated at about 70 °C for 15 h under extensive stirring condition maintaining the pH of the solution at ~12 with drop wise addition of NaOH solution. After this high pH and temperature treatment, color of the solution turned to yellow and showed intense fluorescence under UV light (inset of Figure 5.3 (a)). To prepare the solid powdered samples required for magnetic study (Vibrating sample magnetometer, VSM) and fourier transform infrared (FTIR) spectroscopic measurements, we dialyzed T-Co_3O_4 NCs solution (to remove excess ligands) and lyophilized followed by drying over a water bath.

5.2.3. Catalysis

For the study of catalysis, 100 μL T-Co_3O_4 NCs (containing ~1.20 mg NCs) were added in the 7.8 μM aqueous solution of bilirubin (BR) kept in a quartz cuvette in the dark maintaining the pH of the solution ~7, with stirring condition and the absorbance of BR in the reaction mixture was measured time to time by the UV-visible spectrophotometer.

For the study of photocatalysis we used 8 W UV lamp as UV light source from Philips. 5 µM aqueous solution of methylene blue (MB) and 100 µL functionalized Co_3O_4 NCs (containing ~1.20 mg NCs) were homogeneously mixed for 1 h in a quartz cuvette in the dark maintaining the pH of the solution ~3. Then the cuvette was placed ~2 cm apart from the light source and the absorbance of MB in the reaction mixture was measured time to time by the UV-visible spectrophotometer.

5.3. Result and Discussions

TEM study has been carried out to evaluate the morphology and monodispersity of the solvothermally synthesized Co_3O_4 NCs. As shown in Figure 5.1 (a), as-prepared Co_3O_4 NCs have nearly homogeneous size distribution (6-11 nm) with an average size of 8.65 ± 0.22 nm (Figure 5.1 (b)). The corresponding SAED (selected area electron diffraction) pattern in Figure 5.1 (c) and HRTEM (high resolution transmission electron microscopy) image in Figure 5.1 (d) confirms the crystallinity of the NCs. The calculated interplanar distance between the lattice fringes is about 0.243 nm which corresponds to the distance between (311) planes of Co_3O_4 crystal lattice. EDX (Energy dispersive X-ray) spectroscopic analysis of Co_3O_4 NCs (Figure 5.1 (e)) confirms the elemental composition of only cobalt, and oxygen. Figure 5.1 (f) shows the XRD pattern of the as-prepared Co_3O_4 NCs, all the diffraction peaks in the figure perfectly match with the cubic spinel structure (JCPDS 42-1467) of Co_3O_4 NCs as obtained from the literature.[15]

In order to solubilize Co_3O_4 NCs, we have functionalized the NCs with tartrate ligands. Figure 5.2 (a) shows the TEM image of T-Co_3O_4 NCs with an average size of ~7.4 nm (Figure 5.2 (b)). From the SAED pattern (lower inset of Figure 5.2 (a) and HRTEM image (upper inset of Figure 5.2 (a)) of T-Co_3O_4 NCs, highly crystalline nature of the NCs is clearly evident. The calculated interplanar distance between the fringes has been found to be 0.243 nm corresponding to (311) plane of the crystal lattice, which is similar with as prepared Co_3O_4 NCs, also

strongly suggests that functionalization of Co_3O_4 NCs with Na-tartrate ligands does not significantly alter the crystalline phase of as prepared Co_3O_4 NCs.
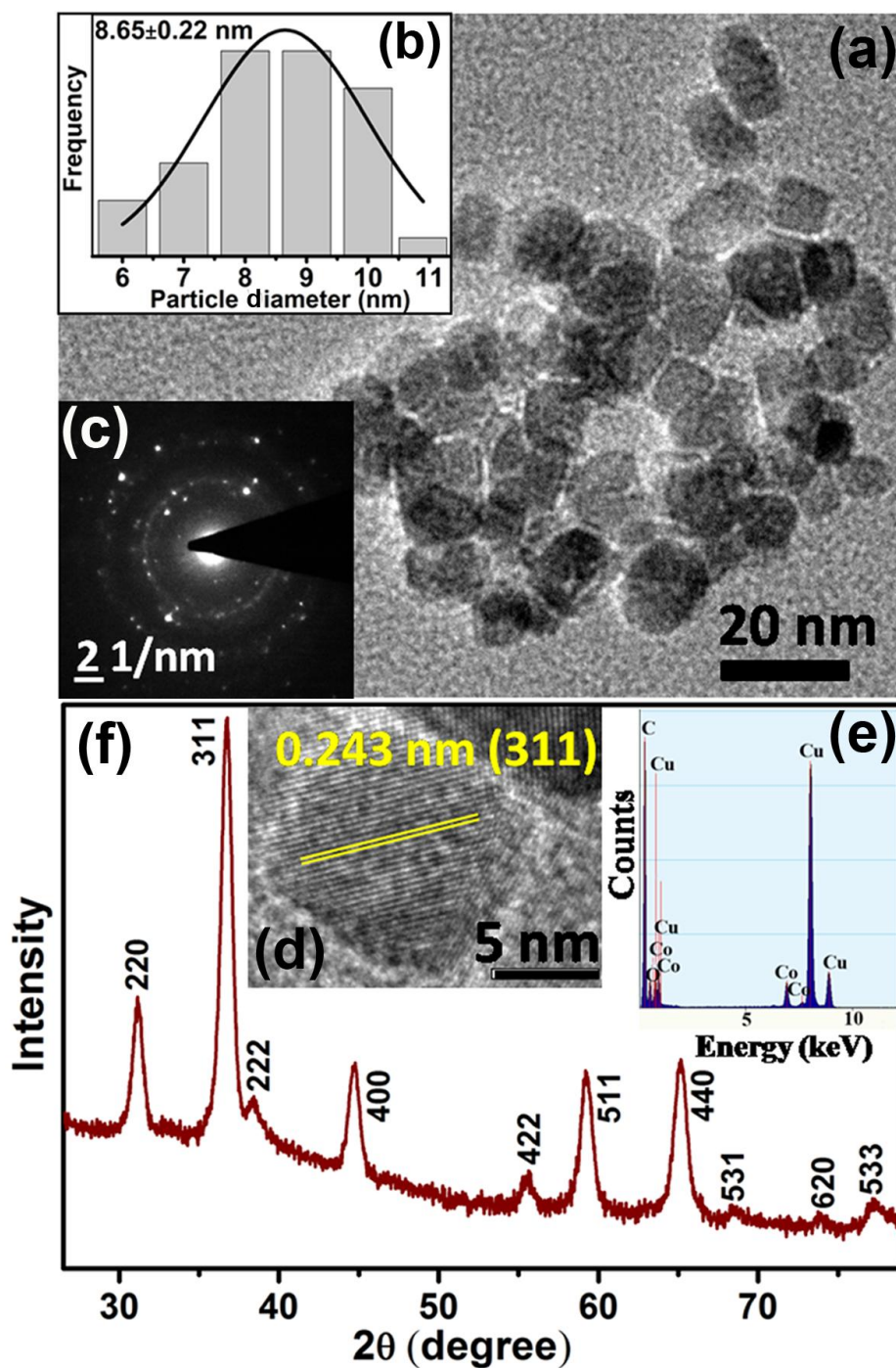
Figure 5.1. (a) TEM image of the as-prepared bare Co_3O_4 NCs. (b) Size distribution of the as-prepared Co_3O_4 NCs. (c) SAED pattern of the as-prepared bare Co_3O_4 NCs (d) Corresponding HRTEM image indicates high crystallinity and shows lattice fringes. (e) EDX spectrum of the NCs indicating the presence of only Co, and O. (f) XRD pattern of as-prepared Co_3O_4 NCs. All diffraction peaks in the figure are perfectly indexed in the literature to the cubic spinel structure of Co_3O_4 NCs.
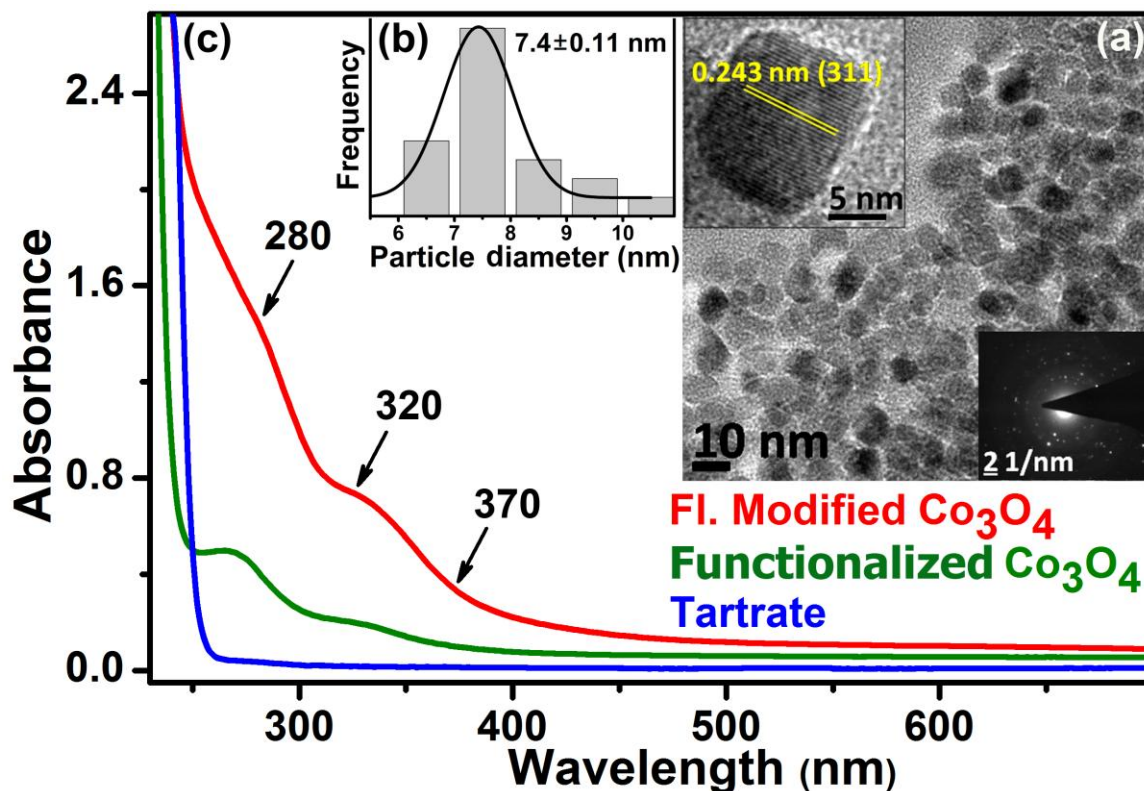
Figure 5.2. (a) TEM image of highly dispersible surface modified Co_3O_4 NCs, in aqueous medium. In the upper inset, lattice fringes in the corresponding HRTEM image, indicating high crystalline nature of the NCs even after functionalization. In the lower inset, SAED pattern of the functionalized Co_3O_4 NCs. (b) Size distribution of Co_3O_4 NCs after solubilization in water. (c) UV-visible absorption spectrum of the functionalized Co_3O_4 NCs before and after heat and pH treatment along with Na-tartrate alone.

As shown in Figure 5.2 (c), the T-Co_3O_4 NCs (at pH ~7) exhibit distinct absorption pattern in the UV-visible region, which indicates significant variation to the surface electronic structure of the NCs upon functionalization with tartrate ligand. The observed peak at around 280 and 320 nm has relatively higher optical density as compared to another peak at 370 nm. Interestingly, upon exciting the sample at both 280 and 322 nm, we observed a photoluminescence peak having maxima at 418 nm. While exciting at 355 nm we obtained a photoluminiscence peak with maxima at 460 nm, although with a low intensity. To increase the photoluminescence intensity, we carried out further surface modification of the solubilized NCs by heating after increasing the pH, which gave rise to generation of two more photoluminescence peaks with multiple fold increase in overall intensity,

upon excitation at proper wavelengths. The reason for enhancement of the photoluminescence intensity as well as generation of multiple optical bands upon surface modification could be due to increased coordination between the ligand functional groups (carboxylate and hydroxyl moieties) and $Co^{2+/3+}$ centers at the NC surface as evident from our detailed FTIR study as discussed in chapter 6.

Figure 5.3 (a) shows normalized steady-state photoluminescence emission spectra obtained from surface modified Co_3O_4 NCs. Upon excitation at wavelengths of 322, 355, 410, and 520 nm, the NCs solution gave rise to intense photoluminescence peaks at 418, 460, 503, and 562 nm, respectively.[16] Photographs of the aqueous solution of surface modified Co_3O_4 NCs under visible and UV light are presented in the inset of Figure 5.3 (a). The amazing fluorescence micrographs, as shown in Figure 5.3 (c), demonstrate that the black powder of functionalized Co_3O_4 NCs under bright field, generates fluorescent colors like cyan, green, and red upon excitation at 365, 436, and 546 nm, respectively, by using proper filters. Figure 5.4 shows that the fluorescence micrographs of as-prepared bare Co_3O_4 NCs under identical conditions have no such fluorescence. Fluorescence quantum yields (QYs) of the functionalized Co_3O_4 NCs, have been calculated by following the relative method of Williams et al.,[17] involving the use of well characterized standard fluorescent compounds with known QY values. Fluorescence QYs of 12% (for 418 nm band), 1.3% (for 460 nm band), 5.38% (for 503 nm band) and 0.23% (for 562 nm band) were obtained relative to the standard fluorescent compounds such as 2-aminopurine (2AP), 4′, 6-diamidino-2-phenylindole (DAPI), Hoechst 33258, and Rhodamine B (RhB), respectively.
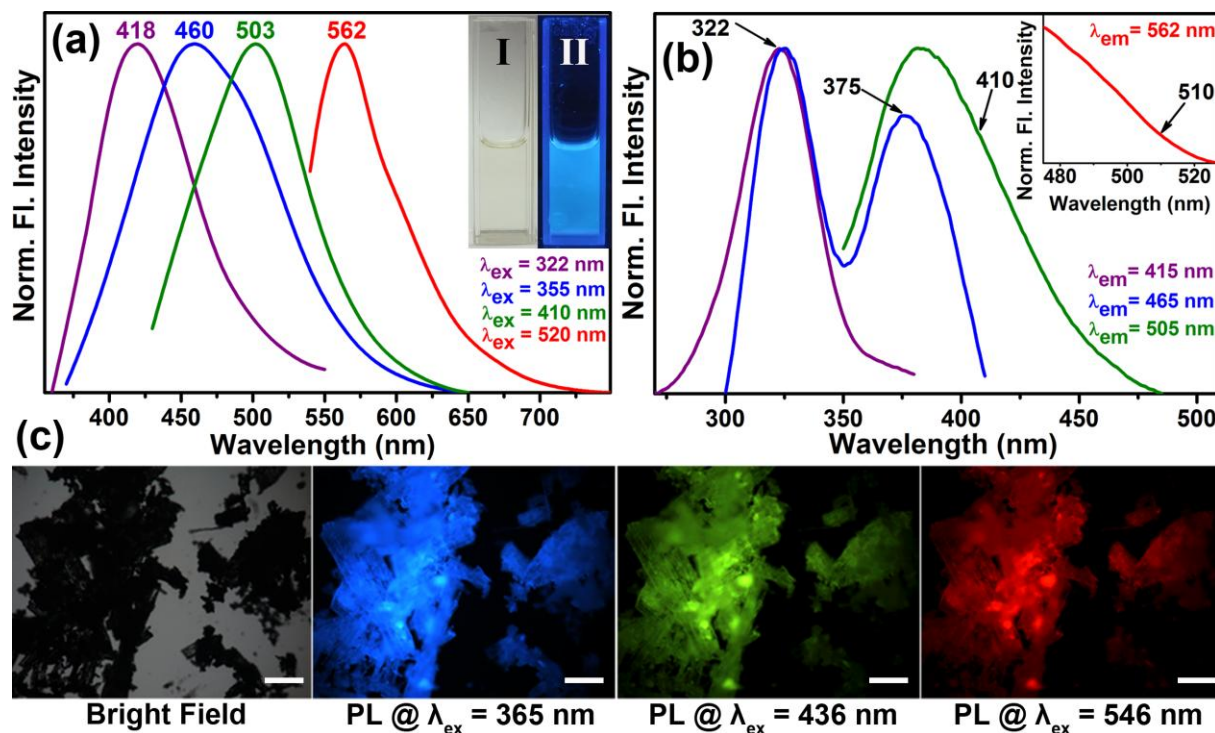
Figure 5.3. (a) Normalized steady-state fluorescence emission spectra collected from surface modified Co_3O_4 NCs with four different excitation wavelengths of 322, 355, 410, and 520 nm. Image I and II in the inset show the photograph of aqueous surface modified Co_3O_4 NCs solution under visible and UV light respectively. (b) Fluorescence excitation spectra of surface modified Co_3O_4 NCs at different emission maximum of 415, 465, 505, and 562 nm. (c) Fluorescence micrographs of surface modified Co_3O_4 NCs powder under bright field, UV (365 nm), blue (436 nm) and green (546 nm) light irradiation. The scale bars in all the images are 500 µm.
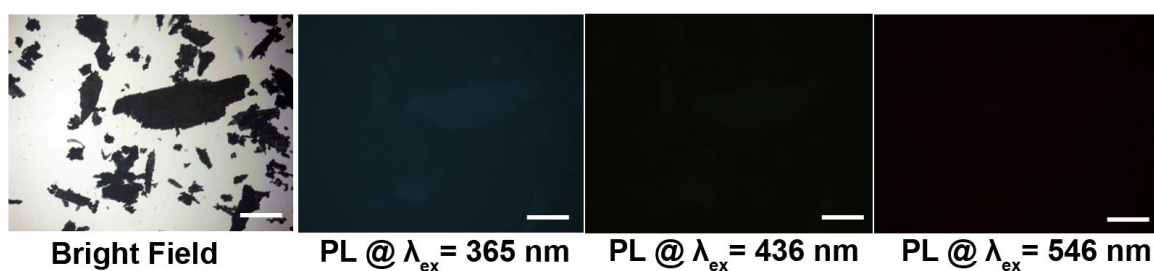
Figure 5.4. Fluorescence micrographs of bare Co_3O_4 NCs, under bright field, UV, blue, and green light. The scale bars in all the images are 500 µm.

Thus, the emergence of multicolor fluorescence in Co_3O_4 NCs was induced by tartrate ligand functionalization, which can be explained by ligand field theory. The

observed absorption peaks at around 285 and 320 nm, for functionalized Co_3O_4 NCs, which gives rise to photoluminescence at 418 nm can be attributed to the LMCT (ligand to metal charge-transfer) involving HOMO (Highest occupied molecular orbital) of tartrate ligand and LUMO (lowest unoccupied molecular orbital) centered over metal ion $Co^{2+/3+}$ on the NCs' surface.[18, 19] Additional three photoluminescence peaks having maxima at 460, 503, and 562 nm, against excitation at 355, 410, and 520 nm, can arise due to the possible d-d transitions involving $Co^{2+/3+}$ ions in the T-Co_3O_4 NCs surface (presence of both Co^{2+} and Co^{3+} before and after functionalization of Co_3O_4 NCs is confirmed by XPS, X-ray photoelectron spectroscopy, study as shown in Figure 5.5. In order to investigate the surface state of the NCs before and after functionalization with tartrate ligands, we have carried out XPS analysis on Co_3O_4 NCs. In the high-resolution spectra of Co 2p of Co_3O_4 before functionalization (Figure 5.5 (a)), the $2p_{3/2}$–$2p_{1/2}$ doublet has been observed to be at 780.2 and 795.2 eV, respectively, with a spin-orbit splitting (difference between the binding energy values of the Co $2p_{3/2}$ and Co $2p_{1/2}$ levels) value of 15 eV, and the shake-up satellites (marked by *) with a low intensity at ca. 8.8 eV from the main spin-orbit components exactly match with those of pure Co_3O_4.[20] The O 1s peaks (Figure 5.5 (b)) at 530.1 and 531.6 eV are also in good agreement with literature report for pure Co_3O_4.[20] Similarly, in case of tartrate functionalized Co_3O_4 NCs also (Figure 5.5 (c)), the $2p_{3/2}$–$2p_{1/2}$ doublet for Co 2p has been observed to be at 780.50 and 796.41 eV, respectively. The thick layer of tartrate ligand surrounding the NCs, might be the reason for low signal of the functionalized NCs. The presence of thick tartrate layer is also further evident from the O 1s spectrum of functionalized NCs (Figure 5.5 (d)). As shown in the figure, along with two characteristic signatures of Co_3O_4 at 530.1 and 531.6 eV, a new high intensity peak at 533 eV have appeared, which is typically observed for carboxylate oxygen.[21] So, from XPS study we can infer that there is minimum change in the surface states of the NCs upon functionalization. We can explain the generation of the three excitation bands (375, 410, and 510 nm) as shown in excitation spectra Figure 5.3 (b), in terms of spectroscopic term symbols, due to transitions of $^4T_{1g}$ (F) $\rightarrow$ $^4A_{2g}$ (F), $^4T_{1g}$ (F) $\rightarrow$ $^4T_{1g}$ (P), and $^4T_{1g}$ (F) $\rightarrow$ $^4T_{2g}$ (F), respectively, where these energy levels are obtained from Tanabe-Sugano diagram

of Co^{2+}.[18] Additional contribution for the emission peaks having maxima at 460 and 503 nm may also come from the d-d transitions ($^1A_{1g} \rightarrow {}^1T_{2g}$ and $^1A_{1g} \rightarrow {}^1T_{1g}$, respectively) involving the energy levels of Co^{3+} as obtained from Tanabe-Sugano diagram.[18] Among the d-d transitions except the peak at around 370 nm, other excitation bands at around 410 and 520 nm were not observed in the absorption spectrum (Figure 5.2 (c)), presumably due to masking by the more intense LMCT bands.
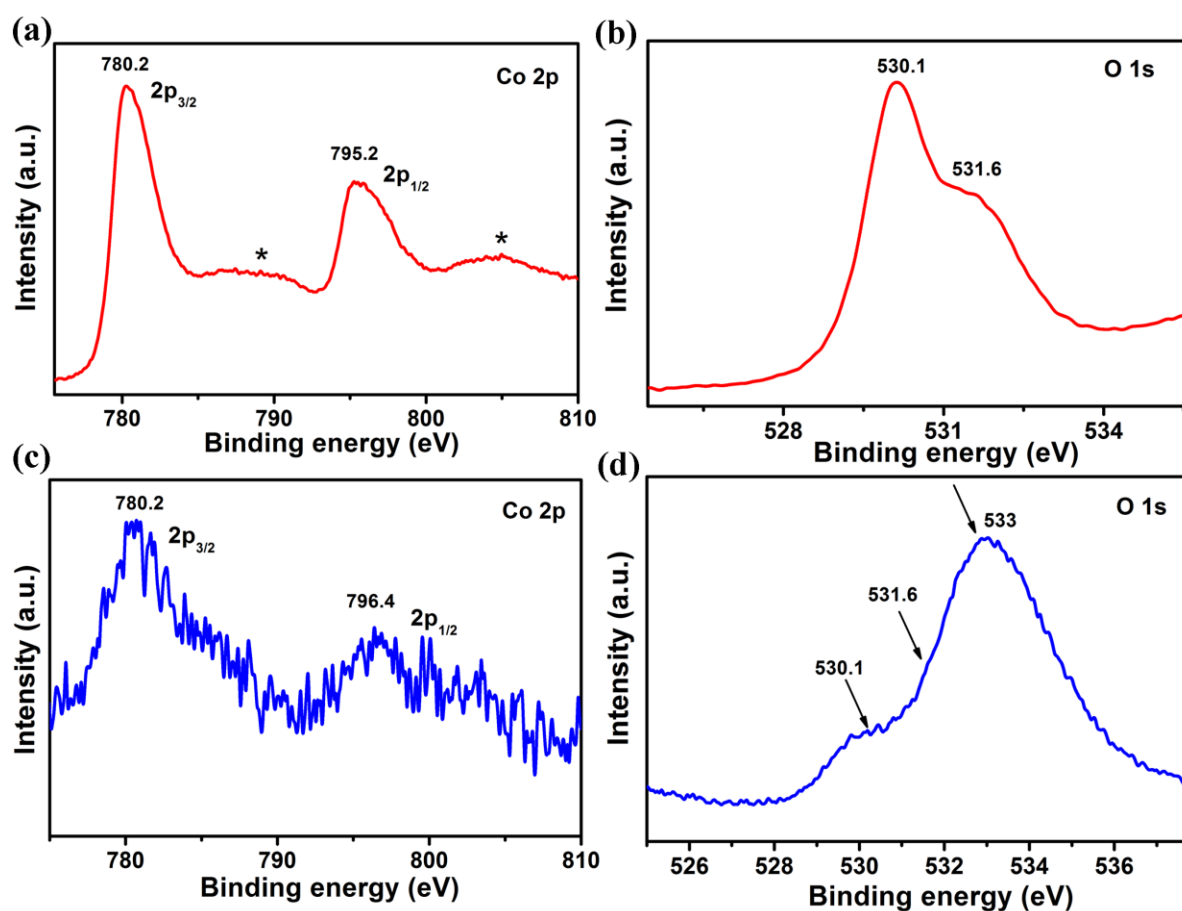
Figure 5.5. High resolution XPS spectrum of bare Co_3O_4 NCs showing (a) Co $2p_{3/2}$ and $2p_{1/2}$ core-level signals with binding energy at 780.2, and 795.2 eV, respectively, along with low intensity shakeup satellites at ~8.8 eV from the main spin-orbit components, and (b) oxygen species (O1s) with binding energy at 530.1, and 531.6 eV. High resolution XPS spectrum of functionalized Co_3O_4 NCs showing (c) Co 2p core-level signals with binding energy at 780.2 and 796.4 eV for $2p_{3/2}$–$2p_{1/2}$ doublet, and (d) oxygen species (O1s) with binding energy at 530.1, 531.6 and 533 eV.

Table 5.1. Lifetime values of picosecond time-resolved photoluminescence transients of T-Co_3O_4 NCs, detected at photoluminescence maxima of 410 and 460 nm upon excitation at 294 and 377 nm wavelengths, respectively. The relative weight percentages of the corresponding time components are mentioned in parentheses.

System	Excitation wavelength, λ_{ex} (nm)	Fluorescence peak, λ_{em} (nm)	τ_1 (ns)	τ_2 (ns)	τ_3 (ns)	τ_{av} (ns)
Fl. modified T-Co_3O_4 NCs	294	410	3.27 (29.1)	8.55 (18.4)	0.55 (52.5)	2.81
	377	460	1.73 (19.04)	6.9 (3.76)	0.26 (77.2)	0.79

To have further reliable evidence for our proposed mechanism for the appearance of multiple photoluminescence, we have performed picosecond-resolved fluorescence decay transient measurements of functionalized Co_3O_4 NCs employing TCSPC (Time-correlated single-photon counting) technique. Figure 5.6 (a) represents the time resolved fluorescence decay transients of functionalized Co_3O_4 NCs at two different fluorescence maxima of 410 and 460 nm using two different pulsed diode laser excitation sources of 294 and 377 nm wavelengths, respectively. As evident from the figure, significantly larger average excited-state lifetime (τ_{av}) of the functionalized Co_3O_4 NCs observed for 410 nm fluorescence band (2.81 ns) compared to that for 460 nm fluorescence band (0.79 ns), strongly suggests mechanistic difference in the origin of these two fluorescence peaks. The lifetime components and their corresponding weight percentages are mentioned in Table 5.1. With this photoluminescence lifetime study, proposition with regard to the origin of this multiple fluorescence made from steady state experiments are verified, and we rationally conclude that LMCT excited state is responsible for 410 nm photoluminescence, while 460 nm photoluminescence is attributed to d-d transition.

Moreover, we can safely state that other two lower energy photoluminescence at 503 and 562 nm would also correspond to other plausible d-d transitions.
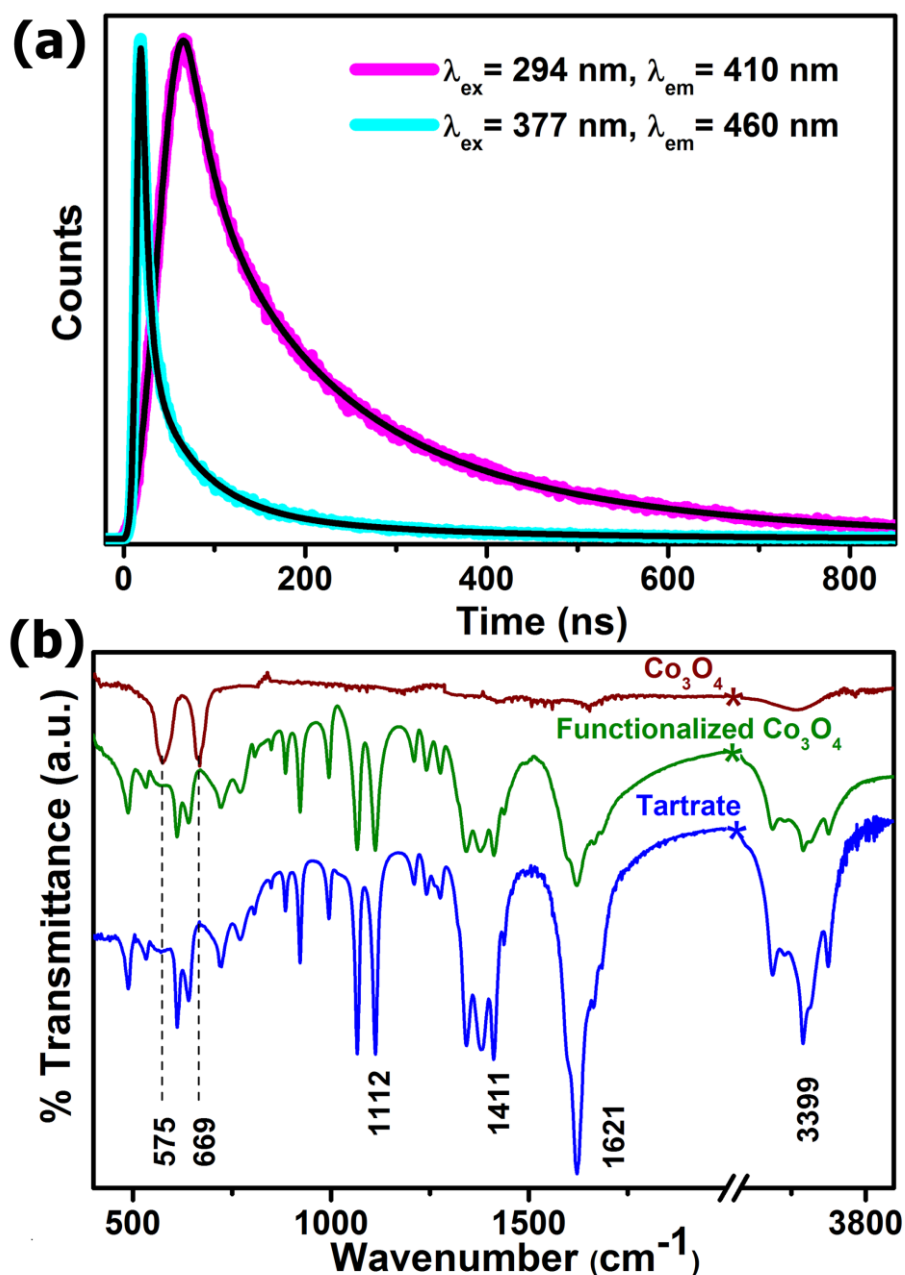
Figure 5.6. (a) Picosecond-resolved fluorescence transients of T-Co_3O_4 NCs studied at emission wavelengths of 410 and 460 nm upon excitation with laser sources of 294 and 377 nm wavelengths, respectively. (b) FTIR spectra of as-prepared Co_3O_4 NCs and T-Co_3O_4 NCs along with Na-tartrate alone.

In order to affirm the attachment of tartrate ligands to the NCs' surface, comparative FTIR spectroscopic study was carried out on bare and T-Co_3O_4 NCs along with Na-tartrate alone (Figure 5.6 (b)). Co_3O_4 NCs show two strong bands at 575 cm^{-1} (stretching vibration of $(Co^{3+})-O-(Co^{3+})_3$) and 669 cm^{-1} (stretching vibration of $(Co^{2+})-(Co^{3+})-O_3$),[22] which are disappeared after functionalization. In case of tartrate, two sharp peaks arising at 1066 and 1112 cm^{-1} are due to the C–OH stretching modes,[23] and peaks at 1412 and 1622 cm^{-1} are associated with symmetric and asymmetric stretching modes of the carboxylate groups (-COO$^-$) of tartrate, respectively.[24] Upon interaction with the NC surface i.e. in case of T-Co_3O_4 NCs, all these different bands of tartrate are perturbed notably, accompanied with the band at 3400 cm^{-1} corresponding to the stretching vibrational modes of hydroxyl group (-O−H),[23] clearly proves the involvement of both –COO$^-$ and –OH groups in the functionalization process.
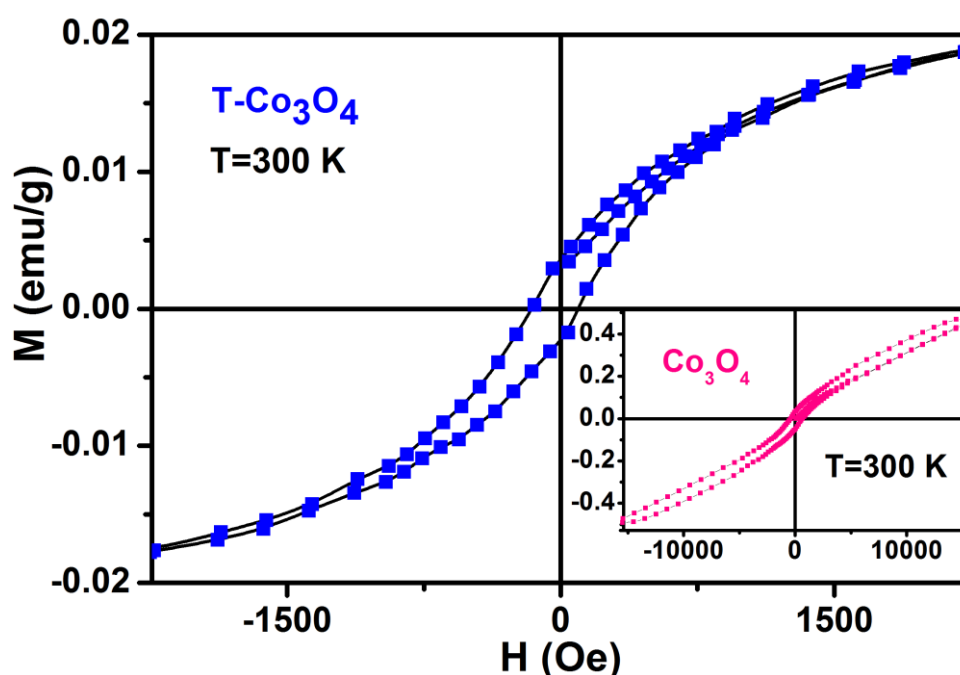
Figure 5.7. Plot of magnetization versus applied magnetic field (M-H) for T-Co_3O_4 NCs at 300 K. Inset shows M-H plot for as-prepared Co_3O_4 NCs at 300 K.

Figure 5.7 shows the magnetic study of both as-prepared and T-Co_3O_4 NCs at room temperature. Inset shows the plot of magnetization versus the applied

magnetic field for as-prepared Co_3O_4 NCs, which is approximately linear with a fine hysteresis loop having coercivity of 532 Oe and remanent magnetization of 0.04 emu/g, however, the maximum field applied (15 kOe) cannot saturate the magnetization, and the magnetization goes up to 0.47 emu/g. So, it is evident that as-prepared Co_3O_4 NCs show antiferromagnetic behavior with very weak ferromagnetic nature. In spite of antiferromagnetic behavior arising due to super exchange among each Co^{2+} ion in the tetrahedral-site and its four neighboring Co^{2+} ions of opposite spins in case of bulk Co_3O_4,[25] very weak ferromagnetic behavior of as prepared NCs can be attributed to the finite size effects leading to uncompensated surface spins.[26] Moreover, the ferromagnetic nature becomes more prominent after functionalization with Na-tartrate, which can be ascribed to the ligand mediated strong pining of the uncompensated spins of surface Co^{2+} ions. But the coercivity decreases significantly to 130 Oe along with the decrease in saturation magnetization to 0.03 emu/g. This phenomenon can be explained by ligand field theory. Tartrate ligand containing both the σ-donor (-OH) and π-donor (-COO⁻) functional groups,[27] favors the quenching of magnetic moments of Co^{2+} ions on the surface of T-Co_3O_4 NCs, leading to decrease in the saturation magnetization.[28] Again, quenching of the magnetic moments reduces its spin-orbit coupling, resulting in diminution of magnetocrystalline anisotropy, which causes reduction of coercivity[29] in the case of functionalized Co_3O_4 NCs as compared to the as-prepared NCs.

Considering the recent significant progress of nanocatalysis through rational engineering and manipulation of various materials at the nanoscale to accelerate the rate of different beneficial reactions having direct biological and environmental significance, we intended to utilize the functionalized Co_3O_4 NCs in degradation of biologically relevant organic dye, bilirubin (BR), the pigment responsible for yellow coloration of skin in jaundice. Figure 5.8 (a) shows the degradation of BR with time, in presence of T-Co_3O_4 NCs at pH ~ 7, which has been found to follow the first order rate equation with kinetic rate constant (k) 2.2 x 10^{-2} min^{-1}. We have also verified the reusability of the catalyst, in degradation of BR, by adding same amount (which was added 1st time to the reaction mixture, i.e. 7.8 µM) of BR to the reaction mixture at every 100 min up to 5 doses, keeping the catalyst concentration fixed (added only

once at the 1st cycle), and measured the BR decomposition rate of different cycles by monitoring the decrease of BR absorbance at 440 nm using UV-visible spectroscopy. As shown in Figure 5.8 (b), the plot of relative concentration of BR versus time, up to 5 consecutive cycles, confirms the reusability of the T-Co$_3$O$_4$ NCs catalyst with almost unchanged efficiency.
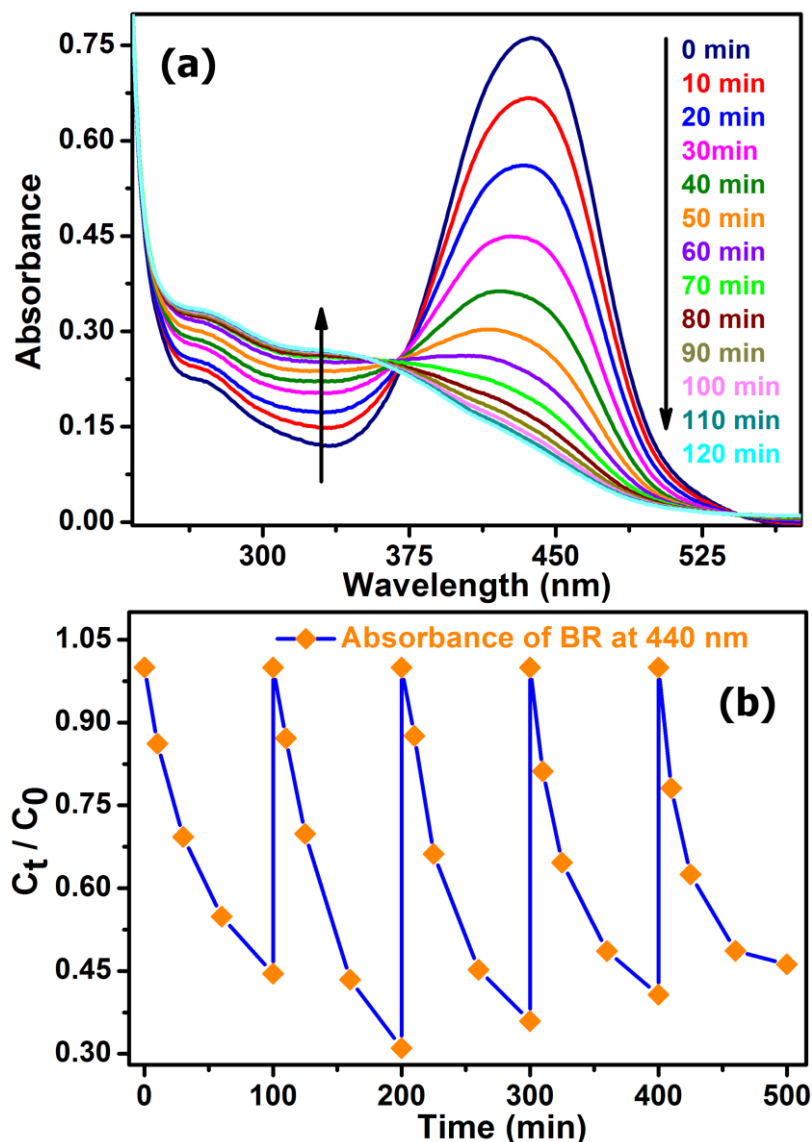
Figure 5.8. (a) UV-visible spectral changes of aqueous solution of bilirubin (BR) in presence of T-Co$_3$O$_4$ NCs (at pH~7) with time. (b) The plot of relative concentration of BR monitored at 440 nm versus time for consecutive 5 cycles, showing reusability of functionalized Co$_3$O$_4$ NCs in BR degradation.

Notably, as shown in Figure 5.8 (a), an isosbestic point was obtained at ~370 nm due to increase in absorbance at 319 nm with simultaneous decrease in absorbance at 440 nm with time. According to reported literature on BR, the peak at 319 nm arises due to the absorption of methylvinylmaleimide (MVM), a photo-oxidation product of BR in aqueous medium.[30] Detailed mechanistic investigation of functionalized NP assisted BR degradation has been discussed in chapter 6.
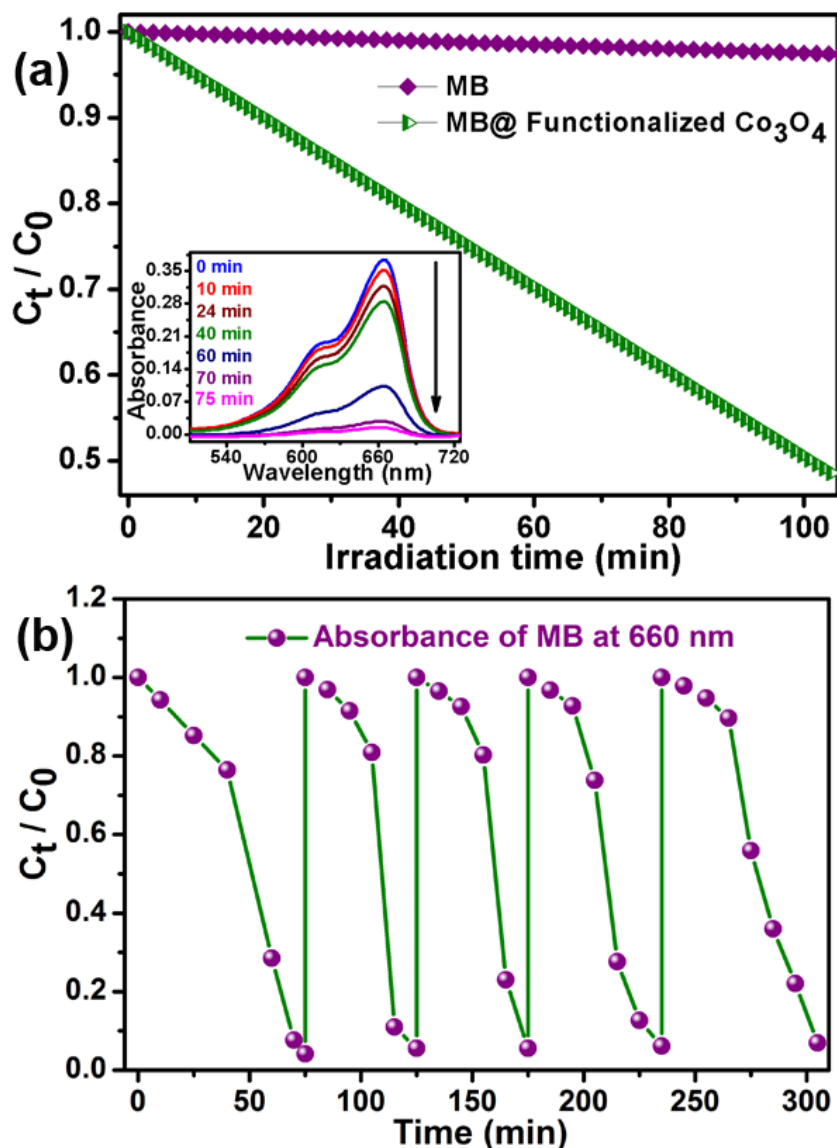
Figure 5.9. (a) UV-visible spectral changes of aqueous solution of methylene blue (MB) in presence of functionalized Co_3O_4 NCs with time, under UV irradiation. (b) The plot of relative concentration of MB monitored at 660 nm versus time for consecutive 5 cycles, showing reusability of functionalized Co_3O_4 NCs in MB degradation under UV light.

Furthermore, being inspired by the significant efficiency of T-Co$_3$O$_4$ NCs in degradation of biologically harmful pigment, we attempted to utilize the strong excitation of the T-Co$_3$O$_4$ NCs in the UV region, in photocatalysis for waste-water treatment. T-Co$_3$O$_4$ NCs showed excellent photocatalytic property (as shown in Figure 5.9 (a)) towards the degradation of methylene blue (MB), a model water-contaminant and commonly used dye in textile industries, upon UV light irradiation. We have found that, the T-Co$_3$O$_4$ NCs catalyzed photodegradation of MB takes place exponentially with time, following first-order rate equation with a kinetic rate constant (k) of 2.23×10^{-2} min^{-1}. To check the reusability of the catalyst, we added same dose of MB (5 μM) into the reaction mixture up to 5 dose, keeping the catalyst concentration fixed (without addition of extra catalyst after the 1st cycle). MB decomposition rates of different cycles were monitored by measuring the decrease of MB absorbance at 660 nm with UV-visible spectroscopy. Figure 5.9 (b) demonstrates the plots of relative concentration of MB versus time, up to 5 consecutive cycles, indicating the reusability of T-Co$_3$O$_4$ NCs catalyst with a consistent degradation rate. Having evidence from several other photochemical reactions and tartrate capped MnFe$_2$O$_4$ NPs assisted MB degradation as discussed in chapter 4, we propose that the photodegradation process may follow reactive oxygen species (ROS) mediated radical pathway.

5.4. Conclusions

In summary, we have demonstrated an easy fabrication procedure of multifunctional Co_3O_4 NCs. By facile functionalization of as-prepared NCs with Na-tartrate ligand, we have been able to develop intrinsic multicolor fluorescence covering almost whole visible region. Systematic investigation through UV-visible absorption, steady state, and time-resolved photoluminescence study reveals that ligand-to-metal charge transfer transition from tartrate ligand to lowest unoccupied energy level of $Co^{2+/3+}$ of the NCs and d−d transitions centered over $Co^{2+/3+}$ ions in the NCs play the important role behind the generation of multiple fluorescence from the ligand functionalized Co_3O_4 NCs. Magnetic study exhibits that, antiferromagnetic nature of Co_3O_4 NCs turns to ferromagnetic after surface modification. The newly developed magnetofluorescent Co_3O_4 NCs can open up new horizon in the field of bio-imaging and drug delivery. The functionalized Co_3O_4 NCs also show good catalytic efficiency for degradation of BR, a biologically harmful pigment, which reveals their budding therapeutic application in severe hyperbilirubinemia. Moreover, their good photocatalytic efficiency in degradation of MB, a model water contaminant, may give rise to their potential application in waste water treatment.

Bibliography

1.   Mu, J.; Wang, Y.; Zhao, M.; Zhang, L., Intrinsic Peroxidase-like Activity and Catalase-like Activity of Co_3O_4 Nanoparticles. *Chem. Commun.* **2012,** *48* (19), 2540-2542.

2.   Kwak, G.; Hwang, J.; Cheon, J.-Y.; Woo, M. H.; Jun, K.-W.; Lee, J.; Ha, K.-S., Preparation Method of Co_3O_4 Nanoparticles Using Ordered Mesoporous Carbons as a Template and Their Application for Fischer–Tropsch Synthesis. *J. Phys. Chem. C* **2013,** *117* (4), 1773-1779.

3.   Wen, Z.; Zhu, L.; Mei, W.; Li, Y.; Hu, L.; Sun, L.; Wan, W.; Ye, Z., A Facile Fluorine-Mediated Hydrothermal Route to Controlled Synthesis of Rhombus-Shaped Co_3O_4 Nanorod Arrays and their Application in Gas Sensing. *J. Mater. Chem. A*   **2013,** *1* (25), 7511-7518.

4.   Hu, L.; Yan, N.; Chen, Q.; Zhang, P.; Zhong, H.; Zheng, X.; Li, Y.; Hu, X., Fabrication Based on the Kirkendall Effect of Co_3O_4 Porous Nanocages with Extraordinarily High Capacity for Lithium Storage. *Chem. Eur. J.* **2012,** *18* (29), 8971-8977.

5.   Kim, Y.; Lee, J.-H.; Cho, S.; Kwon, Y.; In, I.; Lee, J.; You, N.-H.; Reichmanis, E.; Ko, H.; Lee, K.-T.; Kwon, H.-K.; Ko, D.-H.; Yang, H.; Park, B., Additive-Free Hollow-Structured Co_3O_4 Nanoparticle Li-Ion Battery: The Origins of Irreversible Capacity Loss. *ACS Nano* **2014,** *8* (7), 6701-6712.

6.   Shim, H.-W.; Lim, A.-H.; Kim, J.-C.; Jang, E.; Seo, S.-D.; Lee, G.-H.; Kim, T. D.; Kim, D.-W., Scalable One-pot Bacteria-templating Synthesis Route toward Hierarchical, Porous-Co_3O_4 Superstructures for Supercapacitor Electrodes. *Sci. Rep.* **2013,** *3*.

7.   Xiong, S.; Yuan, C.; Zhang, X.; Xi, B.; Qian, Y., Controllable Synthesis of Mesoporous Co_3O_4 Nanostructures with Tunable Morphology for Application in Supercapacitors. *Chem. Eur. J.* **2009,** *15* (21), 5320-5326.

8.   Xiao, Y.; Liu, S.; Li, F.; Zhang, A.; Zhao, J.; Fang, S.; Jia, D., Hierarchical Nanoarchitectures: 3D Hierarchical Co_3O_4 Twin-Spheres with an Urchin-Like

Structure: Large-Scale Synthesis, Multistep-Splitting Growth, and Electrochemical Pseudocapacitors *Adv. Funct. Mater.* **2012,** *22* (19), 4051-4051.

9.   Wang, G.; Shen, X.; Horvat, J.; Wang, B.; Liu, H.; Wexler, D.; Yao, J., Hydrothermal Synthesis and Optical, Magnetic, and Supercapacitance Properties of Nanoporous Cobalt Oxide Nanorods. *J. Phys. Chem. C* **2009,** *113* (11), 4357-4361.

10.   Pang, H.; Gao, F.; Chen, Q.; Liu, R.; Lu, Q., Dendrite-like Co_3O_4 Nanostructure and its Applications in Sensors, Supercapacitors and Catalysis. *Dalton Trans.* **2012,** *41* (19), 5862-5868.

11.   Mu, J.; Zhang, L.; Zhao, M.; Wang, Y., Catalase Mimic Property of Co_3O_4 Nanomaterials with Different Morphology and Its Application as a Calcium Sensor. *ACS Appl. Mater. Interfaces* **2014,** *6* (10), 7090-7098.

12.   Kou, J.; Bennett-Stamper, C.; Varma, R. S., Hierarchically Triangular Prism Structured Co_3O_4: Self-Supported Fabrication and Photocatalytic Property. *Nanoscale* **2011,** *3* (12), 4958-4961.

13.   Papis, E.; Rossi, F.; Raspanti, M.; Dalle-Donne, I.; Colombo, G.; Milzani, A.; Bernardini, G.; Gornati, R., Engineered Cobalt Oxide Nanoparticles Readily Enter Cells. *Toxicol. Lett.* **2009,** *189* (3), 253-259.

14.   Zhao, J.; Huang, Z.; Zeng, J.; Deng, M.; Yin, G.; Liao, X.; Gu, J., Histidine-Assisted Synthesis and Cellular Compatibility of Magnetic Cobalt Oxide Nanoparticles at Room Temperature. *J. Inorg. Organomet. Polym. Mater.* **2012,** *22* (2), 492-499.

15.   Dong, Y.; He, K.; Yin, L.; Zhang, A., A Facile Route to Controlled Synthesis of Co_3O_4 Nanoparticles and their Environmental Catalytic Properties. *Nanotechnology* **2007,** *18* (43), 435602.

16.   Pal, M.; Singh, A. K.; Rakshit, R.; Mandal, K., Surface Chemistry Modulated Introduction of Multifunctionality within Co_3O_4 Nanocubes. *RSC Adv.* **2015,** *5* (21), 16311-16318.

17.   Williams, A. T. R.; Winfield, S. A.; Miller, J. N., Relative Fluorescence Quantum Yields Using A Computer-Controlled Luminescence Spectrometer. *Analyst* **1983,** *108* (1290), 1067-1071.

18.   Huheey, J. E.; Keiter, E. A.; Keiter, R. L.; Medhi, O. K., *Inorganic Chemistry: Principles of Structure and Reactivity*. Pearson Education: 2006.

19.   Giri, A.; Goswami, N.; Bootharaju, M. S.; Xavier, P. L.; John, R.; Thanh, N. T. K.; Pradeep, T.; Ghosh, B.; Raychaudhuri, A. K.; Pal, S. K., Emergence of Multicolor Photoluminescence in $La_{0.67}Sr_{0.33}MnO_3$ Nanoparticles. *J. Phys. Chem. C* **2012,** *116* (48), 25623-25629.

20.   Barreca, D.; Gasparotto, A.; Lebedev, O. I.; Maccato, C.; Pozza, A.; Tondello, E.; Turner, S.; Van Tendeloo, G., Controlled Vapor-phase Synthesis of Cobalt Oxide Nanomaterials with Tuned Composition and Spatial Organization. *CrystEngComm* **2010,** *12* (7), 2185-2197.

21.   Bootharaju, M. S.; Pradeep, T., Uptake of Toxic Metal Ions from Water by Naked and Monolayer Protected Silver Nanoparticles: An X-ray Photoelectron Spectroscopic Investigation. *J. Phys. Chem. C* **2010,** *114* (18), 8328-8336.

22.   Agiral, A.; Soo, H. S.; Frei, H., Visible Light Induced Hole Transport from Sensitizer to Co_3O_4 Water Oxidation Catalyst across Nanoscale Silica Barrier with Embedded Molecular Wires. *Chem. Mater.* **2013,** *25* (11), 2264-2273.

23.   Kaneko, N.; Kaneko, M.; Takahashi, H., Infrared and Raman Spectra and Vibrational Assignment of Some Metal Tartrates. *Spectrochim. Acta, Part A* **1984,** *40* (1), 33-42.

24.   Ramakrishnan, V.; Maroor, J. M. T., IR and Raman Studies of Gel Grown Manganese Tartrate. *Infrared Phys.* **1988,** *28* (4), 201-204.

25.   Dutta, P.; Seehra, M. S.; Thota, S.; Kumar, J., A Comparative Study of the Magnetic Properties of Bulk and Nanocrystalline Co_3O_4. *J. Phys. Condens. Matter* **2008,** *20* (1), 015218.

26.   Ozkaya, T.; Baykal, A.; Toprak, M. S.; Koseoğlu, Y.; Durmuş, Z., Reflux Synthesis of Co_3O_4 Nanoparticles and its Magnetic Characterization. *J. Magn. Magn. Mater.* **2009,** *321* (14), 2145-2149.

27.   Pal, M.; Rakshit, R.; Mandal, K., Facile Functionalization of Fe_2O_3 Nanoparticles to Induce Inherent Photoluminescence and Excellent Photocatalytic Activity. *Appl. Phys. Lett.* **2014,** *104* (23), -.

28.   Rakshit, R.; Mandal, M.; Pal, M.; Mandal, K., Tuning of Magnetic Properties of $CoFe_2O_4$ Nanoparticles through Charge Transfer Effect. *Appl. Phys. Lett.* **2014,** *104* (9), -.

29.   Vestal, C. R.; Zhang, Z. J., Effects of Surface Coordination Chemistry on the Magnetic Properties of $MnFe_2O_4$ Spinel Ferrite Nanoparticles. *J. Am. Chem. Soc.* **2003,** *125* (32), 9828-9833.

30.   Kurtin, W. E., Spectroscopy And Photochemistry Of Birubin Photoproducts. I. Methylvinylmaleimide*. *Photochem. Photobiol.* **1978,** *27* (5), 503-509.

Chapter 6 | Surface Modification of CoFe₂O₄ Nanoparticles

This chapter demonstrates improvement of fluorescence, magnetic, and catalytic property upon surface modification of CoFe₂O₄ nanoparticles due to incorporation of Fe within the Co based oxide system.

6. Ligand Induced Evolution of Intrinsic Fluorescence and Catalytic Activity from CoFe₂O₄ Nanoparticles

6.1. Preamble

Among different ferrites, $CoFe_2O_4$ has attracted enormous attention due to their high coercivity, saturation magnetization, physical, and chemical stability, leading to their various applications ranging from high density magnetic data storage, sensing, lithium-oxygen batteries, oxygen evolution, catalysis, and biomedical diagnosis to therapy.[1-13] But, the development of intrinsic fluorescence upon tailoring the surface chemistry of $CoFe_2O_4$ NPs is sparse in existing literature.

The excellent efficiency of $Co^{2+/3+}$ in development of intrinsic multicolor fluorescence covering the whole visible region influenced us to incorporate Fe within the Co oxide system to improve magnetic property and we focused on $CoFe_2O_4$ NPs. In this chapter, we have synthesized $CoFe_2O_4$ NPs by wet chemical route following a previous report by Sun et al., with some modification.[14] Interestingly, we have developed intrinsic multicolor fluorescence of $CoFe_2O_4$ NPs, covering the whole visible region, ranging from blue, cyan, and green to red by facile functionalization and subsequent further surface modification of the NPs with Na-tartrate. Systematic investigation through UV-visible absorption, followed by steady state and time-resolved fluorescence study reveals that ligand-to-metal charge transfer transition from the highest occupied energy level of tartrate ligand to the lowest unoccupied energy level of $Co^{2+/3+}$ or Fe^{3+} and d-d transitions centered over $Co^{2+/3+}$ ions on the NPs' surface play the crucial role behind the development of multicolor fluorescence from the ligand functionalized $CoFe_2O_4$ NPs (called as T-CoFe₂O₄ NPs). FTIR (Fourier transform infrared spectroscopy) study speculates the attachment of ligand to $CoFe_2O_4$ NPs' surface. Magnetic study reveals that the superparamagnetic nature remains unchanged after surface modification of NPs with the ligands. Moreover, T-CoFe₂O₄ NPs show excellent catalytic efficiency (in absence of any photo activation) towards degradation of bilirubin (BR, the pigment whose elevated level indicates jaundice), and in photodegradation of methylene blue (MB, a model water

contaminant), which widens its plausible applications toward therapeutic as well as waste water treatment. So, by incorporating superparamagnetism, intrinsic fluorescence and catalytic properties within T-CoFe$_2$O$_4$ NPs simultaneously, we have developed multifunctional T-CoFe$_2$O$_4$ NPs that may find pioneering diverse applications ranging from diagnostics, therapeutics, to environmental remediation.[15]

6.2. Experimental Section

6.2.1. Material Used

Sodium hydroxide (NaOH), Fe (III) acetylacetonate, oleylamine, methylene blue (MB), 2-amino-purine (2AP), 4′, 6-diamidino-2-phenylindole (DAPI), Hoechst 33258, and Rhodamine B (RhB) were obtained from Sigma-Aldrich. Co (II) acetate, cetyl alcohol, diphenyl ether, oleic acid, and bilirubin (BR) were received from Loba Chemie. Tartaric acid, ethanol, and potassium bromide were purchased from Merck. All the reagents were of analytical grade and used without further purification.

6.2.2. Synthesis Procedure and Functionalization of CoFe$_2$O$_4$ NPs

CoFe$_2$O$_4$ NPs were prepared by template free wet chemical process following a previous report with some modification,[14] which involves the high-temperature (270 ^{o}C) reflux of Co(ac)$_2$ and Fe(acac)$_3$ in di-phenyl ether in the presence of cetyl alcohol, oleylamine, and oleic acid. As-synthesized CoFe$_2$O$_4$ NPs were cyclomixed with 0.5 M Na-tartrate solution (prepared in Milli-Q water and pH of the solution were made ~7) for 6 h at room temperature. The unsolubilized CoFe$_2$O$_4$ NPs were removed by passing through a syringe filter of 0.22 μm diameter. In this way we obtained pale yellow colored filtrate, tartrate functionalized CoFe$_2$O$_4$ NPs, called T-CoFe$_2$O$_4$ NPs. To amplify their optical response, T-CoFe$_2$O$_4$ NPs were heated at about 70 ^{o}C for 6 h under extensive stirring condition maintaining the pH of the solution at ~12 after dropwise addition of NaOH solution. After this high pH and temperature treatment, color of the solution got darker and showed intense fluorescence under UV light irradiation (inset of Figure 6.3 (a)). The solid powdered samples required for FTIR

spectroscopic measurements and magnetic study (VSM, vibrating sample magnetometer) were prepared by dialysis and lyophilization of the T-$CoFe_2O_4$ NPs solution (to remove excess ligands) followed by drying over a water bath.

6.2.3. Catalysis

For the study of catalysis, 50 µL aqueous T-$CoFe_2O_4$ NPs (containing 0.60 mg NPs) were added in the 13.4 µM aqueous solution of bilirubin (BR) kept in a quartz cuvette in the dark maintaining the pH of the solution ~7, with stirring condition and the absorbance of BR in the reaction mixture was measured time to time by the UV-visible spectrophotometer.

For the study of photocatalysis we used 8 W UV lamp as UV light and a 100 W incandescent light bulb as visible light source from Philips. 5 µM aqueous solution of methylene blue (MB) and 50 µL aqueous T-$CoFe_2O_4$ NPs (containing 0.60 mg NPs) were homogeneously mixed for 1 h in a quartz cuvette in the dark maintaining the pH of the solution ~3. Then the cuvette was kept ~2 cm apart from the light source and the absorbance of MB in the reaction mixture was recorded time to time by the UV-visible spectrophotometer.

6.3. Result and Discussions

To get an idea about the morphology and particle size of the as synthesized $CoFe_2O_4$ NPs, we carried out TEM (Transmission electron microscopy) analysis. As shown in Figure 6.1 (a), the NPs have homogeneous and narrow size distribution having spherical shape with an average diameter of 4.89 ± 0.08 nm (Figure 6.1 (b)). HRTEM (high-resolution transmission electron microscopy) image, as shown in Figure 6.1 (c), implies high crystalline nature of the $CoFe_2O_4$ NPs. The calculated interplanar distance between the lattice fringes is about 0.253 nm, which corresponds to the distance between (311) planes of the $CoFe_2O_4$ crystal lattice. EDX spectrum of $CoFe_2O_4$ NPs in Figure 6.1 (d) confirms the elemental composition of only cobalt, iron, and oxygen.
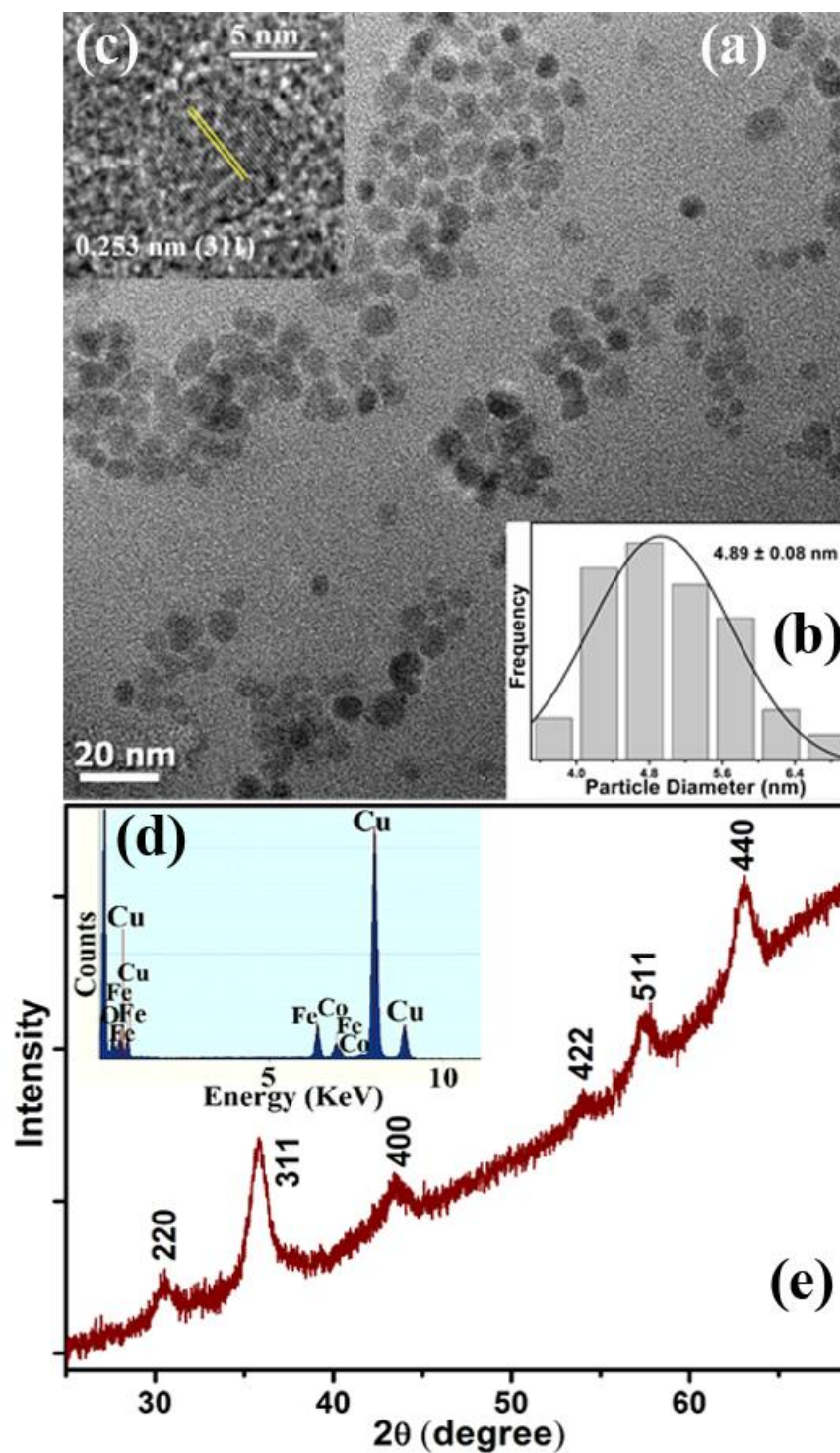
Figure 6.1. (a) TEM image of the as-prepared bare CoFe$_2$O$_4$ NPs. (b) Size distribution plot of as-prepared CoFe$_2$O$_4$ NPs. (c) HRTEM image consisting lattice fringes indicates high crystallinity. (d) EDX spectrum of the NPs indicating the presence of only Co, Fe, and O. (e) XRD pattern of as-prepared CoFe$_2$O$_4$ NPs. All diffraction peaks perfectly resemble the cubic inverse spinel structure of CoFe$_2$O$_4$ NPs.
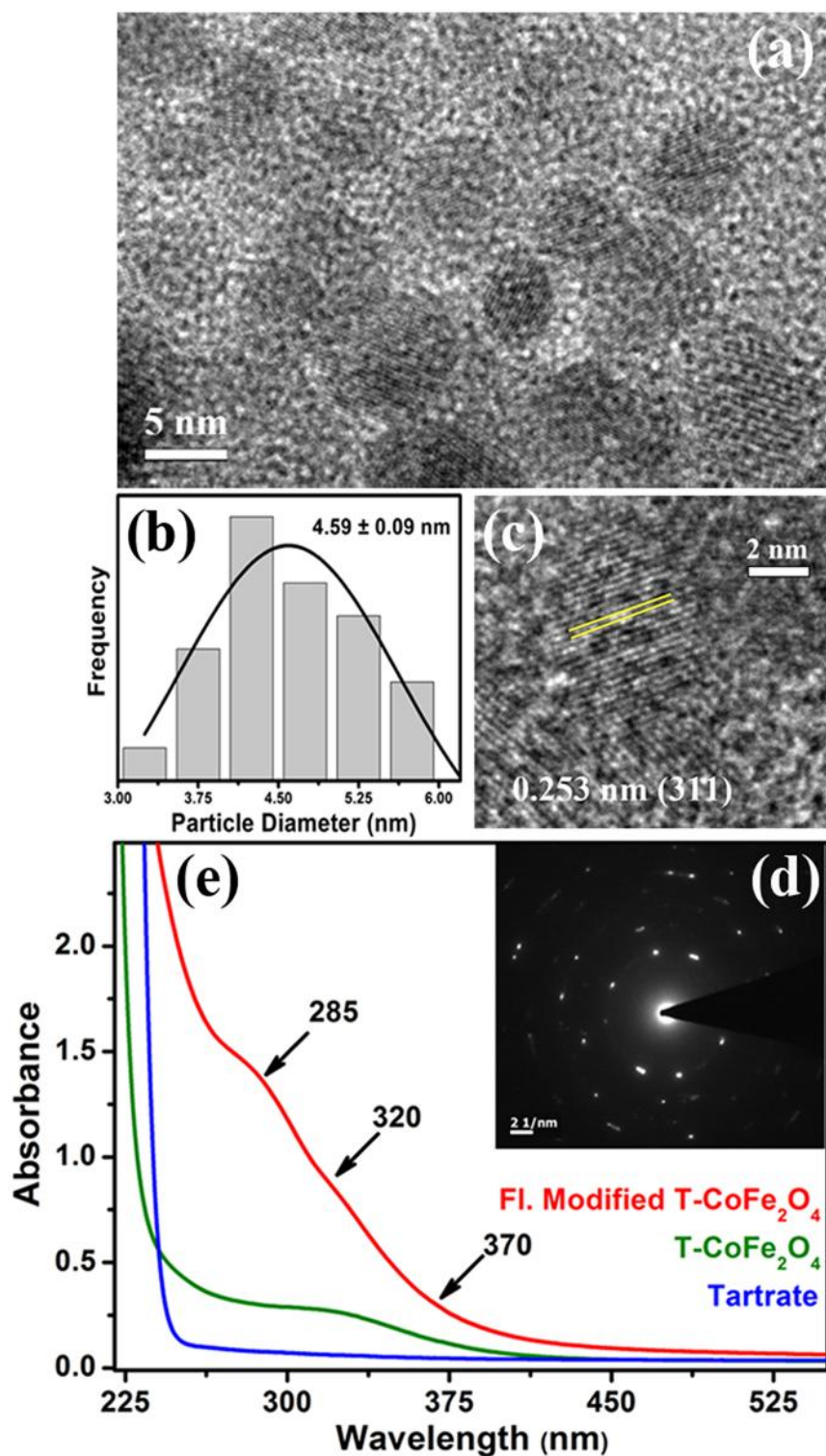
Figure 6.2. (a) TEM image of water dispersible T-CoFe$_2$O$_4$ NPs. (b) Size distribution of T-CoFe$_2$O$_4$ NPs. (c) Lattice fringes in the HRTEM image, indicating retention of high crystalline nature of the NPs even after functionalization. (d) SAED pattern of T-CoFe$_2$O$_4$ NPs indicates high crystallinity. (e) UV-visible absorption spectra for as-prepared and fluorescence modified T-CoFe$_2$O$_4$ NPs along with Na-tartrate.

XRD pattern as shown in Figure 6.1 (e) demonstrates that all the peaks perfectly match with the cubic inverse spinel structure of $CoFe_2O_4$ NPs as reported in the literature (JCPDS file no. 22-1086).[16, 17]

To solubilize the $CoFe_2O_4$ NPs in aqueous medium, we have functionalized them with the tartrate ligands. Figure 6.2 (a) shows the TEM image of the T-$CoFe_2O_4$ NPs having spherical shape with an average diameter of 4.59 ± 0.09 nm (Figure 6.2 (b)). The HRTEM image (shown in Figure 6.2 (c)) and SAED (selected area electron diffraction) pattern (shown in Figure 6.2 (d)) confirm the highly crystalline nature of T-$CoFe_2O_4$ NPs. The calculated interplanar distance between the fringes has been found to be 0.253 nm corresponding to the (311) plane of the crystal lattice. Figure 6.2 (e) shows UV-visible absorption pattern of T-$CoFe_2O_4$ NPs (pH ~7) which consists of bands near 285, 320, and 370 nm. Interestingly, upon exciting the NPs at 285, and 316 nm, we observed fluorescence having maxima at 413 nm and excitation at 355 nm gives fluorescence having maxima at 460 nm, although with low intensity. To increase the fluorescence intensity, we further modified the T-$CoFe_2O_4$ NPs by heat and higher pH treatment (the pH of the as-prepared T-$CoFe_2O_4$ NPs was adjusted to ~12, by dropwise addition of NaOH solution, followed by heat treatment at 70 °C for 8 h), which resulted in generation of additional two fluorescence peaks (at 514 and 560 nm) upon excitation with proper wavelengths with overall increment in intensity.[15]

Figure 6.3 (a) exhibits the normalized multicolor fluorescence emission spectra obtained from fluorescence modified (fl. modified) T-$CoFe_2O_4$ NPs. Corresponding excitation spectra are shown in Figure 6.3 (b). The observed absorption peaks at 285 and 320 nm, for fl. modified T-$CoFe_2O_4$ NPs, which give rise to fluorescence at 413 nm may be attributed to the ligand-to-metal charge transfer (LMCT) transition involving the highest occupied energy level of tartrate ligands and the lowest unoccupied energy levels of $Co^{2+/3+}$ or Fe^{3+} metal ion centers on the NPs' surface.[18, 19] Co^{2+} and Fe^{3+} are inherently present in $CoFe_2O_4$ NPs, moreover, Co^{3+} is more stable than Co^{2+} in the case of aqueous complexes,[20] so, the involvement of Co^{3+} in generation of fluorescence is very much likely. Additional three fluorescence peaks having maxima at 460, 514, and 560 nm, against excitation at 355,

435, and 525 nm, respectively, might be originated due to the possible d-d transitions involving $Co^{2+/3+}$ ions in the fl. modified $T\text{-}CoFe_2O_4$ NPs surface.[21] Fe^{3+} being a d^5 system, the involvement of d-d transition is both Laporte and spin forbidden, so its contribution in the observed optical property will be much lower as compared to the allowed transitions associated with Co^{2+} and Co^{3+}, which are d^7 and d^6 systems, respectively. Moreover, this issue is further evident from our findings with tartrate capped Fe_2O_3 NPs (as discussed in chapter 3), where only LMCT transition involving the highest occupied energy level of tartrate ligands and the lowest unoccupied energy levels of Fe^{3+} metal ion centers on the NPs' surface can generate considerable fluorescence, but d-d transitions involving only Fe^{3+} is not at all efficient to develop intense fluorescence.[22]

We can explain the generation of the three excitation bands having maxima at 370, 430, and 525 nm, in terms of spectroscopic term symbols, due to transitions of $^4T_{1g}$ (F)$\rightarrow$$^4A_{2g}$ (F), $^4T_{1g}$ (F) $\rightarrow$$^4T_{1g}$ (P), and $^4T_{1g}$ (F) $\rightarrow$$^4T_{2g}$ (F), respectively, where these energy levels are picked up from Tanabe-Sugano diagram of Co^{2+}.[23] Additional contribution for the emission peaks having maxima at 460 and 514 nm can be interpreted to the d-d transitions ($^1A_{1g}$$\rightarrow$$^1T_{2g}$ and $^1A_{1g}$$\rightarrow$$^1T_{1g}$ respectively) involving the energy levels of Co^{3+} as obtained from Tanabe-Sugano diagram.[23] Among the d-d transitions only the peak at 370 nm is visible in the UV-visible absorption spectra, probably other peaks are masked due to their low intensity as compared to the LMCT bands.
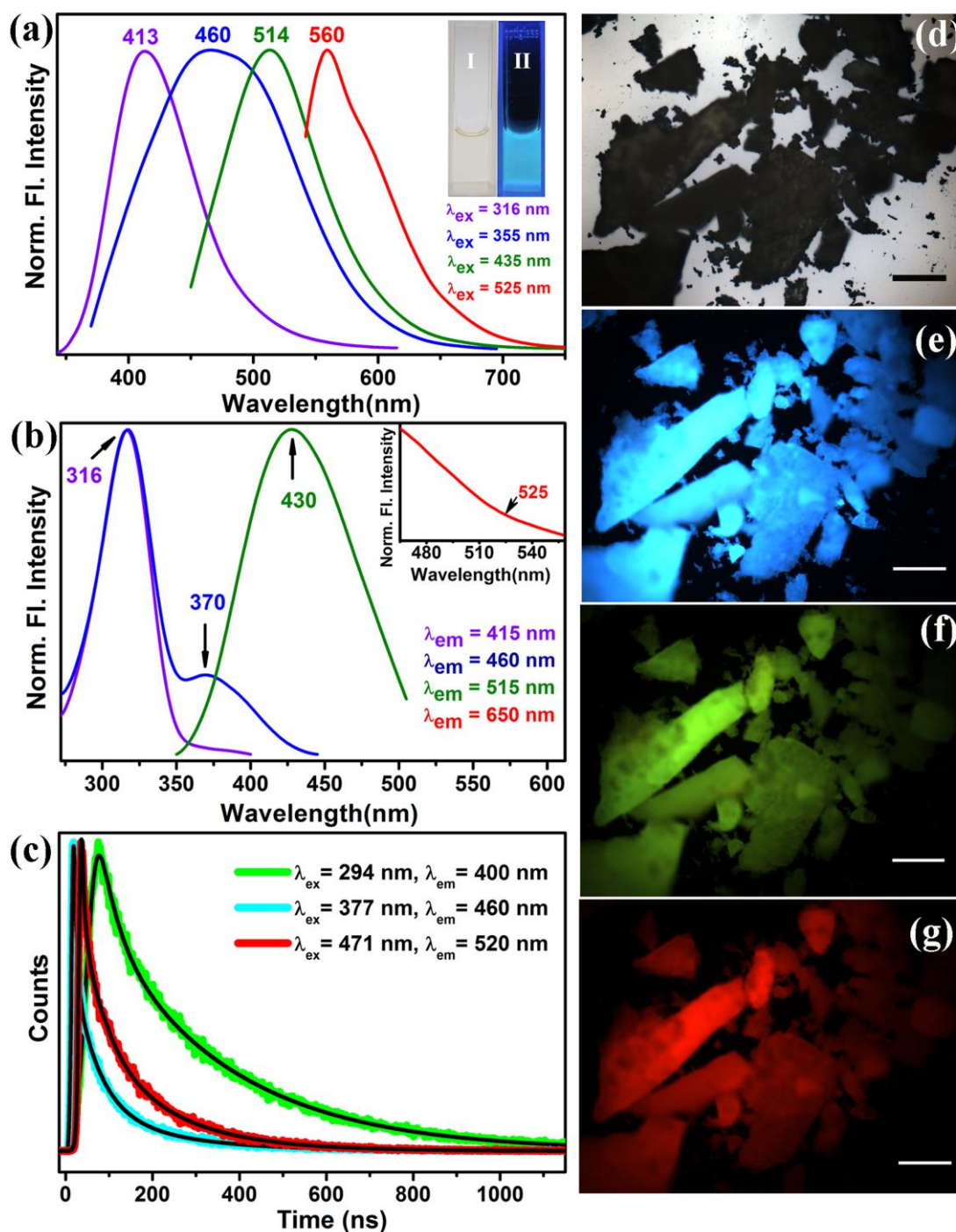
Figure 6.3. (a) Normalized steady-state fluorescence emission spectra obtained from fl. modified T-CoFe$_2$O$_4$ NPs by excitation of four different wavelengths at 316, 355, 435, and 525 nm. Image I and II in the inset show the photographs of fl. modified T-CoFe$_2$O$_4$ NPs solution under visible and UV light respectively. (b) Fluorescence excitation spectra of fl. modified T-CoFe$_2$O$_4$ NPs at different emission maxima, such as 415, 460, 515, and 650 nm. (c) Picosecond-resolved fluorescence transients of fl. modified T-CoFe$_2$O$_4$ NPs studied at emission wavelengths of 400, 460, and 520 nm upon excitation with laser sources of 294, 377, and 471 nm wavelengths, respectively. Fluorescence micrographs of fl. modified T-CoFe$_2$O$_4$ NPs powder under (d) bright field, (e) UV (365 nm), (f) blue (436 nm), and (g) green (546 nm) light irradiation. The scale bars in all the images are 500 µm.

To have further decisive mechanistic insight for the appearance of multicolor photoluminescence, we have performed picosecond-resolved fluorescence decay transient measurements of fl. modified T-CoFe$_2$O$_4$ NPs employing TCSPC (time-correlated single photon counting) technique. Figure 6.3 (c) represents the time resolved fluorescence decay transients of fl. modified T-CoFe$_2$O$_4$ NPs at three different fluorescence maxima of 400, 460, and 520 nm using three different pulsed diode laser excitation sources of 294, 377, and 471 nm wavelengths, respectively. As evident from the figure, significantly larger average excited-state lifetime (τ_{av}) of the fl. modified T-CoFe$_2$O$_4$ NPs observed for 400 nm fluorescence band (5.27 ns) compared to that for 460 nm (1.03 ns), and 520 nm (0.97 ns) fluorescence bands strongly suggests mechanistic difference in the origin of the fluorescence peak at 413 nm from rest of the peaks. Whereas, the strong resemblance between the lifetime values of fluorescence bands at 460 and 520 nm reveals their mechanistic similarity. Corresponding weight percentages are mentioned in Table 6.1. With this fluorescence lifetime study, proposition with regard to the origin of this multicolor fluorescence made from steady state experiments are rechecked and rationally can be concluded that LMCT excited state is responsible for 413 nm fluorescence, while 460 and 514 nm fluorescence is attributed to d-d transition. Moreover we can safely conclude that other lower energy fluorescence at 560 nm would also correspond to another d-d transition.

The fluorescence micrographs of fl. modified T-CoFe$_2$O$_4$ NPs, demonstrate that the black powder of fl. modified T-CoFe$_2$O$_4$ NPs under bright field (Figure 6.3 (d)), give rise to fluorescent colors like cyan, green, and red upon excitation at 365 (Figure 6.3 (e)), 436 (Figure 6.3 (f)), and 546 (Figure 6.3 (g)) nm, respectively, by using proper filters. The fluorescence micrographs of as prepared CoFe$_2$O$_4$ NPs, demonstrate no fluorescence under identical condition as shown in Figure 6.4. Fluorescence quantum yields (QYs) of the fl. modified T-CoFe$_2$O$_4$ NPs have been calculated following the relative method of Williams et al.,[24] which involves the use of well-characterized standard fluorescent compounds with known QY values. Fluorescence QYs of 7% (for 413 nm band), 2.11% (for 460 nm band), 1.68% (for 514 nm band), and 0.68% (for 560 nm band) were obtained relative to the standard

fluorescent compounds, such as 2-aminopurine (2AP), 4′,6- diamidino-2-phenylindole (DAPI), Hoechst 33258, and Rhodamine B (RhB), respectively. Thus, the emergence of multicolor fluorescence in $CoFe_2O_4$ NPs was induced by tartrate functionalization and then strengthened by further surface modification. Moreover, as evident from Figure 6.5, the size and morphology of the T-$CoFe_2O_4$ NPs remain unchanged even after fluorescence modification upon high pH and heat treatment.

Bright Field   PL@λ_{ex}= 365 nm   PL@λ_{ex}= 436 nm   PL@λ_{ex}= 546 nm
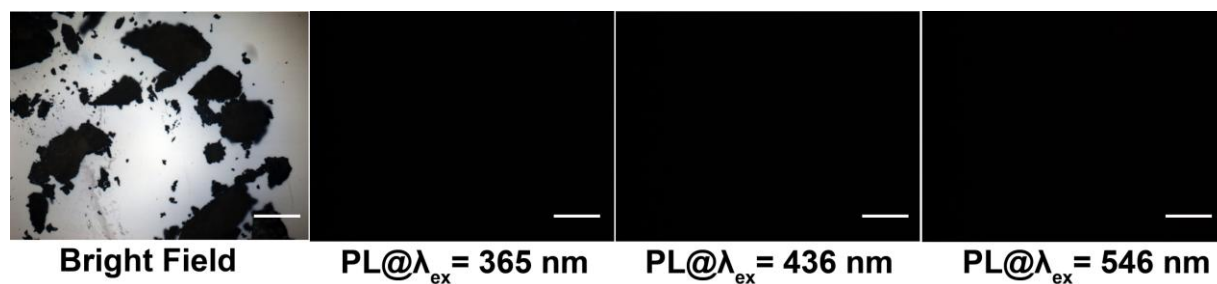
Figure 6.4. Fluorescence micrographs of bare $CoFe_2O_4$ NPs, under bright field, UV, blue, and green light. The scale bars in all the images are 500 µm.
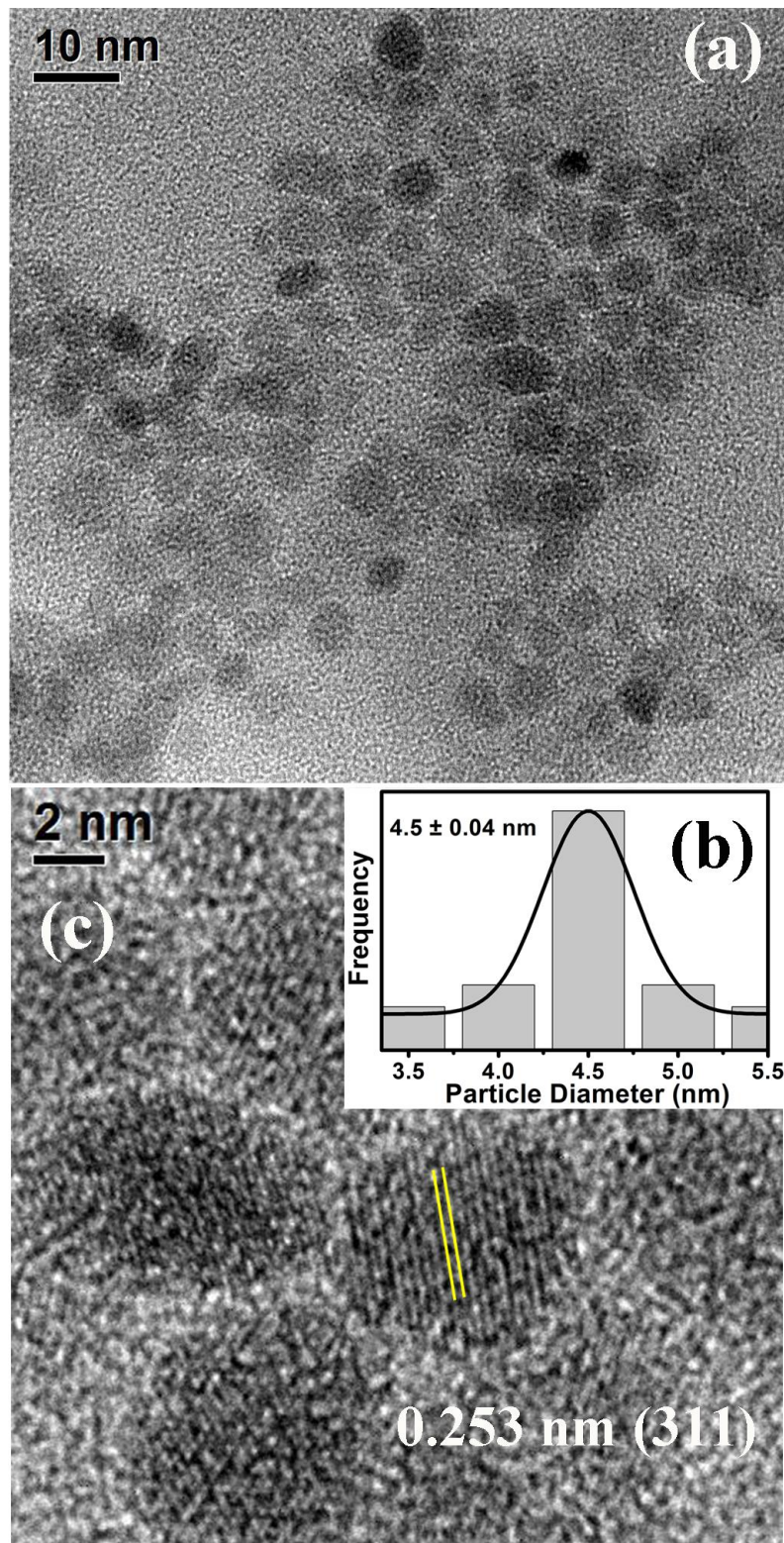
Figure 6.5. (a) TEM image of the fluorescence modified T-CoFe$_2$O$_4$ NPs. (b) Size distribution plot of fluorescence modified T-CoFe$_2$O$_4$ NPs. (c) HRTEM image consisting lattice fringes indicates high crystallinity.

Table 6.1. Lifetime values of picosecond time-resolved photoluminescence transients of fl. modified T-CoFe$_2$O$_4$ NPs, detected at photoluminescence maxima of 400, 460, and 520 nm upon excitation at 294, 377, and 471 nm wavelengths, respectively. The relative weight percentages of the corresponding time components are mentioned in parentheses.

System	Excitation wavelength, λ_{ex} (nm)	Fluorescence peak, λ_{em} (nm)	τ_1 (ns)	τ_2 (ns)	τ_3 (ns)	τ_{av} (ns)
Fl. modified T-CoFe$_2$O$_4$ NPs	294	400	1.1 (42.9)	8.4 (57.1)	-	5.27
	377	460	1.58 (27.8)	5.64 (8.6)	0.17 (63.6)	1.03
	471	520	1.4 (13.63)	4.8 (13.64)	0.17 (72.73)	0.97

FTIR studies (shown in Figure 6.6 (a)) were carried out for CoFe$_2$O$_4$ NPs before and after functionalization with tartrate ligand, along with the ligand alone, to confirm the attachment of the tartrate ligands to the NPs' surface. As shown in the figure, the peak at 587 cm^{-1} arising due to stretching vibration of metal-oxygen bonds of CoFe$_2$O$_4$ NPs is absent in case of T-CoFe$_2$O$_4$ NPs. In case of tartrate, two sharp peaks at 1066 and 1112 cm^{-1} arise due to the C–OH stretching modes,[25] peaks at 1411 and 1621 cm^{-1} are attributed to symmetric and asymmetric stretching modes of the carboxylate groups (–COO$^-$) of tartrate, respectively.[26] In case of T-CoFe$_2$O$_4$ NPs, because of interaction between functional group moieties of ligand and NPs' surface, all these different bands are perturbed significantly along with the band at 3399 cm^{-1}, generated due to the stretching vibrational modes of hydroxyl group (O-H),[25] which clearly indicates that both –COO$^-$ and –OH groups are involved in the functionalization process. In addition, upon base treatment followed by heating of the T-CoFe$_2$O$_4$ NPs, this broadening of carboxylate and hydroxyl peaks become further enhanced, as evident from Figure 6.7 (a, b), indicating combined strengthening of metal-ligand interaction.
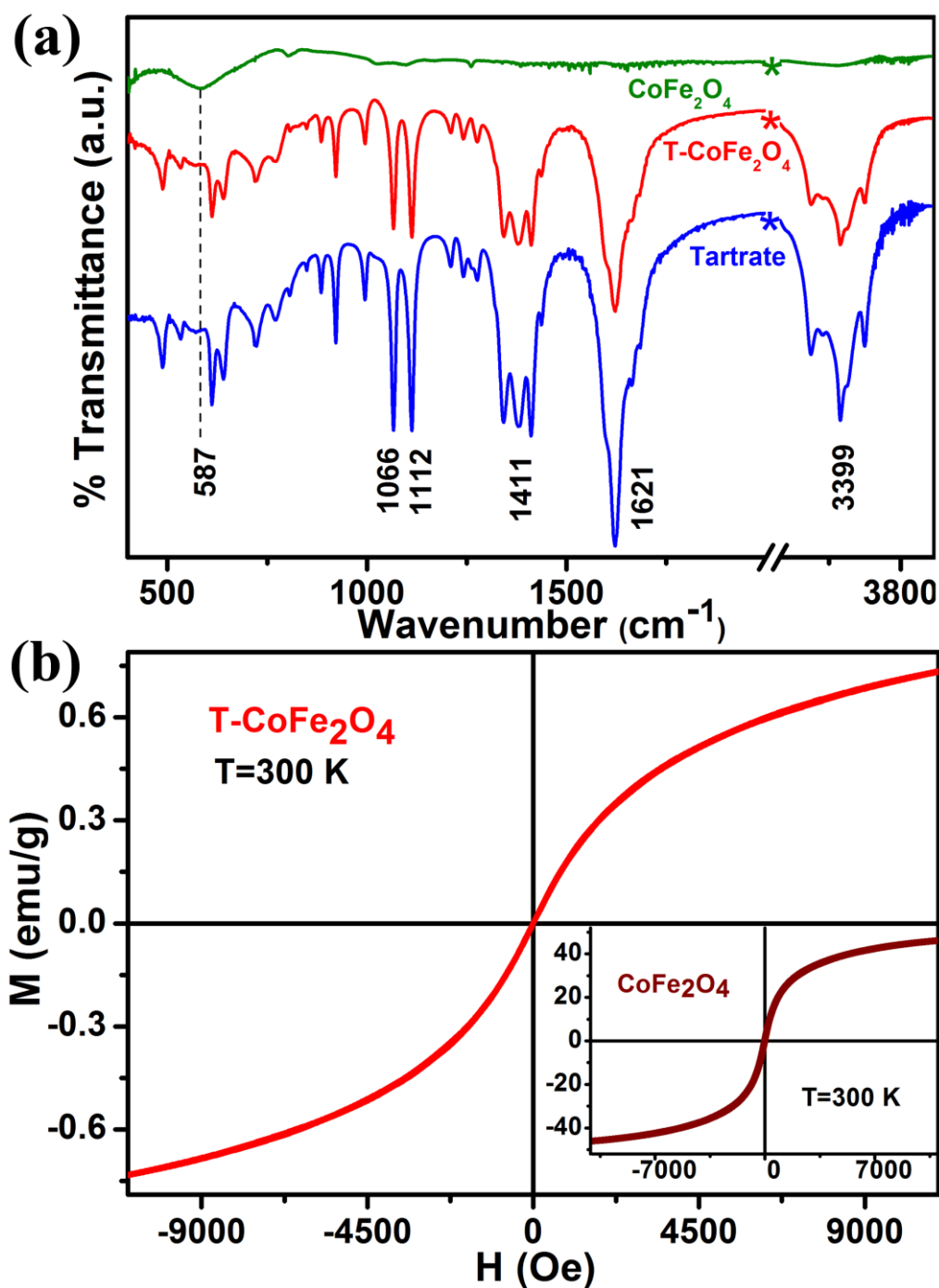
Figure 6.6. (a) FTIR spectra of as-prepared CoFe$_2$O$_4$ and T-CoFe$_2$O$_4$ NPs along with Na-tartrate alone. (b) Plot of magnetization versus applied magnetic field (M-H) for T-CoFe$_2$O$_4$ NPs at 300 K. Inset shows M-H plot for as-prepared CoFe$_2$O$_4$ NPs, obtained at identical condition.
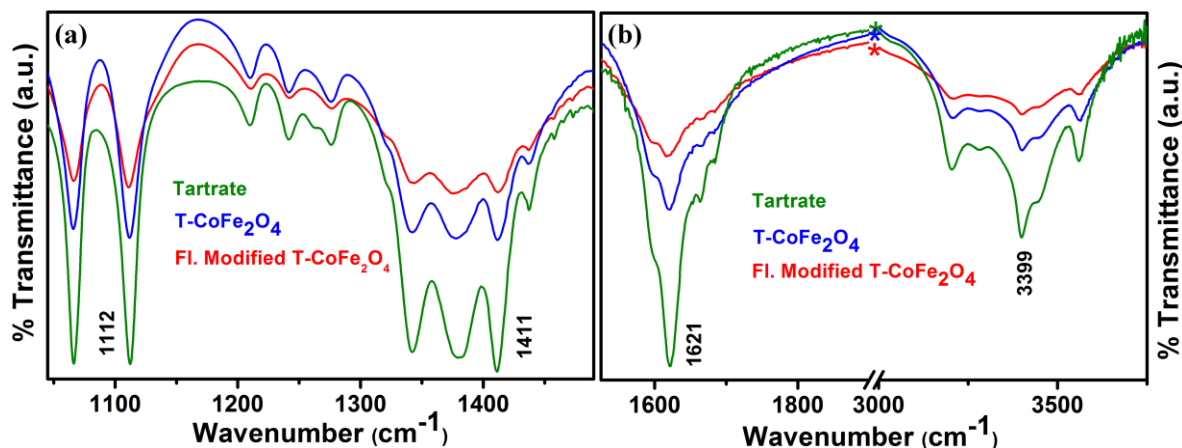
Figure 6.7. (a,b) FTIR spectra of T-CoFe$_2$O$_4$ NPs and fluorescence modified T-CoFe$_2$O$_4$ NPs along with Na-tartrate alone.

To have an idea about magnetic behavior of CoFe$_2$O$_4$ NPs before and after functionalization, we have carried out applied field dependent magnetization study (M-H) using VSM. As shown in Figure 6.6 (b), the superparamagnetic nature of the as-prepared bare CoFe$_2$O$_4$ NPs (shown in the inset) remains unchanged after functionalization, with significant decrease in saturation magnetization. Moreover, the decrease of saturation magnetization in case of fl. modified T-CoFe$_2$O$_4$ NPs is more prominent as shown in Figure 6.8. This phenomenon can be explained by ligand field theory. As evident from FTIR study, after fl. modification interaction among carboxylate (-COO$^-$) and hydroxyl (O-H) groups of tartrate and metal centers in the NPs' surface get enhanced. Tartrate ligand containing both the σ-donor (-OH) and π-donor (-COO$^-$) functional groups,[22, 27] favors the quenching of magnetic moments of Co$^{2+/3+}$ or Fe^{3+} ions on the surface of T-CoFe$_2$O$_4$ NPs, leading to decrease in the saturation magnetization.[28]
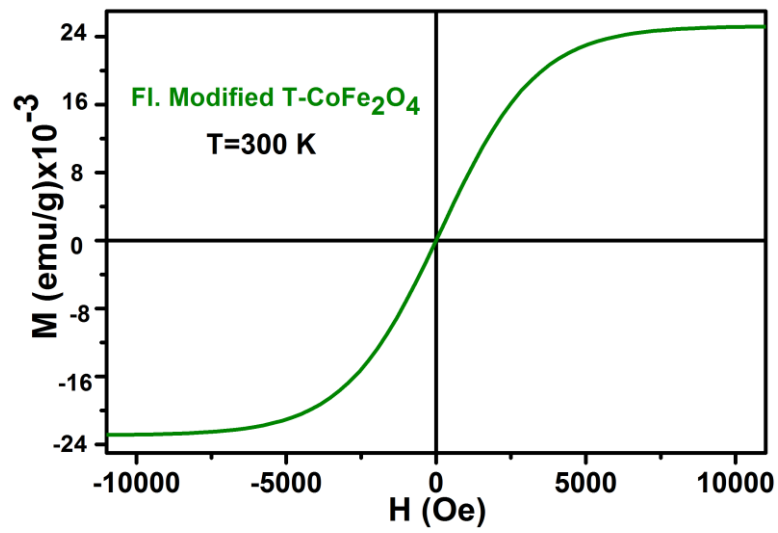
Figure 6.8. Plot of magnetization versus applied magnetic field (M-H) for fluorescence modified T-CoFe$_2$O$_4$ NPs at 300 K.
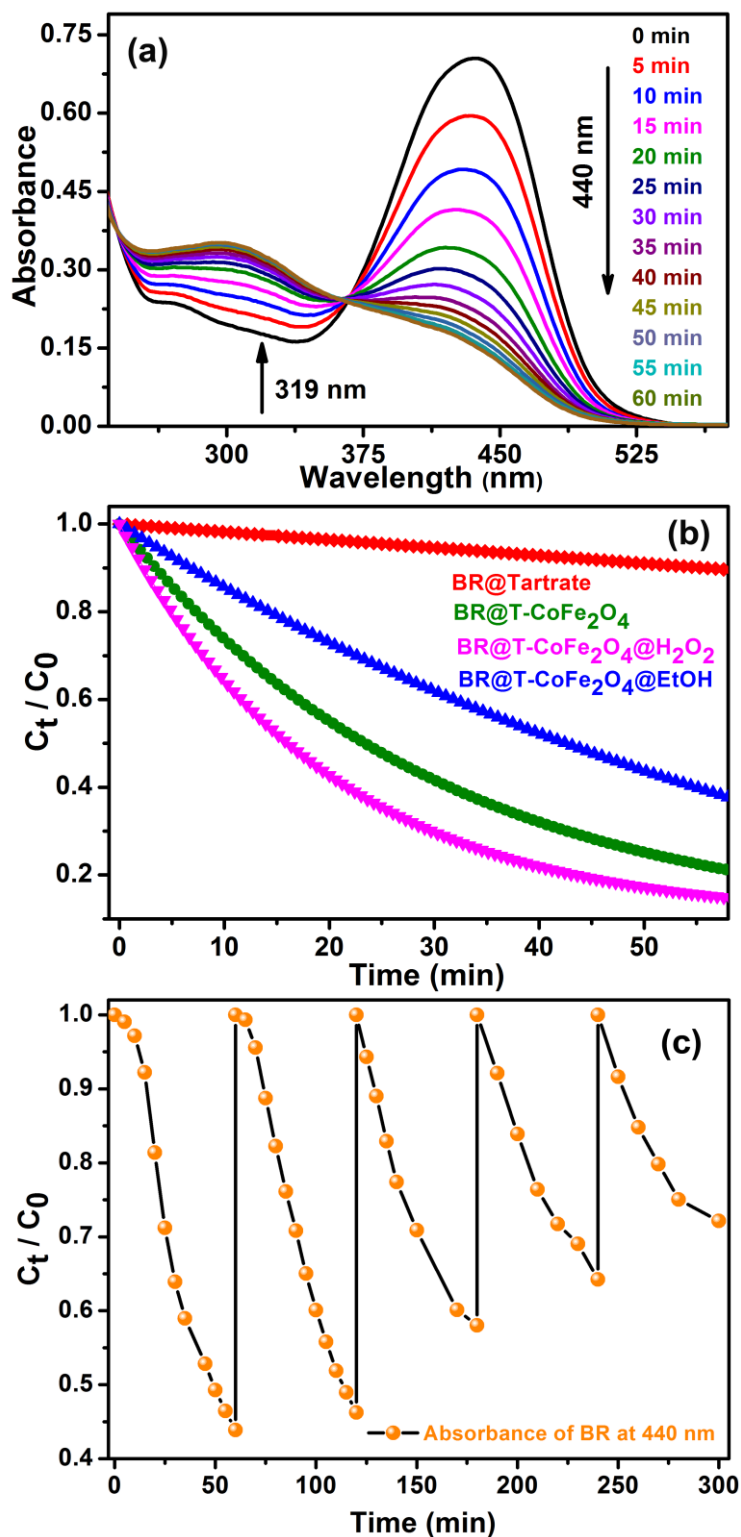
Figure 6.9. (a) The UV−visible spectral changes of aqueous solution of bilirubin (BR) in the presence of T-CoFe$_2$O$_4$ NPs with time, under stirring condition. (b) Comparative study for degradation of BR (monitored at 440 nm) in presence of tartrate, T-CoFe$_2$O$_4$ NPs, T-CoFe$_2$O$_4$ NPs@H$_2$O$_2$, and T-CoFe$_2$O$_4$ NPs@EtOH. (c) The plots of relative concentration of BR monitored at 440 nm versus time for 5 consecutive cycles, showing reusability of T-CoFe$_2$O$_4$NPs in degradation of BR.

Interface of catalysis and nanoscience have paved the way toward green chemistry. In this regard we were curious to know the catalytic efficiency of the T-CoFe$_2$O$_4$ NPs in degradation of bilirubin (BR), the pigment whose elevated level indicates jaundice. Interestingly, T-CoFe$_2$O$_4$ NPs exhibit excellent catalytic efficiency in the degradation of BR at room temperature and most importantly without any photo excitation at pH ~7, as shown in Figure 6.9 (a). It was found that T-CoFe$_2$O$_4$ NPs catalyzed BR degradation follows the first order rate equation with kinetic rate constant (k) 3.3 x 10^{-2} min^{-1}. To clarify whether the reaction follows radical pathway, we carried out the reaction in presence of radical initiator (H$_2$O$_2$), radical scavenger (EtOH), and Na-tartrate (as blank), as shown in Figure 6.9 (b). In presence of Na-tartrate, degradation of BR takes place negligibly. We have observed significant increment of rate (k = 5 x 10^{-2} min^{-1}) of catalysis in presence of small amount of H$_2$O$_2$ (5 µL). Again in presence of EtOH, the rate (k = 1.3 x 10^{-2} min^{-1}) of reaction decreased significantly. Notably, an isosbestic point was observed at 365 nm due to increase in absorbance at 319 nm with decrease in absorbance at 440 nm with time. To separate the BR degradation products, we have performed phase transformation of products from aqueous to chloroform medium, in order to avoid possible interference of the water soluble T-CoFe$_2$O$_4$ NPs catalysts in the characterization process, and also considering solubility of previously reported BR degradation products in less polar solvents. Figure 6.10 demonstrates the UV-visible absorbance peaks of BR degradation product in chloroform and the emission spectra of the same having maximum at ~450 nm, by exciting the degradation product at 350 nm wavelength. The absorbance and emission patterns of the degradation product of BR exactly match with the previously reported photo-oxidation product of BR, methylvinylmaleimide (MVM).[29, 30] Those experiments along with the generation of photo-oxidation product indicate that, T-CoFe$_2$O$_4$ NPs assisted BR degradation takes place via radical pathway. We have also investigated the recyclability of the catalyst, in degradation of BR, by adding same dose (which was initially added to the reaction mixture i.e. 13.4 µM) of BR to the reaction mixture at every 60 min up to 5 doses, keeping the catalyst concentration fixed (without addition of extra catalyst after the 1st cycle), and measured the BR decomposition rates by monitoring the

decrease of BR absorbance at 440 nm using UV-visible spectroscopy. The plot of relative concentration of BR with time up to 5 consecutive cycles as demonstrated in Figure 6.9 (c), confirms the reusability of the T-CoFe$_2$O$_4$ NPs catalyst.
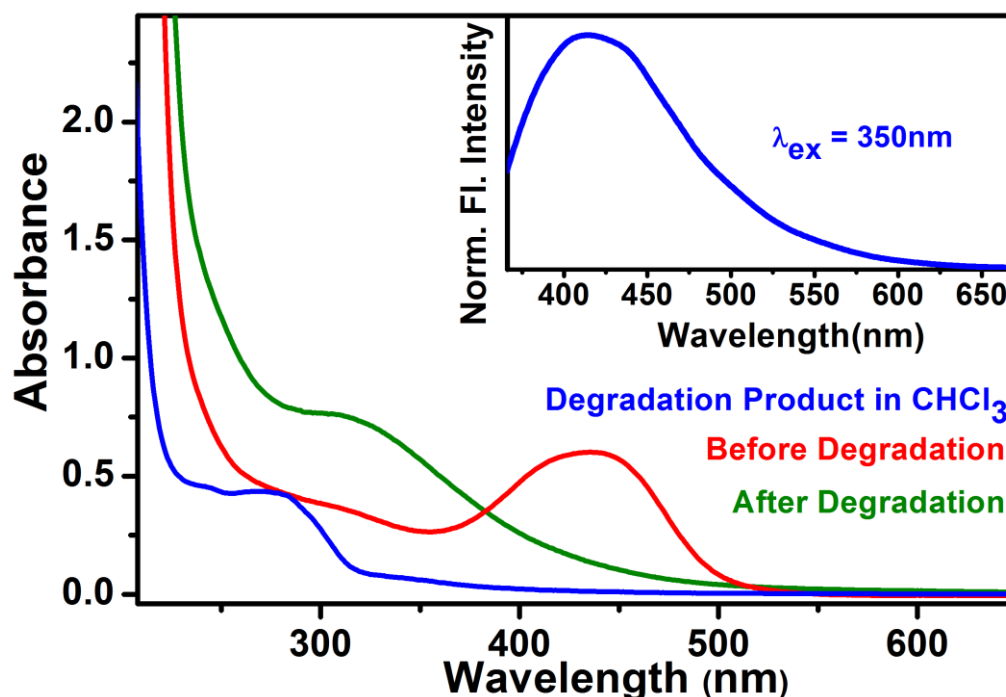
Figure 6.10. UV-visible absorbance spectra of aqueous bilirubin (BR) solution in presence of T-CoFe$_2$O$_4$ NPs before degradation (red line) and after complete degradation (green line) in aqueous medium. UV-visible absorbance spectrum of BR degradation product in chloroform (blue line). Inset shows the emission spectrum of BR degradation product in chloroform.

Having knowledge about the excellent efficiency of T-CoFe$_2$O$_4$ NPs in degradation of biologically harmful pigment, we got interested to check their role in degradation of model water pollutant. We intended to utilize the strong broad optical excitation of the T-CoFe$_2$O$_4$ NPs extended throughout the UV-visible region, in photo degradation of methylene blue (MB), an organic dye commonly found in waste water of textile industries. As shown in Figure 6.11 (a), T-CoFe$_2$O$_4$ NPs show unprecedented photocatalytic activity in the degradation of MB upon UV light irradiation. Inset shows the full absorption spectra of the MB in presence of T-CoFe$_2$O$_4$ NPs at pH ~ 3 with increasing time, under UV light irradiation. We have found that the photodegradation of MB in presence of T-CoFe$_2$O$_4$ NPs follows the first order rate equation with kinetic rate constant (k) 14.96 x 10^{-2} min^{-1}. But in

presence of only tartrate the degradation takes place negligibly. We have also checked the recyclability of the catalyst, by adding same dose of MB to the reaction mixture at every 25 min up to 5 doses, keeping the catalyst concentration fixed (without addition of extra catalyst after the 1st cycle), and measured the MB decomposition rates by monitoring the decrease of MB absorbance at 660 nm using UV-visible spectroscopy (as shown in Figure 6.11 (b)), which confirms the reusability of the T-CoFe$_2$O$_4$ NPs catalyst. Having evidence from various photochemical reactions of MB and tartrate capped MnFe$_2$O$_4$ NPs assisted MB degradation as discussed in chapter 4, we propose that photo degradation process is associated with a radical pathway involving reactive oxygen species (ROS).[31, 32] Furthermore, we have investigated the efficiency of T-CoFe$_2$O$_4$ NPs in degradation of MB in presence of visible light. Figure 6.11 (c) shows that T-CoFe$_2$O$_4$ NPs can degrade MB in presence of visible light also, although with a slower degradation rate as compared to the UV light irradiation, having 1st order kinetic rate constant (k) of 48 x 10^{-4} min^{-1}. The decrease in rate of photocatalysis in presence of visible light can be attributed to the lower energy of the visible light than UV light as well as lower absorbance of T-CoFe$_2$O$_4$ NPs in the visible region in comparison with UV region.
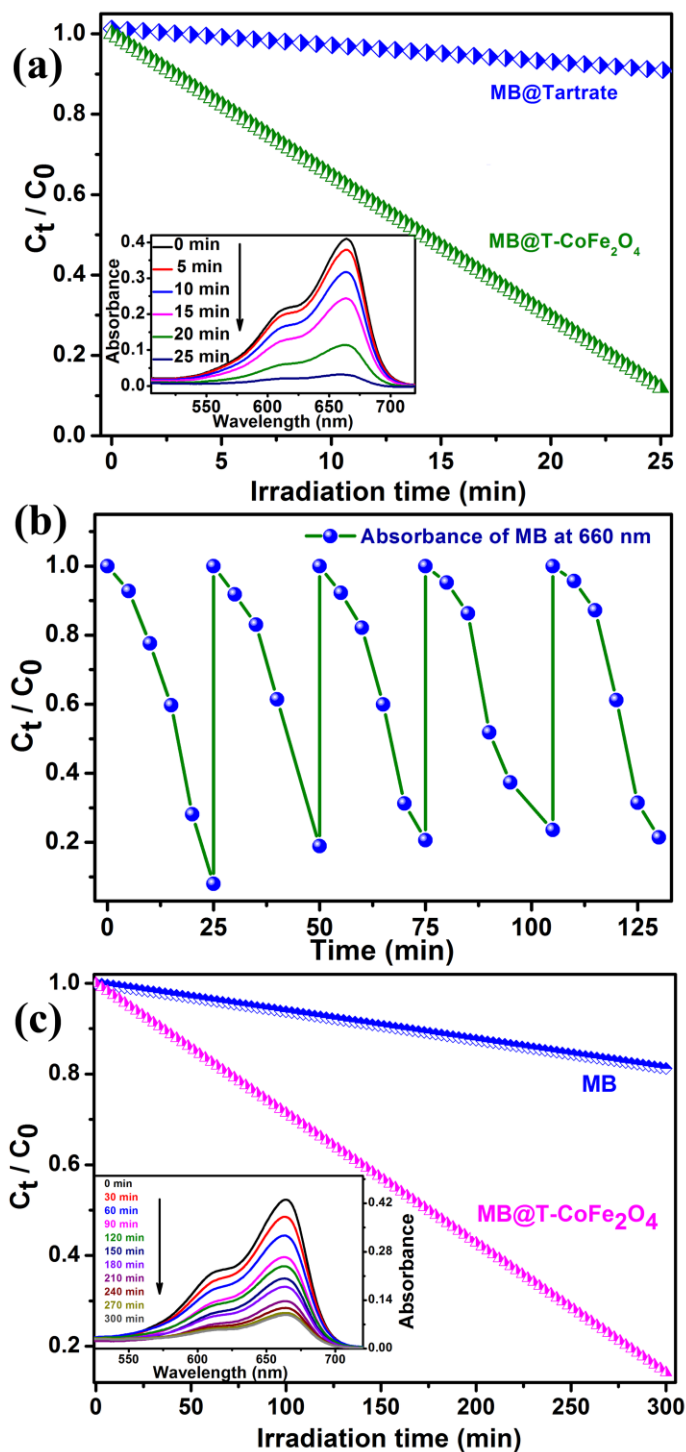
Figure 6.11. (a) The plots of relative concentration of methylene blue (MB) (monitored at 660 nm) under UV irradiation in the presence of Na-tartrate, and T-CoFe$_2$O$_4$ NPs, separately. Inset shows the UV−visible spectral changes of aqueous solution of MB in the presence of T-CoFe$_2$O$_4$ NPs with time, under UV irradiation. (b) The plots of relative concentration of MB monitored at 660 nm versus time for 5 consecutive cycles, showing reusability of T-CoFe$_2$O$_4$ NPs in MB degradation under UV light. (c) The plots of relative concentration of MB (monitored at 660 nm) in the absence and presence of T-CoFe$_2$O$_4$ NPs under visible light. Inset shows the full absorption spectra of MB in the presence of T-CoFe$_2$O$_4$ NPs with time, under visible light irradiation.

6.4. Conclusions

In conclusion, by facile surface modification of CoFe$_2$O$_4$ NPs with Na-tartrate ligands, we have developed multifunctional nanoprobe having simultaneously intrinsic fluorescence covering the whole visible region ranging from blue, cyan, and green to red, superparamagnetism, and biocompatibility. Moreover, T-CoFe$_2$O$_4$ NPs have unprecedented catalytic and photocatalytic activity in degradation of biologically (BR) and environmentally (MB) harmful pigments, respectively. Systematic investigation through UV−visible absorption, steady state, and time-resolved photoluminescence study reveals that ligand-to-metal charge transfer transition from highest occupied energy level of tartrate ligand to lowest unoccupied energy levels of Co$^{2+/3+}$ or Fe^{3+} metal ion centers and d−d transitions centered over Co$^{2+/3+}$ ions on the NPs' surface play the crucial role behind the generation of multicolor fluorescence from the T-CoFe$_2$O$_4$ NPs. We hope that the multifunctional T-CoFe$_2$O$_4$ NPs will pioneer new opportunities in the field of diagnostics such as bioimaging, and therapeutics like drug delivery, as well as waste water treatment.

Bibliography

1.   Cao, Y.; Cai, S.-R.; Fan, S.-C.; Hu, W.-Q.; Zheng, M.-S.; Dong, Q.-F., Reduced Graphene Oxide Anchoring $CoFe_2O_4$ Nanoparticles as an Effective Catalyst for Non-aqueous Lithium-oxygen Batteries. *Faraday Discuss.* **2014**.

2.   Joshi, H. M.; Lin, Y. P.; Aslam, M.; Prasad, P. V.; Schultz-Sikma, E. A.; Edelman, R.; Meade, T.; Dravid, V. P., Effects of Shape and Size of Cobalt Ferrite Nanostructures on Their MRI Contrast and Thermal Activation. *J. Phys. Chem. C* **2009,** *113* (41), 17761-17767.

3.   Yinglin, X.; Xiaomin, L.; Jiantao, Z.; Kaixue, W.; Yong, G.; Bo, L.; Qianyan, H.; Xuefeng, Q., $CoFe_2O_4$-graphene Nanocomposites Synthesized through An Ultrasonic Method with Enhanced Performances as Anode Materials for Li-ion Batteries. *Micro Nano Lett.* **2014,** *6* (4).

4.   Tang, D.; Yuan, R.; Chai, Y.; An, H., Magnetic-Core/Porous-Shell $CoFe_2O_4/SiO_2$ Composite Nanoparticles as Immobilized Affinity Supports for Clinical Immunoassays. *Adv. Funct. Mater.* **2007,** *17* (6), 976-982.

5.   Torres, T. E.; Roca, A. G.; Morales, M. P.; Ibarra, A.; Marquina, C.; Ibarra, M. R.; Goya, G. F., Magnetic Properties and Energy Absorption of $CoFe_2O_4$ Nanoparticles for Magnetic Hyperthermia. *J. Phys.: Conf. Ser.* **2010,** *200* (7), 072101.

6.   Kargar, A.; Yavuz, S.; Kim, T. K.; Liu, C.-H.; Kuru, C.; Rustomji, C. S.; Jin, S.; Bandaru, P. R., Solution-Processed $CoFe_2O_4$ Nanoparticles on 3D Carbon Fiber Papers for Durable Oxygen Evolution Reaction. *ACS Appl. Mater. Interfaces* **2015,** *7* (32), 17851-17856.

7.   Peddis, D.; Cannas, C.; Musinu, A.; Ardu, A.; Orrù, F.; Fiorani, D.; Laureti, S.; Rinaldi, D.; Muscas, G.; Concas, G.; Piccaluga, G., Beyond the Effect of Particle Size: Influence of $CoFe_2O_4$ Nanoparticle Arrangements on Magnetic Properties. *Chem. Mater.* **2013,** *25* (10), 2005-2013.

8.   Georgiadou, V.; Tangoulis, V.; Arvanitidis, I.; Kalogirou, O.; Dendrinou-Samara, C., Unveiling the Physicochemical Features of $CoFe_2O_4$ Nanoparticles Synthesized via a Variant Hydrothermal Method: NMR Relaxometric Properties. *J. Phys. Chem. C* **2015,** *119* (15), 8336-8348.

9.   Limaye, M. V.; Singh, S. B.; Date, S. K.; Kothari, D.; Reddy, V. R.; Gupta, A.; Sathe, V.; Choudhary, R. J.; Kulkarni, S. K., High Coercivity of Oleic Acid Capped $CoFe_2O_4$ Nanoparticles at Room Temperature. *J. Phys. Chem. B* **2009,** *113* (27), 9070-9076.

10.   Cannas, C.; Musinu, A.; Peddis, D.; Piccaluga, G., Synthesis and Characterization of $CoFe_2O_4$ Nanoparticles Dispersed in a Silica Matrix by a Sol−Gel Autocombustion Method. *Chem. Mater.* **2006,** *18* (16), 3835-3842.

11.   Peddis, D.; Mansilla, M. V.; Mørup, S.; Cannas, C.; Musinu, A.; Piccaluga, G.; D'Orazio, F.; Lucari, F.; Fiorani, D., Spin-Canting and Magnetic Anisotropy in Ultrasmall $CoFe_2O_4$ Nanoparticles. *J. Phys. Chem. B* **2008,** *112* (29), 8507-8513.

12.   Fan, Y.; Huang, Y., The Effective Peroxidase-like Activity of Chitosan-functionalized $CoFe_2O_4$ Nanoparticles for Chemiluminescence Sensing of Hydrogen Peroxide and Glucose. *Analyst* **2012,** *137* (5), 1225-1231.

13.   Cao, Q.; Liu, Z.; Che, R., Ordered Mesoporous $CoFe_2O_4$ Nanoparticles: Molten-salt-assisted Rapid Nanocasting Synthesis and the Effects of Calcining Heating Rate. *New J. Chem.* **2014,** *38* (7), 3193-3198.

14.   Sun, S.; Zeng, H.; Robinson, D. B.; Raoux, S.; Rice, P. M.; Wang, S. X.; Li, G., Monodisperse MFe_2O_4 (M = Fe, Co, Mn) Nanoparticles. *J. Am. Chem. Soc.* **2003,** *126* (1), 273-279.

15.   Pal, M.; Kundu, A.; Rakshit, R.; Mandal, K., Ligand-Induced Evolution of Intrinsic Fluorescence and Catalytic Activity from Cobalt Ferrite Nanoparticles. *ChemPhysChem* **2015,** *16* (8), 1627-1634.

16.   Ren, X.; Tong, L.; Chen, X.; Ding, H.; Yang, X.; Yang, H., Deposition of Luminescent $Y_2O_3{:}Eu_{3+}$ on Ferromagnetic Mesoporous $CoFe_2O_4@mSiO_2$ Nanocomposites. *Phys. Chem. Chem. Phys.* **2014,** *16* (22), 10539-10547.

17.   Andersen, H. L.; Christensen, M., In Situ Powder X-ray Diffraction Study of Magnetic $CoFe_2O_4$ Nanocrystallite Synthesis. *Nanoscale* **2015,** *7* (8), 3481-3490.

18.   Giri, A.; Goswami, N.; Bootharaju, M. S.; Xavier, P. L.; John, R.; Thanh, N. T. K.; Pradeep, T.; Ghosh, B.; Raychaudhuri, A. K.; Pal, S. K., Emergence of Multicolor Photoluminescence in $La_{0.67}Sr_{0.33}MnO_3$ Nanoparticles. *J. Phys. Chem. C* **2012,** *116* (48), 25623-25629.

19. Giri, A.; Makhal, A.; Ghosh, B.; Raychaudhuri, A. K.; Pal, S. K., Functionalization of Manganite Nanoparticles and their Interaction with Biologically Relevant Small Ligands: Picosecond Time-resolved FRET Studies. *Nanoscale* **2010,** *2* (12), 2704-2709.

20. Collins, R. N.; Kinsela, A. S., The Aqueous Phase Speciation and Chemistry of Cobalt in Terrestrial Environments. *Chemosphere* **2010,** *79* (8), 763-771.

21. Pal, M.; Singh, A. K.; Rakshit, R.; Mandal, K., Surface Chemistry Modulated Introduction of Multifunctionality within Co_3O_4 Nanocubes. *RSC Adv.* **2015,** *5* (21), 16311-16318.

22. Pal, M.; Rakshit, R.; Mandal, K., Facile Functionalization of Fe_2O_3 Nanoparticles to Induce Inherent Photoluminescence and Excellent Photocatalytic Activity. *Appl. Phys. Lett.* **2014,** *104* (23), -.

23. Huheey, J. E.; Keiter, E. A.; Keiter, R. L.; Medhi, O. K., *Inorganic Chemistry: Principles of Structure and Reactivity*. Pearson Education: 2006.

24. Williams, A. T. R.; Winfield, S. A.; Miller, J. N., Relative Fluorescence Quantum Yields Using A Computer-Controlled Luminescence Spectrometer. *Analyst* **1983,** *108* (1290), 1067-1071.

25. Kaneko, N.; Kaneko, M.; Takahashi, H., Infrared and Raman Spectra and Vibrational Assignment of Some Metal Tartrates. *Spectrochim. Acta, Part A* **1984,** *40* (1), 33-42.

26. Ramakrishnan, V.; Maroor, J. M. T., IR and Raman Studies of Gel Grown Manganese Tartrate. *Infrared Phys.* **1988,** *28* (4), 201-204.

27. Giri, A.; Goswami, N.; Pal, M.; Zar Myint, M. T.; Al-Harthi, S.; Singha, A.; Ghosh, B.; Dutta, J.; Pal, S. K., Rational Surface Modification of Mn_3O_4 Nanoparticles to Induce Multiple Photoluminescence and Room Temperature Ferromagnetism. *J. Mater. Chem. C* **2013,** *1* (9), 1885-1895.

28. Rakshit, R.; Mandal, M.; Pal, M.; Mandal, K., Tuning of Magnetic Properties of $CoFe_2O_4$ Nanoparticles through Charge Transfer Effect. *Appl. Phys. Lett.* **2014,** *104* (9), -.

29. Giri, A.; Goswami, N.; Sasmal, C.; Polley, N.; Majumdar, D.; Sarkar, S.; Bandyopadhyay, S. N.; Singha, A.; Pal, S. K., Unprecedented Catalytic Activity of

Mn$_3$O$_4$ Nanoparticles: Potential Lead of a Sustainable Therapeutic Agent for Hyperbilirubinemia. *RSC Adv.* **2014,** *4* (10), 5075-5079.

30.   Kurtin, W. E., Spectroscopy and Photochemistry of Bilirubin Photoproducts. I. Methylvinylmaleimide. *Photochem. Photobiol.* **1978,** *27* (5), 503-509.

31.   Pal, M.; Rakshit, R.; Mandal, K., Surface Modification of MnFe$_2$O$_4$ Nanoparticles to Impart Intrinsic Multiple Fluorescence and Novel Photocatalytic Properties. *ACS Appl. Mater. Interfaces* **2014,** *6* (7), 4903-4910.

32.   Jing, H.-P.; Wang, C.-C.; Zhang, Y.-W.; Wang, P.; Li, R., Photocatalytic Degradation of Methylene blue in ZIF-8. *RSC Adv.* **2014,** *4* (97), 54454-54462.

Chapter 7

Improved Electrochemical Properties of Co$_3$O$_4$ Nanocubes

This chapter shows improvement of electrochemical property by surface modification through scaling down the size of material and development of electrode with very high supercapacitance by growing ultra small Co$_3$O$_4$ nanocubes by one step facile solvothermal process.

7. Remarkable Supercapacitance of Co₃O₄ Nanocubes

7.1. Preamble

In an attempt to alleviate the critical problems of escalating energy crisis and greenhouse gas pollution derived from excessive consumption of fossil fuels, some alternative energy technologies have been formulated.[1-4] As an emerging advanced electrochemical energy storage system, supercapacitors (SCs) can offer higher power density, longer cycling life, and better safety as compared to batteries. Moreover SCs have higher energy density than capacitors. SCs store energy on the basis of either charge accumulation (electric double layer capacitors, EDLC) or fast reversible Faradaic reactions (pseudocapacitors) on the surface of electrode. In order to improve SCs' energy density, numerous efforts have been directed to investigate pseudocapacitive transition metal oxides or hydroxide (such as RuO_2,[5] MnO_2,[6] NiO,[7, 8] Co_3O_4,[9, 10] $Ni(OH)_2$,[11] $Co(OH)_2$,[12] $NiCo_2O_4$[13, 14] etc.), which have potential to produce higher specific capacitance, in comparison with typical carbonaceous materials used in EDLC. In spite of recent progress, it is imperative to improve supercapacitance along with long term stability by rational manipulation of morphology and size of various potential materials.

Among various available pseudocapacitive materials, Co_3O_4 is notably attractive for application in SCs, due to its low cost, low environmental footprint, great redox activity, and especially, extremely high theoretical specific capacitance (ca. 3560 F g^{-1}).[15] In the nano regime the benign character gets further enhanced. So, in the past decade, microspheres,[16] nanosheets,[17] nanorods,[18] nanowires,[19] porous flower-like nanostructures[20] etc. have been explored for superior performance in the field of supercapacitance. However, the observed specific capacitance values for Co_3O_4 are much lower than its theoretical value, and it is an ongoing challenge to further improve its energy storage capability.

In this chapter, we have demonstrated fabrication of electrode by growing Co_3O_4 nanocubes (NCs) directly on Ni foam through facile one step solvothermal route. SEM (Scanning electron microscopy) shows the formation of extended NCs

arrays throughout the Ni foam. Detailed characterization through XRD (X-ray diffraction) and TEM (Transmission electron microscopy) confirms that the array consists of uniform Co_3O_4 NCs of small size (~8 nm) with narrow size distribution. Electrochemical study reveals an enhanced pseudocapacitive performance of the Co_3O_4 NCs with high rate capability, coulombic efficiency (88.7%), specific capacitance (1913 F g^{-1} at 8 A g^{-1}), energy density (44.7 Wh kg^{-1}), power density (782.6 kW kg^{-1}) and good cyclability. The remarkable supercapacitance can be attributed to facile one step fabrication of electrode by growing the NCs directly over Ni foam, very small size of NCs with nanopores leading to high surface area, larger interaction of electrolyte and active material even in the interior region of the electrode, fast ion and electron transfer. Having the excellent electrochemical performance of Co_3O_4 NCs, it holds promise to be used as an alternative electrode for forthcoming supercapacitor devices.

7.2. Experimental Section

7.2.1. Material Used

Co (II) acetate was received from Loba Chemie. Ethanol, ammonia, and potassium hydroxide (KOH) were purchased from Merck. All the reagents were of analytical grade and used without further purification.

7.2.2. Fabrication Procedure of Co_3O_4 Nanocubes Electrode

Co_3O_4 NCs of size ~ 8 nm were grown over Ni foam by one step solvothermal route as described in chapter 5.[21, 22] In a typical procedure, 0.70 g of Co $(CH_3COO)_2 \cdot 4H_2O$ was dissolved in 35 ml of ethanol, and 12 ml of 25% ammonia was added under vigorous stirring. The mixture was stirred in air for about 10 min to form homogeneous slurry. Then the suspension was transferred into a 50 ml teflon lined autoclave. A piece of Ni foam substrate having 3 x 1 cm^2 size was washed with half diluted HCl, followed by water and finally with acetone for several times and immersed into the reaction solution. Then the autoclave was sealed and maintained

at 150 ^{o}C for 3 h, followed by cooling to room temperature naturally. The black solid product deposited Ni foam, was washed with water, and ethanol. Then that was dried under vacuum. Mass of deposited product was determined by careful weighing the piece of Ni foam before and after reaction.

7.2.3. Electrochemical Analysis

The electrochemical properties of the Co_3O_4 NCs were investigated with cyclic voltammetry (CV) tests by using a software controlled conventional three-electrode electrochemical cell (potentiostat AutoLab-30) consisted of Co_3O_4 NCs over Ni foam as the working electrode, saturated Ag/AgCl/saturated KCl as the reference electrode, and a highly pure Pt wire as the counter electrode in a 0.5 M KOH electrolyte, at room temperature. The CV measurements were performed at different scan rates of 2, 10, 25, 50, and 100 mV s^{-1}, at room temperature within a potential window in the range of 0.1 to 0.7 V. Galvanostatic charging-discharging (GCD) experiments were carried out at different current densities, such as 8, 10, 30, 70, and 100 A g^{-1} to study specific capacitance, power density, and energy density. Long cycle stability test was performed by GCD method at current density of 8 A g^{-1}.

7.3. Result and Discussions

Co_3O_4 NCs array was grown directly over Ni foam through quick, facile one step solvothermal process. To evaluate whether NCs were grown over Ni foam, SEM study was performed for fresh Ni foam and after growing Co_3O_4 NCs over it as shown in Figure 7.1 (a) and Figure 7.1 (b), respectively. Figure 7.1 (c) and 7.1 (d) show the high resolution image of Co_3O_4 NCs over Ni foam. Figure 7.1 (d) exhibits formation of extended nano block arrays.
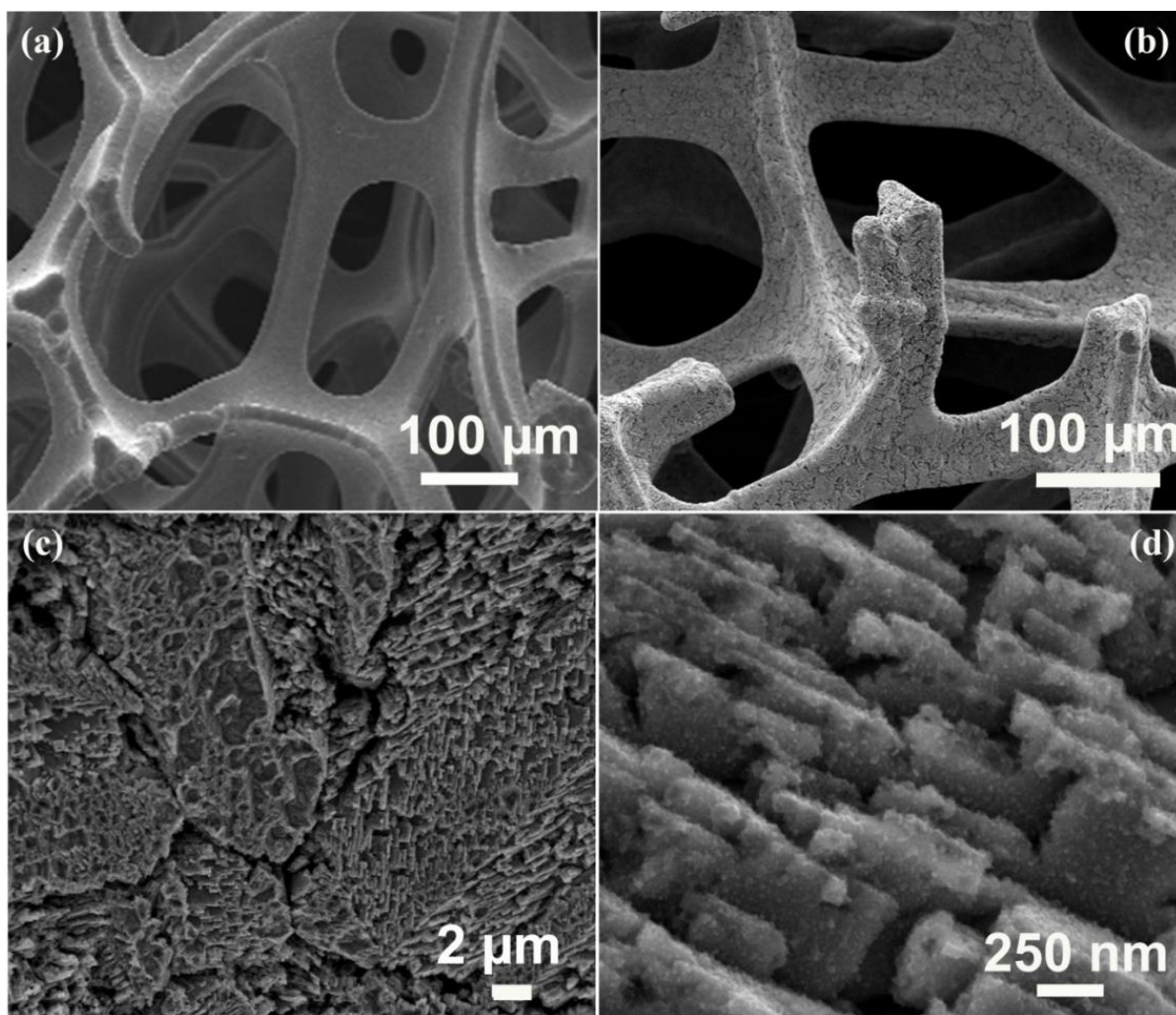
Figure 7.1. (a) SEM image of fresh Ni foam. (b) SEM image of Ni foam after growing Co_3O_4 NCs over it. (c) and (d) high resolution SEM image of Co_3O_4 NCs grown over Ni foam.

For further elucidation of particle size and morphology, TEM analysis has been performed. TEM image as shown in Figure 7.2 (a), reveals that the nano block arrays consist of ultra small Co_3O_4 NCs, having nearly homogeneous size distribution (6-11 nm) with an average size of 8.65 ± 0.22 nm (Figure 7.2 (b)), tightly cross-linked on Ni foam substrate. The corresponding SAED (selected area electron diffraction) pattern in Figure 7.2 (c) and HRTEM (high resolution transmission electron microscopy) image in Figure 7.2 (d) confirms the crystallinity of the NCs. The calculated interplanar distance between the lattice fringes is about 0.243 nm which corresponds to the distance between (311) planes of Co_3O_4 crystal lattice. EDX

spectroscopic analysis of Co_3O_4 NCs (Figure 7.2 (e)) confirms the elemental composition of only cobalt, and oxygen.
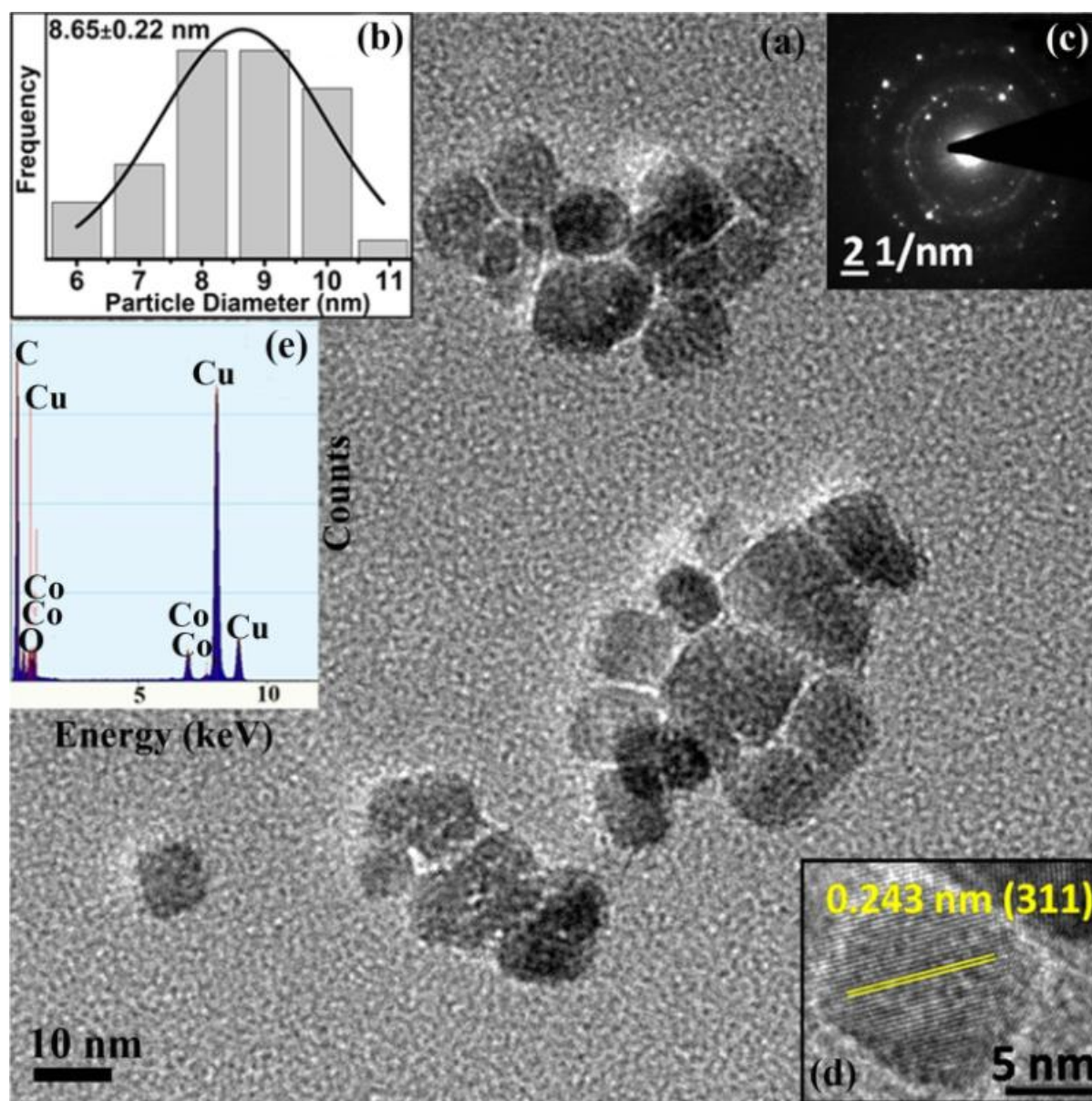
Figure 7.2. (a) TEM image of the as-prepared Co_3O_4 NCs. (b) Size distribution of the as-prepared Co_3O_4 NCs. (c) SAED pattern of the as-prepared Co_3O_4 NCs (d) Corresponding HRTEM image indicates high crystallinity and shows lattice fringes. (e) EDX spectrum of the NCs indicating the presence of only Co, and O.

XRD study was employed to confirm the crystal phase of Co_3O_4 NCs. Figure 7.3 (a) shows the XRD pattern of the as-prepared Co_3O_4 NCs. All the diffraction peaks in the figure perfectly match with the cubic spinel crystal structure (JCPDS 42-1467) of Co_3O_4 as obtained from the literature.[21-23] Subsequently, XPS measurements

were performed to have information about the composition of the NCs. The Co 2p XPS spectrum, as shown in Figure 7.3 (b), consists of two major peaks with binding energies at 780.2 and 795.2 eV, corresponding to Co $2p_{3/2}$ and $2p_{1/2}$, respectively. More importantly, the band gap of 15 eV between $2p_{3/2}$ and $2p_{1/2}$ along with low intensity shakeup satellites at ~8.8 eV from the main spin-orbit components are the distinctive traits of the Co_3O_4 phase. Figure 7.3 (c) exhibits high-resolution XPS for the O1s region with binding energy at 530.1, and 531.6 eV.

We performed BET (Brunauer-Emmett-Teller) gas-sorption measurements to investigate the specific surface area and the porous nature of the Co_3O_4 NCs. N_2 adsorption-desorption isotherms of Co_3O_4 NCs are shown in Figure 7.3 (d), and inset illustrates the corresponding BJH pore size distribution plot. These isotherms can be categorized as type IV, with a hysteresis loop observed in the range 0.8-1.0 p/p_o (Figure 7.3 (d)). The BET specific surface area and pore volume of the Co_3O_4 NCs are found to be 74.80 m^2 g^{-1} and 0.0731 cc g^{-1}, respectively, which are quite higher as compared to previously reported larger nanocubes.[24] According to the BJH (Barret-Joyner-Halenda) plots, the average pore diameter of the Co_3O_4 NCs is 2.5 nm. Pores within the Co_3O_4 NCs facilitate the diffusion controlled reactions, particularly essential in electrochemistry, sensing, and catalysis.[25-27]
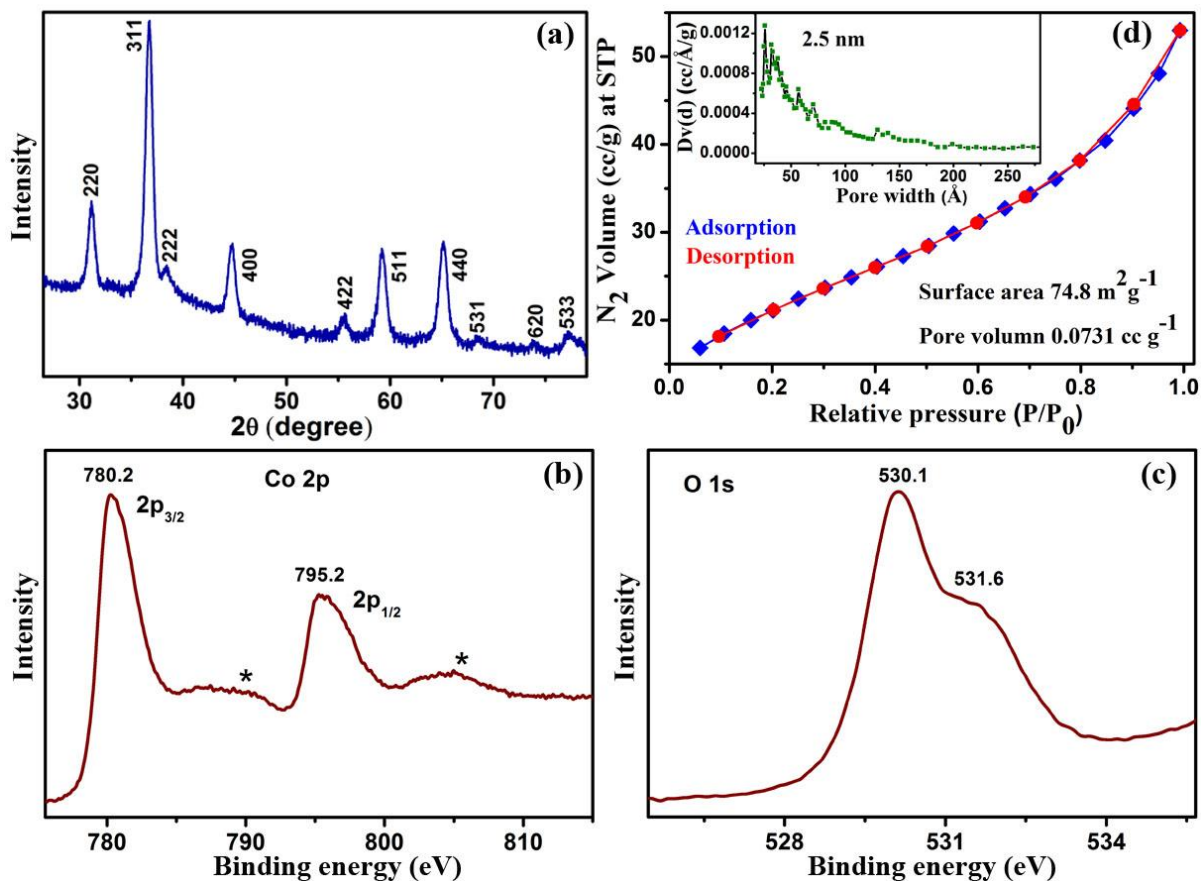
Figure 7.3. (a) XRD pattern of as-prepared Co_3O_4 NCs. All diffraction peaks in the figure are perfectly indexed in the literature to the cubic spinel structure of Co_3O_4 NCs. High resolution XPS spectrum of bare Co_3O_4 NCs showing (b) Co $2p_{3/2}$ and $2p_{1/2}$ core-level signals with binding energy at 780.2, and 795.2 eV, respectively, along with low intensity shakeup satellites at ~8.8 eV from the main spin-orbit components, and (c) oxygen species (O1s) with binding energy at 530.1, and 531.6 eV. (d) N_2 adsorption/desorption isotherms and corresponding pore size distribution (inset) for the Co_3O_4 NCs.

With growing progress of size and morphology controlled Co_3O_4 nanomaterials in enhancement of supercapacitance, we got interested to study the electrochemical properties of the ultra small Co_3O_4 NCs. We fabricated electrode by growing Co_3O_4 NCs directly over Ni foam and carried out electrochemical measurements by a three electrode cell system. Figure 7.4 (a) shows the typical CV curves of the Co_3O_4 NCs in the potential range of 0.1 V– 0.7 V at various scan rates ranging from 2 to 100 mV/s. The shape of the CV curves clearly reveals the pseudocapacitive behaviour of the electrode, originating from fast reversible redox reaction, which is totally different from that of the rectangular shape for EDLC. Two

oxidation and reduction peaks are clearly distinguishable in case of lower scan rate like 2 mV/s, but in case of the higher scan rates due to higher peak current and close proximity of redox potentials, they merges with each other.[28] Origin of two oxidation and reduction, can be explained based on literature reports regarding the CV curves of Co_3O_4 system in alkaline electrolytes, involving conversion of oxidation states of Co from +2 to +3 to +4 through the $Co_3O_4/CoOOH/CoO_2$ transformation associated with OH^- anions, following redox reactions.[29, 30]

$$Co_3O_4 + OH^- + H_2O \leftrightarrow 3\ CoOOH + e^- \qquad (7.1)$$
$$CoOOH + OH^- \leftrightarrow CoO_2 + H_2O + e^- \qquad (7.2)$$
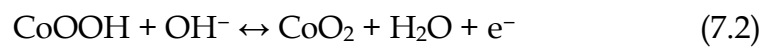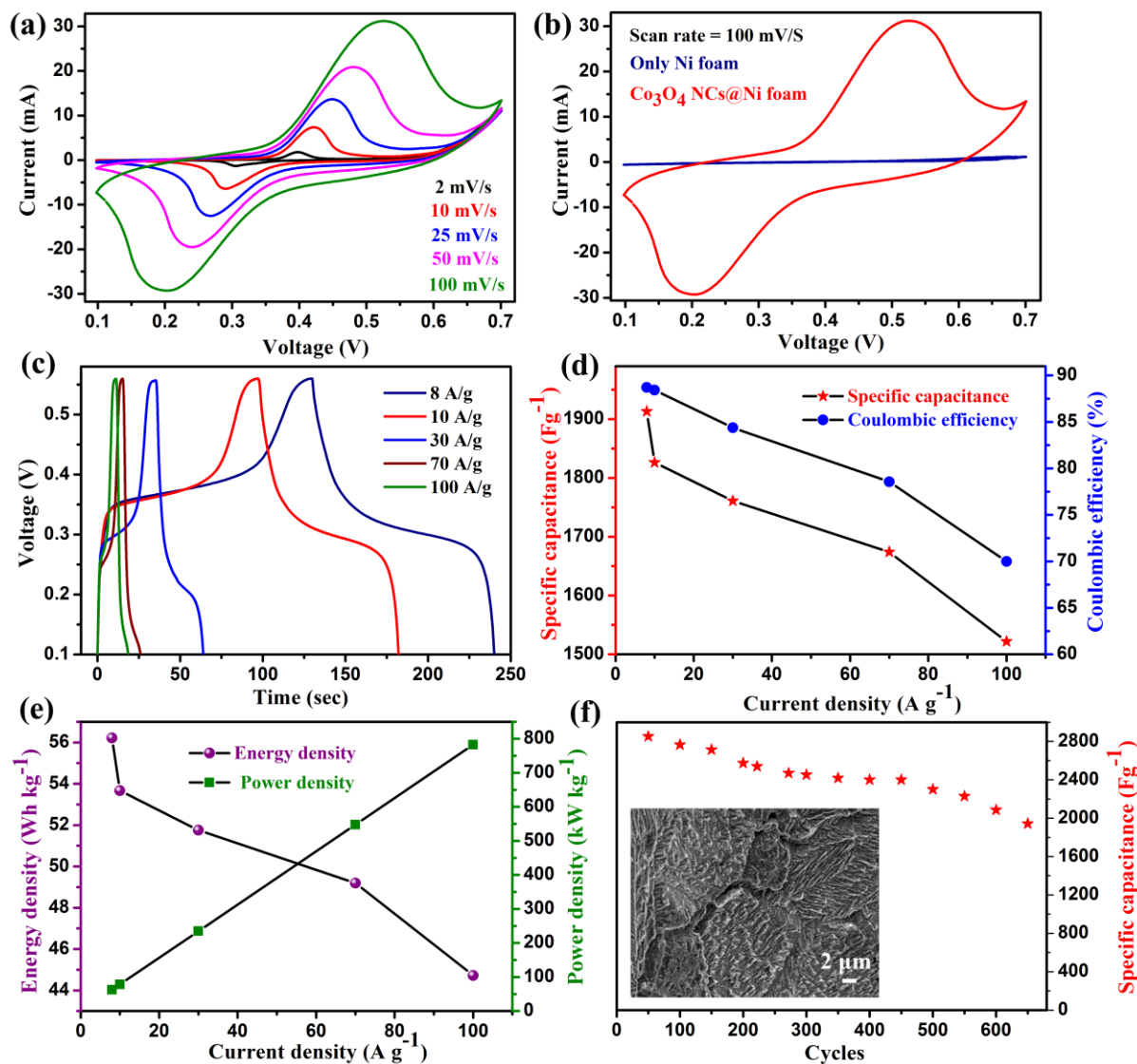
Figure 7.4. (a) CV curves of Co_3O_4 NCs at different scan rates in a 0.5 M KOH solution at room temperature. (b) Comparison between the CV curves of only Ni foam and Co_3O_4 NCs over Ni foam at scan rate of 100 mV s^{-1}. (c) GCD curves at different current densities, (d) plot of coulombic efficiency and specific capacitance versus current density, (e) variation of energy density and power density as a function of current density and (f) the cycling performance of Co_3O_4 NCs. Inset of (f) shows the SEM image of electrode after around thousand cycles.

With the increase of scan rate, both the potential and current at the oxidation and reduction peaks shifted away from each other, which can be attributed to lower internal diffusion of electrolyte within the NCs with increasing scan rates.[29] Interestingly, the peak potential shifts only about 100 mV for 50 times increase in the scan rate, suggesting low polarization of the electrode for the excellent electrical

conductivity of Ni foam support. The current response was found to increase proportionally with increasing scan rates, resulting linear plot for the peak current (*I*) of CV loops at different scan rates with the square root of scan rate voltage ($f^{1/2}$) as shown in Figure 7.5, which confirms a fast electron transfer rate during the diffusion-controlled redox reactions.[31] Our comparative investigation with only Ni foam and Co_3O_4 NCs grown over Ni foam at a scan rate of 100 mV/s, as demonstrated in Figure 7.4 (b) reveals that, only Ni foam has negligible contribution to the total capacitance.
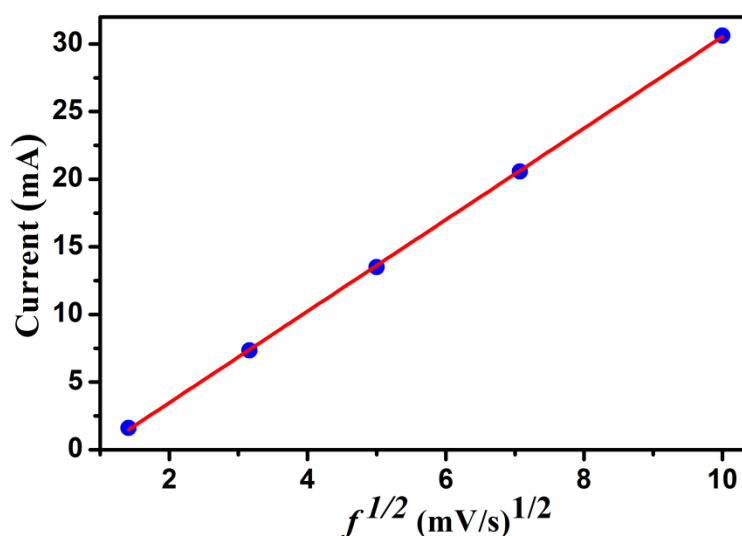
Figure 7.5. The plot of peak current versus square root of scan rate (*f*) for electrode fabricated by growing Co_3O_4 NCs over Ni foam.

To further elucidate the application potential of the ultra small Co_3O_4 NCs grown over Ni foam as an electrode for supercapacitors, GCD measurements were carried out between 0.1 and 0.56 V at various current densities ranging from 8 to 100 A g^{-1}, as shown in Figure 7.4 (c). Nearly symmetric potential-time curves at different current densities imply the high charging-discharging coulombic efficiency and low polarization of the electrode.

The specific capacitance (C_{sp}) and coulombic efficiency (η) of the electrode at different current densities can be calculated by using formula (7.3) and (7.4), respectively,

$$C_{sp} = \frac{I\Delta t_d}{m\Delta V} \qquad (7.3)$$

$$\eta = \frac{\Delta t_d}{\Delta t_C} \qquad (7.4)$$

Where I is the current density, Δt_c and Δt_d are the time required for complete charging and discharging, respectively, ΔV is the potential drop during discharging, and m is the mass of active material. The specific capacitance values are 1913, 1826, 1761, 1674, and 1522 F g^{-1} for Co$_3$O$_4$ NCs electrode at current densities of 8, 10, 30, 70, and 100 A g^{-1}, respectively. Coulombic efficiency decreases from 88.7 to 70% upon increasing current density from 8 to 100 A g^{-1}, which reveals that the ion and electron transfer rate decreases with increment of current density. Figure 7.4 (d) shows the variation of specific capacitance and coulombic efficiency with current density. These plots demonstrate that nearly 80% of specific capacitance and coulombic efficiency retain upon increasing current density from 8 to 100 A g^{-1}.

Furthermore, the energy (E) and the specific power (P) densities of the electrodes were calculated by using the equations,[11]

$$E = \frac{1}{2} C_{sp}(\Delta V)^2 \qquad (7.5)$$

$$P = \frac{E}{\Delta t_d} \qquad (7.6)$$

Where, E, C_{sp}, ΔV, Δt_d, and P are the energy density, specific capacitance, the potential window, discharging time, and power density, respectively. Figure 7.4 (e) demonstrates the variation of energy density and power density with current density for the system, which shows the maximum power density of 782.6 kW kg^{-1} and energy density of 44.7 Wh kg^{-1} at current density of 100 A g^{-1}. Moreover, the system can achieve the maximum energy density of 56.2 Wh kg^{-1}, while retaining the power density of 62.6 kW kg^{-1} at current density of 8 A g^{-1}. The cycle charging-discharging test was employed to examine the service life of the Co$_3$O$_4$ NCs

electrode. Figure 7.4 (f) exhibits the cyclic performance of the Co_3O_4 NCs electrode, which exhibits excellent cycling life and specific capacitance retention, tested over 650 cycles at current density of 8 A g^{-1}. The capacitance retention of Co_3O_4 NCs electrode after 650 cycles is about 70 %. Inset of Figure 7.4 (f) shows the SEM image of electrode after around thousand cycles of charging and discharging, which looks almost similar to the SEM image of the electrode before use (Figure 7.2 (c)), indicating maintenance of structural integrity after several cycles. The electrode exhibits good long term electrochemical stability and high specific capacitance retention after a long cycle test in aqueous KOH solution, which are very important requirements for supercapacitors.

The excellent electrochemical performance leading to superior coulombic efficiency, rate capability, specific capacitance, energy density, power density, and long cycling life of Co_3O_4 NCs can be attributed to the ultra small size of Co_3O_4 NCs enriched with nanopores and the fabrication procedure of the electrode by growing the NCs directly over current collector, Ni foam, by quick single step solvothermal route. Notably, the Ni foam substrate having micro holes and zigzag flow channels, results in excellent mass transport property and large surface area per unit volume of the electrode. Moreover, all the NCs have its own electrical contact with the current collector facilitating participation of all NCs in the electrochemical reaction, which ensures the maximum utilization of active material. Furthermore, the open structure of Ni foam ensures the diffusion of electrolyte into the inner region of the electrode, enhancing the contact area among electrolyte and Co_3O_4 NCs, resulting greater interactions. Consequently, our NCs can achieve the remarkable supercapacitance activity.

7.4. Conclusions

In summary, we have demonstrated a self-supported Co_3O_4 NCs array grown over nickel foam through quick single step solvothermal method as an interesting material for pseudocapacitors with high coulombic efficiency, rate capability, specific capacitance, energy density, power density, and good cyclability. We believe that its outstanding performance develops due to the ultra small porous morphology of Co_3O_4 NCs, greater interaction of electrolyte and active material, fast OH^- diffusion and electron transfer. We hope, ultra small Co_3O_4 NCs with their ease of large scale fabrication and excellent electrochemical efficiency will be a promising candidate for their application in the field of high performance supercapacitors.

Bibliography

1.   Arico, A. S.; Bruce, P.; Scrosati, B.; Tarascon, J.-M.; van Schalkwijk, W., Nanostructured Materials for Advanced Energy Conversion and Storage Devices. *Nat. Mater.* **2005,** *4* (5), 366-377.

2.   Yang, N.; Zhai, J.; Wang, D.; Chen, Y.; Jiang, L., Two-Dimensional Graphene Bridges Enhanced Photoinduced Charge Transport in Dye-Sensitized Solar Cells. *ACS Nano* **2010,** *4* (2), 887-894.

3.   Wu, Z.-S.; Ren, W.; Wen, L.; Gao, L.; Zhao, J.; Chen, Z.; Zhou, G.; Li, F.; Cheng, H.-M., Graphene Anchored with Co_3O_4 Nanoparticles as Anode of Lithium Ion Batteries with Enhanced Reversible Capacity and Cyclic Performance. *ACS Nano* **2010,** *4* (6), 3187-3194.

4.   Yao, X.; Xin, X.; Zhang, Y.; Wang, J.; Liu, Z.; Xu, X., Co_3O_4 Nanowires as High Capacity Anode Materials for Lithium Ion Batteries. *J. Alloys Compd.* **2012,** *521*, 95-100.

5.   Wang, W.; Guo, S.; Lee, I.; Ahmed, K.; Zhong, J.; Favors, Z.; Zaera, F.; Ozkan, M.; Ozkan, C. S., Hydrous Ruthenium Oxide Nanoparticles Anchored to Graphene and Carbon Nanotube Hybrid Foam for Supercapacitors. *Sci. Rep.* **2014,** *4*.

6.   Xie, X.; Zhang, C.; Wu, M.-B.; Tao, Y.; Lv, W.; Yang, Q.-H., Porous MnO_2 for Use in a High Performance Supercapacitor: Replication of a 3D Graphene Network as a Reactive Template. *Chem. Commun.* **2013,** *49* (94), 11092-11094.

7.   Singh, A. K.; Sarkar, D.; Khan, G. G.; Mandal, K., Unique Hydrogenated Ni/NiO Core/shell 1D Nano-heterostructures with Superior Electrochemical Performance as Supercapacitors. *J. Mater. Chem. A* **2013,** *1* (41), 12759-12767.

8.   Pang, H.; Lu, Q.; Li, Y.; Gao, F., Facile Synthesis of Nickel Oxide Nanotubes and their Antibacterial, Electrochemical and Magnetic Properties. *Chem. Commun.* **2009,** (48), 7542-7544.

9.   Meher, S. K.; Rao, G. R., Ultralayered Co_3O_4 for High-Performance Supercapacitor Applications. *J. Phys. Chem.C* **2011,** *115* (31), 15646-15654.

10.   Tummala, R.; Guduru, R. K.; Mohanty, P. S., Nanostructured Co_3O_4 Electrodes for Supercapacitor Applications from Plasma Spray Technique. *J. Power Sources* **2012,** *209*, 44-51.

11.   Singh, A. K.; Sarkar, D.; Khan, G. G.; Mandal, K., Hydrogenated NiO Nanoblock Architecture for High Performance Pseudocapacitor. *ACS Appl. Mater. Interfaces* **2014,** *6* (7), 4684-4692.

12.   Wang, R.; Yan, X.; Lang, J.; Zheng, Z.; Zhang, P., A Hybrid Supercapacitor Based on Flower-like $Co(OH)_2$ and Urchin-like VN Electrode Materials. *J. Mater. Chem. A* **2014,** *2* (32), 12724-12732.

13.   Wu, H. B.; Pang, H.; Lou, X. W., Facile Synthesis of Mesoporous $Ni_{0.3}Co_{2.7}O_4$ Hierarchical Structures for High-Performance Supercapacitors. *Energy Environ. Sci.* **2013,** *6* (12), 3619-3626.

14.   Liu, X.; Shi, S.; Xiong, Q.; Li, L.; Zhang, Y.; Tang, H.; Gu, C.; Wang, X.; Tu, J., Hierarchical $NiCo_2O_4$@$NiCo_2O_4$ Core/Shell Nanoflake Arrays as High-Performance Supercapacitor Materials. *ACS Appl. Mater. Interfaces* **2013,** *5* (17), 8790-8795.

15.   Cheng, H.; Lu, Z.; Deng, J.; Chung, C. Y.; Zhang, K.; Li, Y., A Facile Method to Improve the High Rate Capability of Co_3O_4 Nanowire Array Electrodes. *Nano Res.* **2010,** *3* (12), 895-901.

16.   Feng, C.; Zhang, J.; Deng, Y.; Zhong, C.; Liu, L.; Hu, W., Hollow Co_3O_4 Microspheres with Nano-sized Shells: One-step Large-scale Synthesis, Growth Mechanism and Supercapacitor Properties. *RSC Adv.* **2015,** *5* (52), 42055-42062.

17.   Xiong, S.; Yuan, C.; Zhang, X.; Xi, B.; Qian, Y., Controllable Synthesis of Mesoporous Co_3O_4 Nanostructures with Tunable Morphology for Application in Supercapacitors. *Chem. Eur. J.* **2009,** *15* (21), 5320-5326.

18.   Wang, G.; Shen, X.; Horvat, J.; Wang, B.; Liu, H.; Wexler, D.; Yao, J., Hydrothermal Synthesis and Optical, Magnetic, and Supercapacitance Properties of Nanoporous Cobalt Oxide Nanorods. *J. Phys. Chem. C* **2009,** *113* (11), 4357-4361.

19.   Wang, Y.; Zhou, T.; Jiang, K.; Da, P.; Peng, Z.; Tang, J.; Kong, B.; Cai, W.-B.; Yang, Z.; Zheng, G., Reduced Mesoporous Co_3O_4 Nanowires as Efficient Water Oxidation Electrocatalysts and Supercapacitor Electrodes. *Adv. Energy Mater.* **2014,** *4* (16), n/a-n/a.

20.   Deori, K.; Ujjain, S. K.; Sharma, R. K.; Deka, S., Morphology Controlled Synthesis of Nanoporous Co_3O_4 Nanostructures and Their Charge Storage Characteristics in Supercapacitors. *ACS Appl. Mater. Interfaces* **2013,** *5* (21), 10665-10672.

21.   Pal, M.; Singh, A. K.; Rakshit, R.; Mandal, K., Surface Chemistry Modulated Introduction of Multifunctionality within Co_3O_4 Nanocubes. *RSC Adv.* **2015,** *5* (21), 16311-16318.

22.   Dong, Y.; He, K.; Yin, L.; Zhang, A., A Facile Route to Controlled Synthesis of Co_3O_4 Nanoparticles and their Environmental Catalytic Properties. *Nanotechnology* **2007,** *18* (43), 435602.

23.   Venkateswara Rao, K.; Sunandana, C. S., Co_3O_4 Nanoparticles by Chemical Combustion: Effect of Fuel to Oxidizer Ratio on Structure, Microstructure and EPR. *Solid State Commun.* **2008,** *148* (1–2), 32-37.

24.   Guo, B.; Li, C.; Yuan, Z.-Y., Nanostructured Co_3O_4 Materials: Synthesis, Characterization, and Electrochemical Behaviors as Anode Reactants in Rechargeable Lithium Ion Batteries. *J. Phys. Chem.C* **2010,** *114* (29), 12805-12817.

25.   Mao, Y.; Li, W.; Liu, P.; Chen, J.; Liang, E., Topotactic Transformation to Mesoporous Co_3O_4 Nanosheet Photocathode for Visible-Light-driven Direct Photoelectrochemical Hydrogen Generation. *Mater. Lett.* **2014,** *134*, 276-280.

26.   Zhang, Q.; Tang, X.; Ning, P.; Duan, Y.; Song, Z.; Shi, Y., Enhancement of N_2O Catalytic Decomposition Over Ca Modified Co_3O_4 Catalyst. *RSC Adv.* **2015,** *5* (63), 51263-51270.

27.   Wang, S.; Xiao, C.; Wang, P.; Li, Z.; Xiao, B.; Zhao, R.; Yang, T.; Zhang, M., Co_3O_4 Hollow Nanotubes: Facile Synthesis and Gas Sensing Properties. *Mater. Lett.* **2014,** *137*, 289-292.

28.   Xia, X.-h.; Tu, J.-p.; Zhang, Y.-q.; Mai, Y.-j.; Wang, X.-l.; Gu, C.-d.; Zhao, X.-b., Freestanding Co_3O_4 Nanowire Array for High Performance Supercapacitors. *RSC Adv.* **2012,** *2* (5), 1835-1841.

29.   Wang, H.; Zhang, L.; Tan, X.; Holt, C. M. B.; Zahiri, B.; Olsen, B. C.; Mitlin, D., Supercapacitive Properties of Hydrothermally Synthesized Co_3O_4 Nanostructures. *J. Phys. Chem.C* **2011,** *115* (35), 17599-17605.

30.   Wang, Y.; Lei, Y.; Li, J.; Gu, L.; Yuan, H.; Xiao, D., Synthesis of 3D-Nanonet Hollow Structured Co_3O_4 for High Capacity Supercapacitor. *ACS Appl. Mater. Interfaces* **2014,** *6* (9), 6739-6747.

31.   Yuan, C.; Li, J.; Hou, L.; Zhang, X.; Shen, L.; Lou, X. W., Ultrathin Mesoporous $NiCo_2O_4$ Nanosheets Supported on Ni Foam as Advanced Electrodes for Supercapacitors. *Adv. Funct. Mater.* **2012,** *22* (21), 4592-4597.

Chapter 8 | Conclusion and Scope for Future Work

This chapter gives an overall conclusion of the work described so far and the scopes for further work in this specific field.

8.1. Epilogue

In this thesis, we have mainly focused our work on the synthesis of transition metal oxide (Fe_2O_3, $MnFe_2O_4$, Co_3O_4, and $CoFe_2O_4$) based magnetic nanostructures (nanoparticles (NPs), and nanocubes (NCs)) by different chemical synthesis procedures followed by functionalization with small organic ligands to make the nanomaterials water dispersible, a very essential criteria for their biological applications. We have chosen Na-tartrate as biocompatible hydrophilic organic ligand. We started with Fe_2O_3 NPs (size ~50 nm), as it is extensively used in several biological applications. Very interestingly, the functionalized Fe_2O_3 NPs show intrinsic multicolor fluorescence. Through systematic study by various spectroscopic tools, we have discovered the chemistry behind the development of multicolor fluorescence from the ligand functionalized nanostructures. Proper investigation through UV-visible absorption and steady state photoluminescence study along with theoretical report in literature has revealed that ligand to metal charge transfer (LMCT) transition from highest occupied energy level of ligand to lowest unoccupied energy level of Fe^{3+} of the NPs and weakly allowed d-d transitions centered over Fe^{3+} ions in the NPs play the key role behind the generation of multicolor fluorescence from the functionalized Fe_2O_3 NPs. But the fluorescence intensity was low because of larger size of NPs and both Laporte and spin forbidden d-d transitions in case of Fe^{3+} ions being a d^5 system. Then we focused on $MnFe_2O_4$ NPs due to its highest magnetization and decreased the size upto ~5 nm to enhance surface to volume ratio. Detailed investigation through UV-visible absorption, steady state, and time-resolved photoluminescence study has revealed that LMCT transition from highest occupied energy level of ligand to lowest unoccupied energy level of $Mn^{2+/3+}$or Fe^{3+} and Jahn-Teller distorted d-d transitions centered over Mn^{3+} ions (d^4 sytem) in the $MnFe_2O_4$ NPs play the key role behind the generation of intense multicolor fluorescence from the functionalized NPs. In order to explore other spin allowed d-systems, such as d^6 and d^7 that is in case of Co^{3+} and Co^{2+}, we have selected Co_3O_4 nanocubes. Functionalized Co_3O_4 nanocubes exhibit strong fluorescence covering whole visible region. VSM measurements have exhibited

antiferromagnetic behavior of Co_3O_4 NCs changes to ferromagnetic due to pinning of surface spins by the ligands. To improve magnetism we incorporated Fe within system and concentrated to functionalization of $CoFe_2O_4$ NPs, which also exhibits remarkable fluorescence. VSM measurements have exhibited superparamagnetic nature of $CoFe_2O_4/MnFe_2O_4$ NPs remains unchanged after surface modification. Additionally, we have observed excellent efficiency of the functionalized nanostructures in degradation of biologically harmful (bilirubin) and unprecedented photocatalytic activity in removal of environmentally harmful (methylene blue) pigments, which can be attributed to metal ion assisted ROS (reactive oxygen species) mechanism. So, incorporating improved magnetic, optical, and catalytic properties simultaneously, we have developed multifunctional nanostructures that may find pioneering diverse applications ranging from diagnostics, therapeutics to environmental remediation.

To utilize the enhanced surface to volume ratio of very small nanostructures to solve energy problem, we have fabricated electrode by growing ultra small Co_3O_4 NCs directly on Ni foam through facile one step solvothermal route. Electrochemical study reveals an enhanced pseudocapacitive performance of the Co_3O_4 NCs with high rate capability. The remarkable supercapacitance can be attributed to facile one step fabrication of electrode by growing the NCs directly over Ni foam, very small size of NCs with nanopores leading to high surface area, larger interaction of electrolyte and active material even in the interior region of the electrode, fast ion and electron transfer. Due to the excellent electrochemical performance of Co_3O_4 NCs, it holds promise in the field of high performance supercapacitor devices.

8.2. Scope for Future Work

Our developed intrinsic multicolor fluorescent magnetic nanostructures can simultaneously be used in imaging, MRI, and targeted drug delivery. We are planning, *in vitro* experiments for dual imaging of MRI and fluorescence along with rigorous toxicological study of the NPs on different cell line of the animal organs.

The functionalized nanostructures having excellent catalytic activity in degradation of biologically harmful pigment, bilirubin, can be efficiently used in treatment of hyperbilirubinemia. Moreover, due to the unprecedented photocatalytic activity of functionalized nanostructures in degradation of environmentally harmful dye, methylene blue, they can be used in waste water treatment.

Our developed new functionalization strategy can be explored in case of other spin allowed d-systems such as d^1, d^2, d^3, d^8, d^9 systems. For example multifunctional NiO, and $NiFe_2O_4$ NPs can be fabricated utilizing allowed d-d transitions of Ni^{2+}, which is a d^8 system.

Fabrication of electrodes for supercapacitors made of transition metal oxide (such as NiO, Co_3O_4, MnO_2, Fe_2O_3, TiO_2, V_2O_5 etc.) based nanomaterials having various morphologies and size have attracted immense attention of researchers to maximize their surface to volume ratio leading to improved energy storing capacity per unit mass as high as possible and it is an ever growing challenge to solve accelerating energy crisis. Not only the active material but also rational designing of appropriate substrate with high conductivity and surface area can improve the supercapacitive performance of the electrode significantly.